Role of Surface Passivation and Doping on the Development of Quantum Dot Solar Cells

by

Debranjan Mandal
10CC17A26016

A thesis submitted to the
Academy of Scientific & Innovative Research
for the award of the degree of

DOCTOR OF PHILOSOPHY
in
SCIENCE

Under the supervision of
Dr. Arup K. Rath

CSIR-National Chemical Laboratory, Pune

Academy of Scientific and Innovative Research
AcSIR Headquarters, CSIR-HRDC campus
Sector 19, Kamla Nehru Nagar,
Ghaziabad, U.P. – 201 002, India

April, 2021

Certificate

This is to certify that the work incorporated in this Ph.D. thesis entitled, *"Role of Surface Passivation and Doping on the Development of Quantum Dot Solar Cells"*, submitted by *Debranjan Mandal* to the Academy of Scientific and Innovative Research (AcSIR) in fulfillment of the requirements for the award of the Degree of *Doctor of Philosophy in Science*, embodies original research work carried-out by the student. We, further certify that this work has not been submitted to any other University or Institution in part or full for the award of any degree or diploma. Research material(s) obtained from other source(s) and used in this research work has/have been duly acknowledged in the thesis. Image(s), illustration(s), figure(s), table(s) etc., used in the thesis from other source(s), have also been duly cited and acknowledged.

Debranjan Mandal	Dr. Arup K. Rath
(Research Student)	(Research Supervisor)
09.04.2021	09.04.2021

STATEMENTS OF ACADEMIC INTEGRITY

I Debranjan Mandal, a Ph.D. student of the Academy of Scientific and Innovative Research (AcSIR) with Registration No. 10CC17A26016 hereby undertake that, the thesis entitled "Role of Surface Passivation and Doping on the Development of Quantum Dot Solar Cells" has been prepared by me and that the document reports original work carried out by me and is free of any plagiarism in compliance with the UGC Regulations on *"Promotion of Academic Integrity and Prevention of Plagiarism in Higher Educational Institutions (2018)"* and the CSIR Guidelines for "*Ethics in Research and in Governance (2020)"*.

Signature of the Student
Date : 09.04.2021
Place : Pune

It is hereby certified that the work done by the student, under my/our supervision, is plagiarism-free in accordance with the UGC Regulations on *"Promotion of Academic Integrity and Prevention of Plagiarism in Higher Educational Institutions (2018)"* and the CSIR Guidelines for "*Ethics in Research and in Governance (2020)"*.

Signature of the Supervisor
Name : Dr. Arup K. Rath
Date : 09.04.2021
Place : Pune

This dissertation is dedicated to my little nephew "Argha"

Acknowledgments

During the entire period of my doctoral research, I have been acquainted, accompanied, and supported by many people. Herein I take this opportunity to express my heartfelt gratitude to all of them.

First of all, I would like to express my heartfelt thanks to my supervisor, Dr. Arup. K. Rath, for his constant support and guidance throughout this journey. His precious knowledge, wise advice about life, and generous help have significantly shaped the course of my doctoral journey and made me grow, not only as a researcher but also as a wise and responsible human being. I feel immensely privileged to be a part of his esteemed research group at CSIR-National Chemical Laboratory. It is this very place where I have learned to nurture a blend of hard work and discipline to shape my professional and personal aspects of life. Under his supervision and guidance, I have learned not only the art of culturing science but also the art of thinking out of the box. What I have gained and learned from him can never be repaid in any possible form. I wish him the best of luck in his quest to perturb the limits of materials science, and may nothing, but great things happen to him and his family.

I owe to thank my doctoral advisory committee (DAC) members, Dr. Sreekumar Kurungot, Dr. Sayan Bagchi, and Dr. Shatabdi Porel Mukherjee, for their constant support extended with guidance and suggestions.

I am grateful to Prof. Dr. Ashish K. Lele (Director, CSIR-NCL), Prof. Dr. Ashwini K. Nangia (Former Director, CSIR-NCL), Prof. Dr. Sourav Pal (Former Director, CSIR-NCL), Dr. P. A. Joy (Former HoD, Division of Physical & Materials Chemistry, CSIR-NCL) and Dr. B. L. V Prasad (HoD, Division of Physical & Materials Chemistry, CSIR-NCL) for giving me this opportunity and providing me with advanced research infrastructure and facilities.

I would like to express my gratitude to Dr. K. Selvaraj, Mr. R. S. Gholap, and his team, especially Venkatesh and Pankaj, for help in HR-TEM, FE-SEM measurements, Mr. Abhijit Bera for help in XRD measurements, Mr. Srinivas Deo for her help in XPS measurements and Dr. Satyajit Sahu (IIT Jodhpur) and his doctoral student Mr. Jayanta Bera for their AFM measurements.

My list of acknowledgments would be incomplete without mentioning the name of Dr. Dulal Senapati (SINP Kolkata), who had effectively incepted in me a deep sense of interest in the field of materials science. I have got my first exposure and experience in laboratory research under his guidance. Besides, he has also provided me with valuable knowledge regarding the art of nanomaterials synthesis that has helped me in this very journey. I would also like to thank Prof. M. V. Sangaranarayanan (IIT Madras), under the guidance of whom I have completed my M. Sc. Dissertation and gained immense knowledge in fundamental physical chemistry and electrochemistry. I have also acquired skills in handling electrochemical instruments.

It's my immense pleasure to thank my lab mates Prasenjit, Ashish, Rangarajan, Anupam, Apoorva, Saptam, Chandan, Neha, and Asif for devoting their precious time and providing me with valuable suggestions. A special thank you also goes to my co-author Prasenjit for his effortless help to make me understand the device physics. I would especially like to thank Mr. Abhijit bera for his fruitful suggestions and moral support throughout my research time. I would also like to express my heartfelt thanks to Pranab Deb and Tapas Halder for assisting me in my research projects.

No words are sufficient to acknowledge my prized friends in and out of NCL who have helped me at various stages of my life and my research work. First of all, I don't know how to quantify the amount of love and support I have got from my roommates Tamal Das, Subhrashis Banerjee, and Tapas Halder to complete this PhD journey. I would love to thank Dr. Krisahnu Mondal, Dr. Saibal Bera, Dr. Subrata Mukherjee, Dr. Sivaprasad Midya, Dr. Manjur Oyasim Akram, Dr. Arunava Maity, Dr. Shantigopal Mondal, Dr. Monoj Nandi, Dr. Bipul Biswas, Dr. Sudip Sashmal, Dr. Atreyee Banerjee, Dr. Suvendu Karak, Kousik Maji, Asish Bera, Pronoy Das, Rahul Chowdhury, Sandipan Jana, Himadri Sashmal, Anirban Sen, Amarnath Singham, Swapnil Halnor, Sanjukta Pahar, Pooja Dhorge, Milan Bisai, Anagh Mukherjee, Bittu Chandra, Ujjwal Nandi, Pankaj Shaw, Varre Swamy, Srijan Chatterjee, Deborin Ghosh, Samadhan Deshmukh, Sushil Sakhpal, Somnath Kashid, Sutanu Biswas for being a valuable part of my NCL family. I would also like to thank my friend outside of NCL, namely, Dr. Samrat Das Adhikari, Dr. Suman Bera, Dr. Subrata Mondal, Dr. Sourav Karmakar, Dr. Ashish Das, Dr. Barun K. Maity, Pradip Maji, Sushovan Samanta, Narayan Sau, and Ayan Maji for being there as constant moral support. I really enjoyed the time that I spent with these awesome people.

Without the funding that I have received, this Ph. D. would not have been possible. Hence, I would like to express my sincere appreciation to CSIR for fellowship.

Words are inadequate to express my feelings and gratitude to my family for their unconditional love, care, and support throughout my life. I would not have achieved anything without my mom and dad's support, who gave me the freedom to explore my world and explore who I am. With immense gratitude and reverence, I acknowledge my mom, Mrs. Anjali Mandal, and my dad, Mr. Pranab Kr. Mandal for shaping my life and making me who I am today. I would also like to give special thanks to my brother Nistharanjan and Pritiranjan for their continuous support during my hard times. I would also like to express my sincere thanks to my brother-in-law Kamal Mahapatra, for his constant inspiration throughout my research journey.

I am indebted to the eminent scientific community, whose achievements are a constant source of inspiration for me.

Finally, with immense respect and gratitude, I bow down in front of the almighty for all that has been offered to me. I am and will remain thankful for everything that has ever happened in my PhD journey, the good and the bad, for everything that I have achieved and the few that I have lost. Some were blessings, and some were lessons worth learning.

Debranjan Mandal

Table of Contents

Contents	Page No
Abbreviations	viii
List of Figures	xii
List of Tables	xxiv
Synopsis report	xxvi
Chapter 1: Introduction	**1-43**
1.1 Solar energy	2
1.2 Solar Cells	3
1.2.1 Fundamentals of solar cells	3
1.2.2 Characteristics of solar cells	6
1.2.3 Carrier collection	9
1.2.4 Efficiency limitations	11
1.2.5 Non-ideal effects	13
1.3 Current status of solar cells technology	14
1.4 Quantum Dots	15
1.4.1 Basics of Quantum Dots	15
1.4.2 Colloidal Synthesis of Quantum Dots	18
1.4.3 PbS Quantum Dots and their surface chemistry	21
1.5 PbS Quantum Dots photovoltaics	23
1.5.1 Surface Passivation for Quantum Dots Solar cell	23
1.5.2 Doping of nanocrystals	28
1.5.3 Device engineering of Quantum Dots Solar cell	29
1.5.4 Progress in Quantum Dots Solar cell	34
1.5.5 Challenges	35

1.6 Thesis Overview 36
1.7 References 37

Chapter 2: 44-74

Low temperature processed niobium doped TiO_2 as n-type electron transport layer in quantum dot solar cell

2.1 Introduction 45
2.2 Experimental Details 47
2.2.1 Preparation of TiO_2 sol gel 47
2.2.2 Preparation of Nb doped TiO_2 sol gel 47
2.2.3 Synthesis of Colloidal PbS QDs 47
2.2.4 Device Fabrication 48
2.2.5 Materials Characterization Techniques 49
2.2.6 Device Characterization Techniques 49
2.3 Results and Discussions 51
2.3.1 XPS analysis of TiO_2 51
2.3.2 XRD characteristics of TiO_2 53
2.3.3 TEM analysis of TiO_2 54
2.3.4 Surface SEM image of TiO_2 films 55
2.3.5 Absorption study of TiO_2 thin films 55
2.3.6 Cyclic Voltammetry study of TiO_2 56
2.3.7 Absorbance spectra of PbS QDs 57
2.3.8 TEM image of PbS QDs 57
2.3.9 J-V characteristics of solar cell 58
2.3.10 Time dependant J_{sc} measurement 61
2.3.11 EQE spectrum 62
2.3.12 Statistical distribution of PCE 62
2.3.13 Cap-V analysis 63

2.3.14 Simulation study 65
2.3.15 Mobility measurement from MSM device 67
2.4 Conclusion 70
2.5 References 71

Chapter 3: 75-106

Comparative study of surface passivating organic ligands in determining the electronic properties of quantum dots solids and their impact on solar cell performance

3.1 Introduction 76
3.2 Experimental Details 79
3.2.1 Preparation of TiO_2 sol gel 79
3.2.2 Device Fabrication 79
3.2.3 Materials Characterization Techniques 80
3.2.4 Device Characterization Techniques 80
3.3 Results and Discussions 82
3.3.1 FT-IR analysis 82
3.3.2 J-V Characteristics of PV device 83
3.3.3 Photo-CELIV analysis 84
3.3.4 Series Resistance calculation 87
3.3.5 Cap-V analysis 88
3.3.6 Transient photovoltage and photocurrent study 90
3.3.7 Intensity dependant J_{sc} & V_{oc} study 92
3.3.8 Temperature dependant V_{oc} study 93
3.3.9 Device Stability 96
3.3.10 XPS study 97
3.3.11 Thin film absorption & UPS study 99
3.4 Conclusion 101

3.5 References 102

Chapter 4: 107-139

Butylamine catalyzed 2D matrix engineering on quantum dot surface for solar cell application

4.1 Introduction 108
4.2 Experimental Details 111
4.2.1 ZnO nanocrystals preparation 111
4.2.2 Synthesis of Colloidal PbS QDs 111
4.2.3 Ligand exchange of PbS QDs 111
4.2.4 Device Fabrication 112
4.2.5 Materials Characterization Techniques 112
4.2.6 Device Characterization Techniques 113
4.3 Results and Discussions 113
4.3.1 XRD analysis 113
4.3.2 Absorption and PL study 120
4.3.3 FT-IR study 121
4.3.4 Reaction mechanism 123
4.3.5 XPS analysis 124
4.3.6 TEM image analysis 126
4.3.7 Cross sectional SEM image of solar cell 127
4.3.8 J-V characteristics 128
4.3.9 EQE spectrum 129
4.3.10 Statistical distribution of PCE 130
4.3.11 Thickness optimization of device 131
4.3.12 Carrier lifetime and D.O.S calculation 132
4.3.13 Bias dependant transient time study 133
4.4 Conclusion 135

4.5 References 135

Chapter 5: 140-171

Hybrid passivated quantum dot ink attains thinner shell growth and clean energy bandgap for photovoltaic application

5.1 Introduction 141
5.2 Experimental Details 143
5.2.1 Partial Ligand exchange of PbS QDs 143
5.2.2 Halometallate Ligand exchange of PbS QDs 143
5.2.3 Device Fabrication 144
5.2.4 Materials Characterization Techniques 144
5.2.5 Device Characterization Techniques 144
5.3 Results and Discussions 145
5.3.1 XPS analysis 145
5.3.2 UPS study 148
5.3.3 Ligand structure characteristics 150
5.3.4 Absorption and PL study 151
5.3.5 TEM image analysis 154
5.3.6 Surface SEM and AFM image 156
5.3.7 Cross sectional SEM image of device 158
5.3.8 J-V characteristics 159
5.3.9 Device Thickness optimization 160
5.3.10 EQE spectrum 161
5.3.11 Cap-V analysis 162
5.3.12 Power dependant V_{oc} study 163
5.3.13 Device stability 163
5.3.14 Photo-CELIV analysis 164
5.3.15 Carrier lifetime and D.O.S calculation 165

5.4 Conclusion 166
5.5 References 167

Chapter 6: 172-204
Control over ligand ratio on thiol, halometallate mediated one-step hybrid passivation of quantum dots for photovoltaics

6.1 Introduction 173
6.2 Experimental Details 175
6.2.1 Ligand exchange of PbS QDs 175
6.2.2 Device Fabrication 175
6.2.3 Materials Characterization Techniques 176
6.2.4 Device Characterization Techniques 176
6.3 Results and Discussions 177
6.3.1 NMR study 177
6.3.2 FT-IR analysis 179
6.3.3 Absorption and PL study 180
6.3.4 TEM image analysis 185
6.3.5 Surface SEM image 187
6.3.6 Cross sectional SEM image of device 188
6.3.7 J-V characteristics 189
6.3.8 Device thickness optimization 192
6.3.9 Power dependant V_{oc} study 193
6.3.10 Device stability 194
6.3.11 Cap-V analysis 195
6.3.12 Lifetime and D.O.S calculation 196
6.3.13 Mobility calculation 197
6.4 Conclusion 199
6.5 References 200

Chapter 7: **205-209**

Conclusion and future work

7.1 Conclusion of thesis findings 205

7.2 Future work 207

7.3 References 209

Abbreviations

List of Acronyms

AC	Alternative current
AFM	Atomic force microscope
AM	Air Mass
ATR	Attenuated total reflectance
a.u.	Arbitrary unit
B.P.	Boiling Point
BE	Binding energy
CB	Conduction Band
Cap-V	Capacitance-Voltage
CELIV	Charge extraction by linearly increasing voltage
CQD	Colloidal quantum dot(s)
DFT	Density functional theory
DOS	Density of states
DSSC	Dye sensitized solar cell
ETL	Electron transport layer
EQE	External quantum efficiency
FF	Fill factor
FWHM	Full-width at half-maximum
FTIR	Fourier transform infrared
HOMO	Highest occupied molecular orbital
HRTEM	High-resolution transmission electron microscope
HTL	Hole transporting layer
IR	Infrared
LUMO	Lowest unoccupied molecular orbital
LED	Light emitting diode
LBL	Layer by layer
MSM	Metal-semiconductor-metal
NC	Nanocrystal(s)
NIR	Near infrared
NMR	Nuclear magnetic resonance

OPV	Organic photovoltaic
PCE	Power conversion efficiency
PL	Photoluminescence
PLQY	Photoluminescence quantum yield
PV	Photovoltaic
QD	Quantum dot(s)
RPM	Revolutions per minute
SAED	Small area electron diffraction
SCAPS	Solar cell capacitance simulator
SEM	Scanning electron microscope
SPLE	Solution phase ligand exchange
SSLE	Solid state ligand exchange
TEM	Transmission electron microscope
TPV	Transient photovoltage
TPC	Transient photocurrent
UV	Ultraviolet
UPS	Ultraviolet photoelectron spectroscopy
VB	Valance band
XRD	X-ray Diffraction
XPS	X-ray photoelectron spectroscopy

List of Symbols

A	Ampere
Å	Angstrom
a_B	Bohr exciton radius
δ	Chemical shift
°C	Degree Centigrade
cm	centimetre
e	Elementary charge
E	Energy
eV	Electron volt
E_a	Activation energy

E_F	Fermi level
E_{Fi}	Intrinsic Fermi level
E_{Fn}	n-type Quasi Fermi level
E_{Fp}	p-type Quasi Fermi level
E_g	Bandgap
E_{photon}	Energy of photon
ε	Dielectric constant
Φ	Work function
η	Power conversion efficiency
h	Planck's constant
Hz	Hertz
I	Current
J	Current density
J_0	Reverse saturation current density
J_d	Diode current density
J_{ph}	Photocurrent density
J_m	Maximum power point short-circuit current density
J_{sc}	Short-circuit current density
k	Boltzmann's constant
K	Kelvin
kHz	Kilohertz
L_D	Diffusion length
M	Molar
mBar	Millibar
MHz	Megahertz
mA	Milliampere
mg	Milligram
mL	Millilitre
mm	millimetre
mmol	Millimole
mM	Millimolar
mV	Millivolt
µL	Microlitre

µs	Microsecond
µm	Micrometre
nm	Nanometre
Ω	Ohm
q	Electronic charge
λ	Wavelength
P	Power
%	Percentage
R	Resistive load
R_{sh}	Shunt resistance
R_s	Series resistance
T	Temperature
V	Voltage
V_m	Maximum power point open circuit voltage
V_{oc}	Open circuit voltage
V_{bi}	Built-in voltage
s	Second
W	watt

Chemical Notations

AI	Ammonium iodide
BA	Butylamine
CPT	3-Chloro-1-propanethiol
$CdCl_2$	Cadmium chloride
DMF	N, N-Dimethylformamide
EDT	1,2-Ethanedithiol
FTO	Fluorine doped tin oxide
ITO	Indium doped tin oxide
MAI	Methylammonium Iodide
MoO_3	Molybdenum trioxide
MPA	3-Mercaptopropinoic acid
OA	Oleic Acid
ODE	1-Octadecene

PbI_2	Lead iodide
$PbBr_2$	Lead bromide
PbS	Lead sulfide
TGA	Thioglycolic Acid
TLA	Thiolactic Acid
$(TMS)_2S$	Hexamethyldisilathiane

List of Figures

Figure No	Figure Caption	Page No
Figure 1.1	Solar spectrum irradiance collected just outside of earth's atmosphere (AM 0), globally averaged terrestrial data (AM 1.5G), and a blackbody approximation of the sun assuming the sun's surface temperature of about 5800K.	2
Figure 1.2	Representation of simplified *p-n* junction under thermal equilibrium, "-" represents negatively charged acceptor atoms, and "+" represents positively charged donor atoms. The light blue junction presents the metallurgical junction separating *p*-type and *n*-type semiconductors.	4
Figure 1.3	Band diagram of *p-n* junction under thermal equilibrium (dark conditions). 'e' represents the elementary charge, and V_{bi} is the built-in voltage.	4
Figure 1.4	Band diagram of the ideal *p-n* junction and band diagrams under (a,d) zero bias, (b,e) forward bias, and (c,f) reverse bias.	5
Figure 1.5	*p-n* junction solar cell with a resistive load under photo illumination.	7
Figure 1.6	Current-voltage characteristics of a solar cell under illumination.	8
Figure 1.7	Energy band diagram of the *p-n* diode to represent different region and carrier transport characteristics.	10
Figure 1.8	Single-junction solar cell efficiency vs. semiconductor bandgap (Eg).	12

Figure 1.9	Schematic representation of band structure from bulk material to quantum dots and change in bandgap.	18
Figure 1.10	La Mer and Dinegar nucleation and growth model of CQDs.	20
Figure 1.11	Schematic representation of hot injection method to synthesize PbS NCs.	21
Figure 1.12	A schematic presentation of oleic acid capped cuboctahedral PbS NC and facet specific binding of long-chain oleic acid molecules.	23
Figure 1.13	Schematic band diagram presentation of passivated and un-passivated NCs.	25
Figure 1.14	Schematic of different ligand exchange process, (a) Replacement of long-chain insulating molecules by smaller ligand (L) (b) Solid-state ligand exchange (c) Solution phase ligand exchange.	26
Figure 1.15	Band diagram of Schottky junction solar cell constructed by *p*-type PbS CQDs with a low work function material like aluminium.	30
Figure 1.16	Device architecture of PbS CQDs Schottky solar cell with the integration of thin LiF layer.	31
Figure 1.17	Schematic representation of depleted heterojunction PbS CQDs solar cell (a) Device architecture (b) Band diagram.	32
Figure 1.18	Different architecture of bulk heterojunction solar cells.	32
Figure 1.19	Schematic representation of graded doping PbS CQDs device (a) Device architecture (b) Band diagram.	33
Figure 2.1	High resolution XPS scan for Ti, O, C and Nb of samples TiO_2-500°C, TiO_2-150°C, 2.5%Nb/ TiO_2-150°C, 5%Nb/TiO_2-150°C are given in chronological manner. (a) Ti 2P spectra (b) O 1s spectra (c) C 1s spectra and (d) Nb 3d spectra.	51
Figure 2.2	X-ray diffraction pattern of TiO_2 films processed at different temperature and low-temperature Nb-doped TiO_2 film.	53
Figure 2.3	HRTEM image of (a) TiO_2-150°C and (b) 2.5Nb/TiO_2-150°C. The selected area electron diffraction (SAED) pattern is shown at the inset of the respective image.	54
Figure 2.4	Surface SEM images of (a) TiO_2-500°C (2) TiO_2-150°C and (c) 2.5Nb/ TiO_2-150°C films. Insets show the higher magnification image of the films.	55

Figure 2.5	(a) Absolute absorbance of the TiO_2 thin films measured using integrating sphere spectrometer. (b) Tauc plot of the films to determine optical bandgap. The intersection of the extrapolation of the linear region of $(\alpha h\nu)^2$ vs. E (eV) plots indicated the optical bandgap of the corresponding films.	56
Figure 2.6	Cyclic voltammetry of (a) TiO_2-150°C, 2.5Nb/ TiO_2-150°C and 5Nb/ TiO_2-150°C thin films on top of ITO and (b), cyclic voltammetry of TiO_2-500°C thin film on FTO.	56
Figure 2.7	Absorbance spectra of PbS QDs dispersed in toluene. The first excitonic peak position of the QDs arises at 945 nm.	57
Figure 2.8	(a) TEM image, (b) Particle size distribution of oleic acid capped PbS NCs.	57
Figure 2.9	(a) J-V characteristics of PV devices for different *n*-type layers under dark condition. Before and after twenty minutes, light soaking situations are represented by lines and scatter symbols, respectively. (b) J-V characteristics of solar cells under 1.5 AM illumination after photodoping saturation.	58
Figure 2.10	Forward and reverse scan of (a) TiO_2-500°C, (b) TiO_2-150 °C and (c) 2.5Nb/ TiO_2-150°C based PV devices under 1.5 A.M. solar illumination.	60
Figure 2.11	Short circuit current density (J_{sc}) Vs. time for PV devices measured under continuous solar illumination.	61
Figure 2.12	Comparison of EQE spectrum of PV devices with different *n*-type layers.	62
Figure 2.13	Statistical variation in photovoltaic efficiency of (a) TiO_2-150°C (b) 2.5 Nb/ TiO_2-150°C based solar cells.	63
Figure 2.14	Cap-V characteristics of the PV devices, (a) before (b) after light soaking, respectively.	64
Figure 2.15	Depletion width vs. applied bias plots of PbS layer.	64
Figure 2.16	(a) represents the experimental (scatter) and simulated (line) J -V plot for 2.5Nb/TiO_2-150°C PV device under dark and 1.5 AM illumination condition under saturation condition. (b) Simulated dark J-V response of the device for varied electron mobility of	67

2.5Nb/TiO_2-150°C layer, from 1x 10^{-3} $cm^2V^{-1}s^{-1}$ to 1x 10^{-9} $cm^2V^{-1}s^{-1}$. Black symbol+line in (b) represents the experimental J-V curve of the device under dark before light soaking.

Figure 2.17 (a) represents current vs time plot for MSM devices made of 2.5Nb/TiO_2-150°C and 5Nb/TiO_2-150°C, measured at constant 0.3V applied bias. For both devices, the current remains invariant with time under the dark condition as marked by an arrow in the plot. Under solar illumination, the current of the devices increases monotonically with time. The "Light on" position is marked to guide the eye. (b) shows the decay of current with time at constantly applied bias 0.3V, for MSM - 5Nb/TiO_2-150°C device after the solar illumination is taken off. 68

Figure 2.18 Current vs. time for MSM-5Nb/TiO_2-150°C device at different illumination wavelengths measured at 0.3V applied bias. The current of the device did not change for illumination wavelength of 600 nm and 400 nm, whereas current increases consistently with time under 330 nm wavelength illuminations. 69

Figure 3.1 ATR FT-IR spectra under reflective mode for PbS QD films treated with various surface ligands on a glass substrate. 82

Figure 3.2 Current density vs. voltage characteristics of PbS QD based solar cells, treated with various ligands. 83

Figure 3.3 Typical results for CELIV measurements are shown to explain different parameters of equations 3.1 and 3.2. 85

Figure 3.4 (a)-(d) represent the photo-CELIV measurements for MPA, TGA, TLA and CPT treated PbS QD solar cells, respectively. Current evolution and the applied voltage pulse, as a function of time, are shown in the same plot for the respective devices. 86

Figure 3.5 (a) variations in hole mobility and (b) dielectric constant of PbS QD layers treated with various ligands. 87

Figure 3.6 Current density vs. voltage plots of solar cells for various surface ligands under dark condition are shown. 87

Figure 3.7 Capacitance-voltage (C-V) and $1/C^2$-V plots for solar cells treated with various ligands are shown in (a) and (b), respectively. 89

Depletion width at zero bias and carrier density as determined from C-V and $1/C^2$-V plots for the PbS layers with different surface ligand types are shown in (c).

Figure 3.8 (a) Comparison of photocarrier lifetime for various ligand types as determined from transient photovoltage measurements. (b) Current transit times for various ligand types at short circuit condition. 90

Figure 3.9 Intensity dependent (a) current density and (b) open-circuit voltage variation for solar cells treated with different ligands. Monochromatic illumination of 635 nm laser light is used for the intensity-dependent study. 93

Figure 3.10 Temperature-dependent V_{oc} of photovoltaic devices for different ligand types measured at 1.5 A.M. solar illuminations is shown. Extrapolation of the high-temperature linear region of V_{oc} to determine E_a for various ligands are shown by dashed lines. 94

Figure 3.11 Stability of solar cells for different ligand passivation. (a) shows the evolution of normalized power conversion efficiency (PCE) with storing time for three ligands. Evolution of (b) V_{oc}, (c) J_{sc} and (d) fill factor (FF) with time is shown. V_{oc}, $J_{sc,}$ and FF values are normalized for clear presentation. 96

Figure 3.12 Comparison of XPS S 2p spectra for (a) MPA (b) TGA and (c) TLA passivated PbS QD films. Gray (scatter + line) represents the experimental data, and the black line represents the fitted experimental results. Peak positions corresponding to binding energy 160.30 eV and 161.48 eV are attributed (red) to the doublet splitting of S for PbS. Peaks at 161.38 eV (blue), 162.56 eV (wine line), 164.8 eV (olive), and 166.1 eV (orange) correspond to S-C bond, S-S bond, $PbSO_3$and $PbSO_4$ respectively. 97

Figure 3.13 Absorption spectrums of PbS QD films treated with various surface ligands with as-synthesized oleic acid capped QDs. 99

Figure 3.14 (a) shows the full energy range UPS spectra of PbS QD films for different ligands. (b) and (c) show the magnified view of secondary energy cut-off (SEC) and onset energy region, respectively. He-Iα radiation of energy 21.22 eV is used for the UPS measurement. (d) 100

shows the valence band (VB) and conduction band (CB) positions as determined from absorption spectrum and UPS measurement.

Figure 4.1 XRD pattern of the annealed (70°C) PbS QD film treated with AI and MAI. The peak positions correspond to PbS and $(BA)_2PbI_4$ are marked in blue and red color, respectively. 114

Figure 4.2 XRD spectrum of PbI_2 and $PbAc_2$ powder. 115

Figure 4.3 XRD spectrum for different ligands. Olive and red lines indicate the equidistant peaks correspond to the 2D Pb-amine complex and $(BA)_2PbI_4$ perovskite, respectively. 115

Figure 4.4 Comparison of the XRD spectrum of AI treated PbS QDs films deposited from 4:1 BA: HA mixed solvent and only BA. 116

Figure 4.5 Evolution of XRD pattern at various stages of the AI ligand exchange process. Thin films of PbS QDs are measured (i) pristine OA caped, (ii) intermediate stage of ligand exchange in DMF, (iii) deposited from BA but not annealed, and (iv) deposited from BA and annealed at 70°C. 117

Figure 4.6 (a) Magnified view of the XRD peaks of PbS QDs at various stages of the AI ligand exchange process. XRD spectrum of QDs is shown for (i) pristine OA caped, (ii) intermediate stage of ligand exchange in DMF, (iii) deposited from BA but not annealed, and (iv) deposited from BA and annealed at 70°C. The peaks are fitted using Gaussian fitting. (b) Evolution of QDs size, (c) Change in 2θ value and (d) PbS axis length at different stages of the ligand exchange process for both (111) and (200) planes. 118

Figure 4.7 Comparison of the XRD spectrum for AI treated QD films for non-annealed and annealed films. 2D BA_2PbI_4 peak intensities (as marked in the plot) increases in the annealed sample. 119

Figure 4.8 The schematic illustration of the change in QD size and shape at different stages of the ligand exchange process is deconstructed from the XRD results. 119

Figure 4.9 Absorption spectrum of the oleic acid capped PbS QD film. 120

Figure 4.10 Spectroscopic characterization of the 2D crystalline matrix. (a) absorption spectra of AI and MAI treated non-annealed and 121

annealed PbS QD films. (b) absorption and (c) PL spectra of the thin films of the ligands deposited on the quartz substrate. (d) PL spectra of QD films on a quartz substrate. The excitation wavelength is 380 nm.

Figure 4.11 (a) ATR-FTIR spectroscopy of the QD film treated with different ligands (as marked in the plot) and FTIR spectrum of the pure BA in CCl_4 solution. The shift in the N-H stretching frequency and the N-H scissor mode frequency are shown in the plot. (b) ATR-FTIR spectra of $Pb(Ac)_2$+BA complex film. The appearance of a single N-H stretching peak indicates the formation of secondary amine. 122

Figure 4.12 (a) and (b) shows the Pb4f XPS signal of AI and MAI treated QDs, respectively. The Pb4f signal is deconvoluted to Pb-ligand, Pb-S, and Pb-metallic signals to fit the spectrum. 124

Figure 4.13 XPS spectrum of S2p orbital of PbS QD film treated with (a) AI and (b) MAI ligand. The fitting parameters for the $S2p_{3/2}$ and $S2p_{1/2}$ signals are summarized in Table 4.2. 125

Figure 4.14 (a) XPS signal of I3d orbital of AI and MAI treated PbS QDs, respectively. (b) XPS signal of N1s orbital AI and MAI treated PbS QDs. 126

Figure 4.15 The high-resolution TEM images of (a) oleic acid capped PbS QDs, (b) AI, and (c) MAI treated PbS QDs deposited from BA and annealed at 70 °C. 127

Figure 4.16 The cross-section SEM image of a representative solar cell device structure. 127

Figure 4.17 J-V characteristics (under reverse scan) of the solar cells under AM1.5 simulated solar illumination. 128

Figure 4.18 J-V characteristics show hysteresis under forward and reverse scan for a) AI and b) MAI treated solar cells. 128

Figure 4.19 The full-spectrum EQE of AI and MAI treated solar cells. The axis on the right-hand side shows the calculated J_{sc} from the EQE under simulated solar illumination. 129

Figure 4.20 Batch to batch variation in solar cell PCE for AI and MAI treated solar cells. 130

Figure 4.21	(a) Change of PCE with thickness for AI and MAI treated solar cells. (b) and (c) represents the variation of J_{sc} and FF with thickness for AI and MAI treated solar cells, respectively.	131
Figure 4.22	(a) represents a characteristics photovoltage decay profile and (b) shows a characteristics photocurrent decay profile.	132
Figure 4.23	(a) Carrier lifetime measured from TPV at different V_{oc}. The V_{oc} has been varied by changing the illumination intensity of the solar simulator. (b)The density of intermediate trap states at different open-circuit voltages for AI and MAI treated solar cells.	133
Figure 4.24	Photocurrent transients at a different applied bias of (a) AI and (b) MAI treated photovoltaic devices. (c) The charge carrier mobility is estimated from the slope of $\frac{d^2}{\tau_{tr}}$ vs. applied bias plot (where d is film thickness and τ_{tr} is the carrier transit time).	134
Figure 5.1	(a) High-resolution XPS spectrum of Cl2p orbital of CPT+AI treated PbS QD film. (b) XPS spectrum of S2p orbital, indicating an increase in intensity and broadening of $S2p_{3/2}$ and $S2p_{1/2}$ peaks for CP+AI treated QD films. The background signal has been subtracted for the presentation.	145
Figure 5.2	Deconvoluted high-resolution XPS spectrum of (a) Pb4f, (b) I3d, and (c) S2p binding energies for AI and CPT+AI treated QD films. The splitting of orbital energies is fitted using CASA XPS software.	146
Figure 5.3	(a) High-resolution XPS spectrum of O1s orbital and (b) N1s orbital for AI and CPT+AI treated PbS QD films.	147
Figure 5.4	(a) Full-scale UPS spectrum of AI and CPT+AI treated PbS QD films. (b) and (c) shows the magnified view of the UPS spectrum to illustrate the valance band onset (low binding energy) and secondary cutoff regions (high binding energy), respectively. (d) The energy band positions of PbS QDs for different surface passivation are deduced from their UPS and absorption measurements.	148
Figure 5.5	Full-scale UPS spectrum of ZnO (ETL) and EDT-PbS (HTL) layer.	149

Figure 5.6	Valance band, Fermi energy, and conduction band position of different layers used in solar cells, determined from UPS and absorbance measurements. The layers are shown as per their arrangement in photovoltaic devices.	150
Figure 5.7	(a) XRD spectrum of PbI_2+AI+BA ligand film deposited on the glass substrate. The parallel peaks pertaining to BA_2PbI_4 and Pb-amine complex are shown by red and blue lines, respectively. (b) Absorbance and emission spectrum of the PbI_2+AI+BA ligand film deposited on the glass substrate. The excitation wavelength is 380 nm.	151
Figure 5.8	HRTEM image of the (PbI_2+AI+BA) ligand.	151
Figure 5.9	(a) The absorbance spectrum of OA capped PbS QDs and partially ligand-exchanged with CPT in toluene. (b) PL emission spectra of PbS QDs for different ligands in DMF solution. The concentration (0.16 mg/mL) and the excitation wavelength (550nm) are kept constant for both the ligands.	152
Figure 5.10	Normalized absorption and photoluminescence of PbS QD films treated with different surface ligands. The emission spectra are recorded for the excitation wavelength of 550 nm.	152
Figure 5.11	The absorbance spectra of PbS QD films treated with different ligands for the entire wavelength range of absorption. AI and CPT+AI treated PbS QDs films are deposited from their BA solution. The peak at 500 nm (as marked) is attributed to BA_2PbI_4 perovskite shell absorption.	153
Figure 5.12	(a) TEM image and (b) particle size distribution of oleic acid capped QDs.	154
Figure 5.13	TEM images of (a) AI and (b) CPT+AI passivated PbS QDs. (c) shows the distribution of particle size (PbS core and ligand shell) for different ligand treatments. The average shell thicknesses for the respective ligands are shown at the inset.	155
Figure 5.14	Magnified HRTEM images of (a) AI and (b) CPT+AI passivated and (c) oleic acid capped PbS QDs.	156

Figure 5.15	The SEM images of AI (a & b) and CPT+AI (c & d) treated PbS QD films for different magnifications (5μm and 1μm).	157
Figure 5.16	The AFM images of (a) AI treated and (b) CPT+AI treated PbS QD films. The average roughness for AI and CPT+AI treated film are found to be 15 nm and 5 nm, respectively.	157
Figure 5.17	The cross-sectional image of a solar cell indicating distinguishable different layers.	158
Figure 5.18	Reverse and forward scan J-V characteristics (scan rate 0.1V s^{-1}) for AI and CPT+AI treated solar cells under AM1.5 simulated solar illumination.	159
Figure 5.19	The statistical variation of (a) V_{oc}, (b) J_{sc}, (c) FF%, and (d) PCE% for different batches of AI and CPT+AI treated solar cells.	160
Figure 5.20	Thickness dependent J-V curves for (a) AI and (b) CPT+AI treated solar cells.	161
Figure 5.21	The evolution of PCE of the solar cells with active absorber layer thickness for (a) AI and (b) CPT+AI ligand passivation.	161
Figure 5.22	EQE (%) of AI and CPT+AI ligand treated the solar cells. The axis on the right side indicates the predicted J_{sc} under simulated solar illumination from the EQE spectrums.	162
Figure 5.23	Capacitance-voltage characteristics of the solar cells measured at 1K Hz at a scan rate of 0.1V s^{-1}. The depletion widths for the respective solar cells (right-hand axis) at different voltages are shown.	162
Figure 5.24	Change of V_{oc} at varied light intensity (ϕ). From the slope of the V_{oc} vs. ln(ϕ) plot, the diode ideality factor (η) is determined for the solar cells.	163
Figure 5.25	Stability data for the un-encapsulated solar cells stored in Argon glove box and measured at different time intervals in ambient air.	163
Figure 5.26	Photo-CELIV measurement of (a) AI and (b) CPT+AI treated solar cells. The evolution of solar cell current under the influence of linearly increasing voltage pulse is shown.	164
Figure 5.27	(a) Photo carrier lifetime and (b) density of trap states at different V_{oc} of AI and CPT+AI treated solar cells.	165

Figure 6.1	NMR spectra of CPT ligand in DMF and presence of NH_4I+PbI_2 precursor in DMF solvent. A small amount of $CDCl_3$ is used as a reference solvent for standardization.	177
Figure 6.2	^{1}H NMR spectrum of CPT ligand in $CDCl_3$ solvent.	178
Figure 6.3	Solution phase FT-IR spectra of -SH functional group of CPT ligand in DMF-D7 and mixed solution of CPT+ NH_4I+PbI_2 precursor in DMF-D7 solvent.	179
Figure 6.4	Solution phase FT-IR spectroscopy of -SH functional group of CPT ligand in $CDCl_3$ (2581cm^{-1}) and DMF-D7(2541cm^{-1}) solvent and in the presence of AI (2542 cm^{-1}), PbI_2 (2539 cm^{-1}), and both AI and PbI_2 (2539 cm^{-1}) in DMF D-7 solvent.	179
Figure 6.5	(a) Absorbance and (b) Photoluminescence (PL) spectra of PbS QDs in DMF solvent for different concentration of CPT ligand. All the spectral measurements are carried out after 30 minutes of ligand exchange in the DMF phase. The PL spectra are recorded at the 550 nm excitation wavelength. The absorbance spectra are normalized at excitonic peak position, and PL spectra are normalized at band edge emission peak for comparative study.	180
Figure 6.6	Shows the comparative PL intensity of PbI_3^- and hybrid PbI_3^- +CPT ligand exchanged PbS QDs. CPT ligand concentration is varied from 0.1mM to 300 mM for the fixed 100 mM PbI_3^- ligand. Throughout the measurements, the excitation and emission bandwidth of the fluorometer were kept constant, and all the measurements were carried out at 550 nm excitation wavelength.	183
Figure 6.7	Urbach energy calculation from the conversion of diffuse reflectance of thin films into absorption spectra by implying Kubel-Munk function F(R).	183
Figure 6.8	HRTEM images of oleic acid capped PbS QDs, (a) lower magnified image, (b) higher magnified image to show crystal fringes, and (c) particle size distribution of oleic acid capped QDs.	185
Figure 6.9	HRTEM images of halometallate treated PbS QDs, (a) lower magnified image, (b) higher magnified image to show crystal	186

fringes, and (c) particle size distribution of halometallate treated QDs.

Figure 6.10 HRTEM image of PbI_3^-+10mM CPT treated QD PbS QDs, (a) lower magnified image, (b) higher magnified image to show crystal fringes, and (c) particle size distribution of PbI_3^-+10 mM CPT exchanged PbS QDs. 187

Figure 6.11 SEM image of (a) halometallate passivated QDs and (b) hybrid PbI_3^-+10mM CPT passivated QDs. 188

Figure 6.12 Cross-sectional image represents all the layers of integrated PbS QDs solar cell. 188

Figure 6.13 (a) J-V curves of solar cells under 1.5 AM illumination condition, and (b) Change of PCE with CPT ligand concentrations. 189

Figure 6.14 J-V characteristics (reverse and forward scan) of champion halometallate and hybrid halometallate+10mM CPT ligand exchanged QDs constructed device under AM 1.5 solar illumination. 190

Figure 6.15 Statistical variation of photovoltaic parameters and PCE for different batches of PbI_3^- and PbI_3^-+10mM CPT ligand exchanged QDs solar cells, (a) V_{oc} (b) J_{sc} (c) FF% and (d) PCE%. 191

Figure 6.16 Thickness dependent J-V curves for (a) PbI_3^- and (b) PbI_3^-+10mM CPT treated solar cells. 192

Figure 6.17 Comparison of PCE of the solar cell with active layer thickness for halometallate and hybrid halometallate+10mM CPT ligand exchanged QDs. 193

Figure 6.18 Light intensity(ϕ) dependant V_{oc} of the solar cells. The diode ideality factor (η) is calculated from the slope of the V_{oc} vs. $\ln(\phi)$ plot for the solar cells. 194

Figure 6.19 Device stability data of the unwrapped solar cells stored in Argon glovebox and measured in different time intervals. 194

Figure 6.20 Capacitance- voltage characteristics of halometallate and mixed halometallate+CPT (for three different CPT ligand ratio) ligand treated QDs integrated device. The depletion width of the 195

	respective solar cells (left-hand axis) at different voltages are represented.	
Figure 6.21	(a) Photocarrier lifetime and (b) density of trap states at different V_{oc} values for halometallate and mixed halometallate+CPT (three different CPT concentration) exchanged QDs constructed device.	196
Figure 6.22	Photo-CELIV measurement of (a) PbI_3^- and (b) PbI_3^-+10mM CPT ligand treated solar cells. The change of solar cell current under the influence of linearly increasing voltage pulse is represented.	197
Figure 6.23	Cross-Sectional image of solar cells used for Photo-CELIV measurements, (a) PbX_3^- exchanged and (b) PbX_3^- +10mM CPT exchanged PbS QDs.	198
Figure 6.24	Bias dependent transient photocurrent decay profile of (a) PbI_3^- and (b) PbI_3^-+10mM CPT exchanged QDs solar cells. The carrier transit time changes with the application of different bias.	198
Figure 6.25	Charge carrier mobility is calculated from the slope of d^2/τ vs. applied bias plot for PbX_3^- and PbX_3^-+10mM CPT treated device.	199
Figure 7.1	Schematic representation of bulk heterojunction device architecture.	208

List of Tables

Table No	Table Caption	Page No
Table 2.1	XPS peak position and FWHM values of different element present in different TiO_2 films	52
Table 2.2	Atomic concentration of various elements presents in the thin films of *n*-type layers.	53
Table 2.3	Comparison of solar cell performances on varying Nb doping concentrations.	59
Table 2.4	Solar cell performance of 2.5% Nb-doped TiO_2 layer on processing temperature.	60
Table 2.5	Comparison of photovoltaic performances for different *n*-type layers under forward and reverse bias scan.	61
Table 2.6	Electron densities of various *n*-type layers for before and after light soaking conditions, from Cap-V measurement.	65

Table 2.7	SCAPS model parameter.	65
Table 2.8	Mobility of *n*-type layers before and after three hours of white light soaking.	68
Table 3.1	Comparison of photovoltaic performances.	84
Table 3.2	Series resistance of solar cells treated with the different ligand are shown under dark and under solar illumination.	88
Table 3.3	Diffusion and drift lengths of PbS layer for different surface ligands.	92
Table 3.4	XPS data analysis of S 2p spectra of PbS QD films treated with different ligands.	98
Table 4.1	Atomic percent of different components determined from Pb4f XPS spectrum of AI and MAI treated PbS QDs shown in Figure 4.12 (a) and (b).	124
Table 4.2	Fitting parameters and quantitative analysis of S2p spectra of AI and MAI treated PbS QD film as shown in Figure 4.13 (a) and (b).	125
Table 4.3	Photovoltaic parameters of AI and MAI treated PbS QD solar cells.	129
Table 5.1	Atomic ratio of different elements for AI and CPT+AI treated PbS QDs from XPS.	146
Table 5.2	Absorbance and emission properties of PbS QD films for different surface passivation.	153
Table 5.3	Photovoltaic parameters for optimized solar cells.	159
Table 6.1	Tabular representation of absorption and PL spectral data of oleic acid capped PbS QDs in octane and PbS QDs for different ligands in DMF phase.	181
Table 6.2	Urbach energy calculation from Reflectance spectra of PbS QDs for different ligand passivation.	184
Table 6.3	Tabular representation of solar cells device J-V curves parameters for different ligand treated PbS QDs thin film.	190
Table 6.4	Photovoltaic parameters of optimized solar cells.	191
Table 6.5	Photovoltaic parameters of active layer thickness varied PbI_3^- treated solar cells.	192
Table 6.6	Photovoltaic parameters of thickness dependant studies of PbI_3^- +10mM CPT treated solar cells.	193

AcSIR	**Synopsis of the thesis to be submitted to the Academy of Scientific and Innovative Research for award of the degree of Doctor of philosophy in Chemical Sciences**
Name of the Candidate	**Debranjan Mandal**
Enrollment No. and Date	**Ph.D. in Chemical Science (10CC17A26016)** **14th August 2017**
Title of the Thesis	**Role of Surface Passivation and Doping on the Development of Quantum Dot Solar Cells**
Research Supervisor	**Dr. Arup K. Rath (CSIR-NCL Pune)**
Research Co-Guide	**NA**

1. Introduction and Statement of Problem

The constantly growing requirement of energy and fast consumption of conventional energy sources like fossil fuels claims a secure, renewable, sustainable, low cost, and widespread energy source. One of the most convenient ways to figure out the world's energy crisis could be to make use of solar power, which is enormously abundant and uniformly distributed over the most part of the earth. As photovoltaic devices can convert solar energy into electricity, therefore, they are of huge interest. The advancement of nanotechnology has enabled us to consider for unique solutions to the grand old problem. Solar cells based on quantum dots (QDs) could be a feasible alternative to the conventional materials (like Si solar cell, CIZS solar cell, etc) due to their many distinct advantages like facile processability, tunability, flexibility, and low material cost. Despite significant breakthroughs over the fifteen years in the development of QD solar cells, low performance has remained the major roadblock for their commercialization. It has been understood that primary reasons for the underperformance of QD solar cells are originated from not so high carrier mobility, low open circuit voltage, and high charge recombination rate in QDs based solar cells. All these drawbacks could effectively be mitigated by a comprehensive surface passivation strategy, which would prohibit trap state formation and allow fast transportation of photo carriers through the QD solids. In nanometer dimensions, PbS QDs show rock salt crystal structure, and crystal surfaces are terminated by polar (100) and non-polar (111) crystal facets. In the case of polar (111) crystal facets, only Pb atoms are present and terminated by anionic ligands, whereas for non-polar (100) facets both Pb and S atoms constitute terminal facets[1]. PbS (100) facets are electronically neutral and protected by electrostatic interaction of neutral ligands. So, both facets have different ligand passivation

criteria to protect them from air oxidation and aggregation[1,2]. Significant advancements have been made over the years in this direction through a wide variety of surface ligands to achieve the desirables in QD solids[3]. Among various passivation strategies, small chain organic molecules, inorganic ligands, atomic inorganic ligands have been used successfully in the development of high performance optoelectronic devices using QDs and nanocrystals[3]. Depending upon the nature of ligand passivation, the semiconductor characteristics of PbS QDs is also tuned. In general, thiol ligand passivation makes a p-type semiconductor, and iodide passivation leads to the n-type semiconductor[3]. Quantum dot Solar cell devices are initially constructed by forming the simple p-n junction of n-type TiO_2 or ZnO and p-type PbS QDs[4]. The Devices are further engineered to extract more charge carriers by increasing the carrier depletion width. As a result, these impact solar cell efficiency. During the period of the progress of QDs solar cell, mainly three kinds of device structure are developed, those are:(I) n-n-p junction by n-type TiO_2 or ZnO, n-type PbS and p-type PbS[5], (II) n-p-n heterojunction by n-type TiO_2/ZnO, p-type PbS and n-type PbS[6] (III) bulk heterojunction by the mixture of n-type PbS and p-type PbS[7] or n-type ZnO and p-type PbS[8].

2. Objectives

a) Finding the origin of surface induced mid gap traps states formation of PbS QDs.
b) Efficient surface passivation strategy to reduce mid gap trap states and enhancing QDs solar cell performance.
c) Development of solution phase ligand exchanged QDs for one-step deposition.
d) Making low cost, flexible, and high power conversion efficient QDs solar cell using low temperature processed TiO_2 and single layer PbS QDs ink.

4. Methodology

This thesis presents the aspect of surface passivation of lead sulfide quantum dots, the doping effect on electron extracting layer titanium dioxide, and device engineering on the development of lead sulfide quantum dots solar cells. The thesis contains a total number of five working chapters where the enhancement of solar cell efficiency from 3.5% to 10.6% are reported with strategic modifications. The first working chapter is based on Nb-doped low temperature processed TiO_2 integration as an efficient n-type electron extracting layers in PbS QDs solar cells. In the second chapter, a comparative study is discussed on the effect of different size, shape, and functional groups of small organic ligands on QDs passivation and its impact on the electronic properties of QDs as well as device performance. The third

chapter illustrates the growth of the 2D matrix on butylamine dispersed halometallate passivated QDs ink. This chapter correlates between the matrix cell thickness on QDs surface and device performance. To further tune the matrix thickness and compact passivation, a two-step hybrid passivation technique by combining organic small 3-chloro-1-propanethiol (CPT) molecule and inorganic halometallate anion is explained in the fourth chapter of the thesis. Further development on hybrid passivation is carried out in the fifth chapter of the thesis, where instead of two-step hybrid passivation, a one-step simplified hybrid passivation procedure is introduced to more control over the ratio between organic CPT molecule and halometallate ion on QDs surface. The last working chapter reports 10.6% efficiency of QDs solar cell which is the maximum efficiency achieved in this thesis.

Chapter I: **Low temperature processed niobium doped TiO_2 as n-type electron transport layer in quantum dot solar cell**

Performance enhancements of quantum dot solar cells have been achieved via controlling the intermediate trap state formation of active layers and embracing advanced architectural platforms for improved carrier collection. To collect the photogenerated electrons in QDs solar cells, anatase phase TiO_2 is one of the most extensively used n-type electron transport layers. Anatase phase TiO_2 is processed at high temperature (~500°c). The requirement of high temperature processing step is the major disadvantage for flexible solar cell applications, roll to roll processing and other commercial implications. In this chapter, we reportTiO_2 and niobium (Nb) doped TiO_2 thin films processed in between 80°c -150°c, which can act as an electron transport layer after few minutes of solar light soaking. Solar light exposure on low temperature processed TiO_2 and Nb doped TiO_2 thin films lead to a remarkable increment in their electron densities and electron mobilities, which implements them as an efficient n-type layer in quantum dot solar cells. These films show photoinduced high conducting states in presence of light. After switching off the light, it takes a few minutes to back to the normal low conducting state. The process is reversible, and the high conducting state can be retraced by soaking under solar illumination. Whereas, high temperature processed TiO_2 exhibits the least photoinduced increment in electron densities and mobilities. Photovoltaic devices of p-n junction configuration are fabricated by depositing p-type PbS QDs on top of n-type TiO_2. Low temperature processed TiO_2 based QDs solar cell has shown better performance than high temperature processed TiO_2 device. Due to Nb doping in low temperature processed TiO_2 films, the electron densities and conductivities are further increased than undoped low temperature processed TiO_2 films. Nb

doped low temperature processed TiO_2 based devices have shown the maximum power conversion efficiency (7.69%) than low temperature processed TiO_2 (6.54%) and high temperature processed TiO_2 (3.70%).

Chapter II: **Role of surface passivating organic ligands in determining the electronic properties of quantum dots solids and photovoltaic application**

The electronic properties of QD solids are strongly dependent on the surface chemistry of QD. Surface ligands restrict the QDs from fusion and maintain the size and shape of the individual QD in solids, to conserve the clean band energy gap of the individual nanocrystal. This controls the charge carrier conduction across the solid films and regulates their photovoltaic performance. In this chapter, we comparatively study the effect of size, shape, and functional groups of small organic ligands on the QD surface passivation and how those ligands make a change in carrier mobility, dielectric constant, and carrier doping density of QD solids. Moreover, we associate these results with the performance, stability, and recombination process of the respective solar cells. We take four ligands to study, those are 3-mercaptopropionic acid (MPA), thioglycolic acid (TGA), thiolactic acid (TLA), and 3-chloro-1-propanethiol (CPT). MPA and TGA both ligands have the same functional groups (-SH and -COOH) but their sizes are different, MPA is longer in size than TGA. In between TGA and TLA, the distance between -SH and -COOH functional group is constant, whereas their shape is different due to the presence of an extra methyl group in the TLA ligand. The functional groups of CPT ligand are different (-SH and -Cl) in comparison with the other three ligands (-SH and -COOH) although CPT ligand has similarity in size and shape with MPA. We interpret all the details of ligand mediated electronic and physical properties of PbS QD solids and justify their corresponding photovoltaic performance. This study shows the way to design a new ligand for the development of high performance QD solar cells.

Chapter III: **Butylamine catalyzed 2D matrix engineering on quantum dot surface for solar cell application**

In the previous two working chapters, PbS QDs are passivated by small organic ligands, and ligand exchange is carried out in the solid state. Solar cell devices are fabricated by layer-by-layer (LBL) deposition and each solar cell device consists of 7-12 layers. It takes almost thirty minutes to make one device. LBL solid state ligand exchange process assists inhomogeneity in QD film through random packing and heterogeneous aggregation. The inhomogeneous QD fusion promotes site energy disorder, which renders the charge carrier transport process and reduces the open circuit voltage generation in QD solar cells. In this

chapter, we discuss on solution phase ligand exchange of PbS QD using halometallate anion (PbX_3^-) and with different counter cation methylammonium (MA^+) and ammonium (NH_4^+) ion. The solution-phase ligand exchange process allows homogenous surface passivation, improved QD packing, and deposition of a thick conducting QD ink from a one-step spin coating process. For thick QD ink preparation, butylamine is used as a volatile solvent to disperse halometallate ligand capped QD. Here, we report butylamine acts more than a solvent, as it reacts with halometallate ligands and forms the 2D crystalline matrix in solid films. The matrix layer is composed of two sets of 2D crystalline components which are recognized to be a Pb-amine complex and a $(BA)_2PbI_4$ perovskite layer. The 2D crystalline matrix is coupled with PbS QD solids. We reduce matrix thickness by varying counter cation from MA^+ ion to NH_4^+ ion. This increases the charge carrier mobility, carrier recombination lifetime, and diffusion length in QD solids, as a consequence solar cell efficiency is also enhanced from 7.80% to 9.1%.

Chapter IV: **Hybrid passivated quantum dot ink attains thinner shell growth and clean energy bandgap for photovoltaic application**

The development of the solution phase ligand exchange process with lead halide based halometallate ligand has made the processing of the QDs remarkable facile and efficient. In the previous chapter, we have discussed on the one-layer deposition of halometallate passivated QD ink and the growth of 2D matrix embedded QD solids. The matrix shell layer plays a key role in surface passivation and charge transport in QD solids. All the Pb atoms of PbS (111) facets are not passivated by halometallate anion due to steric repulsion between them during binding two adjacent Pb atoms of (111) facets. In the second chapter, we have talked about small organic thiol molecules which have been used to construct QD solar cells using the solid-state ligand exchange process. But, solution phase ligand exchange with small organic thiol molecules is not feasible due to the poor solubility of thiol passivated QD ink in common solvents. Here, we report a two-step hybrid passivation strategy using 3-chloro-1-propanethiol and halometallate as ligands to prepare the QD ink. In the first step, we partially exchange the as synthesized oleic acid capped QDs with CPT ligand, and then proceed for halometallate ligand exchange to make QD ink. Due to the flexible nature of organic molecules, they can adjust in between two halometallate ion and bind to the uncoordinated Pb atoms of PbS (111) facets, and Pb atoms of PbS (100) facets electrostatically interact with lone pair of sulfur atoms of thiol molecules to protect from air oxidation. The hybrid passivated QDs exhibit a 50% reduction in matrix shell thickness,

reduced trap density, and improved monodispersity in solid films. These improvements allow a four-time increase in carrier mobility and doubling of the diffusion length, which permits the carrier extraction from a thicker QD absorbing layer. Solar cells made of hybrid passivated QDs show high efficiency of 10.3% and reduced hysteresis effect. The advancements of surface passivation impact to reduce oxygen doping and improved the ambient stability of the solar cells.

***Chapter V:* Control over ligand ratio on thiol, halometallate mediated one-step hybrid passivation of quantum dots for photovoltaics**

In the previous work, a two-step hybrid passivation process is deployed to passivate QDs, where in the first step small organic CPT ligands are introduced. The major drawback of this two-step procedure is the limitation of CPT ligand amount integration on the QD surface. For 70 mg PbS QDs, we can only treat with the maximum of 0.18mM (19.8mg) CPT. Here we report a one-step CPT, halometallate ligand exchange process to prepare QD ink. In this process, CPT concentration is varied from 0.1mM to 0.3M, and simultaneously halometallate concentration also can be changed from 0.05M to 0.2Mfor 70 mg PbS QDs. This process allows us to incorporate more amount of CPT and to find a suitable ligand ratio between CPT and halometallate for compact surface passivation. We have studied the optical and electronic properties of the QDs with different ligand ratio of CPT and halometallate and their corresponding device performance. We find the best optimum concentration of CPT lies in between 0.01M to 0.02M and halometallate concentration around 0.1M for 70 mg PbS QDs. Due to the controlled treatment of hybrid ligands, the mutually passivated QDs exhibit significant improvement in optoelectronic properties with preserving clean band energy gap and monodispersity. The CPT ligands on the QD surface also disturb the growth of the 2D matrix shell which allows compact QD arrangement in solid films. They show lesser FWHM of excitonic and emission peaks and reduction in stoke shift in comparison to the only halometallate passivated QDs. The hybrid passivated QDs maintain their band to band emission for a longer period whereas halometallate passivated QDs degrade very fast and exhibit larger stokes shift. We surmise that more amount of CPT loading along with halometallate ligand compactly passivate the Pb atoms of PbS (111) facets and Pb and S atoms of PbS (100) facets by electrostatic interaction. As a consequence, we observe these photophysical improvements of QDs, which are further highlighted in photovoltaic devices. The photovoltaic device of hybrid passivated QDs has shown remarkable improvement in open-circuit voltage as well as in short-circuit current and lesser

hysteresis effect. As a whole, we have achieved 10.6% efficient solar cells made by hybrid passivated QDs which is also the maximum reported efficiency in this thesis.

5. Summary:

- Low temperature processed Nb doped TiO_2 is developed to make flexible QDs solar cells, PCE increased from 3.7% to 7.7%
- The photovoltaic figure of merits for various surface ligands with varied sizes, shapes, and functionalities, more than the size impact of surface coverage of QDs is more important.
- For the development of QDs ink butylamine is used as a volatile solvent, where we have shown butylamine reacts with passivated halometallate ligand and forms the 2D crystalline matrix
- 2D matrix is composed of two sets of complex Pb-amine and $(BA)_2PbI_4$ perovskite, we have tuned matrix layer thickness by changing counter cation and achieved 9% PCE.
- Two-step thiol, halometallate hybrid ligand passivation is developed to reduce matrix layer thickness and compact passivation, 2D matrix thickness reduced to 50% compared to only halometallate passivation and PCE reached to 10.3%.
- One step hybrid thiol and halometallate ligand passivation is developed, which further reduces 70% of matrix shell thickness. Band edge emission sustains for a longer period, carrier type of QDs tuned with thiol introduction, and PCE reached 10.6%.

6. Future directions:

From Shockley-Queisser's theoretical calculation, a single p-n junction photovoltaic cell can reach a maximum of 33.7% PCE. So, there is still plenty of rooms to improve the PbS QD solar cell performance. We are planning to construct a bulk heterojunction solar cell, where the mixture of n-type and p-type PbS QDs ink will be deposited as the main absorbing layer to extend the charge collection network. Halometallate (PbI_3^-) ligand passivated QDs show n-type semiconductor characteristics. Here we are proposing to develop p-type PbS QD ink by surface passivating with the combination of $Pb(SCN)_2$, NH_4SCN, and CPT ligands. We are hopeful that this strategy will further enhance the PCE of PbS QD solar cells.

7. Publications:

(I) Mandal, D.; Goswami, P. N.; Rath, A. K. "Colossal photo-conductive gain in low temperature processed TiO_2 films and their application in quantum dot solar cells". *Appl. Phys. Lett*, **2017**, *110*, 123902**.**

(II) Goswami, P. N.; Mandal, D.; Rath, A. K. "The role of surface ligands in determining the electronic properties of quantum dot solids and their impact on photovoltaic figure of merits". *Nanoscale*, **2018**, *10*, 1072-1080.

(III) Mandal, D.; Rath, A. K. "Quantum Dots Coupled to an Oriented Two-Dimensional Crystalline Matrix for Solar Cell Application". *ACS Appl. Mater. Interfaces*, **2018**, *10*, 39074−39082.

(IV) Mandal, D.; Goswami, P. N.; Rath, A. K. "Thiol and Halometallate, Mutually Passivated Quantum Dot Ink for Photovoltaic Application". *ACS Appl. Mater. Interfaces*, **2019**, *11*, 26100−26108.

8. References

(1) Zherebetskyy, D.; Scheele, M.; Zhang, Y. J.; Bronstein, N.; Thompson, C.; Britt, D.; Salmeron, M.; Alivisatos, P.; Wang, L. W. Hydroxylation of the surface of PbS nanocrystals passivated with oleic acid. *Science* **2014,** *344* (6190), 1380-1384.

(2) Boles, M. A.; Ling, D.; Hyeon, T.; Talapin, D. V. The surface science of nanocrystals. *Nat. Mater.* **2016,** *15*, 141–153.

(3) Carey, G. H.; Abdelhady, A. L.; Ning, Z.; Thon, S. M.; Bakr, O. M.; Sargent, E. H. *Chem. Rev.* **2015**, *115*, 12732−12763.

(4) Ip, A. H.; Thon, S. M.; Hoogland, S.; Voznyy, O.; Zhitomirsky, D.; Debnath, R.; Levina, L.; Rollny, L. R.; Carey, G. H.; Fischer, A.; Kemp, K. W.; Kramer, I. J.; Ning, Z. J.; Labelle, A. J.; Chou, K. W.; Amassian, A.; Sargent, E. H. Hybrid Passivated Colloidal Quantum Dot Solids. *Nat. Nanotechnol*. **2012**, *7*, 577−582.

(5) Chuang, C. H. M.; Brown, P. R.; Bulovic, V.; Bawendi, M. G. Improved performance and stability in quantum dot solar cells through band alignment engineering. *Nat. Mater.* **2014,** *13* (8), 796-801.

(6) Ning, Z. J.; Voznyy, O.; Pan, J.; Hoogland, S.; Adinolfi, V.; Xu, J. X.; Li, M.; Kirmani, A. R.; Sun, J.-P.; Minor, J.; Kemp, K. W.; Dong, H.; Rollny, L.; Labelle, A.; Carey, G.; Sutherland, B.; Hill, I.; Amassian, A.; Liu, H.; Tang, J.; Bakr, O. M.; Sargent, E. H. Air-Stable n-Type Colloidal Quantum Dot Solids. *Nat. Mater*. **2014**, *13*, 822−828.

(7) Choi, M.-J.; Baek, S.-W.; Lee, S.; Biondi, M.; Zheng, C.; Todorovic, P.; Li, P.; Hoogland, S.; Lu, Z.-H.; de Arquer, F. P. G.; Sargent, E. H. Colloidal Quantum Dot Bulk Heterojunction Solids with Near-Unity Charge Extraction Efficiency. *Adv. Sci.* **2020**, *7*, 2000894.

(8) Rath, A. K.; Garcia de Arquer, F. P.; Stavrinadis, A.; Lasanta, T.; Bernechea, M.; Diedenhofen, S. L.; Konstantatos, G. Remote Trap Passivation in Colloidal Quantum Dot Bulk Nano-heterojunctions and Its Effect in Solution-Processed Solar Cells. *Adv. Mater*. **2014**, *26*, 4741−4747.

Chapter 1

Introduction

Abstract:

This introductory chapter states an overview of the fundamental development of colloidal quantum dots solar cells. After introducing the key requirements of photovoltaic research and the relevant device physics of solar cells, the chemical and physical properties of colloidal quantum dots are discussed extensively. A brief history of the progress of quantum dots solar cell is reviewed. In the end, a draft of this thesis is presented.

1.1 Solar energy

The constantly growing global requirement for energy has accelerated the consumption of non-renewable energy sources based on fossil fuels (oil, coal, and natural gases). In 2015, the global energy requirement was 15 terawatts and is expected to reach 30 terawatts by 2050.[1] Recent study shows that 76% of global energy demands are supplied by fossil fuels, and the predicted estimation assumes that this requirement will further increase hugely in the future. At the same time, global climate change or global warming is now a serious threat to this planet, for the gigatons of the CO_2 gas pouring from energy sources like coal, oil, natural gas power plants, and different human-made industries in the atmosphere.[2] Now, we are at a phase where the revolutionary change to our energy paradigm is very much essential due to rising concerns of the current trends in energy use and to continue these trends to meet future needs.[3]

One of the most sustainable and clean energy sources of our energy paradigm is solar energy, which is particularly more fascinating due to its abundance and near uniform distribution across the planet earth. Our sun is a constant source of blackbody radiation at 5800K (Figure 1.1), and it supplies around 1.74×10^{17} W solar energy with an intensity of 1366 Wm^{-2} to the earth's upper atmosphere.[4]

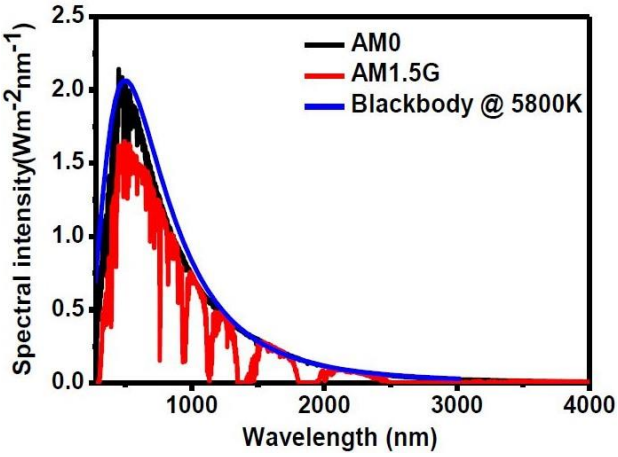

Figure 1.1: Solar spectrum irradiance collected just outside of earth's atmosphere (AM 0), globally averaged terrestrial data (AM 1.5G), and a blackbody approximation of the sun assuming the sun's surface temperature of about 5800K. Data is copied from reference 5.

This amount of solar power is known Air mass zero (AM 0) (Figure 1.1). Due to atmospheric light absorption and scattering, the solar light intensity is reduced to 1000 Wm^{-2} when it reaches to earth's surface.[6] This value is set as a standard for any solar energy-related device performance characterization and quantified as AM 1.5G (Figure 1.1). Although various issues like seasonal changes or sporadicity due to the cloud disturb the penetration of solar radiation on the earth's surface, this is still the most equally distributed and accessible energy source of any part of the world[7] compared to all other sources. There are several ways of harvesting solar energy like (i) solar thermal collection (heating water, solar air conditioning, etc.), (ii) Solar cells or photovoltaic devices, (iii) concentrated solar power, (iv) photocatalytic hydrogen generation, etc. This thesis focuses only on the solar cell device technology for harvesting solar energy.

1.2 Solar cells

The most conventional method of converting solar light into electricity is through solar cells or photovoltaic devices. A solar cell is made of semiconductors that absorb the solar light and convert the light energy into electricity. The simplified model of a solar cell is nothing but a *p-n* junction diode. This section reviews the basic working principle, characteristics, and limiting efficiencies of a solar cell modelled with a *p-n* junction diode.

1.2.1 Fundamentals of solar cells

The device physics of a *p-n* junction diode represents the basic working principle of a solar cell. A *p-n* junction is a junction between a *p*-doped semiconductor and an *n*-doped semiconductor. For *p*-doped semiconductor majority charge carriers are holes, while electrons are majority charge carriers for *n*-doped semiconductor. Figure 1.2 represents an ordinary *p-n* junction diode with no external applied bias. When *p*-type semiconductor and *n*-type semiconductor are in contact, the majority of holes carriers from *p*-type semiconductor diffuse into the *n*-type semiconductor. Therefore, a negatively charged region builds on the *p*-side due to the diffusion of holes. Similarly, majority electron carriers from the *n*-type semiconductor diffuse into the *p*-type semiconductor, resulting in a positively charged region on the *n*-type semiconductor. The developed positive and negative charged region near the junction is called the depletion region or space charge region (Figure 1.2). The region outside of the depletion region is called the quasi-neutral region. A built-in electric field is created in the depletion region; hence a built-in potential V_{bi} arises across the junction, which further prevents the diffusion charge carriers.

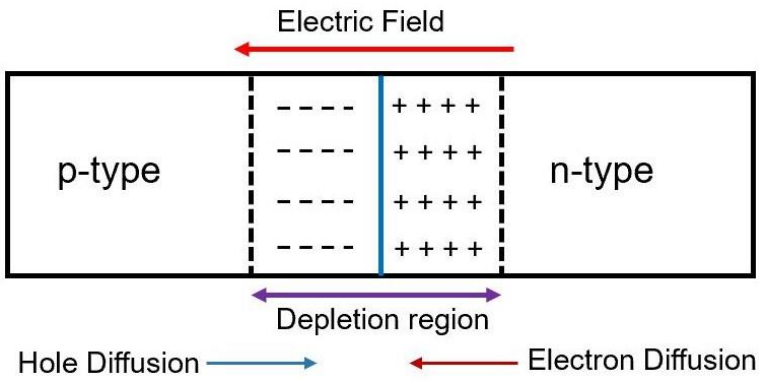

Figure 1.2: Representation of simplified *p-n* junction under thermal equilibrium, "-" represents negatively charged acceptor atoms, and "+" represents positively charged donor atoms. The light blue junction presents the metallurgical junction separating *p*-type and *n*-type semiconductors.

The Fermi energy (E_{Fi}) level of an intrinsic semiconductor is located in the middle of the bandgap, so $E_{Fi} = \frac{E_{VB}+E_{CB}}{2}$, in between the valance band (E_{VB}) and conduction band (E_{CB}) of the semiconductor. For *n*-type semiconductor, the Fermi energy (E_{Fn}) level is shallower (i.e., near to conduction band side) than the intrinsic Fermi level ($E_{Fn}>E_{Fi}$), while E_{Fp} level is deeper (close to valance band) in the *p*-type semiconductor ($E_{Fp}<E_{Fi}$). Under dark condition at zero bias (thermal equilibrium), the Fermi energy of the *p-n* junction remains constant in the entire device.

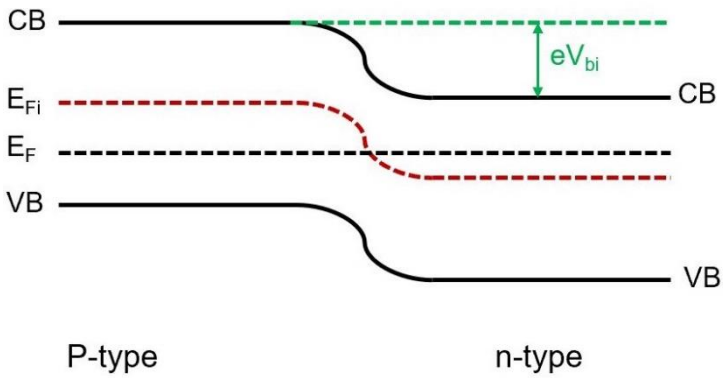

Figure 1.3: Band diagram of *p-n* junction under thermal equilibrium (dark conditions). 'e' represents the elementary charge, and V_{bi} is the built-in voltage.

The bands in the depletion region bend to maintain the constant E_F in each semiconductor. In both *n*-type and *p*-type semiconductors, the V_{bi} conserves the equilibrium between the majority and minority charge carriers (both electrons and holes). So, there is no net current

flow between the semiconductors under thermal equilibrium condition (Figure 1.3). The V_{bi} also determines the rectifying characteristics of the diode during the bias application.

When the forward bias (positive voltage to *p*-type side with respect to *n*-type side, V>0) is employed to the device, the potential barrier ($V-V_{bi}$) is reduced (Figure 1.4). The number of carriers that can cross the barrier also increases with V and flow through (electrons flow from the *n*-type side to *p*-type side and holes from the *p*-type region to *n*-type side) the junction. As a result, this allows a net current to flow through the device, and this current is called the diffusion current.

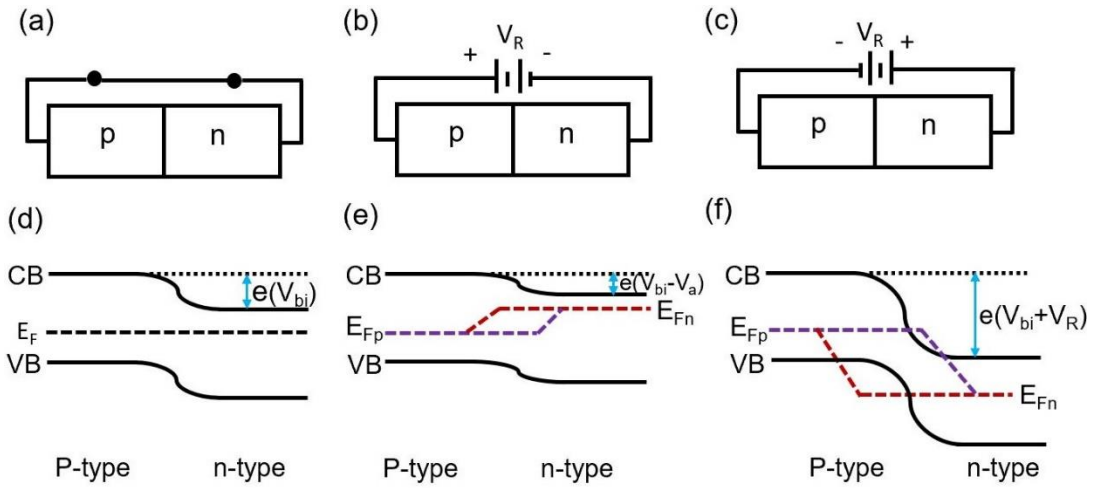

Figure 1.4: Band diagram of the ideal *p-n* junction and band diagrams under (a,d) zero bias, (b,e) forward bias, and (c,f) reverse bias.

Conversely, if the reverse bias (positive voltage to *n*-type side compared to *p*-type side) is applied to the device, the potential barrier is increased (Figure 1.4). The Fermi energy level along the device is no longer flat, instead of that quasi fermi level arises to represent the distribution of electrons and holes. The current flow is controlled by the drifting of the minority charge carriers due to the built-in field to the other side of the junction. Hence, the current flow is minimal under reverse bias condition.

The current-voltage characteristics of the diode can be explained by the Shockley ideal diode equation.[8-10]

$$J = J_0 \left[\exp\left(\frac{qV}{kT}\right) - 1\right] \quad \text{----------} \quad (1.1)$$

Where J is the current density, J_0 is the reverse saturation current density, q is the electronic charge, V is applied bias, k is the Boltzmann constant, and T is the temperature.

Now, when a solar cell is illuminated, an equal amount of photogenerated electrons and holes are formed in the semiconductors. The built-in potential force to drive the photogenerated electrons on the *p*-region to *n*-region and similarly the photogenerated holes on the *n*-side to *p*-side. The flow of these photogenerated excess carriers generate photocurrent (J_{ph}) in an opposite direction of the diode current. Hence, the current-voltage characteristics of the illuminated diode can be written as,[9,10]

$$J = J_d - J_{ph} = J_0 \left[\exp\left(\frac{qV}{kT}\right) - 1\right] - J_{ph} \quad (1.2)$$

where J is the illuminated current density, J_{ph} is photocurrent, and J_d is the same as the ideal diode equation written in equation 1.1. The derived equations 1.1 and 1.2 from *p-n* junction solar cell under dark and light condition are the general forms for most of the solar cells. The Schottky junction solar cells also follow these equations, but the mechanism of contributing to J_0 is a little different, so the functional forms of J_0 is also different from the *p-n* junction diode.[8,9] As this thesis don't focus on Schottky solar cell; the Schottky device physics is not further discussed.

1.2.2 Characteristics of solar cells

To explain the characteristics parameters of a solar cell, a simplified circuit diagram of the *p-n* junction diode under photo illumination is shown in Figure 1.5. As discussed above, the photogenerated current (J_{ph}) flows in the same direction of the built-in electric field of the *p-n* junction diode. The diode current (J_d) can be equivalent to the produced forward bias current upon applying required input power on the resistive load (R) connected to the *p-n* junction diode, as shown in Figure 1.5. So, the net current of the *p-n* junction solar cell under illumination is the difference between J_{ph} and J_d (same as in equation 1.2) or the equivalent forward bias current passing through the resistive load (R) as in Figure 1.5.

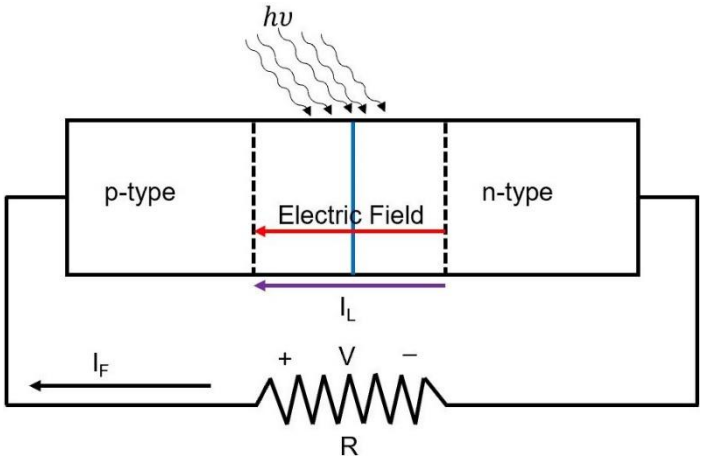

Figure 1.5: *p-n* junction solar cell with a resistive load under photo illumination.

Now, consider two limiting cases, first when the resistive load, R= ∞, that suggests no load connected with the illuminated solar cell ($J = 0$). So, further calculation implies the open-circuit voltage of the solar cell (V_{oc}).[8-10]

$$V_{oc} = \left(\frac{kT}{e}\right)\left(\ln\left(\frac{J_{ph}}{J_0}\right) + 1\right) \text{ ---------- } (1.3)$$

Secondly, if the resistive load, R=0, then the illuminated solar cell is short-circuited; as a result, equation 1.2 simplifies to,

$$J = J_{ph} = J_{sc} \text{ ---------- } (1.4)$$

where J_{sc} signifies the short circuit current.

Now, the power applied to the resistive load can be expressed as,

$$P = JV \text{ ---------- } (1.5)$$

Substituting equation 1.2 in equation 1.5 results

$$P = \left[J_0\left(\exp\left(\frac{eV}{kT} - 1\right)\right) - J_{ph}\right]V \text{ ---------- } (1.6)$$

At the maximum power applied to a resistive load (R), the derivation of equation 1.6 with respect to V becomes zero. The maximum power point voltage is represented as V_m.

$$\frac{dP}{dV} = 0 = J_0\left(\exp\left(\frac{eV_m}{kT} - 1\right)\right) + V_m\left(\frac{e}{kT}\right)J_0\exp\left(\frac{eV_m}{kT}\right) - J_{ph} \text{ ---------- } (1.7)$$

By rearranging the equation 1.7, resulting in the equation 1.8

$$\left(V_m\left(\frac{e}{kT}\right)+1\right)\exp\left(\frac{eV_m}{kT}\right)=\frac{J_{ph}}{J_0}+1 \text{ ---------- (1.8)}$$

V_m is lower than V_{oc} and J_m is lower than J_{sc}.

The ratio between the maximum power P_m and input power P_{in} defines the power conversion efficiency (η).

$$\eta=\frac{P_m}{P_{in}}\times 100\%=\frac{J_mV_m}{P_{in}}\times 100\% \text{ ---------- (1.9)}$$

As V_{oc} and J_{sc} denote the maximum voltage and current respectively as concluded from equation 1.8, another parameter of the solar cell device, fill factor (FF) is defined as,

$$FF=\frac{J_mV_m}{J_{sc}V_{oc}} \text{ ---------- (1.10)}$$

Putting equation 1.9 into 1.10 gives the final equation of Power conversion efficiency,

$$\eta=\frac{J_mV_m}{P_{in}}\times 100\%=\frac{V_{oc}\,J_{sc}\,FF}{P_{in}}\times 100\% \text{ ---------- (1.11)}$$

A characteristics J-V curve of the solar cell is presented in Figure 1.6 with pointing all the parameters (V_{oc}, J_{sc}, and FF) of the device.

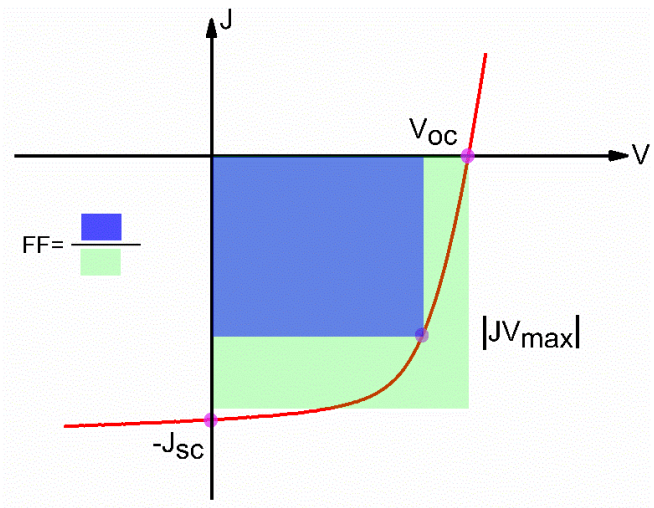

Figure 1.6: Current-voltage characteristics of a solar cell under illumination.

For the characterization of a solar cell, the illuminated light source is standardized based on the solar spectrum AM1.5G (Figure 1.1), discussed in section 1.1. A semiconductor absorbs light when the energy of an illuminating photon is equal to or higher than the bandgap (E_g)

of the semiconductor. In a solar cell device, the generated photocurrent for each wavelength of the entire solar spectrum (AM 1.5G) is measured by external quantum efficiency (EQE) measurements. EQE is calculated from the ratio between the number of charge carriers collected by the solar cells and the number of photons of given energy illuminated on the solar cell.

$$EQE = \frac{electrons/sec}{photons/sec} = \frac{I/q}{P/(\frac{hc}{\lambda})} \quad \text{---------- (1.12)}$$

where I is the measured current, q is the electronic charge, P is the power of the illuminated light, h is Planck's constant, λ is the wavelength of each illuminated photon, and c is the velocity of light.

The total photocurrent of a solar cell is calculated from the integration area of the EQE spectrum.

$$J_{ph}(V) = e\int_0^{\infty} EQE(\lambda, V)\gamma_i(\lambda)d\lambda \quad \text{---------- (1.13)}$$

e is the electronic charge, V is voltage, $\gamma_i(\lambda)$ presents the AM1.5G spectrum. For the short-circuit, current measurement voltage is set to zero. The calculated short circuit current (J_{sc}) from the integration area of the EQE spectrum should match with the J_{sc} measured from the $J - V$ curve.

1.2.3 Carrier collection

Under solar illumination, the semiconductor layers of the *p-n* junction diode absorb solar light and generate charge carriers. The major challenge of a solar cell is to extract those photogenerated charge carriers from the device before recombining inside the device. The photogenerated charge carrier's extraction mechanism of a solar cell depends on the position of the device where the carriers are generated. There are mainly two different carrier extraction mechanisms for two different regions (Figure 1.7); (i) inside the depletion region (extraction mainly by drifting) and (ii) quasi-neutral region (extraction mainly by diffusion).

In the case of photocarriers generated inside the depletion region, the built-in electric field can drive the photogenerated electrons to the *n*-side and holes to the *p*-side effectively. The collection probability of the generated carriers inside the depletion region is near unity. Hence, a wide depletion width enhances the carrier collection.

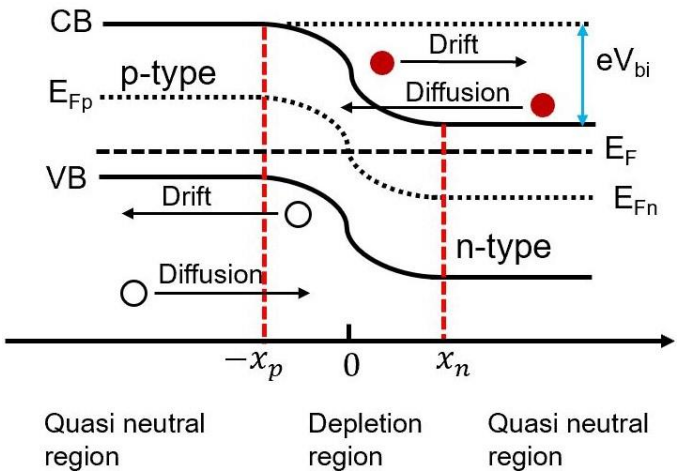

Figure 1.7: Energy band diagram of the *p-n* diode to represent different region and carrier transport characteristics.

For a *p-n* junction solar cell with the doping concentration of holes (N_a) in *p*-type semiconductor and *n*-type semiconductor with the doping concentration of electrons (N_d), the depletion width on the *p*-side (W_p) and *n*-side (W_n) is written in equation (1.14) and (1.15), respectively.[8,9] The overall depletion width (W)is the sum of (W_p) and (W_n).

$$W_n = \sqrt{\frac{2\varepsilon_r N_a}{q\, N_d(N_a+N_d)}(V_{bi} - V)} \quad \text{(1.14)}$$

$$W_p = \sqrt{\frac{2\varepsilon_r N_d}{q\, N_a(N_a+N_d)}(V_{bi} - V)} \quad \text{(1.15)}$$

$$W = W_n + W_p = \sqrt{\frac{2\varepsilon_r(N_a+N_d)}{q\, N_a N_d}(V_{bi} - V)} \quad \text{(1.16)}$$

The charge neutrality condition of the diode implies the relation (equation 1.17) between depletion width and doping concentration on the two sides.

$$W_n N_d = W_p N_a \quad \text{(1.17)}$$

This relation states that the lower the doping concentration in the *p*-side higher the depletion width on the *p*-side, and vice versa.

Now, the collection probability of the photogenerated carriers in the quasi-neutral region depends on the distance to the boundary of the depletion region and the diffusion length (L_D) of the generated carriers. As there is no built-in electric field in the quasi-neutral

region, the extraction of those photogenerated carriers is driven by diffusion. If an electron in the quasi-neutral region can reach to the edge of the depletion region, then it can be captured by into the *n*-side by the built-in driving force of the depletion region. Otherwise, those electrons would recombine with holes or lose their energy by non-radiative recombination. The carrier concentration near the edge of the depletion region is near to zero but rises with the distance from the depletion edge to the quasi-neutral region. This concentration gradient is the driving force for the diffusion of those generated carriers. However, the collection probability of these carriers is strongly dependant on the probability of the carrier's successful diffusion to the edge of the depletion region within its lifetime. This can be understood by solving the 1-D diffusion equation (1.18) to find out the carrier diffusion length (equation 1.19).[8-10]

$$P(x) \approx e^{-x/L_D} \quad (1.18)$$

$$L_D = \sqrt{D\tau} \quad (1.19)$$

where x is the distance from the edge of the depletion region to the position of the quasi-neutral region. L_D is the diffusion length, D is the diffusion constant, and τ is the generated carrier lifetime. The diffusion coefficient is again proportional to the carrier mobility. Thus, the higher diffusion coefficient and carrier lifetime lead to higher diffusion length and increase the generated carrier collection probability from the quasi-neutral region.

1.2.4 Efficiency Limitations

In 1961, W. Shockley and H. Queisser first calculated the maximum obtainable efficiency of a solar cell theoretically; later, this was known as the Shockley-Queisser limit.[11] The calculation considers a perfect *p-n* junction solar cell that can absorb 100% of the photons of solar light with the above energy of the bandgap of semiconductors and capture all the photogenerated carrier's photocurrent. The incident solar energy spectrum is estimated in that calculation by the black body radiation at 6000K, and the corresponding J-V characteristics are obtained using equation 1.2, in which J_0 is considered as the radiative recombination of thermally generated electrons and holes. According to Shockley-Queisser theoretical limit, a single *p-n* junction solar cell with a 1.33 eV bandgap can achieve a maximum of 33.7% efficiency under the AM1.5G solar spectrum at 1-sun intensity (Figure 1.8).

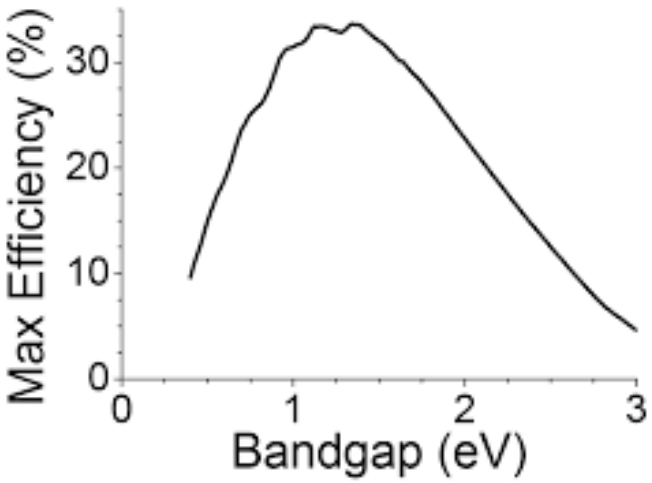

Figure 1.8: Single-junction solar cell efficiency vs. semiconductor bandgap (Eg). The figure is reprinted from reference 11.

An ideal solar cell can lose solar energy in several ways. The most important part of the energy loss is the transmission loss, as a semiconductor cannot absorb photons whose energy is lower than its bandgap E_g ($E_g > E_{photon}$). The other way of energy loss is because of carrier thermalization. In this case, when a semiconductor absorbs photons with energy E_{photon} higher than its bandgap E_g ($E_g < E_{photon}$), the excited carriers go to higher energy states and rapidly release their excess energy as heat to come back at the band edge. Fast radiative recombination of photogenerated carriers due to spontaneous emissions of photons within the solar cell also reduces their extraction probability. Considering these facts, a solar cell constructed with lower bandgap material would have higher J_{sc} due to lower transmission loss and but would have lower V_{oc} due to higher thermalization loss. There is also carrier extraction loss as FF is lower than one and V_{oc} is below E_g/q. Counting all these bandgap dependence energy loss processes, the optimum bandgap for reaching maximum efficiency of a single *p-n* junction solar cell is 1.337 eV.

However, there are ways to exceed Shockley-Queisser limit of a solar cell. Some materials show multi exciton generation property or carrier multiplication effect, where more than one electron-hole pair is created from one incident photon.[12] Solar cells constructed from those materials may cross the theoretical efficiency limit. Concentrator solar cells, which work at higher illumination intensities, can pass the higher efficiency limit using the impact ionization process.[13] The other familiar approach to cross the high-efficiency limit is a multi-junction solar cell or tandem solar cell where multi-layers of

different bandgap materials are used to build a solar cell to absorb different portions of the solar spectrum.[14] However, this Shockley-Queisser limit is only for a single *p-n* junction solar cell. This thesis does not focus on concentrator solar cells or tandem solar cells but mainly deals with single-junction solar cells.

1.2.5 Non-ideal effects

A real solar cell has certain limitations, which prevents them to achieve the maximum efficiency of an ideal solar cell. The most fundamental disadvantage of a real solar cell is trap state formation inside the bandgap of semiconductors due to impurities, defects, or surface oxidation. These intermediate trap states capture the photogenerated electrons or holes and cause recombination of photogenerated carriers. This trap-assisted recombination is known as Shockley-Read-Hall (SRH) recombination.[8-10,15] These trap states formation and followed by recombination will reduce the V_{oc} and J_{sc} of the solar cell. Upon counting this factor, the ideal diode equation 1.2 will be presented as,[8-10]

$$J = J_D - J_{ph} = J_0\left[\exp\left(\frac{qV}{nKT}\right) - 1\right] - J_{ph} \text{ ---------- } (1.20)$$

The additional term, n is known as the diode ideality factor of a solar cell. If the recombination occurs inside the quasi-neutral region, the n value arises to 1, and for recombination inside the depletion region, n value appears to 2.

Another defect of a real solar cell will be the leakage current, which might be due to the presence of an alternate current path in the solar cell. The alternate current path does not allow the carriers to reach their corresponding electrodes. More precisely, the $J - V$ characteristics of a realistic solar cell with a device area A and considering the series resistance (R_s, in series with the diode) and shunt resistance (R_{sh}, parallel to the diode) can be expressed as

$$J = J_D - J_{ph} = J_0\left\{\exp\left[\frac{q(V+Jr_s)}{nKT}\right] - 1\right\} + \frac{V+Jr_s}{r_{sh}} - J_{ph} \text{ ---------- } (1.21)$$

Where $r_s = AR_s$ and $r_p = AR_p$ are the specific series and shunt resistance, respectively. The alternate current path in the solar cell reduces the shunt resistance (R_{sh}) and alternatively, increase the series resistance (R_s), as a result, the FF of the solar cell reduces significantly.

The final problem of a real solar cell might be the optical loss like reflection or absorbance by the front contact of the device, which restricts the solar cell to absorb

sufficient solar light. So, improving materials quality to reduce the trap states formation and optical engineering of solar cells are the subjects of ongoing research in this field.

1.3 Current status of solar cells technology

For practical applications of solar cells, the high-power conversion efficiency is not the only criteria; rather, it should also have a low manufacturing cost and long-term stability. Additionally, a wide range of applications in consumer electronics, and rooftop solar panels demand flexible, thin, portable, and lightweight solar cell devices. In 1976, the average cost per installed watt of solar cells in the United States was 106.1 US$, and it was dropped in 2017 to 0.5 US$.[16] Despite the significant cost reduction, as of today, the cost per watt of solar cells is still higher than the available fossil fuel technologies.[17] To meet the demands of emerging applications, portability and flexibility are two important features that the existing silicon-based solar cells do not comply with. Therefore, further research is required to make flexible, portable, thin lightweight solar cells with reduced cost before the photovoltaic technology can be widely adopted.

To date, the development of photovoltaic technology can be classified into three generations; first, second, and third-generation solar cells.[18] The first-generation solar cell is the wafer-based single *p-n* junction solar cell, made by high purity and high-quality materials such as single crystals. Single crystalline Si and gallium arsenide solar cells are considered first-generation solar cells.[19-21] These solar cells are still the most convenient as well as the most established photovoltaic technology. Till date, the first-generation solar cells have the highest power conversion efficiency as a single junction model solar cell. However, the manufacturing costs are extremely high due to the manufacturing complexities, like requirements of high-quality pure materials and high processing temperature. High manufacturing costs have declined the large-scale manufacturing of these solar cells in recent years.

Second-generation solar cells, also known as thin-film solar cells, are made with less materials and low-temperature manufacturing techniques, which drops their manufacturing cost. This generation includes amorphous silicon, cadmium telluride, and copper indium gallium selenide (CIGS) solar cells.[18] These solar cells also produce high efficiency like amorphous Si -11% - 13%, CdTe - 21%, and CIGS - 23%, but relatively lower than single-crystalline Si solar cell (27.6%).[22] Although these generation solar cells have lower manufacturing costs than the first-generation solar cell, still, the cost is significantly higher

compared to fossil fuels. The use of rare elements like indium and highly toxic cadmium doesn't solve the problem completely. These limitations further demand to find out better technology.

Finally, the third-generation technology covers a wide range of materials like organic small molecules and polymers, inorganic solution-processed quantum dots and nanocrystals, and organic-inorganic hybrid perovskite for the development of solar cells and still is in the developing phase.[18,23-25] The fundamental idea of this generation solar cell is the use of cheaper material and ease of fabrication technologies, which promise the lower manufacturing cost than other groups of solar cells. The solution-processed fabrication technology assures the film construction on curved or flexible substrates. These advantages lead to thinner, light weight and smarter solar cells for versatile applications such as in space research, the military where transportability is a major challenge, household or personal use, and industrial sector. Although, most of these third-generation technologies are still not available in the market, but they draw colossal attention to its research for device efficiency improvement, scalability, and stability.[23-25] Till today, single-junction Si solar (both crystalline and amorphous) cells dominate the current solar cell market. However, continuous research in solution-processed photovoltaic technologies would lead to their successful commercialization in the near future. Colloidal quantum dots[25,26] (CQDs) solar cell technology falls under this category, and this thesis focuses on the development of Lead sulfide (PbS) CQDs based solar cells.

1.4 Quantum Dots

Quantum dots (QDs) are semiconductor nanocrystals with significantly different electronic properties than their bulk counterpart. This section discusses the primary concepts of quantum dots and their colloidal synthesis procedure. This thesis is wholly based on the development of PbS CQDs solar cells. We then discuss the characteristics of PbS quantum dots and their surface chemistry for solar cell device application.

1.4.1 Basics of Quantum Dots

The fundamentals of QDs are built on the concept of the quantum confinement effect.[27] The simplest example to understand the quantum confinement effect is the confinement of a free particle in a 1D potential box. The wavefunctions associated with a

free particle are traveling wave (equation 1.22), and the corresponding energy of the particle is a continuous quantity (equation 1.23).[28]

$$\psi_k(x) = Ae^{iKx} \text{ ---------- } (1.22)$$

Where ψ_k is the wavefunction, x is the position of the particle, K is the wave vector, i is the imaginary part, and A is the amplitude of the wavefunction.[29]

$$E = \frac{\hbar^2 k^2}{2m_0} = \frac{p^2}{2m_0} \text{ ---------- } (1.23)$$

E is the energy of the particle, k is the wavenumber, $\hbar$ is the reduced Planck constant and m_0 is the rest mass of the particle, by implying momentum, $p = \hbar k$, we get equation 1.23. Now, if that same free particle is put inside the infinite potential window confined 1D box, the wavefunction of that particle changes from traveling wavefunctions to standing wavefunctions (equation 1.24). The particle's associated energy no longer stays as continuous; it becomes discrete (equation 1.25).[28]

$$\psi_n(x) = \sqrt{\frac{2}{L}} \sin \frac{n\pi x}{L} \text{ ---------- } (1.24)$$

$$E_n = \frac{(\hbar n \pi)^2}{2m_0 L^2} \text{ ---------- } (1.25)$$

L is the length of the potential wall confined 1D box, and n is a positive integer (1,2,3,4……..) Most interestingly, the energy gap (ΔE) between two discrete levels decreases with increasing the box length (L).

Similarly, when we reduce the bulk material's size lesser than its Bohr exciton (an exciton is defined as an electron-hole pair bound by Coulomb force) radius, they show the quantum confinement effect.[29] This reduced sized (1-100 nm) particles of semiconductor materials are called nanocrystals. All nanocrystals don’t show quantum confinement effect; for example, 5 nm PbS NCs have quantum confinement property while 25 nm PbS NCs don’t exhibit quantum confinement characteristics as the Bohr exciton radius is approximately 18 nm for PbS NCs. The Bohr exciton radius (a_B) of a material is defined as;[29]

$$a_B = \varepsilon_r \left(\frac{m_e}{\mu^*}\right) a_0 \text{ ---------- } (1.26)$$

where ε_r is the dielectric constant of materials, m_e is the mass of a free electron, μ^* is the reduced mass of electron-hole pair (exciton) and a_0 is the Bohr radius (0.053nm) of the hydrogen atom.

Bulk semiconductor crystals are considered as infinite crystals with a periodic arrangement of atoms. As the large number of atoms come together to form a bulk crystal, their atomic orbitals overlap on each other to form a band like electronic structure. While in the case of QDs, the number of atoms per QD is limited (restricted to few hundreds of atoms). The overlap of atomic orbitals of the small number of atoms in QDs does not form a continuous band-like structure; instead, they form discrete energy levels, as shown in Figure 1.9.

The density of states (DOS) of quantum confined nanocrystals have different functional forms depending on the number of confinement dimensions.[30] Materials with 1D confinement are called quantum well, and their electrons and holes can move in two dimensions. In quantum wire, electrons and holes have only one degree of freedom (2D confinement). Whereas, if materials are confined in all three directions, they are called as quantum dots. The DOS of quantum well is independent of energy, while the DOS of quantum wire is proportional to $E^{-1/2}$. Delta functions represent the DOS of QDs.

As we have seen for the particle in 1D box model, with increasing the box length, the energy gap between two levels decreases; similarly, by tuning the size of QDs, we can tune their optical bandgap. In 1986, Brus proposed the relation between the bandgap and the size of the QDs (equation 1.27).[31]

$$E_{g(QD)} \approx E_{g,bulk} + \frac{\hbar^2\pi^2}{2\mu^* L^2} - E_X \quad \text{----------} \quad (1.27)$$

where $E_{g(QD)}$ is the bandgap or band edge absorption energy of QD, $E_{g,bulk}$ is bandgap of the bulk material, L is the size of QD (L should be lesser than Bohr exciton radius of QD) and E_X is the exciton binding energy.

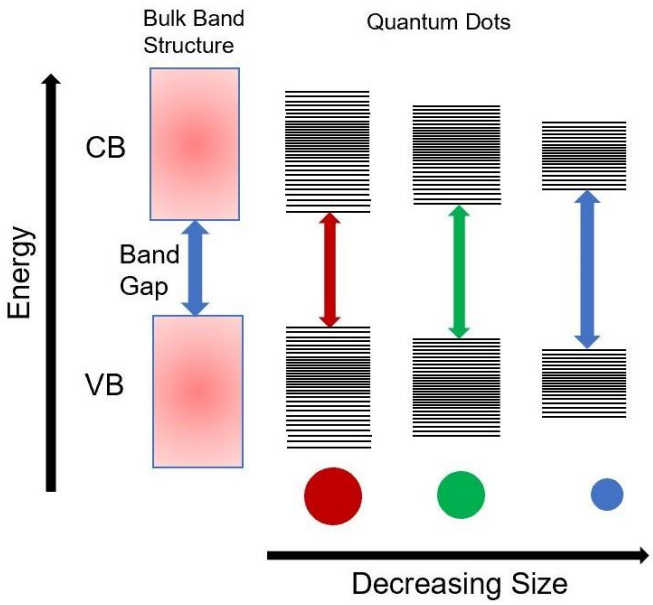

Figure 1.9: Schematic representation of band structure from bulk material to quantum dots and change in bandgap.

For any electronic device application, tuning the bandgap of semiconductors has a notable advantage for band structure engineering. It allows one to construct heterojunctions device with proper electronic properties. For example, solar cells are built from semiconductor heterojunction (preferably type-II heterojunction) for effective charge separation, and collection.

1.4.2 Colloidal Synthesis of Quantum Dots

Colloidal quantum dots (CQDs) are an emerging class of semiconductor materials with facile chemical phase synthesis their facile synthesis and processing. There are mainly three chemical-phase synthesis methods that are used for the synthesis of QDs, namely, hot injection method, non-injection method, and control flow synthesis.[32,33] In this thesis, we focus on the hot injection method due to its superior tunability, control, and reproducibility. A library of good quality colloidal semiconductor nanocrystals such as II-VI (CdS, CdSe, CdTe), III-V (InP, InAs), or IV-VI (PbS, PbSe) are synthesized by this well-established solution-phase hot-injection method.[34] The hot injection method involves the rapid injection of one particular precursor into the high boiling point solvent containing another precursor and surfactant at moderate temperature. For example, the cadmium chalcogenide (CdX) CQDs are synthesized by the rapid injection at a particular temperature of chalcogenide (X=S, Se) precursors into the high boiling point solvent containing Cd precursor with

surfactant molecules. The formation mechanism of CQDs is explained by La Mer and Dinegar nucleation and growth model.[35,36] Three steps mechanism are involved during the formation of CQDs, first induction, then followed by nucleation, and finally the growth step (Figure 1.10).

(I) Induction step: In the induction step, the monomer concentration (n) of CQDs increase after the injection of precursors in the solvent. When the monomer concentration exceeds a critical concentration (n*), directing the beginning of homogeneous nucleation.

(II) Nucleation step: The nucleation rate rises very fast after n*. When the rate of monomer consumption and rate of nucleus formation are equal, the monomer concentration attains the maximum value n_{max}. In a moment, the rate of nucleus formation crosses the rate of monomer consumption and dropping the monomer concentration. When the monomer concentration falls below n*, the nucleation step ends. The other determining factors of controlling nucleation rate are temperature, interfacial tension, and reactivity of monomers. The rate of nucleation increases rapidly with increasing temperature. The reactivity of precursors is controlled by the surfactant molecules comprised of a long hydrocarbon tail and a polar head; such surfactants like oleic acid, oleylamine, trioctylphosphonic acid, dodecanethiol, etc.

(III) Growth step: Followed by nucleation, the formation of CQDs is carried by slow growth. When the monomer concentration drops below the supersaturation level, the CQDs grow epitaxially. The growth process is controlled by two competing methods; diffusion-controlled growth and reaction-controlled growth. Diffusion-controlled growth allows growing uniform, monodispersed particles, whereas reaction-controlled growth is based on the solubility of the particles, which allows growing bigger size particles. In general, diffusion-controlled growth is followed first with an almost symmetrical particle size distribution, and when the average particle size exceeds the critical limit, then the growth is followed by the solubility of the particle, which leads to unsymmetrical particle size distribution.[37] The growth mechanism is also controlled by surfactants molecules; when surfactant molecules concentration is high, the growth of CQDs will be reduced. As a result, the size of CQDs also reduces. The certain huge drop in temperature also decreases QDs size by slowing the growth rate.

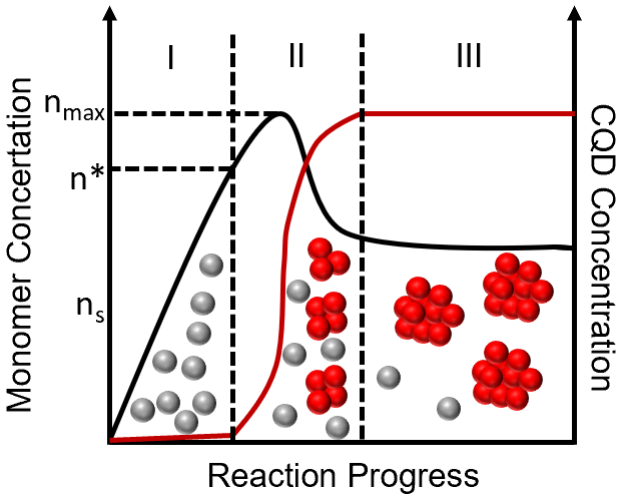

Figure 1.10: La Mer and Dinegar nucleation and growth model of CQDs.

Even after the growth step, the CQDs undergo size focusing and Ostwald ripening, which further influences the monodispersity of the final ensemble of CQDs. Size focusing generally occurs at the very first step of CQDs growth, just after the nucleation step where smaller CQDs grow faster than the larger CQDs and resulting in monodispersity in the CQDs ensemble. The Ostwald ripening process allows the dissolution of smaller CQDs with monomers and diffuses onto larger CQDs.[36] The Ostwald ripening process increases the polydispersity among the smaller size CQDs.

This thesis focuses mainly on the synthesis, surface passivation, and solar cell device fabrication of PbS CQDs. Here, we will shortly describe the synthesis process of PbS CQDs. In the working chapters of this thesis, all the details of PbS CQDs synthesis are discussed. A well-accepted colloidal synthesis for PbS CQDs is developed by Hines and Scholes in 2003.[38] A hot injection method is followed in this method, where sulfur precursor, hexamethyldisilathiane is injected rapidly into hot lead oleate solution (Figure 1.11). Lead oleate precursor is made by in situ reaction of lead oxide and oleic acid in high boiling point solvent Octadecene (B.P.-340°C) at 95°C under high vacuum condition. Then lead oleate precursor solution is switched into argon atmosphere, and injection temperature is fixed. At a fixed temperature, sulfur precursor, hexamethyldisilathiane ($(TMS)_2S$) is injected very first. Upon injection, nucleation is initiated due to induced supersaturation. After rapid injection, the growth temperature is controlled for commencing the growth stage. The size of CQDs is tuned by varying the injection and growth temperature, oleic acid concentration, and volumes of the solution.

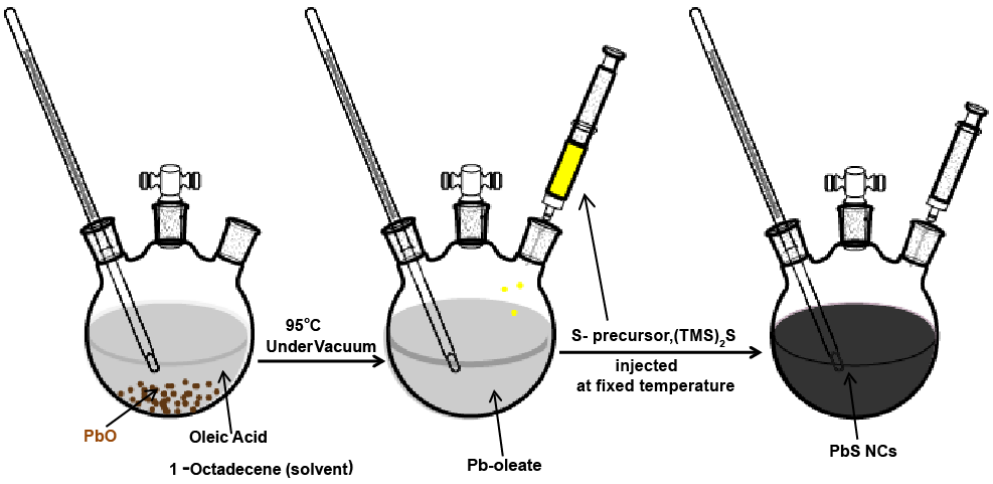

Figure 1.11: Schematic representation of hot injection method to synthesize PbS NCs.

1.4.3 PbS Quantum Dots and their surface chemistry

In the last 20 years, Lead sulfide (PbS) QDs have grabbed a tremendous amount of attention due to their several electronic and optoelectronic device applications such as light-emitting diodes[39], transistors[40], lasers[41], photodetectors[42], and photovoltaics (PV)[32,] which are being still in the development stage. Till to date, research progress in PbS NCs devices has been achieved mainly through improvements in colloidal synthesis of QDs and surface structure modification of QDs by understanding the surface chemistry at the atomic level. PbS CQDs are generally synthesized with the desired size, shape, and composition using oleic acid (long-chain, insulating, bulky ligand) as a surface ligand discussed in section 1.4.2. QDs are generally made up of hundreds to thousands of atoms with a large surface to volume ratio; their surface atoms are terminated by ligands called surface ligands.

The surface structure (surface atoms-ligands binding) of QDs governs the growth and solubility and also strongly impacts the physical and chemical properties of QDs. [32,43-45] Surface ligands direct the nucleation and growth kinetics of QDs during synthesis[44] and restrain their colloidal stability and agglomeration by steric or electrostatic repulsion mechanisms.[45] The surface structure of QDs can also strongly impact their optical, electrical, catalytic, and magnetic properties.[45] So, the surface structure of the QDs needs to be better understood for further finer applications.

PbS exhibits a high symmetric rock salt crystal structure, and its QDs are exposed with well defined (100) and (111) facets. [46,47] To explain these non-identical surface sites and ligand interaction, surface ligands are classified into mainly four types,[45,48] (1) X-type

ligands; these ligands are one electron donor and make a direct two-electron covalent bond with the surface atoms (either having an odd number of valance-shell electrons or monovalent ions), (2) X type-Bound ion pair; These type of ligands are a combination of cation and anion ($[X]^+[B]^-$), where anionic part makes a covalent bond as X-type ligand on QDs surface, and the cationic part provides electrostatic stabilization of QDs. (3) L-type ligands; neutral two-electron donors (Lewis bases) and form a dative bond with surface sites, and (4) Z-type ligands are neutral two-electron acceptors (Lewis acids) that interact with electron-rich surface sites (Lewis bases).

The (100) facets of PbS QDs are made by Pb and S atoms' square arrangements, and these electronically neutral[49,50] facets are covered by oleic acid molecules (L type ligand, neutral donor) through electrostatic interaction with neutral Pb and S atoms ($C_{17}H_{33}C{=}O..(Pb)OH..(S)$).[51] Due to steric repulsion between oleic acid molecules, one Pb-S pair is protected by one oleic acid molecule, while the next Pb-S pair remains empty (Figure 1.12). Density functional theory (DFT) studies predict that oleic acid molecules bind to the (100) facets as a bidentate L type ligand with binding energy 0.16 eV per oleic acid molecule. [51]

On the other hand, (111) facets present a polar hexagonal layer of only uncoordinated Pb atoms.[45,49,51] The oleate and hydroxyl (by-product during synthesis) anions (X-type ligands, one electron donor) bind to cationic Pb^+ atoms of polar PbS (111) facets to maintain the charge neutrality of QDs (Figure 1.12), which is supported by several experimental methods like NMR, XPS, and FT-IR and DFT calculations also suggest the strong covalent binding of oleate and hydroxyl anions with Pb^+ atoms (binding energy 0.52 eV per ligand) of (111) facets.[51,52] It is shown that the presence of the Pb-OH bond on PbS (111) facets reduces the photoluminescence quantum yield (PLQY) of PbS QDs.[53]

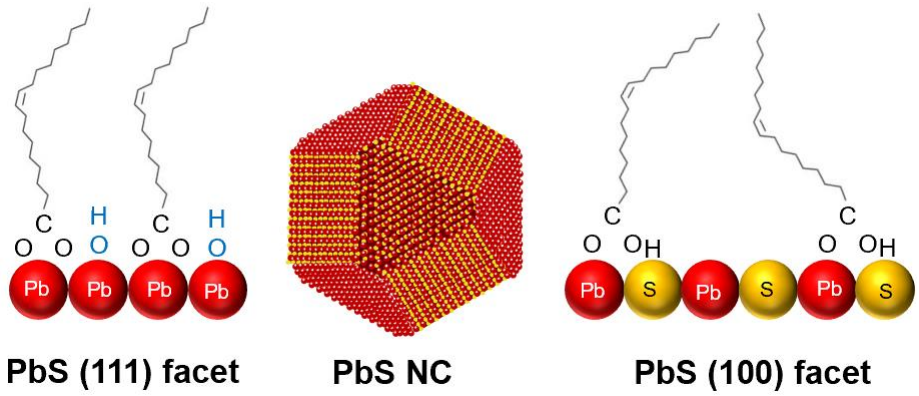

Figure 1.12: A schematic presentation of oleic acid capped cuboctahedral PbS NC and facet specific binding of long-chain oleic acid molecules.

1.5 PbS Quantum Dots photovoltaics

Bulk PbS has a direct bandgap of 0.41 eV. Due to the quantum confinement effect and the large Bohr exciton radius (18nm), the bandgap of PbS CQDs can be tuned in a wide range from approximately 0.6eV to 1.6 eV by changing the size of CQDs during synthesis.[32,33] This wide range covers from visible to infrared range of the solar spectrum. According to the Shockley-Queisser limit, the optimum bandgap for achieving maximum power conversion efficiency from a single *p-n* junction solar cell is 1.34 eV. The bandgap of PbS CQDs can be tuned to 1.34 eV, and absorb most of the solar spectrum. Besides the bandgap tunability and low bandgap, PbS QDs are solution-processable, easy to synthesis, and stable. Moreover, PbS QDs are composed of earth-abundant inexpensive elements. These outstanding properties of PbS CQDs make them an ideal candidate for single-junction and tandem solar cells device application. This section will review the PbS CQDs solar cell fabrication techniques, impact of surface passivation on the PCE of the solar cell, progress in PbS CQDs solar cell, and the challenges associated with further improvement of solar cell PCE. Finally, an outline of this thesis has been given.

1.5.1 Surface Passivation for Quantum Dots Solar cell

Oleic acid capped QDs exhibit immense optical properties like high absorption coefficient, strong emission, lesser FWHM (full width half maximum), and higher monodispersity due to their higher surface coverage and compact surface passivation. [38,44,51] Still, there are two major drawbacks of as-synthesized oleic acid capped PbS QDs (see section 1.4.3); first, the rise of the Pb-OH bond on the PbS (111) facets during synthesis, and second, the presence of unpassivated Pb-S pair on the PbS (100) facets; resulting in a

significant drop in their PLQY.[51,53] To overcome these issues, in-situ surface treatment is carried out during the synthesis of PbS QDs. Zheng *et al.*[54] in 2014 have shown the effect of using lead halide instead of lead oxide during synthesis (see section 1.4.2), where the halide atoms are incorporated on oleic acid capped PbS QDs surface. Instead of hydroxyl (-OH) ion passivation on PbS (111) facets, chloride ions passivate PbS (111) facets (Pb-Cl) and increases the PLQY of as-synthesized PbS QDs. Another unique approach developed by Ip *et al.*[55] is the use of $CdCl_2$ during the growth stage of the synthesis process, where it is understood that small size chloride ions can reach the trap sites, which are not accessed by bulkier oleic acid molecules. This method ensures extensive trap mitigation and increases the PLQY of QDs. However, later it is realized that metals also have a significant influence on the trap passivation, and $CdCl_2$ as a Z-type ligand can passivate the S sites of PbS (100) facets.

However, for the electronic device applications of colloidal PbS NCs, these long-chain insulating ligands do not allow efficient electron transport between the NCs. Replacing these insulating ligands with small ligands is the detrimental step to make superior electronic devices.[45] Improper surface passivation leads to the fusion of NCs through unpassivated facets and air oxidation of the surface, causing the trap state formation inside the valance and conduction band.[32,33,45,55] The fusion of QDs will lead to the polydispersity[56] in the QDs ensemble, resulting in the transfer of energy from higher bandgap QDs to lower bandgap QDs. As the quantum confinement effect of QDs is size dependant, the preservation of QDs size is crucial for solar cell device application. The midgap trap states act as recombination centres where the charge carriers can be recombined in a non-radiative pathway before collecting them (Figure 1.13). It is quite challenging to replace those long-chain oleic acid molecules with small ligands to preserve the size, optical and electronic properties of QDs.

Further, PbS QD has two different exposed surface facets {(111) and (100)} with non-identical patterns of surface atoms (details discussed in section 1.4.3) terminated by oleate anion (covalent binding of oleate anion as X-type ligand) and oleic acid molecules (Figure 1.12, electrostatic interaction of neutral oleic acid as bidentate L-type ligand).

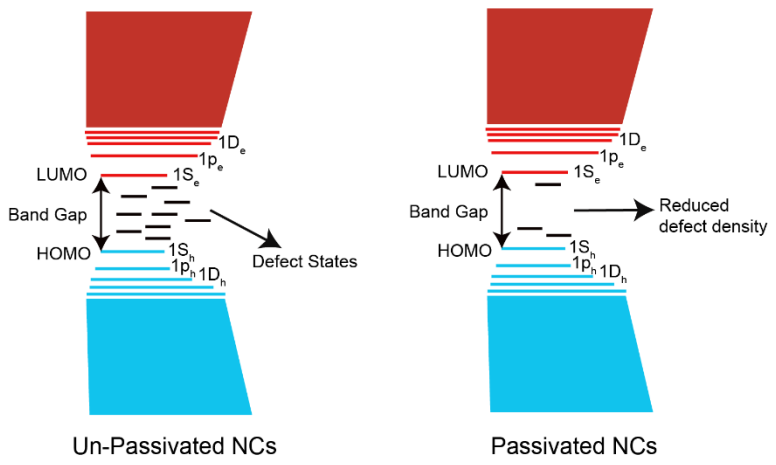

Figure 1.13: Schematic band diagram presentation of passivated and un-passivated NCs.

These criteria demand a different type of shorter surface ligands for passivation of PbS QDs. For PbS (111) facets passivation, X-type shorter ligand is required, while for PbS (100) facets, both Z-type (to protect S atoms) and neutral donor L-type (to passivate Pb atoms) ligands are needed. These requirements for the compact surface passivation, further increases the difficulty level of the ligand exchange process.

In general, two different approaches are followed to exchange the long, oleic acid ligands with shorter conductive ligands for solar cell device fabrication (Figure 1.14a). The first approach is solid-state ligand (SSL) exchange,[32,53,55,57] which proceeds ligand exchange only after casting the CQDs film (Figure 1.14b). The second one is the solution-phase ligand exchange (SPLE) method, and it involves replacing the long native ligands for shorter ligands in the solution phase before fabricating the films (Figure 1.14c).[58,59]

(I) Solid-state ligand exchange:

The solid-state ligand exchange process is a well-established method to fabricate QDs photovoltaic devices. In this method, first, a colloidal suspension of QDs in a non-polar solvent is spin-coated onto a substrate; after that, the grown film is soaked under polar solvent containing the shorter ligand for several seconds to make sure the complete removal of native ligands (Figure 1.14b). The excess ligands are washed away from the films by subsequent rinsing with a polar solvent. However, only 10-20 nm thick film can be grown by this method, because, during the soaking time, the shorter ligands can't penetrate inside the thicker film to replace long-chain oleic acid molecules.

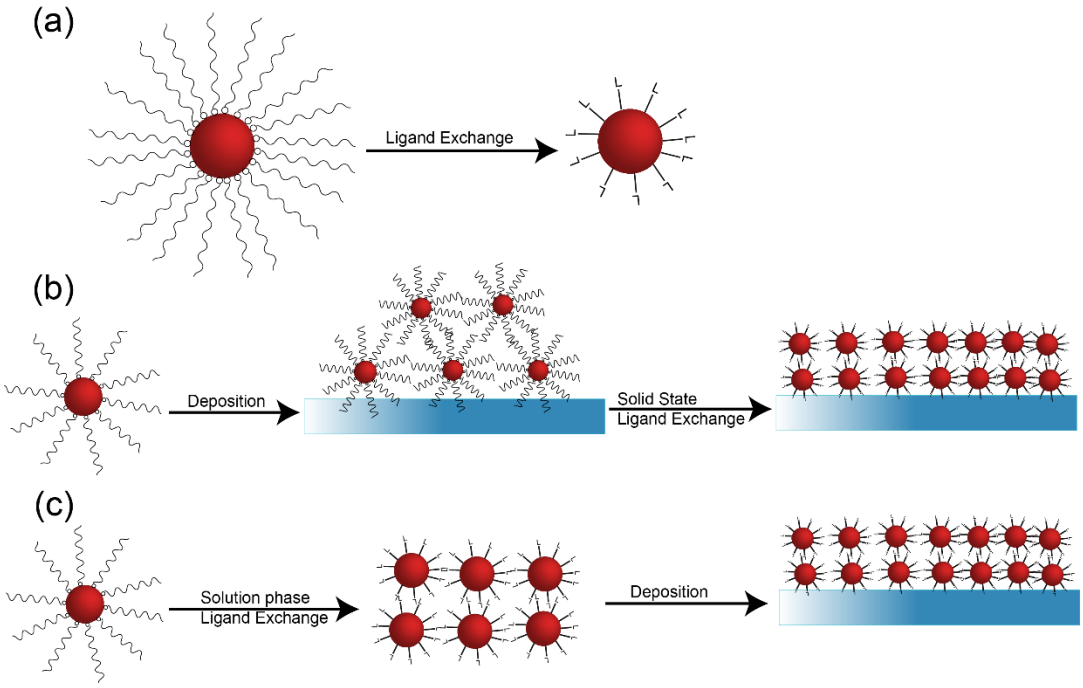

Figure 1.14: Schematic of different ligand exchange process, (a) Replacement of long-chain insulating molecules by smaller ligand (L) (b) Solid-state ligand exchange (c) Solution phase ligand exchange.

The replacement of long-chain oleic acid molecules with shorter ligand leads to significant volume shrinkage in the films, resulting in macro defects such as voids and cracks. To avoid such defects, layer by layer (LBL) growth process is followed. In this approach, film deposition and ligand exchange are repeated several times until the desired thickness is attained. Generally, 10-12 layers are grown to build an optimum thick PbS QDs solar cell. The solid-state ligand exchange depends on exchange kinetics, and the slow exchange rate favours to development of compact QDs film.

The most common organic ligands used in the LBL growth of QDs solar cell are 1,2-ethanedithiol (EDT), 1,3-benzenedithiol (BDT), and 3-mercaptopropanoic acid (MPA). Later, inorganic ligands such as (Cl^-, Br^-, I^-, SCN^- and metal salts like NaCl, RbI, CdI_2, PbI_2, etc.) are also widely used for LBL growth.[60] Although, the LBL solid-state ligand exchange process has reproducibility in laboratory conditions, but its scalable manufacturing, like roll-to-roll processing, spray coating, etc., is questionable. Moreover, it is a very time-consuming process; almost 30 minutes requires constructing a single device. A small error in this method increases the inhomogeneous energy states in CQD films through random and heterogeneous packing.

(II) Solution phase ligand exchange:

To overcome those issues mentioned above, the solution phase ligand exchange (SPLE) method has been developed, where a single step smooth crack-free film is deposited with 100% utilization of materials. [58,59] In this method, the long-chain oleic acid molecules are replaced by shorter ligands in the solution phase before fabricating the films (Figure 1.14b). The major challenge of this process is to preserve the colloidal stability of shorter ligand passivated QDs. Oleic acid capped QDs are stabilized by the steric repulsion of long-chain oleic acid molecules and dispersed in non-polar solvents like octane, toluene hexane due to the negative free energy of long-chain solvent mixing.[44,45] Now, shorter ligands exchanged QDs can't be stabilized by steric repulsion in a non-polar solvent because of the positive free energy of chain solvent mixing, which drives to minimize contact of ligands with surrounding solvent molecules by contraction of ligands and induces aggregation of dispersed QDs. Another way to achieve the colloidal stability of QDs is electrostatic stabilization by adsorbing charged species on their surface. Oppositely charged counterions placed in a diffused region around the QDs compensate their surface charge.[45] Electrostatic stabilization generally achieves in a polar solvent with a high dielectric constant. In such solvents, the proximity of surface charged QDs is prevented by the entropic penalty related to the condensation of counterions in the diffuse double layer.

A biphasic solution-phase ligand exchange process is developed by taking advantage of the electrostatic stabilization mechanism, where oleic acid capped QDs dispersed in a non-polar solvent mixed with polar solvents containing the ionic ligands to replace the long oleic acids molecules. This exchange process carries out in dilute condition to ensure the almost complete replacements of oleic acids. As the polar (generally N, N dimethylformamide) and non-polar (typically octane) phases are immiscible, the mixture is shaken for a couple of minutes for mixing the new ligands and QDs. After a while, the CQDs transfer to the polar phase, resulting from the replacement of oleic acid molecules by the polar solvent compatible ligands. The top transparent non-polar solvent layer is discarded, and the polar phase is washed 2-3 times to remove residual oleic acids. At this step, the exchanged CQDs remain in the dilute polar solvent; however, for one-step film deposition, a concentrated CQDs ink is required. Therefore, the exchanged CQDs are precipitated by adding non-solvent into the polar phase and centrifuged to collect those QDs. After centrifugation, the exchanged CQDs are redispersed to make concentrated ink in a low volatile solvent for one-step deposition. Till now, the most suitable ligand for SPLE of PbS

CQDs is either only lead halide (X=Cl, Br, I) or a mixture of lead halide and halide salts (MX, M= Cs^+, NH_4^+ or MA^+). Such lead halide exchanged QDs inks are passivated by X-type halide or PbX_3^- ligand, and their corresponding counter cation PbX^+ [59], MA^+ [58], Cs^+ [61], NH_4^+ [62] form a diffusive layer to preserve colloidal stability and charge balance to the QDs surface during SPLE in DMF phase. Due to the high boiling point and viscosity of DMF, it is quite impossible to grow thick film from the DMF phase. Volatile butylamine or a mixture of butylamine and hexylamine are used as a solvent to disperse exchanged QDs for deposition of thick QDs films.

There are several benefits to the solution phase ligand exchange procedure compared to the solid-state ligand exchange approach. Large-area deposition techniques like roll-to-roll processing, inkjet printing, and doctor blading are not compatible with the LBL approach. The ligand soaking followed by consecutive washing steps required for each layer is a time-consuming and chemical wasteful technique. In contrast, the concentrated CQDs ink developing from the SPLE process provides a single step deposition to grow thick film. This CQD ink can be employed in small-scale methods such as spin-coating and large-scale deposition techniques for device fabrication.

1.5.2 Doping of nanocrystals

Bonding between the surface ligands frontier orbitals and the QDs surface atoms produce a new set of molecular orbitals with bonding (σ) and antibonding (σ^*) character, with bonding orbitals, stabilized and antibonding orbitals destabilized with respect to the energies of non-interacting surface atom and ligand. This would influence the resultant distribution of energy levels of QDs and also might impact on the doping levels of QDs.[45,63-64] Incorporating other atomic sites of surface ligands not containing Pb and S as binding sites, for example, halides (Br, I), involves the different extent of doping, as shown by the PbS CQD film carrier concentration.[65] Halides (Br, I) passivation of PbS QDs show *n*-type characteristics.[66] Surface oxidation (oxygen doping) of PbS QDs increases *p*-type doping density without loss of mobility as long as ligands bind to the surface atoms.[67] EDT passivated PbS QDs are *p*-type in nature, while hydrazine capped QDs show *n*-type doping.[68]

Two major hypotheses have been suggested to explain the influence of surface ligands on the absolute energy of the QD electronic energy state. The first one is a general proposal on a stoichiometry balance in a QD. For exact stoichiometry, valance orbitals are

completely filled up with a feature of closed-shell electronic configuration and result in an intrinsic material. In the case of off-stoichiometry, deficiency of electrons leads to incomplete fill-up of valance bands and influences in *p*-type doping, while an excess of electrons populates the conduction band and exhibits in *n*-type doping. For example, if iodine substitutes the sulfur atom in PbS QD, to maintain the charge neutrality, an extra electron goes into the conduction band and results in *n*-type doping. Vozny *et al*. has postulated this concept as "charge orbital balance" to predict doping level in QDs.[69]

The second hypothesis originates from the surface-bound ligand induced electric dipole.[70] The direction and magnitude of the surface dipole are predicted from two competing factors: the interfacial dipole configured between the surface atom and ligand head group and any intrinsic dipole allied with ligand structure. The interfacial dipole depends on the electron affinity, ionization potential, and electronic charge of surface atoms and ligands, for example, Lewis basic ligands point the interfacial from the ligand towards the metal centre of QD ($L\delta^- \rightarrow L\delta^+$). The intrinsic dipole of the ligand depends on the chemical structure and binding mode. The intrinsic dipole is zero for atomic ligands (for example, halides, thiocyanate). If the overall final dipole points towards the QD centre, the electric field potential moves all energy levels down, and for the opposite instance, vice versa. Halide ligand passivated QDs exhibit the largest ligand-induced downward shift of electronic energy levels. However, it is still not conclusive as to which assumption is accurate to explain the effect of surface ligands on PbS QD doping and energy levels.

QDs can also be doped by introducing dopants during synthesis. For example, Ag doping in PbS QDs increases the *p*-type doping density (10^{19} cm^{-3}).[71] Similarly, we can introduce heterovalent dopants in TiO_2 or ZnO nanocrystals used as *n*-type electron extracting layer in PbS QDs solar cell, during synthesis for increasing the *n*-type doping density.[72]

1.5.3 Device engineering of Quantum Dots Solar cell

In the earlier two sections, the effect of surface passivation on the optoelectronic properties and electronic structure of QDs is discussed. This section reviews the improvements executed to CQDs solar cell performance via device architectural engineering, along with an attention on the material choice and interfaces. Till to date, mainly four different types of PbS CQDs solar cell device architecture have been developed. Those are Schottky junction solar cell, Depleted heterojunction solar cell, Bulk

heterojunction solar cell, and graded doping architectures. A brief summary of each device architecture is discussed in the following section.

1.5.3.1 Schottky Junction solar cell

The first reported PbS CQD solar cell using PbS CQDs as the main light-absorbing material is a Schottky junction solar cell.[73] Among the different types of device architectures, the Schottky junction solar cell has the most straightforward device architecture: Just PbS CQDs layer is sandwiched between a metal electrode and a transparent electrode. The metal with a low work function (like aluminium) forms a rectifying Schottky junction with the *p*-type PbS CQDs layer, and the transparent electrode (like indium doped tin oxide (ITO)) with a deeper working function makes ohmic conduction with the *p*-type PbS CQDs layer. Band bending happens at the interface between the metal electrode and the semiconductor, which results in the formation of a Schottky barrier and a built-in potential with the height of magnitude estimated from the difference between the *p*-type PbS and metal work function. The built-in potential determines an upper limit to the V_{oc} of the device (Figure 1.15).[74]

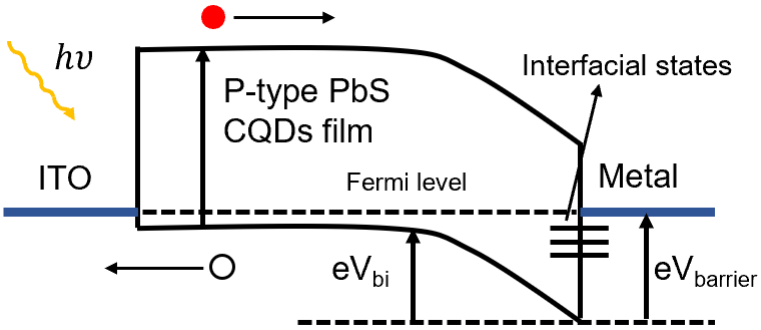

Figure 1.15: Band diagram of Schottky junction solar cell constructed by *p*-type PbS CQDs with a low work function material like aluminium.

Few factors limit the efficiency of Schottky junction solar.[73,74] Firstly, the interfacial states formed at the metal and semiconductor interface pin the Fermi level of the devices. This restricts the actual barrier height and eventually the V_{oc} of the device. Extraction of charge carriers is more efficient when the thickness of the PbS CQDs layers is the sum of carrier diffusion length and depletion width. Restricted bending at the Schottky junction limits the depletion width of the thick PbS CQDs layers and results in lowering the Jsc of the device. The second is the stability of the metal-semiconductor interface, which further

depends on the lability and the reactivity of the ligand towards the metal surface. Thirdly, PbS CQDs Schottky junction devices usually have a lower FF, which might be due to the rise of void space in PbS CQDs layers between metal and the transparent electrode. As void space creates a shunt path for carriers and lowers the shunt resistance. Shunt resistance is directly proportional to the FF of the device.

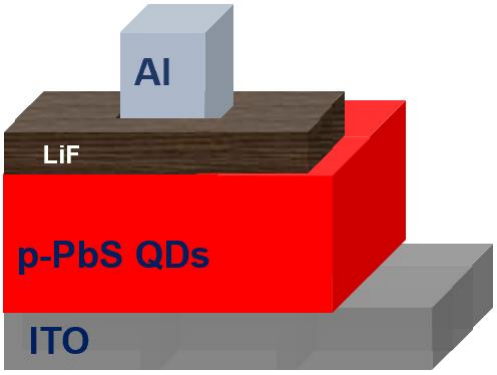

Figure 1.16: Device architecture of PbS CQDs Schottky solar cell with the integration of thin LiF layer.

However, the rise of interfacial states of this device architecture is sorted out by inserting an ultrathin interface layer of lithium fluoride (LiF) between the metal and PbS CQDs layer (Figure 1.16).[75,76] As a result, the Voc, FF, and stability of the device increase significantly. Therefore, the LiF interface layer reduces the interfacial states between the metal and PbS CQDs film, thus restricting the Fermi level pinning effect. It also stays as a barrier between the surface ligands of the PbS CQDs layer and the metal electrode.

1.5.3.2 Depleted heterojunction solar cell

Although the problem of the interfacial state between metal and semiconductor is solved by inserting an ultra-thin layer of LiF layer, but low depletion width is the principal disadvantage in Schottky junction solar cell. In a depleted heterojunction device, a wide bandgap transparent *n*-type material like (TiO_2 or ZnO) is deposited by solution process techniques[77] in between transparent electrode and *p*-type semiconductor and a thin layer of MoO_3 used to reduce the interfacial states between PbS QDs and metal (Figure 1.17a).[55,77]

The depletion width in the *p*-PbS film increases significantly due to the formation of a *p*-*n* junction between *n*-type TiO_2 or ZnO and *p*-type PbS layers.[55] The carriers are extracted in this device by the drift transport mechanism. The first two (second and third

chapter) working chapters of this thesis follow this device architecture to build the PbS CQDs solar cells (Figure 1.17b).

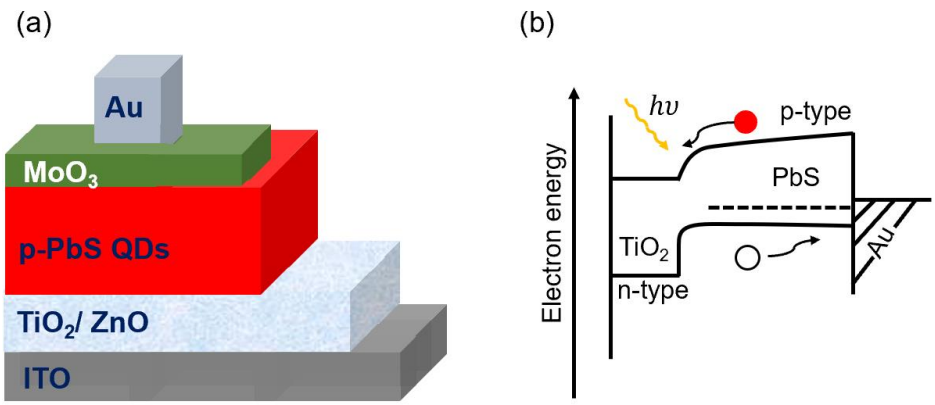

Figure 1.17: Schematic representation of depleted heterojunction PbS CQDs solar cell (a) Device architecture (b) Band diagram.

1.5.3.3 Bulk heterojunction solar cell

The bulk heterojunction solar cell is the modification of the *n*-type layer of depleted heterojunction solar cell. Different nanostructures like porous nanowires,[78] nanorods, or nanopillars[79] of TiO_2 or ZnO NCs are grown to the length of the device's usual depletion width.

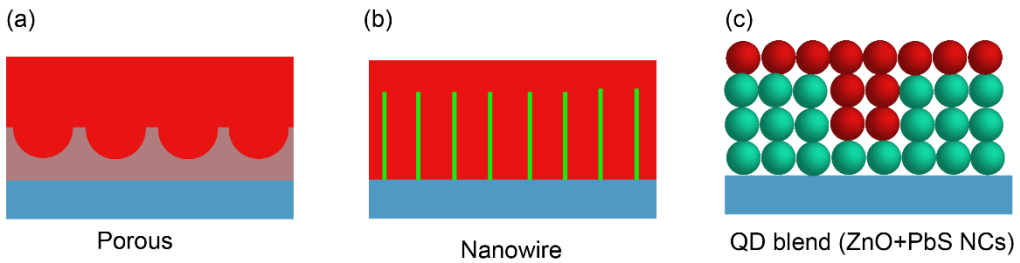

Figure 1.18: Different architecture of bulk heterojunction solar cells.

Another important modification is the blending of *n*-type ZnO NCs and *p*-type PbS to construct a three-dimensional interpenetrating network between two materials.[80] The fundamental concept of bulk heterojunction solar cell lies in two factors: (I) An enlarged surface area of contact between *n*-type layers and *p*-type PbS layers increases the PbS loading and the film thickness light absorption. (II) Influence the light scattering inside the device to absorb a higher amount of light.

1.5.3.4 Graded doping device architecture

This device is the extension of heterojunction or homojunction solar cells. By controlling the dopant level and characteristics of semiconductors and considering the band alignment between different semiconductor layers, doping graded device architecture is developed[57] (Figure 1.19a). If PbS CQDs are passivated by iodide, they have *n*-type characteristics, while EDT treated PbS CQDs are *p*-type in nature. However, the *n*-type TiO_2 or ZnO NCs have higher *n*-doping than iodide passivated *n*-type PbS CQDs; on the other hand, the *n*-doping density difference between *p*-type PbS and *n*-type PbS CQDs is enormous.[53,57] This advantage results in constructing a graded doping device in the following structure: ITO- TiO_2/ZnO-*n* type PbS CQDs (main light-absorbing material, thicker film)-*p*-type PbS CQDs-Au.

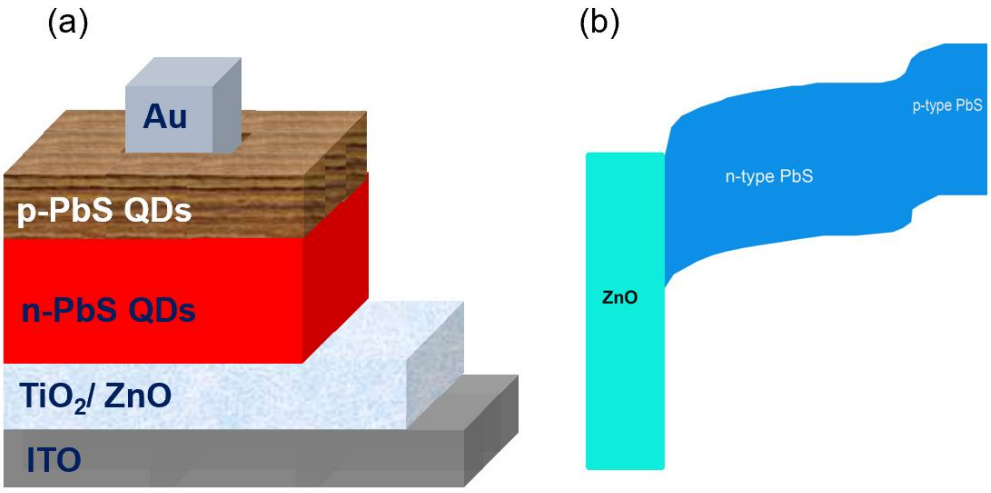

Figure 1.19: Schematic representation of graded doping PbS CQDs device (a) Device architecture (b) Band diagram.

In this device architecture, a strong *p*-*n* junction forms between *p*-type and *n*-type PbS layers, and a weak n-n^+ junction appears between *n*-type TiO_2/ZnO and *n*-type PbS layers. Due to the formation of two junctions at different positions of the device, the depletion width of the device increases significantly, and therefore the photogenerated charge carriers can be extracted from much thicker films compared to other heterojunction solar cells[57] (Figure 1.19b). Another important advantage of this device is the selective extraction of electrons and holes. Holes are extracted through the *p*-type PbS layer, and *n*-type TiO_2/ ZnO layers extract the electrons.[57] The maximum power conversion efficiency is achieved to date by this device architecture.[59] This is the more futuristic approach to boost efficiency. This

device architecture is designed to construct the PbS CQDs solar cell in the last three (fourth, fifth, and sixth chapters) working chapters of this thesis.

1.5.4 Progress in Quantum Dots Solar cell

In initial reports, PbS QDs had been incorporated in a conjugated polymer matrix to construct a polymer-QD solar cell, where both the polymers and PbS QDs absorbed solar light. However, the post-deposition sintering process of these solar cells transformed the PbS QDs into bulk PbS. These solar cells were built from QDs, but not termed as QDs solar cells because the light absorption was not due to the quantum confinement effect. These devices showed inferior performance with AM1.5G PCE **0.7%**.[81]

A significant breakthrough in PbS CQDs solar cell was attained when bidentate ethanedithiol (EDT) ligand was used for solid-state ligand exchange to replace oleic acid molecules. A Schottky junction device was fabricated with EDT treated PbS QDs and showed **3.6%** PCE.[76]

Further improvement was achieved by constructing the depleted heterojunction PbS CQDs solar cell. P. Abraham *et al*. first reported the depleted heterojunction solar cell with **5.1%** PCE. The transparent, wide bandgap TiO_2 layer was incorporated for the first time as an *n*-type layer to form a *p*-*n* junction with *p*-type PbS films in these devices.[77]

The PCE of PbS CQDs solar cell was further improved to **7.6%** by introducing the hybrid surface passivation technique. In situ $CdCl_2$ treatment was carried out during the synthesis of PbS CQDs, and 3-mercapto propanoic acid (MPA) ligand was used for LBL device fabrication.[55]

The Bawendi group proposed the next ground-breaking idea on developing PbS CQDs solar cell, where graded doping device architecture was introduced with n-n^+-p configuration (ZnO (*n*-type) - Iodide treated PbS QDs (n^+) - EDT treated PbS QDs (*p*-type)).[57] The PbS CQDs layers were grown by the LBL method. The maximum PCE was achieved to **8.5%** by this device architecture, and this was the maximum reported efficiency while starting this thesis work. Till to date, this device architecture is followed invariably for boosting the PCE.

During this thesis work, Liu *et al*. prepared solution-phase halometallate ligand exchanged *n*-type CQDs ink for one-step film fabrication and fabricated the graded doped

device with **11.28%** PCE.[59] All the above-mentioned major developments of PbS CQDs solar cells were based on the solid-state ligand exchange method. SPLE process offers a better chance of compact surface passivation of PbS CQDs, and the QDs ink is compatible with large scale processing. This work shows the futuristic pathway to move forward for further improving the PCE of QDs solar cells. This thesis also investigates the surface chemistry of QDs ink and points out its associated problems. The last two working chapters of this thesis sort out those problems and introduce the solution-phase hybrid ligand passivation strategy to improve QDs ink quality.

1.5.5 Challenges

Although the small ligand exchanged NCs show a considerable improvement in carrier mobility, but significantly drop their photoluminescence quantum yield (PLQY), exhibit higher absorption and emission FWHM, and polydispersity in size compared to oleic acid capped NCs. It is essential to translate all the desired properties of as-synthesized NCs from the colloid to the thin film to improve the performance and stability of their electronic devices. Understanding the link between the passivated surface structure and optical properties of QDs is an open challenge in this field.

For the termination of these two facets PbS (111) and (100), different types of surface ligands are required, which will selectively bind to the exposed surface atoms (positively charged Pb^+ atoms of (111), neutral Pb, and S atoms of (100) facets). If the covalent bond between cationic Pb^+ atoms of (111) facets and the ligand is not strong enough, the mid-gap trap states will form in the bandgap of NCs, which are responsible for the non-radiative recombination of charge carriers before extraction. Due to the lower surface energy of (100) facets, the very weak interaction of ligands to (100) facets (easily washed out from the surface) lead to the fusion of NCs through (100) facets during the ligand exchange process[12]. It is very essential to find out suitable ligand combinations to passivate all the uncoordinated atoms of both facets for improving optical properties, electronic properties, and the stability of the devices.

The surface structure of solution-phase ligand exchanged QDs ink need to be analysed in more detail. Preserving the atomic passivation in concentrated QDs ink is also a severe challenge. The development of high-quality QDs ink by passivating all the facets of QDs in the solution-phase ligand exchange process is the key area of research to move forward in this field.

1.6 Thesis Overview

This thesis presents the aspect of surface passivation of lead sulfide quantum dots, the doping effect on electron extracting layer titanium dioxide, and device engineering on the development of lead sulfide quantum dots solar cells. This thesis contains five working chapters and, finally, a conclusive chapter with a future outline. In the five working chapters, the improvement of solar cell power conversion efficiency from 3.5% to 10.6% is reported with strategic modifications.

The second working chapter describes Nb-doped low temperature processed TiO_2 integration as an efficient *n*-type electron extracting layer in PbS QDs solar cells. Hybrid passivated PbS QDs are used for device fabrication.

The third chapter presents various analysis and a deep understanding of the effect of different size, shape, and functional groups of small organic ligands on QDs passivation and its impact on the electronic properties of QDs and device performance.

The fourth chapter shows evidence for the growth of the 2D matrix on butylamine dispersed halometallate passivated QDs ink for one-step deposition. This chapter correlates between the 2D matrix cell thickness on QDs surface and the device performance.

To further tune the 2D matrix thickness and compact passivation, a two-step hybrid passivation technique by combining small organic 3-chloro-1-propanethiol (CPT) molecule and inorganic halometallate anion is developed in the fifth chapter of the thesis.

Further improvement on hybrid passivation is carried out in the sixth chapter of the thesis. Instead of two-step hybrid passivation, a one-step simplified hybrid passivation procedure is introduced to control the ratio between organic CPT molecule and halometallate ion on QDs surface. The last working chapter reports 10.6% efficiency of QDs solar cell, which is the maximum efficiency achieved in this thesis.

The final seventh chapter of the thesis presents the overall summary of all five working chapters with a future outline for further improvement on the QDs solar cell efficiency.

1.7 References

(1) Kleiner, K. Here comes the sun https://www.cifar.ca/cifarnews/2015/04/01/here-comes-the-sun.

(2) Lim, X. *Nature* **2015**, *526*, 628-630.

(3) Graves, C.; Ebbesen, S. D.; Mogensen, M.; Lackner, K. S. Sustainable hydrocarbon fuels by recycling CO_2 and H_2O with renewable or nuclear energy. *Renewable Sustainable Energy Rev*. **2011**, *15*(1), 1-23.

(4) Smil, V. General energetics: energy in the biosphere and civilization. Wiley, **1991**.

(5) Funde, A.; Shah, A. Solar Cells and Modules. Springer, Cham**,** vol 301, **2020**.

(6) Gueymard, C. A.; Myers, D.; Emery, K. Proposed reference irradiance spectra for solar energy systems testing. *Sol. Energy* **2002**, *73*, 443–467.

(7) Maps of Irradiation, Irradiance, and UV, Solar Radiation Data (SoDa). at http://www.soda-is.com

(8) Sze, S. M.; Ng, K. K. Physics of Semiconductor Devices. John Wiley & Sons, Inc. **2006**.

(9) Neamen, D. A. Semiconductor Physics and Devices: Basic Principles. 2nd edition. McGraw-Hill, **2003**.

(10) Streetman, Ben G.; Banerjee, Sanjay Kumar, Solid State Electronic Devices. Pearson Education Limited, **2016**.

(11) Shockley, W.; Queisser, H. J. Detailed Balance Limit of Efficiency of p-n Junction Solar Cells. *J. Appl. Phys.* **1961**, *32*, 510–519.

(12) Semonin, O. E.; Luther, J. M.; Choi, S.; Chen, H. Y.; Gao, J. B.; Nozik, A. J.; Beard, M. C. Peak External Photocurrent Quantum Efficiency Exceeding 100% via MEG in a Quantum Dot Solar Cell. *Science* **2011**, *334*, 1530–1533.

(13) National Renewable Energy Laboratory, *Best Research-Cell Efficiencies*. at http://www.nrel.gov/ncpv/images/efficiency_chart.jpg.

(14) Eperon, G. E.; Hörantner, M. T.; Snaith, H. J. Metal Halide Perovskite Tandem and Multiple-Junction Photovoltaics. *Nat. Rev. Chem.* **2017**, *1* (12), 017- 0095.

(15) Shockley, W.; Read, W. T. Statistics of the recombination of holes and electrons. *Phys. Rev*. **1952**, *87*, 835.

(16) Lafond, F.; Bailey, A. G.; Bakker, J. D.; Rebois, D.; Zadourian, R.; McSharry, P.; Farmer, J. D. How well do experience curves predict technological progress? A method for making distributional forecasts. *Technological Forecasting and Social Change* **2018**, *128*, 104-117.

(17) Levelized Cost and Levelized Avoided Cost of New Generation Resources in the Another energy outlook 2015.
http://www.eia.gov/forecasts/aeo/pdf/electricity_generation.pdf

(18) Sharma, S.; Jain, K. K.; Sharma, A. Solar Cells: In Research and Applications - A Review. *Mater. Sci. Appl.* **2015**, *6*, 1145−1155.

(19) Wenham, S. R.; Green, M. A. Silicon Solar Cells. Prog. *Photovoltaics* **1996**, *4* (1), 3−33.

(20) Saga, T. Advances in Crystalline Silicon Solar Cell Technology for Industrial Mass Production. *NPG Asia Mater*. **2010**, *2* (3), 96−102.

(21) Ghandhi, S. K. VLSI Fabrication Principles Silicon and Gallium Arsenide; John Wiley and Sons: New York, **1983**.

(22) Vigil-Galan, O.; Courel, M.; Andrade-Arvizu, J. A.; Sanchez, Y.; Espíndola-Rodríguez, M.; Saucedo, E.; Seuret-Jimenez, D.; Titsworth, M. Route towards low cost-high efficiency second generation solar cells: current status and perspectives. *J. Mater. Sci.: Mater. Electron.* **2015**, *26*, 5562−5573.

(23) Conibeer, G. Third-generation photovoltaics. *Materials Today* **2007**, *10* (11), 42–50.

(24) Green, M. Third generation photovoltaics. New York: Springer. **2006**.

(25) Beard, M. C.; Luther, J. M.; Semonin, O. E.; Nozik, A. J. Third Generation Photovoltaics Based on Multiple Exciton Generation in Quantum Confined Semiconductors. *Acc. Chem. Res.* **2013**, *46*, 1252–1260.

(26) Itzhaik, Y.; Niitsoo, O.; Page, M.; Hodes, G. Sb2S3-Sensitized Nanoporous TiO2 Solar Cells. *J. Phys. Chem. C* **2009**, *113*, 4254−4256.

(27) Ashoori, R. Electrons in artificial atoms. *Nature* **1996**, *379*, 413–419.

(28) Griffiths, D.J.; Darrel, D. F. Introduction to Quantum Mechanics. Cambridge U.P. **2018**.

(29) Schmidt, H.; Weller, H. Quantum Size Effects in Semiconductor Crystallites: Calculation of the Energy Spectrum for the Confined Exciton. *Chem. Phys. Lett*. **1986**, *129*, 615−618.

(30) Buhro, W.; Colvin, V. Shape matters. *Nat. Mater*. **2003**, *2*, 138–139.

(31) Brus, L. Electronic Wave-Functions in Semiconductor Clusters: Experiment and Theory. *J. Phys. Chem*. **1986**, *90*, 2555−2560

(32) Konstantatos, G., Sargent, E. H. Colloidal Quantum Dot Optoelectronics and Photovoltaics; Cambridge University Press: Cambridge, **2013**.

(33) Klimov, V. I. Nanocrystal Quantum Dots, 2nd edition, Taylor and Francis, **2009**.

(34) Hendricks, M. P.; Campos, M. P.; Cleveland, G. T.; Jen-La Plante, I.; Owen, J. S. A tunable library of substituted thiourea precursors to metal sulfide nanocrystals. *Science* **2015**, *348*, 1226−1230

(35) Lamer, V. K.; Dinegar, R. H. Theory, Production and Mechanism of Formation of Monodispersed Hydrosols. *J. Am. Chem. Soc.* **1950**, *72* (11), 4847–4854.

(36) Peng, X.; Wickham, J.; Alivisatos, A. P. Kinetics of II-VI and III-V Colloidal Semiconductor Nanocrystal Growth: "Focusing" of Size Distributions. *J. Am. Chem. Soc.* **1998**, *120* (21), 5343–5344.

(37) Talapin, D. V.; Rogach, A. L.; Haase, M.; Weller, H. Evolution of an Ensemble of Nanoparticles in a Colloidal Solution: Theoretical Study. *J. Phys. Chem. B* **2001**, *105* (49), 12278–12285.

(38) Hines, M. A.; Scholes, G. D. Colloidal PbS Nanocrystals with Size-Tunable Near-Infrared Emission: Observation of Post-Synthesis Self-Narrowing of the Particle Size Distribution. *Adv. Mater.* **2003**, *15*, 1844−1849.

(39) Kwak, J.; Bae, W. K.; Lee, D.; Park, I.; Lim, J.; Park, M.; Cho, H.; Woo, H.; Yoon, D. Y.; Char, K.; Lee, S.; Lee, C. Bright and Efficient Full-Color Colloidal Quantum Dot Light-Emitting Diodes Using an Inverted Device Structure, *Nano Lett.* **2012,** *12*, 2362.

(40) Klein, L.; Roth, R.; Lim, A. K. L.; Alivisatos, A. P.; McEuen, P. L. A single-electron transistor made from a cadmium selenide nanocrystal, *Nature* **1997**, *389*, 699.

(41) Lim, J.; Park, Y. S.; Klimov, V. I. Optical gain in colloidal quantum dots achieved with direct-current electrical pumping. *Nat. Mater.* **2018**, *17* (1), 42.

(42) Konstantatos, G.; Howard, I.; Fischer, A.; Hoogland, S.; Clifford, J.; Klem, E.; Levina, L.; Sargent, E. H. Ultrasensitive solution-cast quantum dot photodetectors, *Nature* **2006**, *442*, 180.

(43) Talapin, D. V.; Lee, J.-S.; Kovalenko, M. V.; Shevchenko, E. V. Prospects of colloidal nanocrystals for electronic and optoelectronic applications. *Chem. Rev.* **2010**, *110***,** 389–458 (2010).

(44) Yin, Y.; Alivisatos, A. P. Colloidal nanocrystal synthesis and the organic–inorganic interface. *Nature* **2005**, *437*, 664–670.

(45) Boles, M. A.; Ling, D.; Hyeon, T.; Talapin, D. V. The surface science of nanocrystals. *Nat. Mater.* **2016**, *15*, 141–153.

(46) Jun, Y. W.; Lee, J. H.; Choi, J. S.; J. Cheon Symmetry-controlled colloidal nanocrystals: nonhydrolytic chemical synthesis and shape determining parameters. *J. Phys. Chem. B* **2005**, *109*, 14795–14806.

(47) Lee, S. M.; Jun, Y. W.; Cho, S. N.; Cheon, J. Single-crystalline star-shaped nanocrystals and their evolution: programming the geometry of nano-building blocks. *J. Am. Chem. Soc.* **2002**, *124*, 11244–11245.

(48) Anderson, N. C.; Hendricks, M. P.; Choi, J. J.; Owen, J. S. Ligand Exchange and the Stoichiometry of Metal Chalcogenide Nanocrystals: Spectroscopic Observation of Facile Metal-Carboxylate Displacement and Binding. *J. Am. Chem. Soc.* **2013**, *135*, 18536−18548.

(49) Gai, Y.; Peng, H.; Li, J. Electronic properties of nonstoichiometric PbSe quantum dots from first principles. *J. Phys. Chem. C* **2009**, *113*, 21506–21511.

(50) Ma, J. X.; Jia, Y.; Song, Y.; Liang, E.; Wu, L.; Wang, F.; Wang, X.; Hu, X. The geometric and electronic properties of the PbS, PbSe and PbTe (001) surfaces. *Surf. Sci.* **2004**, *551*, 91–98.

(51) Zherebetskyy, D.; Scheele, M.; Zhang, Y. J.; Bronstein, N.; Thompson, C.; Britt, D.; Salmeron, M.; Alivisatos, P.; Wang, L. W. Hydroxylation of the surface of PbS nanocrystals passivated with oleic acid. *Science* **2014**, *344* (6190), 1380-1384.

(52) Moreels, I.; Justo, Y.; Geyter, B. De.; Haustraete, K.; Martins, J. C.; Hens, Z. Size-tunable, bright, and stable PbS quantum dots: A surface chemistry study. *ACS Nano* **2011**, *5*, 2004–2012.

(53) Cao, Y.; Stavrinadis, A.; Lasanta, T.; So, D.; Konstantatos, G. The Role of Surface Passivation for Efficient and Photostable PbS Quantum Dot Solar Cells. *Nat. Energy* **2016**, *1*, 16035.

(54) Zhang, J.; Gao, J.; Miller, E. M.; Luther, J. M.; Beard, M. C. Diffusion-Controlled Synthesis of PbS and PbSe Quantum Dots with *in Situ* Halide Passivation for Quantum Dot Solar Cells. *ACS Nano* **2014**, *8***,** 614–622.

(55) Ip, A. H.; Thon, S. M.; Hoogland, S.; Voznyy, O.; Zhitomirsky, D.; Debnath, R.; Levina, L.; Rollny, L. R.; Carey, G. H.; Fischer, A.; Kemp, K. W.; Kramer, I. J.; Ning, Z.; Labelle, A. J.; Chou, K. W.; Amassian, A.; Sargent, E. H. Hybrid passivated colloidal quantum dot solids. *Nat. Nanotechnol.* **2012**, *7*, 577-582.

(56) Zhitomirsky, D.; Kramer, I. J.; Labelle, A. J.; Fischer, A.; Debnath, R.; Pan, J.; Bakr, O. M.; Sargent, E. H., Colloidal Quantum Dot Photovoltaics: The Effect of Polydispersity. *Nano Lett.* **2012,** *12* (2), 1007-1012.

(57) Chuang, C. H. M.; Brown, P. R.; Bulovic, V.; Bawendi, M. G. Improved performance and stability in quantum dot solar cells through band alignment engineering. *Nat. Mater.* **2014,** *13* (8), 796-801.

(58) Yang, Z. Y.; Janmohamed, A.; Lan, X. Z.; de Arquer, F. P. G.; Voznyy, O.; Yassitepe, E.; Kim, G. H.; Ning, Z. J.; Gong, X. W.; Comin, R.; Sargent, E. H. Colloidal Quantum Dot Photovoltaics Enhanced by Perovskite Shelling. *Nano Lett.* **2015,** *15* (11), 7539-7543.

(59) Liu, M. X.; Voznyy, O.; Sabatini, R.; de Arquer, F. P. G.; Munir, R.; Balawi, A. H.; Lan, X. Z.; Fan, F. J.; Walters, G.; Kirmani, A. R.; Hoogland, S.; Laquai, F.; Amassian, A.; Sargent, E. H. Hybrid organic-inorganic inks flatten the energy landscape in colloidal quantum dot solids. *Nat. Mater.* **2017**, *16* (2), 258-263.

(60) Carey, G. H.; Abdelhady, A. L.; Ning, Z.; Thon, S. M.; Bakr, O. M.; Sargent, E. H. Colloidal Quantum Dot Solar Cells. *Chem. Rev.* **2015**, *115*, 12732−12763.

(61) Zhang, X.; Zhang, J.; Phuyal, D.; Du, J.; Tian, L.; Öberg, V. A.; Johansson, M. B.; Cappel, U. B.; Karis, O.; Liu, J.; Rensmo, H.; Boschloo, G.; Johansson, E. M. J. Inorganic CsPbI3 Perovskite Coating on PbS Quantum Dot for Highly Efficient and Stable Infrared Light Converting Solar Cells. *Adv. Energy Mater.* **2018,** *8*, 1702049.

(62) Mandal, D.; Rath, A. K. Quantum Dots Coupled to an Oriented Two-Dimensional Crystalline Matrix for Solar Cell Application. *ACS Appl. Mater. Interfaces* **2018**, *10*, 39074−39082.

(63) Oh, S. J.; Berry, N. E.; Choi, J.H.; Gaulding, E. A.; Paik, T.; Hong, S. H.; Murray, C. B.; Kagan, C. R. Stoichiometric Control of Lead Chalcogenide Nanocrystal Solids to Enhance Their Electronic and Optoelectronic Device Performance. *ACS Nano* **2013**, *7*, 2413−2421.

(64) Luther, J. M.; Pietryga, J. M. Stoichiometry Control in Quantum Dots: A Viable Analog to Impurity Doping of Bulk Materials. *ACS Nano* **2013**, *7***,** 1845–1849.

(65) Ning, Z.; Zhitomirsky, D.; Adinolfi, V.; Sutherland, B.; Xu, J.; Voznyy, O.; Maraghechi, P.; Lan, X.; Hoogland, S.; Ren, Y.; Sargent, E. H. Graded Doping for Enhanced Colloidal Quantum Dot Photovoltaics. *Adv. Mater.* **2013**, *25*, 1719−1723.

(66) Zhitomirsky, D.; Furukawa, M.; Tang, J.; Stadler, P.; Hoogland, S.; Voznyy, O.; Liu, H.; Sargent, E. H. N-Type Colloidal-Quantum-Dot Solids for Photovoltaics. *Adv. Mater.* **2012**, *24*, 6181–6185.

(67) Klem, E. J. D.; Shukla, H.; Hinds, S.; MacNeil, D. D.; Levina, L.; Sargent, E. H. Impact of Dithiol Treatment and Air Annealing on the Conductivity, Mobility, and Hole Density in PbS Colloidal Quantum Dot Solids. *Appl. Phys. Lett.* **2008**, *92*, 212105.

(68) Talapin, D. V; Murray, C. B. PbSe Nanocrystal Solids for n- and p- Channel Thin Film Field-Effect Transistors. *Science* **2005**, *310*, 86–89.

(69) Voznyy, O.; Zhitomirsky, D.; Stadler, P.; Ning, Z.; Hoogland, S.; Sargent, E. H. A charge-orbital balance picture of doping in colloidal quantum dot solids. *ACS Nano* **2012**, *6*, 8448−8455.

(70) Brown, P. R.; Kim, D.; Lunt, R. R.; Zhao, N.; Bawendi, M. G.; Grossman, J. C.; Bulovic, V. Energy Level Modification in Lead Sulfide Quantum Dot Thin Films through Ligand Exchange. *ACS Nano* **2014**, *8*, 5863−5872.

(71) Liu, H.; Zhitomirsky, D.; Hoogland, S.; Tang, J.; Kramer, I. J.; Ning, Z.; Sargent, E. H. Systematic Optimization of Quantum Junction Colloidal Quantum Dot Solar Cells. *Appl. Phys. Lett.* **2012**, *101*, 151112.

(72) Liu, H.; Tang, J.; Kramer, I. J.; Debnath, R.; Koleilat, G. I.; Wang, X.; Fisher, A.; Li, R.; Brzozowski, L.; Levina, L.; Sargent, E. H. Electron Acceptor Materials Engineering in Colloidal Quantum Dot Solar Cells. *Adv. Mater.* **2011**, *23*, 3832−3837.

(73) Clifford, J. P.; Johnston, K. W.; Levina, L.; Sargent, E. H. Schottky Barriers to Colloidal Quantum Dot Films. *Appl. Phys. Lett.* **2007,** *91*, 253117.

(74) Luther, J. M.; Law, M.; Beard, M. C.; Song, Q.; Reese, M. O.; Ellingson, R. J.; Nozik, A. J. Schottky Solar Cells Based on Colloidal Nanocrystal Films. *Nano Lett*. **2008**, *8*, 3488–3492.

(75) Tang, J.; Wang, X.; Brzozowski, L.; Barkhouse, D. A. R.; Debnath, R.; Levina, L.; Sargent, E. H. Schottky Quantum Dot Solar Cells Stable in Air under Solar Illumination. *Adv. Mater*. **2010**, *22*, 1398−1402.

(76) Tang, J.; Brzozowski, L.; Barkhouse, D. A. R.; Wang, X.; Debnath, R.; Wolowiec, R.; Palmiano, E.; Levina, L.; PattantyusAbraham, A. G.; Jamakosmanovic, D.; Sargent, E. H. Quantum Dot Photovoltaics in the Extreme Quantum Confinement Regime: The Surface-Chemical Origins of Exceptional Air- and Light-Stability. *ACS Nano* **2010**, *4*, 869−878.

(77) Pattantyus-Abraham, A. G.; Kramer, I. J.; Barkhouse, A. R.; Wang, X.; Konstantatos, G.; Debnath, R.; Levina, L.; Raabe, I.; Nazeeruddin, M. K.; Grätzel, M.; Sargent, E. H. Depleted heterojunction Colloidal Quantum Dot Solar Cells. *ACS Nano* **2010**, *4*, 3374−3380.

(78) Jean, J.; Chang, S.; Brown, P. R.; Cheng, J. J.; Rekemeyer, P. H.; Bawendi, M. G.; Gradecak, S.; Bulovic, V. ZnO Nanowire Arrays for Enhanced Photocurrent in PbS Quantum Dot Solar Cells. *Adv. Mater*. **2013**, 25, 2790−2796.

(79) Kramer, I. J.; Zhitomirsky, D.; Bass, J. D.; Rice, P. M.; Topuria, T.; Krupp, L.; Thon, S. M.; Ip, A. H.; Debnath, R.; Kim, H.-C.; Sargent, E. H. Ordered Nanopillar Structured Electrodes for Depleted Bulk Heterojunction Colloidal Quantum Dot Solar Cells. *Adv. Mater*. **2012**, *24*, 2315−2319.

(80) Rath, A. K.; Pelayo Garcia de Arquer, F.; Stavrinadis, A.; Lasanta, T.; Bernechea, M.; Diedenhofen, S. L.; Konstantatos, G. Remote Trap Passivation in Colloidal Quantum Dot Bulk Nano-heterojunctions and Its Effect in Solution-Processed Solar Cells. *Adv. Mater.* **2014**, *26*, 4741–4747.

(81) Watt, A. A. R.; Blake, D.; Warner, J. H.; Thomsen, E. A.; Tavenner, E. L.; Rubinsztein-Dunlop, H.; Meredith, P. Lead Sulfide Nanocrystal: Conducting Polymer Solar Cells. *J. Phys. D: Appl. Phys.* **2005**, *38*, 2006–2012.

Chapter 2

Low temperature processed niobium doped TiO_2 as *n*-type electron transport layer in quantum dot solar cell

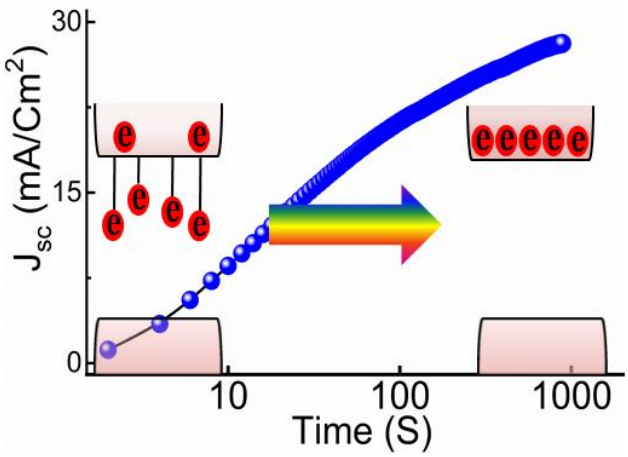

Abstract:

Anatase titanium oxide (TiO_2) is widely studied as *n*-type widow layer for the collection of photogenerated electrons in lead sulfide QD solar cells. The requirement of high temperature (~500°C) processing steps proved to be disadvantageous for their applications in flexible solar cells, roll to roll processing, and also have adverse commercial implications. In this chapter, we will show, solar light exposure to low temperature processed (80°C-150°C) TiO_2 and niobium doped TiO_2 films leads to unprecedented enhancement in their electron densities and electron mobilities, which enables them to be used as an efficient *n*-type layer in quantum dot solar cell. Such photoinduced high conducting states in these films show gradual decay in hours after the light bias is taken off and can be retrieved under photo illumination. On the contrary, light exposure to TiO_2 films processed at 500°C shows little enhancement in their characteristics. In bilayer configuration with PbS QD, photovoltaic devices based on low temperature processed TiO_2 films shows improved performance over high temperature processed TiO_2 film. The stability of the photovoltaic devices also improved in low-temperature processed TiO_2 films under ambient working condition.

2.1 Introduction

Colloidally synthesized inorganic quantum dots are an attractive class of materials for the development of low cost, large area, flexible, and efficient solar cells through their low temperature, chemical phase processability, and size and shape-dependent bandgap tunability.[1-6] Recent advancements in QD solar cells have been realized due to simultaneous progress in device engineering[5,7,8] and material processing.[3,4,6] Series of developments have been made in the device engineering front to suit the carrier extraction process. Device designs, such as metal-semiconductor Schottky junction,[9,10] depleted heterojunction,[11-13] bulk nano-heterojunction[7,14], and more recently double side junction[5,8] structures have been realized successfully. Surface engineering in QD solids has been materialized through passivation of surface atoms by small organic ligands,[11,15] inorganic atomic size halide ligands,[3,6], and organic-inorganic hybrid ligands.[4,5] Better control over the surface state formation reflected in suppression over the photocarrier recombination and higher performances in QD solar cells. Lead chalcogenide QDs (PbS, PbSe) have emerged as the most suitable candidates for the development of high-performance QD solar cells over the years due to their favourable optical and electrical properties.[16] A suitable *n*-type window layer is one of the crucial components for the development of QD solar cells, as it has multiple roles in photovoltaic (PV) processes. Wide bandgap *n*-type layer allows the incident light to directly shine into the photoactive QD layer, provide necessary junction for drift motion of photocarriers, and acts as hole blocking and electron-accepting layer for selective collection of photocarriers.[5,11] Titanium dioxide (TiO_2) has long been used as an *n*-type window layer in DSSC,[17] OPV,[18] perovskite,[19], and QD[20] solar cells for their suitable optical and electronic properties. In order to implement TiO_2 in high performance PV applications, annealing over 500°C is a crucial step to form the calcinated anatase phase TiO_2 layer.[11,20,21] In the case of QD solar cell, preparation of efficient, electron-accepting TiO_2 layer involves multiple high-temperature processing steps and sequential deposition of various size TiO_2 nanoparticle layers and finally, aqueous treatment of $TiCl_4$ layers to achieve desirable electronic properties.[11,20-22] High-temperature annealing requirement has narrowed down the prospect of TiO_2 to be used in flexible solar cells, incompatible with roll-to-roll processing, and hinders the commercial prospect by increasing the processing cost. In addition to this, high temperature processed TiO_2 based solar cells shows strong photo instability, leads to degradation of solar cell performance with time.[23,24] Further, in many device architectures, TiO_2 could not be used as a top or intermediate layer (especially in the case of *p-n* or *p-i-n*

junction and tandem junction formation) as such high-temperature annealing most often damages the layers underneath. Low-temperature processing of TiO_2 films so far resulted in low electrical conductivity, which is unfavourable for fast electron extraction and electron transport in solar cell applications. However, ultrathin low temperature processed TiO_2 layers have been used in the past in OPV,[25,26], and perovskite[27,28] solar cells due to their excellent hole blocking ability and low-temperature processing compatibility. The poor electrical conductivity of low temperature processed TiO_2 films restricted their use to the top complementary layer in addition to key *n*-type layers like PCBM and C_{60} in *p-i-n* or *p-n* junction solar cells. Therefore, the preparation of high mobility *n*-type layer of TiO_2 at low temperatures will be a welcome step forward. This may provide an extra degree of freedom in device engineering to eliminate additional organic *n*-type layer in the development of flexible solar cells.

In this chapter, we demonstrate, TiO_2 and niobium (Nb) doped TiO_2 thin films processed below 150°C can be used as efficient *n*-type layers for QD solar cell applications. We show that solar light exposure to the solar cells for a short period of time leads to a semi-sustainable increase in electron density and electron mobility of the TiO_2 layers, which retains these enhancements for hours after switching off the light bias. This enables us to develop the first *n-p* junction solar cells utilizing low-temperature processed TiO_2 or Nb-doped TiO_2 as an *n*-type layer with *p*-type PbS QDs. The electron extraction efficiency of the developed TiO_2 and Nb-doped TiO_2 layers improves significantly upon solar light exposure, in contrast to the high temperature processed TiO_2, where prolong light exposure leads to gradual degradation in PV performances. Under the saturated light soaking condition, performances of low temperature processed TiO_2, and Nb-doped TiO_2 based solar cells surpass the performance (both measured and reported performance at that time) of high temperature processed TiO_2 based solar cell.[4] Best performance is achieved in 2.5% Nb-doped TiO_2 based solar cells, which has reached an efficiency of 7.69% with a remarkable short circuit of 28.7 mA/cm^2 under 1.5 A.M illumination condition.

2.2 Experimental Details

2.2.1 Preparation of TiO_2 sol-gel

TiO_2 sol-gel was prepared to modify the reported approach.[27] In a typical process, titanium isopropoxide (1.2mmole) was added to 2.53 mL of 2-propanol and stirred for 30 minutes. 14µL (5M) HCl was then taken in 2.53 mL of 2-propanol and added to the solution slowly under continuous stirring. The whole solution was then left stirring for another 30 minutes to form the transparent TiO_2 precursor.

2.2.2 Preparation of Nb-doped TiO_2 sol-gel

1.2 mmol of titanium isopropoxide was added to 2.53 mL of 2-Propanol and stirred for 2 hrs. It was then transferred into the glove box, and a measured amount of niobium ethoxide was added to the solution. Niobium ethoxide concentration was varied to achieve different doping concentrations. In a typical process 0.06 mmol, 0.03 mmol and 0.012 mmol niobium ethoxide was added to form 5%, 2.5% and 1% Nb doping respectively. Further, 2.53 mL 2-propanol was added to the solution and stirred for another 2 hrs in the ambient atmosphere before film deposition.

2.2.3 Synthesis of Colloidal PbS QDs

$CdCl_2$ treated PbS QDs were synthesized following the reported procedure.[4] Octadecene was degassed under vacuum for 12 hrs prior to its use. PbO (0.45gm, 2mmol), 1.5 mL oleic acid (4.75mmol), and 3mL Octadecene were mixed in 3 neck flask and kept under vacuum at 90°C for 16 hrs using a standard schlenk line. Lead oxide was transformed into a transparent lead oleate complex leading to a clear solution during this step. The reaction environment was then switched to Ar slowly. 15 mL Octadecene was added to the reaction bath, and the temperature was set to 120°C. 210µL $(TMS)_2S$ (1mmol) in 10 mL Octadecene was then injected swiftly, and the solution turns to dark brown instantaneously, indicating PbS nucleation. The heating source was switched off at this point but not removed for slow cooling. When the temperature of the reaction bath reached 80°C, 1 mL $CdCl_2$ precursor was injected into the reaction bath under vigorous stirring. $CdCl_2$ precursor was made by dissolving $CdCl_2$ (0.60gm, 3.28mmol) in 10 mL Oleylamine with tetradecyl phosphonic acid (TDPA, 0.066gm, 0.24mmol) under vacuum for 14 hrs at 100°C. This $CdCl_2$ precursor solution was also kept under Ar atmosphere at 80°C to avoid solidification. The reaction bath was allowed to cool down to 35°C naturally for approximately two hours.

60 ml of acetone was then injected into the reaction bath, and the mixture was allowed to stir for two more minutes. PbS QDs were isolated by centrifugation at 3500 RPM for 5 minutes. In order to clean the QDs, they were dispersed in a small amount of toluene and precipitated by a 1:1 mixture of acetone and methanol followed by centrifugation. The QDs were further washed twice by methanol and finally dispersed in Octane. The concentration of the PbS solution was maintained to 35 mg/mL for spin coating film deposition.

2.2.4 Device Fabrication

ITO and FTO substrates were first cleaned in soap solution followed by 10 minutes of sonication each in distilled water, acetone, and ethanol in the given order. Finally, ITO substrates were cleaned in boiling isopropanol for five minutes before film deposition.

For low-temperature process *n*-type TiO_2 or Nb-doped TiO_2 layer deposition, the appropriate precursor solution was spin-coated at 2500 rpm on top of ITO. The films were then annealed at 70°C for 30 minutes. The substrates were then allowed to cool down to room temperature. A small amount of Millipore water was added to them at a steady-state followed by rotation at 2500 rpm for 1 minute. The substrates were then heated to 150°C for another 30 minutes. For TiO_2-500°C film formation, TiO_2 precursor solution was spin coated on top of FTO substrates at 2500 rpm. The films were then heated to 500°C in the air for one hour to form anatase TiO_2 films.

The as-prepared substrates were used for PbS QDs deposition. PbS QDs were deposited via layer by layer solid-state ligand exchange approach under ambient condition.[5] MPA 2% v/v in methanol was used as a ligand for the deposition of PbS QDs. Film deposition steps followed in this work were as follows, firstly PbS QDs were first spin coated at 2500 rpm on the substrates for 30 seconds. Under continuous spinning 6-7, drops of MPA were added dropwise, followed by rinsing with 7-8 drops of methanol. This completes one layer of PbS QD film deposition. The whole sequences were repeated ten times to built 280-300 nm of PbS film as measured from the profilometer. Top electrodes were deposited by thermal evaporator from Hind high vacuum, model BC-300 at a base pressure of 3×10^{-6} mBar. 10 nm MoO_3 was deposited at $0.1 Å s^{-1}$, followed by 50 nm of Au deposition at $0.5 Å s^{-1}$ and finally, 100 nm Ag was deposited at $1 Å s^{-1}$ to complete the film formation.

2.2.5 Materials Characterization Techniques

Optical absorption measurements were carried out by Shimadzu UV-Vis-NIR-3600 Plus spectrophotometer. Total absorption of thin films was measured by integrating sphere (ISR-603), attachment of Shimadzu UV-3600 plus. XRD profiles were recorded on an X'pert Pro model PANalytical diffractometer from Philips PANalytical instruments operated at a voltage of 40 kV and a current of 30 mA with Cu Kα (1.5418 Å) radiation. The TiO_2 samples were scanned in a 2θ range from 5° to 80° with a scan rate of 0.4° per minute. X-ray photoelectron spectroscopy (XPS) of TiO_2 and Nb-doped TiO_2 were recorded with a custom-built ambient pressure photoelectron spectrometer (APPES) (Prevac, Poland), equipped with VG Scienta's R3000HP analyzer. Monochromatic Al Kα x-ray was generated at 400 W from MX650 Monochromator for XPS measurement. Pressure in the chamber was maintained in the range of 5×10^{-10} Torr. The energy resolution of the spectrometer was set at 0.7 eV at a pass energy of 50 eV. Binding energy (BE) was calibrated with respect to Au $4f_{7/2}$ core level at 84.0 eV. Cyclic Voltammetry was carried out by the CH 660D Electrochemical workstation (CH Instruments, USA). TiO_2 substrate (Titanium oxide on FTO) was directly used as a working electrode, Ag/AgCl was used as a reference electrode, and Pt was used as a counter electrode. The experiments were performed in anhydrous acetonitrile of 0.1M tetra butyl ammonium perchlorate (TBAP) solution. Saturated Calomel electrode (SCE) was calibrated by standard ferrocyanide/ferricyanide solution and potential of reference electrode -4.70V with respect to vacuum. Transmission Electron Microscopy (TEM) was executed using TECHNAI G2-20 S-TWIN (T-20) instrument, operating at 200keV, $LaBF_6$ as the source of electrons. TiO_2 and Nb-doped TiO_2 films were mechanically scratch from the glass surface and dispersed in methanol through vigorous sonication and place on a carbon-coated Cu grid for TEM measurement. Surface morphology of TiO_2 and Nb-doped TiO_2 films were carried out by FEI (ESEM) QUANTA 200-3D microscope. EIS spectrum analyzer simulation software was used to simulate the impedance data. SCAPS simulation software was used to simulate the J-V results of photovoltaic devices.

2.2.6 Device Characterization Techniques

2.2.6.1 Current (J) – voltage (V) measurement

Current-voltage measurement was carried out with a Keithley 2634B source-meter under ambient condition. The illumination intensity of AM1.5 was provided using a Class-AAA solar simulator from Peccell technologies (PEC-L01). A shadow mask was used

before the device to match the illuminated area closely with the device area. The light intensity was set 100 mW/cm^2 at the position of the sample, using a Thorlabs flat band thermal sensor S302C (aperture size 9.3 mm).

2.2.6.2 Time dependant short-circuit current (J_{sc}) measurement

Time dependant short circuit current was measured under continuous solar illumination at zero bias condition using the same Keithley 2634B source-meter and PEC-L01 power source-meter. The device was plugged under 100mW/cm^2 light intensity to measure the only J_{sc} (mA/cm^2) for a longer period of time to understand the photodoping effect.

2.2.6.3 External quantum efficiency (EQE) measurement

External quantum efficiency was measured under white light bias by directing the cell into monochromatic illumination. Monochromator from Solar Laser System (SLS-M266) contains power Arc 75W Xe light source, and proper order shorting filters were used to generate monochromatic illumination. Monochromatic power outputs were measured using calibrated Thorlabs detectors, S120VC for 200-1100 nm wavelengths and S122C for 700-1800 nm wavelengths. The response of the cell was recorded by Keithley 2634B Source meter.

2.2.6.4 Capacitance-Voltage and Impedance measurement:

The Cap–V and frequency response of the devices was performed by PSM1735 (N4L) LCR meter. Cap-V measurements were carried out at a frequency of 1 kHz. Impedance measurements were acquired in between the 200 Hz to 2 MHz frequency range. AC perturbation voltage used in these studies was 50 mV.

2.3 Results and Discussions

2.3.1 XPS analysis of TiO_2

TiO_2 and Nb-doped TiO_2 films are synthesized from the facile sol-gel approach. Nb concentration in the solution is varied to obtain different doping ratios. Details of the synthesis process are explained in the experimental section 2.2.1-2. Thin films are deposited by spin coating and annealed at different temperatures prior to their characterizations. Thin films consisting of TiO_2, 2.5% Nb-doped TiO_2 and 5% Nb-doped TiO_2 layers, and annealed at 150°C, will be represented as TiO_2-150°C, 2.5Nb/TiO_2-150°C, and 5Nb/TiO_2-150°C respectively, and TiO_2 film annealed at 500°C will be referred as TiO_2-500°C, for the rest of the chapter. XPS has been carried out to determine the chemical composition of the films.

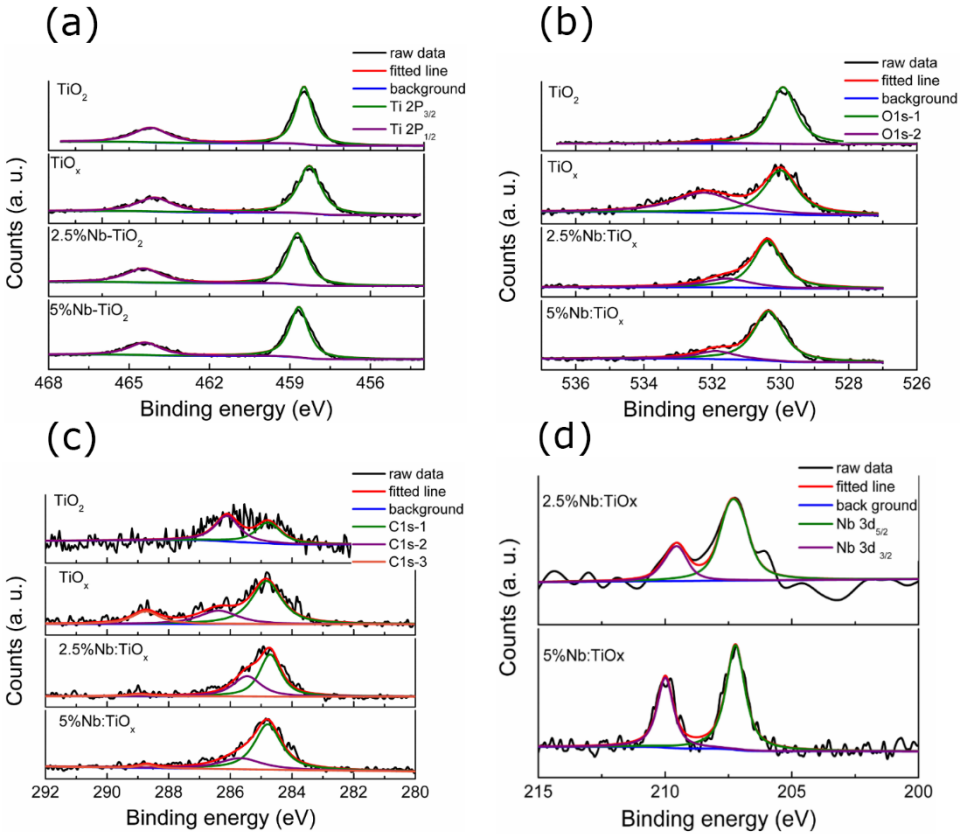

Figure 2.1: High resolution XPS scan for Ti, O, C and Nb of samples TiO_2-500°C, TiO_2-150°C, 2.5%Nb/ TiO_2-150°C, 5%Nb/TiO_2-150°C are given in chronological manner. (a) Ti 2P spectra (b) O 1s spectra (c) C 1s spectra and (d) Nb 3d spectra.

Figure 2.1a shows the high-resolution scan of 'Ti' binding energy for different *n*-type layers. Two peaks correspond to the spin-orbit splitting of p-orbital to $2P_{3/2}$ and $2P_{1/2}$ of 'Ti^{4+}'

oxidation state.[3] The energy difference between $2p_{1/2}$ and $2p_{3/2}$ is 5.74 eV, which agrees well with the 'Ti^{4+}' oxidation state of reported results.[3,4] This also rules out the possibility of the formation of the traceable amount of lower oxidation states of Ti (i.e., Ti^{3+}, Ti^{2+} and Ti^{0}). Figure 2.1b represents the 'O1s' spectrum of the samples. Two peaks observed in the high-resolution scan shows different oxygen binding energies in the samples. The most dominated peak that appeared at 530 eV is attributed to the Ti-O bond and Nb-O bond. The peak at 531.59 eV could be due to oxygen present in the organic compounds in the samples. Three carbon peaks are observed in the XPS data of our samples, shown in Figure 2.1c, which agrees well with the reported results.[3] Peak position corresponds to binding energy 284.76 eV is attributed to the adsorbed carbon species to the material surface, whereas peaks at 286.20 eV and 288.74 eV are considered to be coming from the incomplete decomposition of the starting materials. A high-resolution scan for Nb binding energy (Figure 2.1d) shows that peaks at 207.2 eV and 210 eV correspond to Nb $3d_{5/2}$ and $Nb3d_{3/2}$ orbitals, respectively. These peaks correspond to the Nb^{5+} oxidation states, as confirmed from the literature.[3] A complete list of peak position and FWHM values of the peaks are given in Table 2.1.

Table 2.1: XPS peak position and FWHM values of different element present in different TiO_2 films.

	Ti $2p_{3/2}$		1O S_1		2O S_1		1C S_1		2C S_1		3C S_1		Nb $3d_{5/2}$	
	Peak Position	FWHM	Peak Position	FWHM	Peak Position	FWHM	Peak Position	FWHM	Peak Position	FWHM	Peak Position	FWHM	Peak Position	FWHM
TiO_2-500ºC	457.7	0.75	529.2	0.9	531.3	1.43	284.1	0.96	285.4	0.93				
TiO_2-150ºC	458.1	0.99	529.8	1.1	532.1	2.09	284.8	1.1	286.3	1.5	288.7	1.04		
2.5Nb/TiO_2-150ºC	458.7	0.87	530.4	1	531.5	1.64	284.8	1.1	285.9	1.01	288.9	0.78	207.3	0.9
5Nb/TiO_2-150ºC	458.6	0.83	530.3	1.04	531.8	1.3	284.8	1.03	285.7	1.6	288.7	0.61	207.2	0.89

Chemical compositions of the films were shown in Table 2.2. Ti to O ratios in TiO_2-500°C and TiO_2-150°C samples are found to be 2.08 and 1.97, respectively, indicating a mild deficiency of oxygen in low temperature processed TiO_2 films. The measured concentration of Nb in 2.5% and 5% Nb-doped samples are found to be 4.5% and 5.9%, respectively.

Table 2.2: Atomic concentration of various elements presents in the thin films of *n*-type layers.

	TiO_2-500°C	TiO_2-150°C	2.5Nb/TiO_2-150°C	5Nb/TiO_2-150°C
Ti-$2p_{3/2}$	25.55%	9.47%	14.95%	13.48%
O-S1	53.20%	18.81%	35%	33.50%
O-S1	8.01%	15.51%	7.01%	8.67%
C-S1	11.60%	32.43%	24.20%	20.30%
C-S1	1.60%	17.95%	15.20%	22.01%
C-S1		5.77%	2.58%	1.12%
Nb-$3d_{5/2}$			0.71%	0.84%

2.3.2 XRD characteristics of TiO_2

XRD of TiO_2 films shows (Figure 2.2) formation of anatase phase TiO_2 for samples annealed at 350°C or higher temperatures,[29] whereas no XRD peak is observed for samples annealed below 350°C. XRD pattern of TiO_2-500°C and TiO_2-350°C films are matched with

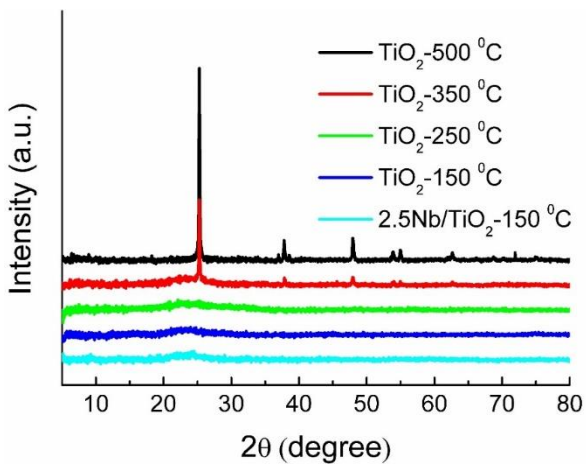

Figure 2.2: X-ray diffraction pattern of TiO_2 films processed at different temperature and low-temperature Nb-doped TiO_2 film.

the anatase phase of TiO_2 as confirmed from JCPDS reference data (PCPDF-86-1157). Lower annealing temperatures do not yield any noticeable diffraction peak in their spectrum. 2.5%Nb/TiO_2-150°C layer also shows no diffraction peak in its XRD pattern.

2.3.3 TEM analysis of TiO_2

The High-resolution TEM study of TiO_2-150°C and 2.5Nb/ TiO_2-150°C reveals that crystal fringes are present even at low temperature (150°C) processed TiO_2 (Figure 2.3). Selected area electron diffraction (SAED) measurement also shows nice diffraction spots (Figure 2.3) for low temperature processed TiO_2 samples, suggesting towards the semi-crystalline nature and nano-meter range grain size in TiO_2 films processed at low temperatures.

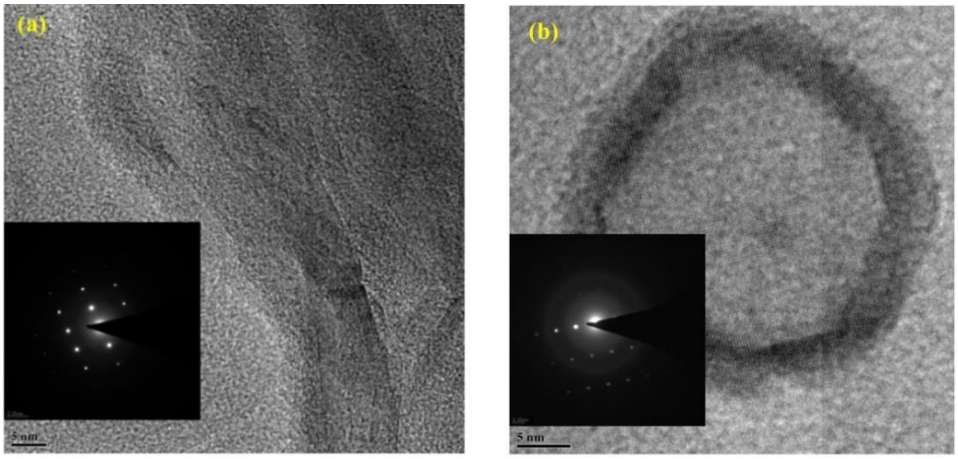

Fig 2.3: HRTEM image of (a) TiO_2-150°C and (b) 2.5Nb/TiO_2-150°C. The selected area electron diffraction (SAED) pattern is shown at the inset of the respective image.

2.3.4 Surface SEM image of TiO_2 films

Surface SEM images of the different TiO_2 films are shown in Figure 2.4. All the films exhibit uniform film depositions with good surface coverage. TiO_2-500°C films have higher compactness compared to other TiO_2 films.

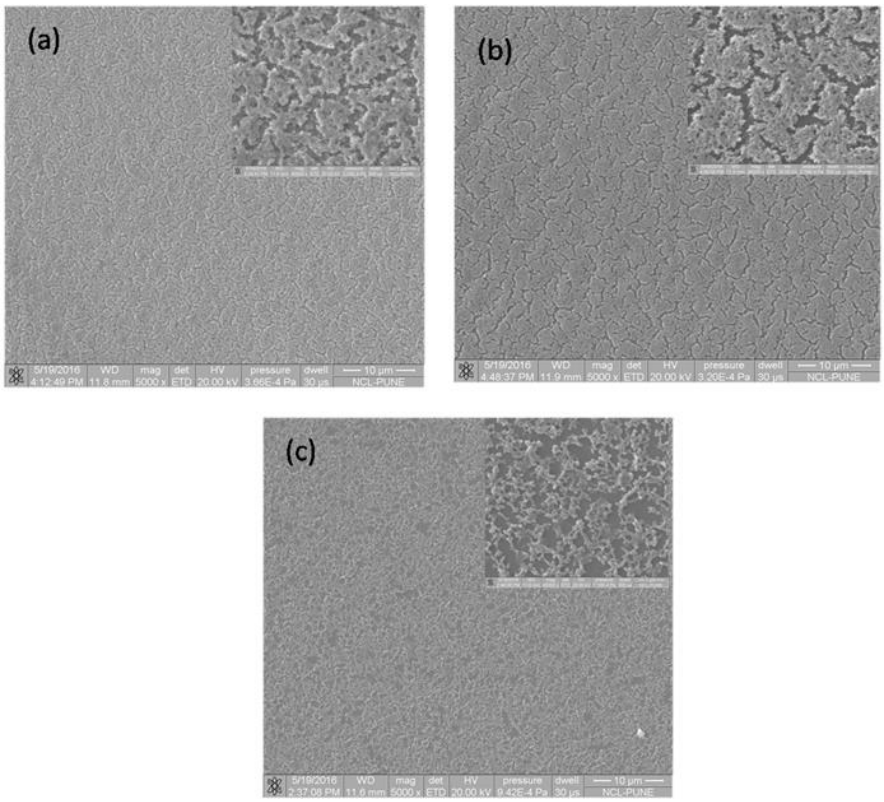

Figure 2.4: Surface SEM images of (a) TiO_2-500°C (2) TiO_2-150°C and (c) 2.5Nb/ TiO_2-150°C films. Insets show the higher magnification image of the films.

2.3.5 Absorption study of TiO_2 thin films

Optical absorption of the thin films is carried out using an integrating sphere spectrometer (Figure 2.5a). The TiO_2 thin films are made by spin coating on top of quartz plate for absorption study. From the absorption study, we have calculated the bandgap of different TiO_2 films. Direct optical band gaps for TiO_2-500°C, TiO_2-150°C, 2.5Nb/ TiO_2-150°C and 5Nb/ TiO_2-150°C films are 3.62 eV, 3.65 eV, 3.68eV and 3.73 eV respectively as determined from the Tauc plot[30] shown in Figure 2.5b. An increase in optical bandgap with an increase in doping concentration could be due to Burstein–Moss effect of filling up of conduction band edge of TiO_2 by the free electrons arises due to Nb doping.[31]

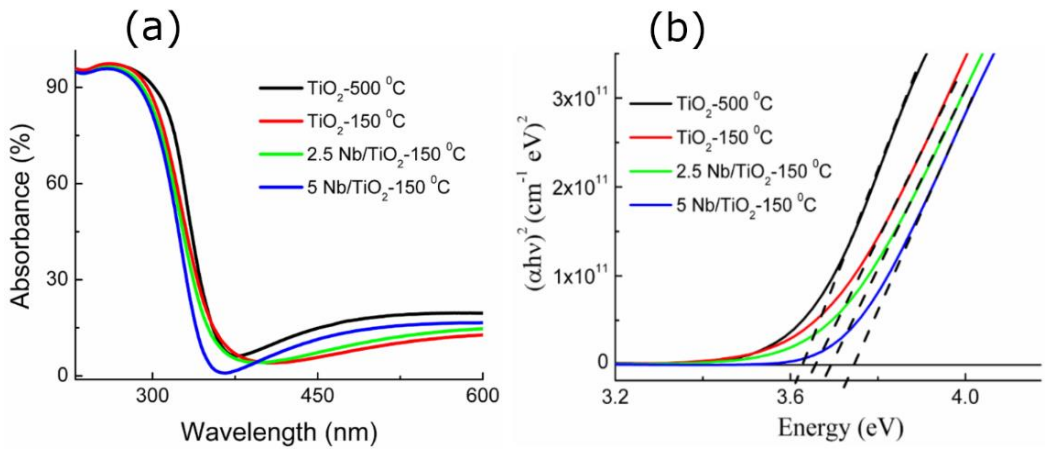

Figure 2.5: (a) Absolute absorbance of the TiO_2 thin films measured using integrating sphere spectrometer. (b) Tauc plot of the films to determine optical bandgap. The intersection of the extrapolation of the linear region of $(\alpha h\nu)^2$ vs. E (eV) plots indicated the optical bandgap of the corresponding films.

2.3.6 Cyclic Voltammetry study of TiO_2

Cyclic Voltammetry is used to determine the conduction band edge from the reduction potential of TiO_2 films (Figure 2.6).[32] Cyclic Voltammetry is measured at a $10mVs^{-1}$ scan rate using Ag/AgCl as reference electrode and Pt wire counter electrode in

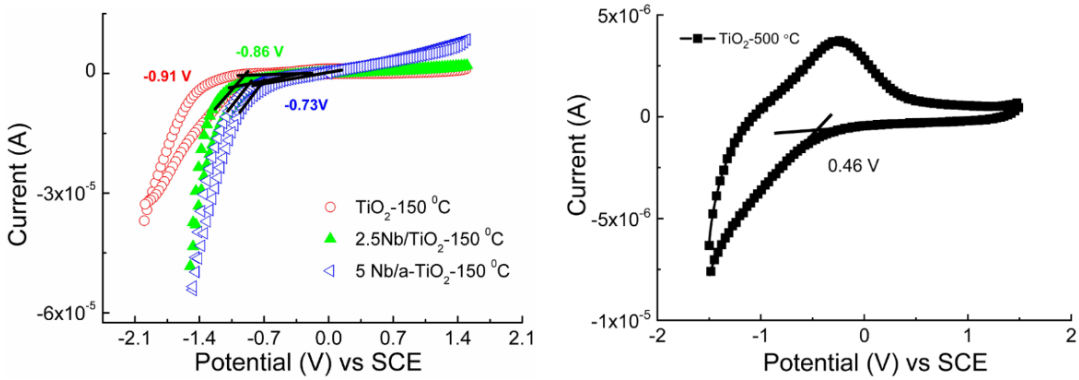

Figure 2.6: Cyclic voltammetry of (a) TiO_2-150°C, 2.5Nb/ TiO_2-150°C and 5Nb/ TiO_2-150°C thin films on top of ITO and (b), cyclic voltammetry of TiO_2-500°C thin film on FTO.

anhydrous acetonitrile with 0.1M Tetra butyl ammonium perchlorate (TBAP) as supporting electrolyte. Conduction band edge position is determined from $E_{CB} = -(E_{red}+4.7)$ eV, where E_{red} is the onset reduction potential obtained from cyclic voltametry. Measured values of

conduction band position for TiO_2-150°C, 2.5Nb/TiO_2-150°C, 5Nb/TiO_2-150°C (Figure 2.6a) and TiO_2-500°C (Figure 2.6b) samples are 3.82 eV, 3.87 eV, 4 eV and 4.27 eV respectively.

2.3.7 Absorbance spectra of PbS QDs

After cleaning, as-synthesized PbS QDs are dispersed in toluene for further characterizations and device fabrications. The absorbance spectra of PbS QDs are shown in (Figure 2.7); the first excitonic peak position arises at 945 nm.

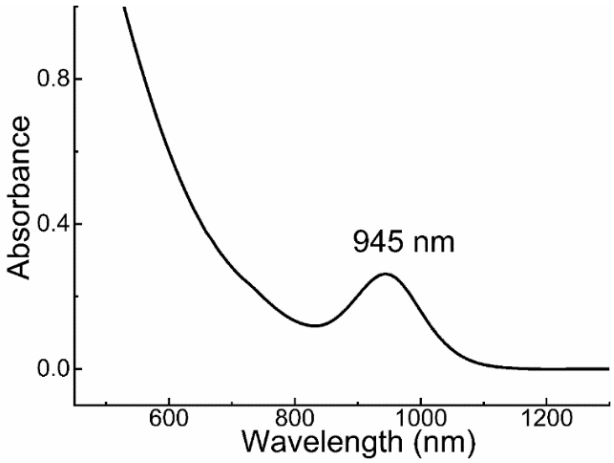

Figure 2.7: Absorbance spectra of PbS QDs dispersed in toluene. The first excitonic peak position of the QDs arises at 945 nm.

2.3.8 TEM image of PbS QDs

TEM image of oleic acid capped QDs is presented in Figure 2.8a. The average diameter of oleic acid capped QDs is around 2.9 nm (Figure 2.8b).

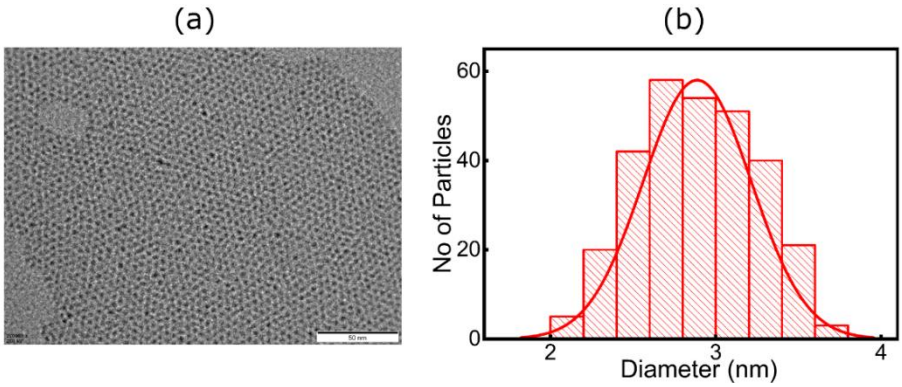

Figure 2.8: (a) TEM image, (b) Particle size distribution of oleic acid capped PbS NCs.

2.3.9 J-V characteristics of solar cell

In order to test the performance of low temperature processed TiO_2 and various Nb-doped TiO_2 films in PV operation, we have chosen the depleted heterojunction[11] device design. The device structure is given as: transparent conducting electrode (TCE)/*n*-type layer/PbS QD/MoO_3/Au/Ag. Light soaking under solar illumination is found to have profound influence on the current voltage characteristics of solar cells, especially for low temperature processed TiO_2 layers. Figure 2.9a shows the current voltage characteristics of solar cells under dark condition for before (lines) and after 20 minutes of light soaking (scatter+line) under 1.5 solar illumination. Solar cells based on TiO_2-150°C, 2.5Nb/TiO_2-150°C and 5Nb/TiO_2-150°C show approximately 10^4 times increase in forward bias current and rectification ratio at 0.8V, whereas TiO_2-500°C based device shows moderate five times improvement due to photodoping. Figure 2.9b, shows the current density vs voltage plot for different solar cells after saturation of photodoping under solar illumination. Steady state parameters for TiO_2-500°C: V_{oc}= 0.6V, J_{sc}= 15.66 mA/cm^2, FF= 39.4, η% = 3.70; TiO_2-150°C: V_{oc}= 0.58 V, J_{sc}= 27.18 mA/cm^2, FF=41.52, η% =6.54; 2.5Nb/TiO_2-150°C: V_{oc}= 0.6 V, J_{sc}= 28.7 mA/cm^2, FF=44.67, η% = 7.69 and 5Nb/TiO_2-150°C: V_{oc}= 0.6 V, J_{sc}= 25.98 mA/cm^2, FF= 37.01, η% = 5.77; are obtained under 1.5 AM illumination condition.

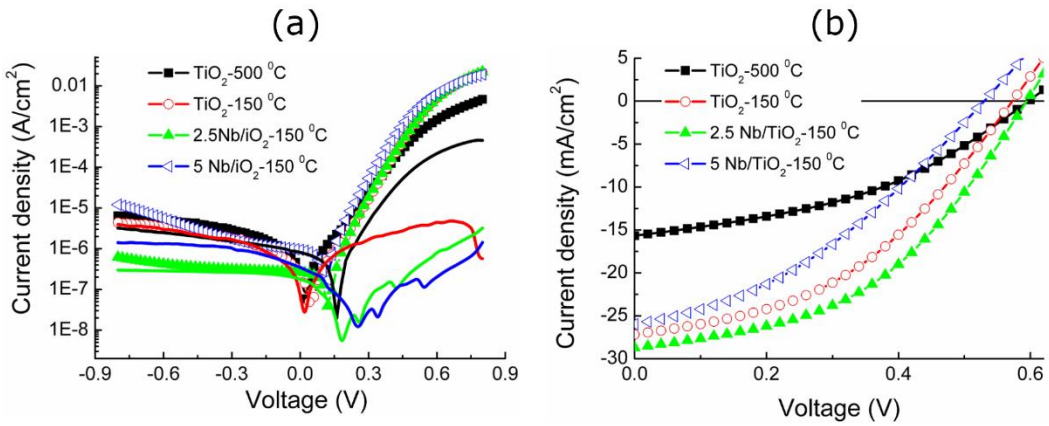

Figure 2.9: (a) J-V characteristics of PV devices for different *n*-type layers under dark condition. Before and after twenty minutes, light soaking situations are represented by lines and scatter symbols, respectively. (b) J-V characteristics of solar cells under 1.5 AM illumination after photodoping saturation.

Nb doping concentration and annealing temperature of the *n*-type layers are varied independently to optimize PV performances. Comparative study of solar cell parameters for

Table 2.3: Comparison of solar cell performances on varying Nb doping concentrations.

Nb doping concentration in TiO_2 film	V_{oc} (V)	J_{sc} (mA/cm^2)	FF (%)	PCE (%)
0%	0.58	27.18	41.52	6.54
0.5%	0.5	9.33	42.54	2
1%	0.56	20.66	45	5.2
2.5%	0.6	28.7	44.7	7.69
5%	0.6	25.98	37.01	5.77

varied Nb doping concentrations are given in Table 2.3. The 2.5% Nb-doped TiO_2 films integrated solar cell device achieve maximum PCE. Due to doping, the optical, electronic as well as surface structure and transparency of TiO_2 thin films change. All these combined phenomena account on the final solar cell device performance. It is observed from thin film absorption study that with increasing Nb doping percentage the band gap of TiO_2 increases due to Burstein-Moss effect. Not only the bandgap, the conduction band position which is calculated from cyclic voltammetry study, also changes for different percentage of Nb doping. The gap between conduction band position of TiO_2 and valance band position of PbS QD determines the V_{oc} of QD solar cell. From 0.5% doping to 1% doping, the Voc increases from 0.5V to 0.56 V and the maximum Voc reaches to 0.6V for 2.5% doping and 5% doping. So, the optimum band alignment happens for 2.5% doping or more than that. The optimal band alignment also favours the photogenerated charge extraction, which enhances the short circuit current of device. However, we observe that with increasing Nb doping percentage, the transparency of TiO_2 films also falls significantly. For higher percentage TiO_2, the adsorption of higher percentage of organic molecules limits the short circuit current. Due to the increased opacity of heavily doped TiO_2 layer, the number of photons incident on the active PbS QD layer reduces. On accounting all these combined effects, the 2.5% doped TiO_2 show maximum PCE. Further annealed temperature of 2.5% Nb-doped TiO_2 films are probed to find a suitable processing temperature. In Table 2.4, solar cell performances on different processing temperatures of TiO_2 films are presented.

Table 2.4: Solar cell performance of 2.5% Nb-doped TiO_2 layer on processing temperature.

Processing Temperature (°C)	V_{oc} (V)	J_{sc} (mA/cm2)	FF (%)	PCE (%)
Room temperature	0.48	13.74	41	2.70
80	0.54	28.59	43.82	6.76
150	0.58	28.6	41.76	6.92
200	0.54	26.3	37.87	5.38
250	0.52	27.39	33.56	4.78
350	0.54	24.15	28.58	3.72
500	0.56	26.25	31.46	4.62

PV devices based on TiO_2 layers processed in between 80°C to 150°C outperform the 500°C annealed TiO_2 layer consistently, which has been perceived as a more suitable *n*-type layer for PV applications.[11,20,21,33] It is found that the TiO_2 layer processed between 80°C to 150°C with 2.5% Nb doping is best suited for optimized photovoltaic performance. However, the hysteresis effect is almost negligible for both low temperature and high temperature processed TiO_2 integrated solar cell devices. There are insignificant differences in photovoltaic performances under forward and reverse scan, as shown in Figure 2.10, and their corresponding photovoltaic parameters are tabulated in Table 2.5.

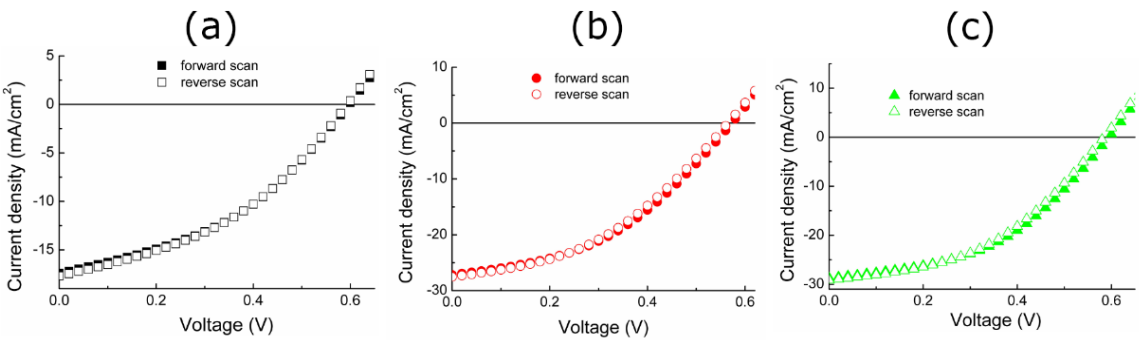

Figure 2.10: Forward and reverse scan of (a) TiO_2-500°C, (b) TiO_2-150 °C and (c) 2.5Nb/ TiO_2-150°C based PV devices under 1.5 A.M. solar illumination.

Table 2.5: Comparison of photovoltaic performances for different *n*-type layers under forward and reverse bias scan.

Device	V_{oc} (V)		J_{sc} (mA/cm^2)		FF (%)		PCE (%)	
	Forward scan	Reverse scan	Forward scan	Reverse scan	Forward scan	Reverse scan	Forward scan	Reverse scan
TiO_2-500°C	0.6	0.6	17.67	17.44	39.38	40.02	4.17	4.18
TiO_2-150°C	0.58	0.56	27.18	27.57	41.52	41.32	6.54	6.38
2.5Nb/ TiO_2-150°C	0.6	0.58	28.7	29.16	44.67	44.17	7.69	7.47

2.3.10 Time dependant J_{sc} measurement

Further, the effect of light soaking is monitored in their short circuit current density (J_{sc}) vs. time plot, shown in Figure 2.11. J_{sc} of TiO_2-150°C, 2.5Nb/TiO_2-150°C, and 5Nb/TiO_2-150°C based PV devices increases steadily with time and takes almost seventeen minutes to saturate.

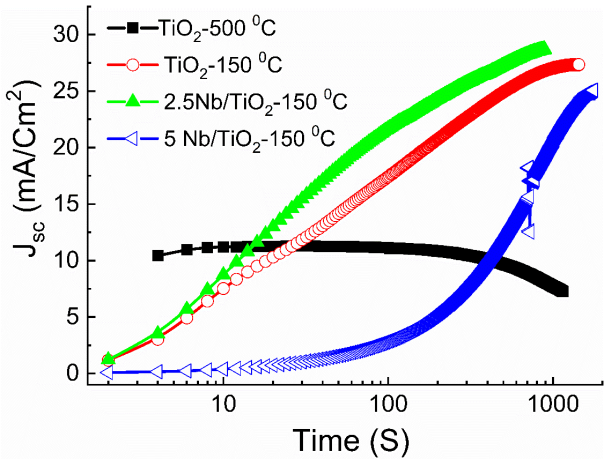

Figure 2.11: Short circuit current density (J_{sc}) Vs. time for PV devices measured under continuous solar illumination.

Whereas, TiO_2-500°C based solar cells show very little increase in J_{sc} within initial 10s and continuous illumination over 100s, leads to a monotonic decrease in J_{sc} with time. Such

degradation effect in TiO_2-500°C based solar cells are reported in the literature[23,34], and is attributed to strong photocatalytic activity of anatase phase TiO_2, which may lead to the gradual degradation of TiO_2/PbS QD junction. In the case of low temperature processed TiO_2 layers, no noticeable degradation in short circuit current is observed during the experiment, and devices show better stability in ambient working conditions.

2.3.11 EQE Spectrum

The EQE spectrum of the different TiO_2 integrated devices for different wavelengths is presented in Figure 2.12. Low temperature processed TiO_2 layers show superior carrier extraction ability than TiO_2-500°C based devices for almost the entire wavelength range. The integrated short circuit current from EQE for TiO_2-500°C, TiO_2-150°C, 2.5Nb/TiO_2-150°C and 5Nb/TiO_2-150°C solar cells are 14.1 mA/cm^2, 24.3 mA/cm^2, 25.8 mA/cm^2 and 21.4 mA/cm^2 respectively. Small discrepancies in measured and predicted short circuit current from EQE for the individual solar cells could be due to unsaturated photodoping by low intensity white light biasing during EQE measurements.

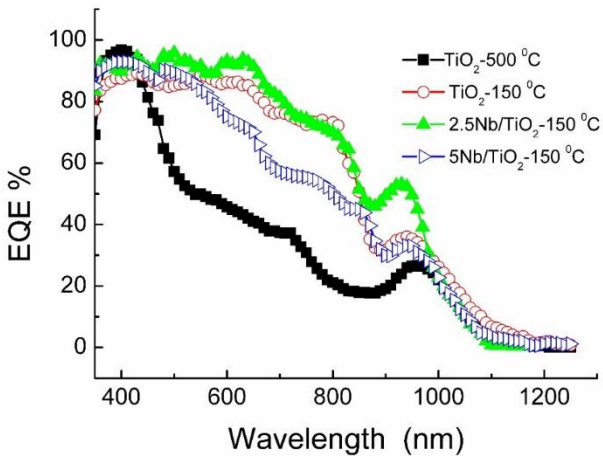

Figure 2.12: Comparison of EQE spectrum of PV devices with different *n*-type layers.

2.3.12 Statistical distribution of PCE

The statistical distribution of PCE for optimized solar cell devices is presented in Figure 2.13. Eight devices are measured in each batch, and the PCE of a total of forty-eight devices are summarized statistically for TiO_2-150°C and 2.5 Nb/ TiO_2-150°C based solar cells.

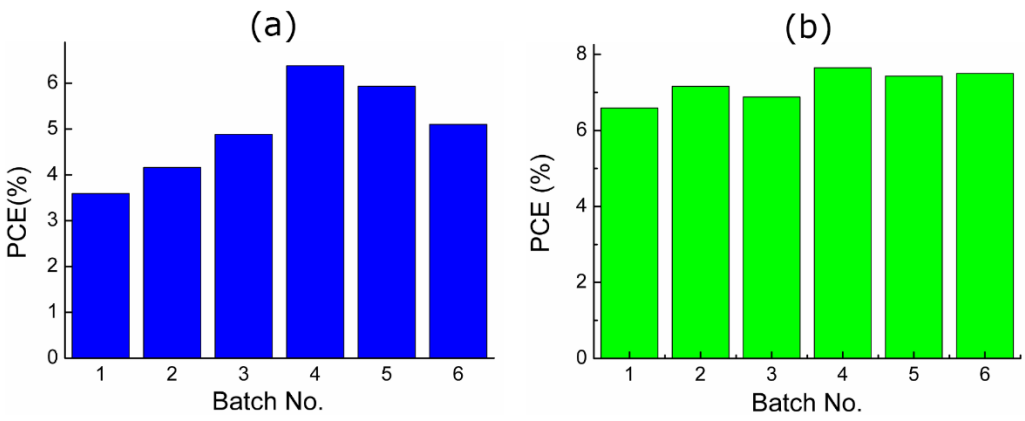

Figure 2.13: Statistical variation in photovoltaic efficiency of (a) TiO_2-150°C (b) 2.5 Nb/ TiO_2-150°C based solar cells.

2.3.13 Cap-V analysis

Capacitance vs. voltage (Cap-V) measurements of PV devices have been used in the past to determine valuable information on depletion width and carrier densities of constituent layers.[9,11,12,35] Figure 2.14a and 2.14b show Cap-V plots of solar cells before and after light soaking, respectively. The effect of light soaking is quite prominent, both in shape and magnitude of Cap-V results. The capacitance of a *p-n* heterojunction solar cell can be written as[36]

$$C = \frac{\varepsilon_0 A}{\frac{X_P}{\varepsilon_p} + \frac{X_n}{\varepsilon_n}} \quad \text{----------(2.1)}$$

Where 'C' is the junction capacitance, 'ε_0' permittivity of air, 'A' area of the device and 'X_p' is depletion width inside PbS, 'X_n'depletion width in the *n*-type layer, ε_p and ε_n are the dielectric constant of PbS and *n*-type layer, respectively. Measured capacitance for all devices saturates with respect to applied bias at high reverse biases and is true for both before and after light soaking conditions. Therefore, we can safely assume that at -0.8V reverse bias condition, the PbS layer is fully depleted[11,12](as shown in Figure 2.14 a and 2.14b). Under saturation condition, X_p would be equivalent to PbS layer thickness, and it is kept constant to 280 nm for all the devices. The relative dielectric constant of MPA treated PbS layer, and TiO_2 layer are 'ε_p'= 50[7], 'ε_n' = 30[8], respectively. Depletion width inside *n*-type layer 'X_n' at -0.8 V reverse bias is determined for all the devices from equation 2.1. The ratio between X_p and X_n should remain unchanged with respect to applied bias.

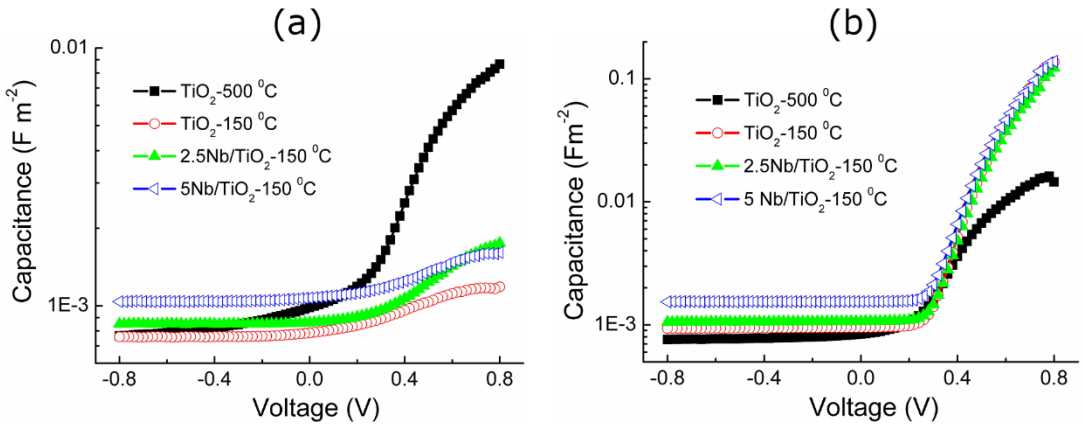

Figure 2.14: Cap-V characteristics of the PV devices, (a) before (b) after light soaking, respectively.

By determining X_p/X_n at -0.8 V reverse bias, we able to determine X_p for different applied bias and has been plotted in Figure 2.15.

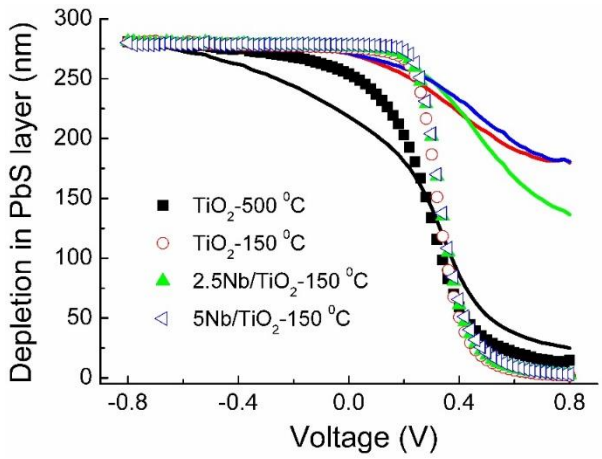

Figure 2.15: Depletion width vs. applied bias plots of PbS layer.

At maximum power point and zero bias condition, depletion width of PbS layer appears to increase for all the devices due to light soaking. This would facilitate carrier extraction from longer depths of the PbS layer. However, depletion of the wide bandgap *n*-type layers does not contribute appreciably to the current generation, but the change in their electron densities due to photodoping has a significant impact on PCE. Electron density of *n*-type layers before and after light soaking is calculated from the following equation considering abrupt *p*-*n* diode approximation.

$N_A \times X_P = N_D \times X_n$ ----------(2.2)

Table 2.6: Electron densities of various *n*-type layers for before and after light soaking conditions, from Cap-V measurement.

n-Type layer	Electron density before light soaking (cm^{-3})	Electron density after light soaking (cm^{-3})
TiO_2-500°C	4.72×10^{16}	4.73×10^{16}
TiO_2-150°C	4.65×10^{16}	7.27×10^{16}
2.5Nb/TiO_2-150°C	5.85×10^{16}	1.10×10^{17}
5Nb/TiO_2-150°C	1.27×10^{17}	1.82×10^{18}

We estimated the carrier density for different *n*-type layers from equation 2.2, shown in Table 2.6. It can be seen that carrier density for the low temperature processed *n*-type layers almost get doubles upon light soaking, whereas it remains almost unchanged for the TiO_2-500°C layer.

2.3.14 Simulation study

In order to have better insights into the underlying mechanism of light induces enhancements in low temperature processed TiO_2 layers, simulation of the current-voltage characteristics of the best performing solar cell using SCAPS simulation,[4,8,37,38] has been carried out. Details of the simulation parameters are shown in Table 2.7.

Table 2.7: SCAPS model parameter.

Parameter	PbS	2.5Nb/TiO_2-150°C
Dielectric constant, ε_r (C/Vm)	50	30
Bandgap (eV)	1.2	3.68
Electron affinity (eV)	3.89	4.065
Electron Mobility (cm^2/Vs)	3.4×10^{-4}	1×10^{-2}
Hole Mobility (cm^2/Vs)	1.0×10^{-3}	1×10^{-3}
N_d (cm^{-3})	1×10^{19}	1×10^{20}
N_a (cm^{-3})	1×10^{19}	1×10^{19}
Doping density (cm^{-3})	3×10^{16}	1.3×10^{17} (after light soaking)/ 5.9×10^{16} (before light soaking)
Thickness (nm)	300	100

Defects Parameter

Parameter	PbS	2.5Nb/TiO_2-150°C
Defect type	Single donor (+/0)	Single acceptor (-/0)
Energetic distribution	Uniform	Uniform
E_t (eV)	0.1	0.2
E_{kar}	0.2	0.1
τ_n (ns)	1200	49
τ_p (ns)	420	180
Total doping density, N_t (cm^{-3})	8 x 10^{15}	3.7 x 10^{16}

Interface defects:

Parameter	(2.5Nb/TiO_2-150°C) / PbS
Defect type	neutral
Energetic distribution	uniform
E_t (eV)	0.1
E_{kar} (eV)	0.07
Total doping density, N_t (cm^{-3})	1 x 10^{16}

In Figure 2.16a (a), at saturated light soaking conditions, simulation results show excellent agreements with measured J-V characteristics of the 2.5Nb/TiO_2-150°C based PV device for both dark and illuminated conditions. In order to simulate the dark J-V characteristics of the solar cell before light exposure, we change the carrier density of 2.5Nb/TiO_2-150°C layer to 5.9 x 10^{16} cm^{-3} (as determined from Cap-V measurement (Table 2.6)) while keeping the rest of the parameters unchanged. It is observed that the simulated curve does not match with the experimental dark J-V curve for before light exposer condition. Since the electrical conductivity depends on carrier density as well as mobility, we vary the electron mobility of the 2.5Nb/TiO_2-150°C layer to simulate the experimental results. As shown in Figure 2.16b, electron mobility is varied independently in between 10^{-3} to 10^{-9} $cm^2V^{-1}s^{-1}$. It is found that for the electron mobility in between 10^{-7} to 10^{-8} $cm^2V^{-1}s^{-1}$ simulated results corroborate well with the dark experimental J-V data.

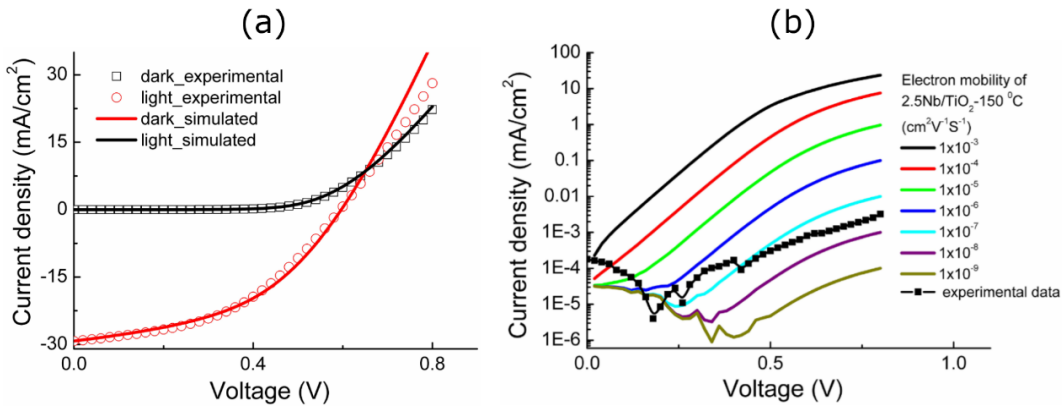

Figure 2.16: (a) represents the experimental (scatter) and simulated (line) J -V plot for 2.5Nb/TiO_2-150°C PV device under dark and 1.5 AM illumination condition under saturation condition. (b) Simulated dark J-V response of the device for varied electron mobility of 2.5Nb/TiO_2-150°C layer, from 1x 10^{-3} $cm^2V^{-1}s^{-1}$ to 1x 10^{-9} $cm^2V^{-1}s^{-1}$. Black symbol+line in (b) represents the experimental J-V curve of the device under dark before light soaking.

Therefore, simulation results suggest that in addition to electron density, the electron mobility of the low temperature processed TiO_2 layer must increase upon light soaking to justify the increase in PV performance.

2.3.15 Mobility measurement from MSM device

To verify the simulation predictions experimentally, we sought to probe the TiO_2 layers individually in simple metal-semiconductor-metal (MSM) device architecture.[39] Single carrier, electron only devices based on 2.5Nb/TiO_2-150°C and 5Nb/TiO_2-150°C layer is developed using ITO as bottom electrode and Ag as the top electrode. At a constant applied bias of 0.3 V, the current of the devices is probed with time under dark and under continuous solar illumination. As illustrated in Figure 2.17a, the current vs. time plot of both devices show a similar trend as their PV devices. Both MSM devices show increases in current with time under continuous solar light exposure, although current saturation in those devices is not attained even after two hours of light soaking. At a low injection regime, current for ohmic conduction can be expressed by $J = \mu nqE$, where J is current density, μ is carrier mobility, n is the electron density, q is the electronic charge, and E is the applied electric field. It is found that for the above measurement range, carrier mobility increases to

~100 times for 2.5Nb/TiO_2-150°C layer and five times for 5Nb/TiO_2-150°C layer due to light soaking (Table 2.8).

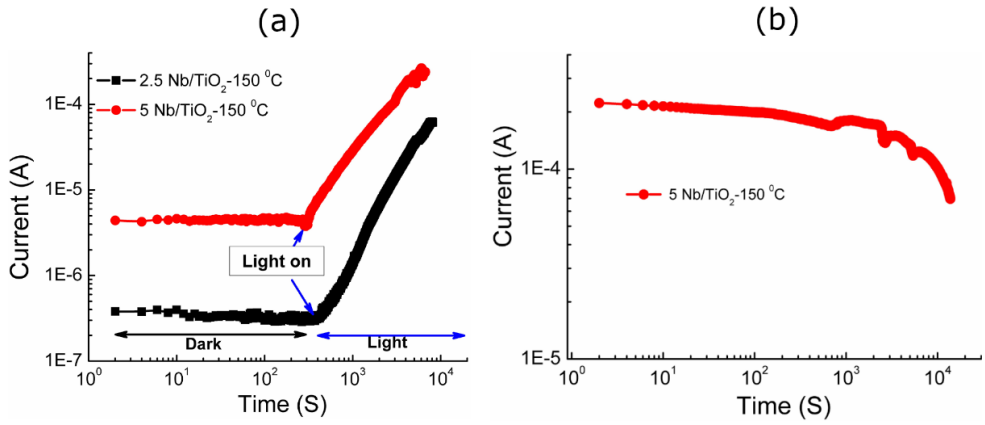

Figure 2.17: (a) represents current vs time plot for MSM devices made of 2.5Nb/TiO_2-150°C and 5Nb/TiO_2-150°C, measured at constant 0.3V applied bias. For both devices, the current remains invariant with time under the dark condition as marked by an arrow in the plot. Under solar illumination, the current of the devices increases monotonically with time. The "Light on" position is marked to guide the eye. (b) shows the decay of current with time at constantly applied bias 0.3V, for MSM - 5Nb/TiO_2-150°C device after the solar illumination is taken off.

Table 2.8: Mobility of *n*-type layers before and after three hours of white light soaking.

n-type layer	Mobility before light soaking ($cm^2V^{-1}s^{-1}$)	Mobility after light soaking ($cm^2V^{-1}s^{-1}$)
2.5Nb/TiO_2-150°C	4.46×10^{-8}	4.86×10^{-6}
5Nb/TiO_2-150°C	3.02×10^{-7}	1.29×10^{-6}

In the case of 5% doping, the free electron amount will be comparatively higher than 2.5% Nb doping, as a result we observe higher mobility in dark condition where no such efficient deadsorption of organic molecules takes place. But under light condition, the deadsorption of small molecules from the surface takes place and further strong adsorption of the atmospheric O_2, CO_2, CO, NO_2, etc molecules occurs at the surface. As in the case of 5% Nb doping free electron concentration is quite higher, the amount of adsorbed atmospheric molecules will be higher compared to 2.5% after same interval of light exposure. For both the cases, the saturation of current does not occur even after two hours of light exposure.

We have calculated the mobility after two hours of exposure for both 2.5% and 5% doped TiO_2, in that period of time, the amount of adsorbed atmospheric molecules might be in higher percentage in 5% doped TiO_2 than 2.5% doping. As a result, we observe lower mobility for 5% doped TiO_2 than 2.5% doped TiO_2 after two hours. Experimental results from MSM devices indeed support the simulation prophecy of an increase in electron mobility of low temperature processed TiO_2 layers upon light exposure. Further, electron mobility before light exposure for 2.5Nb/TiO_2-150°C layer is determined to be 4.46 x 10^{-8} $cm^2V^{-1}s^{-1}$, which is in good agreement with the simulation findings.

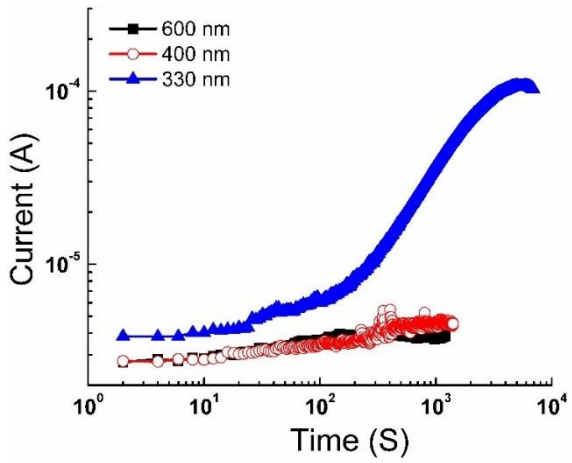

Figure 2.18: Current vs. time for MSM-5Nb/TiO_2-150°C device at different illumination wavelengths measured at 0.3V applied bias. The current of the device did not change for illumination wavelength of 600 nm and 400 nm, whereas current increases consistently with time under 330 nm wavelength illuminations.

In the case of the ZnO-PbS QD solar cell, *Willis et al.*[35] reported the enhancement of electron density of the ZnO layer due to UV light exposure. Our findings suggest that light exposure resulted in enhancement of both electron density and electron mobility in TiO_2 layers, are jointly responsible for their increased conductivity. Figure 2.17b shows the decay of the high conducting state of the 5Nb/TiO_2-150°C layer under continuous probing at 0.3V after the light bias is taken off.

After three hours of continuous probing current decreases to 30% of its initial value, indicating long stability of the high conducting state at dark condition; we identified the wavelength requirement for the incident light to be higher energy than the bandgap energy of the TiO_2 layers in order to observe the light soaking effect in MSM devices, shown in

Figure 2.18. The physical origin of the enhancement in electron mobility and electron concentration under high energy light bias is proposed to be due to the chemical process of adsorptions and exclusion of gas molecules on the TiO_2 surface.[35,40,41] Free electrons of TiO_2 layers can be trapped due to the adsorption of gas molecules such as O_2, NO_2, CO, etc., on TiO_2 surfaces under ambient working conditions. When exposed to high-energy light, removal of gas molecules would take place, and this may give rise to an increase in free-electron density in TiO_2 films. Further, the reduction of surface traps may also enhance the electron mobility of TiO_2 films. The effect of light soaking is more prominent in low temperature processed TiO_2 layers, possibly due to higher accessible sites for gas molecules to absorb in partially crystalline TiO_2 layer compared to calcinated high temperature processed TiO_2 layer. In the case of photovoltaic devices, photoelectron transferred from PbS to TiO_2 layer may accelerate the gas molecule exclusion process, and the top PbS layer could also act as a barrier for the reabsorption of gas molecules on the TiO_2 layer. This may be responsible for faster saturation (less than 20 minutes) of current in PV devices in comparison to MSM devices.

2.4 Conclusion

In summary, we demonstrate low temperature processed TiO_2 and Nb-doped TiO_2 could be used as excellent electron-accepting layers for QD solar cells. Solar light biasing is used to improve the electrical conductivity of TiO_2 films, which retains their properties even hours after light bias is taken off. Light-induced enhancements in electron concentration and electron mobility of low temperature processed TiO_2 layers are confirmed both experimentally and by simulation. Along with performance, the stability of photovoltaic devices increases when the low temperature processed TiO_2 layers are uses as electron extraction layer. For this work, we have opted to use *p*-type $CdCl_2$ treated PbS QDs to furnish the electron excepting properties of low temperature processed TiO_2 layers. Further improvement in device performance would be possible by adopting the most recent advances in PbS QDs processing. Based on the insights of our work, we envisage further improvements in the *n*-type layer could be realized by controlling chemical doping and photodoping effects.

2.5 References

1. Huynh, W. U.; Dittmer, J. J.; Alivisatos, A. P. Hybrid nanorod-polymer solar cells. *Science* **2002**, *295*, 2425-2427.

2. McDonald, S. A.; Konstantatos, G.; Zhang, S. G.; Cyr, P. W.; Klem, E. J. D.; Levina, L.; Sargent, E. H. Solution-processed PbS quantum dot infrared photodetectors and photovoltaics. *Nat. Mater.* **2005**, *4*, 138-142.

3. Tang, J.; Kemp, K. W.; Hoogland, S.; Jeong, K. S.; Liu, H.; Levina, L.; Furukawa, M.; Wang, X.; Debnath, R.; Cha, D.; Chou, K. W.; Fischer, A.; Amassian, A.; Asbury, J. B.; Sargent, E. H. Colloidal-quantum-dot photovoltaics using atomic-ligand passivation. *Nat. Mater.* **2011**, *10*, 765-771.

4. Ip, A. H.; Thon, S. M.; Hoogland, S.; Voznyy, O.; Zhitomirsky, D.; Debnath, R.; Levina, L.; Rollny, L. R.; Carey, G. H.; Fischer, A.; Kemp, K. W.; Kramer, I. J.; Ning, Z.; Labelle, A. J.; Chou, K. W.; Amassian, A.; Sargent, E. H. Hybrid passivated colloidal quantum dot solids. *Nat. Nanotechnol.* **2012**, *7*, 577-582.

5. Chuang, C. H. M.; Brown, P. R.; Bulovic, V.; Bawendi, M. G. Improved performance and stability in quantum dot solar cells through band alignment engineering. *Nat. Mater.* **2014**, *13*, 796-801.

6. Lan, X.; Voznyy, O.; Kiani, A.; de Arquer, F. P. G.; Abbas, A. S.; Kim, G.-H.; Liu, M.; Yang, Z.; Walters, G.; Xu, J.; Yuan, M.; Ning, Z.; Fan, F.; Kanjanaboos, P.; Kramer, I.; Zhitomirsky, D.; Lee, P.; Perelgut, A.; Hoogland, S.; Sargent, E. H. Passivation Using Molecular Halides Increases Quantum Dot Solar Cell Performance. *Adv. Mater.* **2016**, *28*, 299-304.

7. Rath, A. K.; Bernechea, M.; Martinez, L.; Pelayo Garcia de Arquer, F.; Osmond, J.; Konstantatos, G. Solution-processed inorganic bulk nano-heterojunctions and their application to solar cells. *Nat. Photonics* **2012**, *6*, 529-534.

8. Liu, M.; de Arquer, F. P. G.; Li, Y.; Lan, X.; Kim, G.-H.; Voznyy, O.; Jagadamma, L. K.; Abbas, A. S.; Hoogland, S.; Lu, Z.; Kim, J. Y.; Amassian, A.; Sargent, E. H. Double-Sided Junctions Enable High-Performance Colloidal-Quantum-Dot Photovoltaics. *Adv. Mater.* **2016**, *28*, 4142-4148.

9. Luther, J. M.; Law, M.; Beard, M. C.; Song, Q.; Reese, M. O.; Ellingson, R. J.; Nozik, A. J. Schottky Solar Cells Based on Colloidal Nanocrystal Films. *Nano Lett.* **2008**, *8*, 3488-3492.

10. Tang, J.; Wang, X.; Brzozowski, L.; Barkhouse, D. A. R.; Debnath, R.; Levina, L.; Sargent, E. H. Schottky Quantum Dot Solar Cells Stable in Air under Solar Illumination. *Adv. Mater.* **2010**, *22*, 1398-1402.

11. Pattantyus-Abraham, A. G.; Kramer, I. J.; Barkhouse, A. R.; Wang, X.; Konstantatos, G.; Debnath, R.; Levina, L.; Raabe, I.; Nazeeruddin, M. K.; Graetzel, M.; Sargent, E. H. Depleted-Heterojunction Colloidal Quantum Dot Solar Cells. *Acs Nano* **2010**, *4*, 3374-3380.

12. Rath, A. K.; Bernechea, M.; Martinez, L.; Konstantatos, G. Solution-Processed Heterojunction Solar Cells Based on p-type PbS Quantum Dots and n-type Bi2S3 Nanocrystals. *Adv. Mater.* **2011**, *23*, 3712-3717.

13. Gao, J.; Luther, J. M.; Semonin, O. E.; Ellingson, R. J.; Nozik, A. J.; Beard, M. C. Quantum Dot Size Dependent J-V Characteristics in Heterojunction ZnO/PbS Quantum Dot Solar Cells. *Nano Lett.* **2011**, *11*, 1002-1008.

14. Rath, A. K.; Pelayo Garcia de Arquer, F.; Stavrinadis, A.; Lasanta, T.; Bernechea, M.; Diedenhofen, S. L.; Konstantatos, G. Remote Trap Passivation in Colloidal Quantum Dot Bulk Nano-heterojunctions and Its Effect in Solution-Processed Solar Cells. *Adv. Mater.* **2014**, *26*, 4741-4747.

15. Clifford, J. P.; Johnston, K. W.; Levina, L.; Sargent, E. H. Schottky barriers to colloidal quantum dot films. *Appl. Phys. Lett.* **2007**, *91*, 253117.

16. Yuan, M.; Liu, M.; Sargent, E. H. Colloidal quantum dot solids for solution-processed solar cells. *Nat. Energy* **2016**, *1*, 16016.

17. Mathew, S.; Yella, A.; Gao, P.; Humphry-Baker, R.; Curchod, B. F. E.; Ashari-Astani, N.; Tavernelli, I.; Rothlisberger, U.; Nazeeruddin, M. K.; Graetzel, M. Dye-sensitized solar cells with 13% efficiency achieved through the molecular engineering of porphyrin sensitizers. *Nat. Chem.* **2014**, *6*, 242-247.

18. Wang, M.; Wang, X. P3HT/TiO2 bulk-heterojunction solar cell sensitized by a perylene derivative. *Sol. Energ. Mat. and Sol. C.* **2007**, *91*, 1782-1787.

19. Lee, M. M.; Teuscher, J.; Miyasaka, T.; Murakami, T. N.; Snaith, H. J. Efficient Hybrid Solar Cells Based on Meso-Superstructured Organometal Halide Perovskites. *Science* **2012**, *338*, 643-647.

20. Liu, H.; Tang, J.; Kramer, I. J.; Debnath, R.; Koleilat, G. I.; Wang, X.; Fisher, A.; Li, R.; Brzozowski, L.; Levina, L.; Sargent, E. H. Electron Acceptor Materials Engineering in Colloidal Quantum Dot Solar Cells. Light Energy Conversion by Mesoscopic PbS Quantum Dots/TiO2 Heterojunction Solar Cells. *Adv. Mater.* **2011**, *23*, 3832-3837.

21. Etgar, L.; Moehl, T.; Gabriel, S.; Hickey, S. G.; Eychmueller, A.; Graetzel, M. Light Energy Conversion by Mesoscopic PbS Quantum Dots/TiO2 Heterojunction Solar Cells. *Acs Nano* **2012**, *6*, 3092-3099.

22. Barkhouse, D. A. R.; Debnath, R.; Kramer, I. J.; Zhitomirsky, D.; Pattantyus-Abraham, A. G.; Levina, L.; Etgar, L.; Gratzel, M.; Sargent, E. H. Depleted Bulk Heterojunction Colloidal Quantum Dot Photovoltaics. *Adv. Mater.* **2011**, *23*, 3134-3138.

23. Leijtens, T.; Eperon, G. E.; Pathak, S.; Abate, A.; Lee, M. M.; Snaith, H. J. Overcoming ultraviolet light instability of sensitized TiO2 with meso-superstructured organometal tri-halide perovskite solar cells. *Nat. Commun.* **2013,** 4.

24. Burschka, J.; Dualeh, A.; Kessler, F.; Baranoff, E.; Cevey-Ha, N.-L.; Yi, C.; Nazeeruddin, M. K.; Graetzel, M. Tris(2-(1H-pyrazol-1-yl)pyridine)cobalt(III) as p-Type Dopant for Organic Semiconductors and Its Application in Highly Efficient Solid-State Dye-Sensitized Solar Cells. *J. Am. Chem. Soc.* **2011**, *133*, 18042-18045.

25. Kim, J. Y.; Lee, K.; Coates, N. E.; Moses, D.; Nguyen, T. Q.; Dante, M.; Heeger, A. J. Efficient tandem polymer solar cells fabricated by all-solution processing. *Science* **2007**, *317*, 222-225.

26. Chen, L. M.; Hong, Z. R.; Li, G.; Yang, Y. ecent Progress in Polymer Solar Cells: Manipulation of Polymer: Fullerene Morphology and the Formation of Efficient Inverted Polymer Solar Cells. *Adv. Mater.* **2009**, *21*, 1434-1449.

27. Docampo, P.; Hanusch, F. C.; Stranks, S. D.; Doeblinger, M.; Feckl, J. M.; Ehrensperger, M.; Minar, N. K.; Johnston, M. B.; Snaith, H. J.; Bein, T. Solution Deposition-Conversion for Planar Heterojunction Mixed Halide Perovskite Solar Cells. *Adv. Energy Mater.* **2014,** *4*, 1400355.

28. Chen, W.; Wu, Y. Z.; Yue, Y. F.; Liu, J.; Zhang, W. J.; Yang, X. D.; Chen, H.; Bi, E. B.; Ashraful, I.; Gratzel, M.; Han, L. Y. Efficient and stable large-area perovskite solar cells with inorganic charge extraction layers. *Science* **2015**, *350*, 944-948.

29. Li, L.; Zhang, P.; Wang, W.-M.; Lin, H.; Zerdoum, A. B.; Geiger, S. J.; Liu, Y.; Xiao, N.; Zou, Y.; Ogbuu, O.; Du, Q.; Jia, X.; Li, J.; Hu, J. Foldable and Cytocompatible Sol-gel TiO2 Photonics. *Sci. Rep.* **2015**, *5*, 13832.

30. Ghobadi, N. Band gap determination using absorption spectrum fitting procedure. *Int. Nano Lett.* **2013**, *3*, 1-4.

31. Emeline, A. V.; Furubayashi, Y.; Zhang, X. T.; Jin, M.; Murakami, T.; Fujishima, A. Photoelectrochemical behavior of Nb-doped TiO2 electrodes. *J. Phys. Chem. B* **2005**, *109*, 24441-24444.

32. Mandal, D.; Hamann, T. W. Charge Distribution in Nanostructured TiO2 Photoanode Determined by Quantitative Analysis of the Band Edge Unpinning. *Acs Appl. Mater. & Interfaces* **2016**, *8*, 419-424.

33. Paz-Soldan, D.; Lee, A.; Thon, S. M.; Adachi, M. M.; Dong, H.; Maraghechi, P.; Yuan, M.; Labelle, A. J.; Hoogland, S.; Liu, K.; Kumacheva, E.; Sargent, E. H. Jointly Tuned Plasmonic-Excitonic Photovoltaics Using Nanoshells. *Nano Lett.* **2013**, *13*, 1502-1508.

34. Fan, C.; Chen, C.; Wang, J.; Fu, X.; Ren, Z.; Qian, G.; Wang, Z. Enhanced photocatalytic activity of hydroxylated and N-doped anatase derived from amorphous hydrate. *J. Mat.Chem. A* **2014**, *2*, 16242-16249.

35. Willis, S. M.; Cheng, C.; Assender, H. E.; Watt, A. A. R. The Transitional Heterojunction Behavior of PbS/ZnO Colloidal Quantum Dot Solar Cells. *Nano Lett.* **2012**, *12*, 1522-1526.

36. Wolfe, C. M.; Holonyak, N.; Stillman, G. E., *Physical properties of semiconductors*. Prentice Hall: 1989.

37. Kemp, K. W.; Labelle, A. J.; Thon, S. M.; Ip, A. H.; Kramer, I. J.; Hoogland, S.; Sargent, E. H. Interface Recombination in Depleted Heterojunction Photovoltaics based on Colloidal Quantum Dots. *Adv. Energy Mater.* **2013**, *3*, 917-922.

38. Burgelman, M.; Nollet, P.; Degrave, S. Modelling polycrystalline semiconductor solar cells. *Thin Solid Films* **2000**, *361*, 527-532.

39. Kao, K. C.; Hwang, W., *Electrical transport in solids: with particular reference to organic semiconductors*. Pergamon Press: 1981.

40. Atashbar, M. Z.; Sun, H. T.; Gong, B.; Wlodarski, W.; Lamb, R. XPS study of Nb-doped oxygen sensing TiO2 thin films prepared by sol-gel method. *Thin Solid Films* **1998**, *326*, 238-244.

41. Hao Feng, L.; Feng, L.; Gang, L.; Zhi-Gang, C.; Da-Wei, W.; Hai-Tao, F.; Gao Qing, L.; Zhou Hua, J.; Hui-Ming, C. 1.Huynh, W.U., Dittmer, J.J. & Alivisatos, A.P. Hybrid nanorod-polymer solar cells. *Science* **2002**, *295*, 2425-2427.

Chapter 3

Comparative study of surface passivating organic ligands in determining the electronic properties of quantum dots solids and their impact on solar cell performance

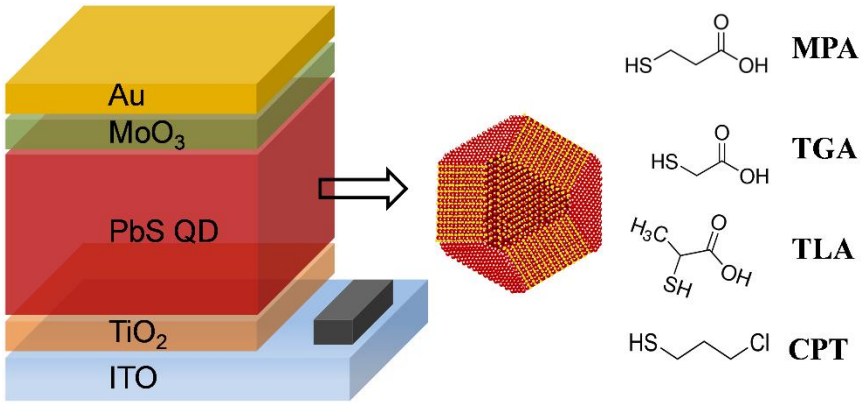

Abstract:

Surface chemistry plays a crucial role in determining the electronic properties of quantum dot solids and may well be the key to mitigate loss processes involved in quantum dot solar cells. Surface ligands help to maintain the shape and size of the individual dots in solid films, to preserve the clean energy band gap of the individual particles, and to control charge carrier conduction across solid films, in turn regulating their performance in photovoltaic applications. In this chapter, we show that the changes in size, shape, and functional groups of small chain organic ligands enable us to modulate mobility, dielectric constant, and carrier doping density of lead sulfide quantum dot solids. Further, we correlate these results with performance, stability, and recombination processes in the respective photovoltaic devices. Our results highlight the critical role of surface chemistry on the electronic properties of quantum dots. The role of the size, functionality, and the surface coverage of the ligands in determining charge transport properties and stability of quantum dot solids have been discussed. Our findings, when applied in designing new ligands with higher mobility and improved passivation of quantum dot solids, can have important implications for the development of high-performance quantum dot solar cells.

3.1 Introduction

The solution process inorganic semiconductor quantum dot based solar cell has shown steady improvements over the years to emerge as a promising contender for next-generation solar cell technology.[1-4] Control over synthesis techniques,[5] advancements on post-synthesis processing[2,6] and maneuver over passivation strategy[3,4,7,8] have contributed critically to their progress in photovoltaic and other optoelectronic applications. Large proportions of surface atoms along with the associated minuscule volume of the quantum dot (QD) particles introduce surface dominance in determining the electronic properties of QD solids. Unsaturated surface atoms often result in the formation of dangling bonds, leading to the creation of intermediate states of varying energies across their band gaps.[9,10] This may give rise to a range of phenomena in QD solids, namely, the formation of band tail, uncontrolled doping, and formation of midgap trap states. Trap states are detrimental to both current and voltage generation as they reduce charge carrier mobility, decrease band edge carrier lifetime, and increase photocarrier recombination by providing alternate pathways through midgap states.[9] Moreover, degradation of interfacial properties by means of Fermi energy pinning and reduction of built-in potential across junction also make the intermediate states unfavorable in photovoltaic applications.[8,11] Surface chemistry plays a crucial role in eliminating the formation of intermediate states in QDs by passivation of surface atoms through appropriate ligands. Surface ligation pushes the intermediate states deep inside the valence band[12] or the conduction band[9] and thus produces a cleaner band gap QD solid.

Lead sulfide (PbS) QD has dominated the spectrum of QD solar cells due to their wide bandgap tunability, solution-phase processability, ambient stability, and high performance.[13] As synthesized PbS QDs are off-stoichiometric (bandgap approximately~ 1.3 eV), where (111) crystal facets are terminated by Pb atoms and (100) facets constitutes both Pb and S atoms.[14,15] The surface ligands are thus designed such that they interact with the empty orbitals of the electron-deficient metal atoms of the QD surface. A plethora of surface ligands that include small chain organic molecules with suitable anchoring groups,[16,17] atomic sizes halide ligands[3,18,] and most recently organic-inorganic halometallate ligands,[4,19] have been studied for effective passivation of the QD surface to develop high-performance photovoltaic devices. Among the various groups tested so far

(SH, COOH, CN, NH_2), thiol (SH) has turned out to be the most suitable anchoring group for PbS QD solar cells.[4,20] Thiol terminated organic ligands generally result in *p*-type doping,[12] whereas iodine[18] and halometallate[4] passivation yield *n*-type doping to PbS QDs. Organic ligands generally yield low mobility QD solids (< 10^{-2} $cm^2V^{-1}s^{-1}$) which have been attributed to their longer dot-to-dot distance and high tunneling barrier for charge carrier transportation, thereby limiting their performance in QD solar cells.[11] In comparison to inorganic ligand passivated QD solar cells, organic ligand passivation has, however, been reported to yield higher open-circuit voltage[8,21,22] and shown improved resilience over ambient degradations.[3,4] To date, the highest performance has been obtained by interfacing *n*-type PbS QD layer passivated by inorganic ligand PbI_3^- with 1,2 ethanedithiol (organic ligand) capped *p*-type PbS QD layer.[4] A better understanding of the ligand-induced modulation of the electronic properties of QDs may inspire designing novel organic ligands that would lead to higher mobility and superior preservation of the QD surface.

Different aspects of the role of surface ligands on the electronic properties of QDs have been revealed in earlier published reports.[8,9,11] Changes in the anchoring group and the dipole moment of the surface ligands have been shown to shift the positions of the valence and the conduction bands of QD solids[17,23,] which enables the modulation of the interfacial properties in photovoltaic applications. The introduction of electron-accepting and electron-donating functional groups in the surface ligands has been used for remote doping of QD films.[24-26] Control over surface coverage and facet selective steric properties of QDs has led to the formation of superstructures with long-range translational and orientational order in QD solids.[27] Recent use of π-conjugated ligands have shown bulk like optical absorption and broadband optical absorption enhancement in colloidal QDs.[28,29] The use of thiophenol derivatives as the ligand in PbS QDs has been reported to result in up to 300% improvement in absorption over bulk values.[28] The drastic increase in the absorption coefficient has been attributed to the mixing of the ground state ligands orbitals leading to a subsequent increase in the density of states of the QDs. The charge carrier mobility of QD solids has been reported to increase exponentially with a decrease in the ligand size when the dielectric constant of the environment is maintained.[30] The mobility of the QD solid, however, strongly depends on the anchoring groups[31,32] and the energy levels (HOMO/LUMO) of the surface ligands.[33] Surface ligands which only produce high mobility QD solid are not necessarily best suitable for photovoltaic applications;[34] effective passivation of the QD surface to create

a clean band gap is also a desirable quality that is deemed from a good ligand.[11] It has been found that longer ligands show high photoluminescence quantum yield, an indication of clean band gap due to the reduction in the dot-to-dot coupling, but leads to inefficient carrier mobility; the opposite is true for shorter ligands.[16,35,36] In the case of the asymmetric ligands having different terminal anchoring groups, the correlation between charge carrier mobility with ligand size and anchoring groups is not well understood to date. For example, it is reported that 3-mercapto propionic acid (MPA) capped PbS QDs show almost an order of magnitude higher mobility than 1,2 ethanedithiol passivated PbS QD films, despite the fact that later ligand is shorter MPA.[16,37] It is safe to say that achieving both the desirables of high electrical mobility and clean band gap are not mutually exclusive and could be attained through a better understanding of the role of ligand-mediated phenomena in QD solids. A detailed study on the impact of various ligand types on the electronic properties of QD solids is, therefore, necessary to develop novel ligands for high-performance solar cell applications.

Given the aforementioned complexities in the choice of surface ligands, we posit to study a series of ligands, chosen judiciously with varied size and functionality, to understand the overall impact of the ligands on the photovoltaic figure of merits. Among the various ligands used in this study, MPA has been extensively studied in quantum dot solar cell development and has reported the highest efficiency to date among organic ligands.[2,7,38,39] The other organic ligands studied here, namely thioglycolic acid (TGA),[36] thiolactic acid (TLA), and 3-Chloro-1-propanethiol(CPT),[40] however, have rarely been explored in earlier reports. TGA and TLA are particularly interesting due to the fact that they possess similar terminal anchoring groups of SH and COOH as MPA, but they are ~ 1.54 Å shorter than MPA.[36] General notion suggests that smaller ligands would reduce the dot-to-dot separation and thereby increase the compactness, carrier mobility, and dielectric constant of the QD solid. Higher mobility and higher dielectric constant are of significant importance in solar cells for fast carrier transport and dielectric screening of Coulomb attraction between photo-generated carriers for their efficient delocalization. Our results suggest PbS QD films, passivated using TGA and TLA, give rise to lower mobility and lower dielectric constant than that of MPA treated PbS QD films. Photovoltaic performance of MPA passivated photovoltaic devices shows higher photocurrent, whereas TGA and TLA passivated solar cells show higher open-circuit voltage and superior stability in their solar cell performance.

Through a series of optoelectronic characterizations, namely photo-CELIV, transient photocurrent, transient photovoltage, light intensity-dependent short circuit current and open-circuit voltage measurements, temperature-dependent study, and XPS measurements, we provide a detailed electronic and physical understanding of ligand-mediated properties of PbS QD solids and corroborate our results to explain their performances in solar cell devices.

3.2 Experimental Details

PbS NCs were synthesized by following the previously discussed method in section 2.2.3.

3.2.1 Preparation of TiO_2 sol-gel

TiO_2 was prepared following our previously reported method (section 2.2.1) with a small change. In a typical synthesis, titanium isopropoxide (2.4 mmol) was added 2.53 mL of 2-propanol and stirred for 30 minutes. 14µL (5M) HCl was then taken in 2.53 mL of 2-propanol and added to the solution slowly under continuous stirring. The whole solution was then left stirring for another 30 minutes to form the transparent TiO_2 precursor.

3.2.2 Device Fabrication

ITO and FTO substrates were cleaned by following the previously mentioned procedure in section 2.2.4. For low-temperature process *n*-type TiO_2, the sol-gel precursor solution was spin coated at 2500 rpm on top of ITO. The films were then annealed at 70°C for 30 minutes. The substrates were then allowed to cool down to room temperature. A small amount of Millipore water was added to them at a steady-state followed by rotation at 2500 rpm for 1 minute. The substrates were then heated to 150°C for another 30 minutes.

The as-prepared substrates were used for PbS QDs deposition. PbS QDs were deposited via layer by layer solid-state ligand exchange approach under ambient condition.[5] For PbS@MPA devices, 5% v/v 3-MPA in methanol solution was used for ligand exchange. For each PbS layer, 30 mg/ml PbS from Octane solution was deposited on the substrate in dynamic condition at 2500 rpm for 40 seconds. Under continuous spinning 6-7, drops of MPA were added, followed by rinsing with 8-9 drops of methanol. The same process was repeated up to 12 layers to achieve the desired thickness. For PbS@TGA and PbS@TLA devices, 10% v/v ligand solutions in methanol were used, and the ligand exchange process

was repeated two times, followed by two times washing with methanol for each PbS layer deposition. Top electrodes were deposited by thermal evaporator from Hind high vacuum, model BC-300 at a base pressure of 3 x 10^{-6} mBar. 10 nm MoO_3 was deposited at 0.1Ås^{-1}, followed by 50 nm of Au deposition at 0.5Ås$^{-1,}$ and finally, 100 nm Ag was deposited at 1Ås^{-1} to complete the film formation.

3.2.3 Materials Characterization Techniques

ATR-FTIR spectra of the thin film were obtained on a Perkin Elmer Spectrum two spectrophotometer in the 4000–400 cm^{-1} range with a resolution of 4 cm^{-1}. Optical absorption measurements were carried out by Shimadzu UV-Vis-NIR-3600 Plus spectrophotometer. Total absorption of thin films was measured by integrating sphere (ISR-603), attachment of Shimadzu UV-3600 plus. X-ray photoelectron spectroscopy (XPS) of TiO_2 and Nb-doped TiO_2 were recorded with a custom-built ambient pressure photoelectron spectrometer (APPES) (Prevac, Poland), equipped with VG Scienta's R3000HP analyzer. Monochromatic Al Kα x-ray was generated at 400 W from MX650 Monochromator for XPS measurement. Pressure in the chamber was maintained in the range of 5×10^{-10} Torr. The energy resolution of the spectrometer was set at 0.7 eV at pass energy of 50 eV. Binding energy (BE) was calibrated with respect to Au $4f_{7/2}$ core level at 84.0 eV. UPS measurement is also carried out by the same instrument. He-Iα radiation of energy 21.22 eV is used for the UPS measurement.

3.2.4 Device Characterization Techniques

J-V measurements and Capacitance-Voltage measurements were followed previously discussed methods in section 2.2.6.1 and 2.2.6.4, respectively.

3.2.4.1 Temperature-dependent V_{oc} and J_{sc} measurement

Temperature-dependent measurements were carried out using liquid nitrogen cooled cryostat equipment (Janis, Model no.VPF-100) controlled by a Lakeshore temperature controller 325 module. Once the system was cool down to 76K, it was kept at this temperature for 30 minutes to stabilize. The instrument was warmed up at a rate of 5 K/min, and data was taken from 160K to 300K temperature.

3.2.4.2 Intensity dependent V_{oc} and J_{sc} measurement

Intensity dependent V_{oc} and J_{sc} were measured using a 658 nm laser source provided by a Laser diode control unit (Newport LQA658-30C) controlled by a function generator (Tektronics, AFG 3021C).

3.2.4.3 Photo-CELIV measurement

The experimental setup consists of a function generator (Tektronics, AFG 3021C), 658 nm Laser diode (Newport LQA658-30C), and a Digital oscilloscope (Tektronics, MDO 3104). The function generator was used to generate voltage pulses of a suitable ramp. It was also used to trigger the laser to generate light pulses. The time delay between the laser pulse and voltage ramp was controlled by providing a suitable delay time between the pulses using the function generator. Solar cells were kept at reverse bias condition for photo-CELIV measurement. Applied voltage ramp and corresponding current evolution were recorded with the help of a digital oscilloscope. In order to record the current evolution, external resistance was set to 50 Ω for the entire measurement range.

3.2.4.4 Transient Photo Voltage (TPV) and Transient Photo Current (TPC) measurement

TPV and TPC measurements were performed using a Laser diode control unit (Newport LQA658-30C) modulated through a function generator (Tektronics, AFG 3021C) to create perturbation light pulses. A solar simulator (Peccell, PEC-L01) was used to generate constant V_{oc} from the solar cells. Light biasing was varied by neutral density filters used to generate different V_{oc} and J_{sc} values. For TPV measurement device under test was connected to the oscilloscope (Tektronics, MDO 3104) through 1 MΩ resistance. Laser pulse intensities were modulated to keep the perturbation voltage below ten mV. TPC measurements were carried out using the laser pulse alone, and the output was measured across 50 Ω resistance.

3.3 Results and Discussions

3.3.1 FT-IR analysis

Photovoltaic devices are fabricated utilizing layer by layer solid-state ligand exchange approach, as reported earlier.[2] The device fabrication process is given in detail in the experimental section 3.2.2. In a typical process, a thin layer of Oleic acid capped PbS QD layer is deposited by a spin coating process. A ligand solution is applied to the PbS thin film for a brief period of time for complete removal of oleic acid and passivation of PbS QD surface by the applied ligand. We have selected MPA, TGA, TLA, and CPT as organic ligands to passivate the PbS QD surface. TGA, TLA, and MPA possess thiol and carboxylic acid as terminal anchoring groups. TGA has one carbon atom less than MPA (straight-chain) and TLA (branched); however, the effective distance between the anchoring groups in both TGA and TLA is one carbon length (~1.54 Å) shorter than MPA. CPT consists of the same number of backbone carbon atoms as MPA, while the terminal acid functional group has been replaced by chlorine. From here on, we would refer to both TGA and TLA as short-chain ligands due to their shorter inter-anchoring-group distances.

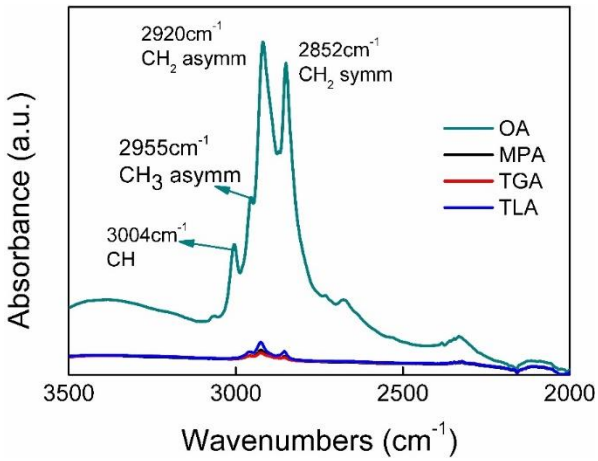

Figure 3.1: ATR FT-IR spectra under reflective mode for PbS QD films treated with various surface ligands on a glass substrate.

Successful completion of the ligand exchange process is confirmed from the attenuated total reflectance (ATR) mode Fourier transformed infrared spectroscopy (FT-IR) study (Figure 3.1). Oleic acid capped PbS QD films show multiple high-intensity peaks within the presented wavenumber (3500-2000 cm^{-1}) range. Peaks correspond to wavenumbers 2955

cm^{-1} and 3004 cm^{-1} are assigned as CH_3 stretch and CH (-C=C-H) stretch, respectively, of oleic acid. After ligand exchange with MPA, TGA, or TLA, both peaks disappeared, suggesting a successful ligand exchange process and removal of oleic acid from the QD surface. Peaks at 2920 cm^{-1} and 2652 cm^{-1} in oleic acid capped PbS QD film correspond to asymmetric and symmetric CH_2 stretching frequencies. A substantial decrease in CH_2 peak strengths after ligands treatment implies a decrease in CH_2 units, which suggests a successful ligand exchange process. Further, the absence of SH stretching peaks in the range of 2550-2600 cm^{-1} suggests that sulfur atoms are bonded to the QD surface.

3.3.2 J-V Characteristics of PV device

Optimized solar cell performances for various ligand passivated PbS QD films are shown in Figure 3.2.

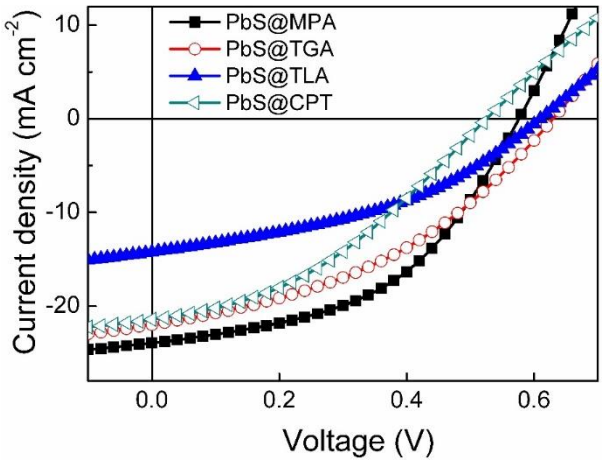

Figure 3.2: Current density vs. voltage characteristics of PbS QD based solar cells, treated with various ligands.

The photovoltaic parameters of solar cell performances under 1.5 A.M. illumination are given in Table 3.1.

Table 3.1: Comparison of photovoltaic performances.

Ligand Type	V_{oc} (V)	J_{sc} (mA/cm^2)	FF (%)	PCE (%)
PbS@MPA	0.576	24.00	47.4	6.55
PbS@TGA	0.629	22.56	44.1	6.25
PbS@TLA	0.610	14.22	40.3	3.50
PbS@CPT	0.526	21.43	38.2	4.31

MPA and TGA treated devices show comparable performances, whereas TLA and CPT treated solar cells yield much lower efficiencies. MPA yields the highest short circuit current density (J_{sc}); however, it is interesting to note that the short-chain ligands (TGA and TLA) give rise to higher open-circuit voltages (V_{oc}) than the longer chain ligands (MPA and CPT). This is of crucial importance due to the fact that QD solar cells suffer from higher open-circuit voltage loss (0.55-0.75 V for 1.1 to 1.4 eV bandgap)[41] compared to CIGS (0.35 V for 1.1 eV), c-Si (0.38 V for 1.12 eV bandgap) and hybrid perovskite (0.4 V for 1.5 eV bandgap) solar cells.[22] Therefore, any reduction in open circuit voltage loss is considered critical for QD solar cell development.

3.3.3 Photo-CELIV analysis

Competition between carrier transit time and carrier recombination time gives rise to the photocurrent generation in solar cells. Carrier transit time in a solar cell is inversely proportional to mobility ($t_{transit} = \frac{d^2}{\mu V}$; d: device thickness, μ: mobility, V: applied voltage). In our studied device structure of *n-p* junction solar cells, the *n*-type layer (TiO_2) acts as a transparent window layer. Under panchromatic solar illumination, a gradient of photogenerated carriers is created across the PbS QD layer thickness, where the majority of the carriers are created close to the junction.[42] In such a scenario, the majority of the photogenerated electrons can easily reach the *n*-type layer, whereas the photogenerated holes need to travel across the full PbS QD layer thickness to reach the counter electrode. Therefore determination of hole mobility may provide valuable insights into the photocurrent generation process for the studied ligands. Photo-CELIV, a powerful technique

to determine majority carrier mobility (a hole, in our case), has been used widely for QD and other thin-film solar cells.[43,44] We utilize the Photo-CELIV technique to determine hole mobility as well as dielectric constants of PbS QDs films treated with various surface ligands. Applied offset voltage, as well as the time delay between the light pulse and the voltage pulse, are kept constant during the measurements, while the voltage ramp for the devices is varied to maintain the condition of lower extraction current as compared to capacitive displacement current.[43] A typical photo-CELIV data is presented in Figure 3.3.

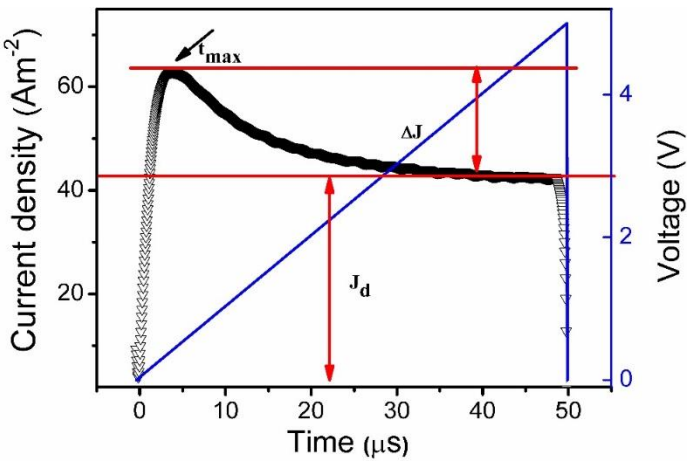

Figure 3.3: Typical results for CELIV measurements are shown to explain different parameters of equations 3.1 and 3.2.

Hole mobility (μ_h) is determined from the photo-CELIV measurements following equation[43,44]

$$\mu_h = \frac{2d^2}{3At_{max}^2\left(1+0.36\frac{\Delta J}{J_d}\right)} \quad \text{if} \quad \Delta J \leq J_d \text{----------(3.1)}$$

Where 'd' is device thickness, 'A' is ramp rate, 't_{max}' is the time for the transient current signal to reach its maximum value, 'ΔJ' is the maximum drift current, and 'J_d' is the displacement current.

The relative dielectric constant (ε_m) is determined from the following equation.

$$\varepsilon_m = \frac{J_d d}{A\varepsilon_0} \text{----------(3.2)}$$

PbS QD layer thickness is kept between 220 nm to 450 nm for the photo-CELIV study. The current evolution and the voltage ramp for various surface ligand treated PbS QD based photovoltaic devices are shown in Figure 3.4 a-d.

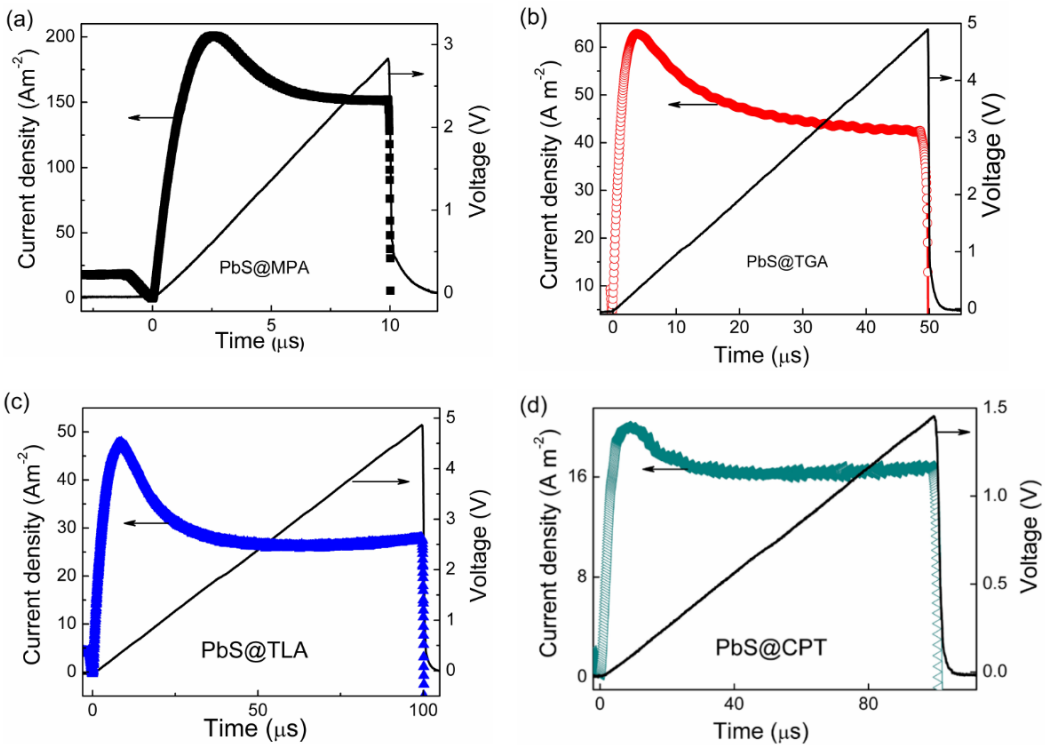

Figure 3.4: (a)-(d) represent the photo-CELIV measurements for MPA, TGA, TLA and CPT treated PbS QD solar cells, respectively. Current evolution and the applied voltage pulse, as a function of time, are shown in the same plot for the respective devices.

Implying equation of (3.1) and (3.2), we have calculated the hole mobility and dielectric constant for different ligand treated solar cells. PbS QD solids treated with longer ligands (MPA and CPT) show higher dielectric constant and mobility as compared with shorter ligand (TGA and TLA) passivation (Figures 3.5 a and b).

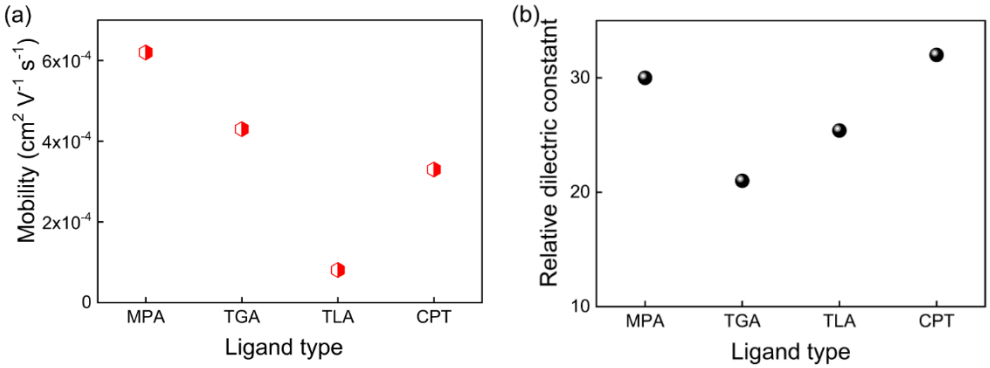

Figure 3.5: (a) variations in hole mobility and (b) dielectric constant of PbS QD layers treated with various ligands.

These observations are in stark contrast with the common notion that shorter ligands would generate higher mobility and higher dielectric constant by reducing the dot-to-dot separation.

3.3.4 Series Resistance calculation

Further, hole mobilities determined from photo-CELIV experiments are correlated with the series resistances of the solar cells. The forward bias J-V characteristics are shown in Figure 3.6, and the corresponding series resistance values of the respective photovoltaic devices are given in Table 3.2.

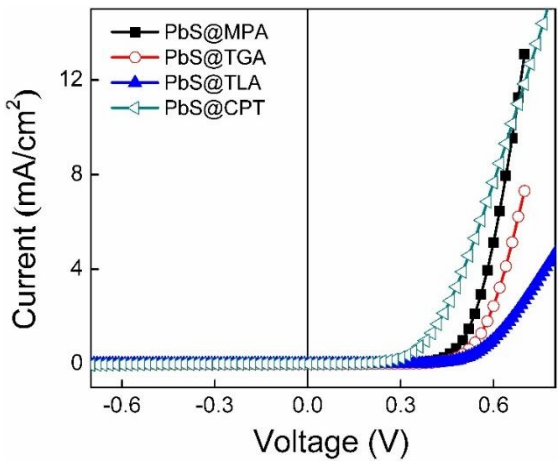

Figure 3.6: Current density vs. voltage plots of solar cells for various surface ligands under dark condition are shown.

The series resistance is calculated from the slope of the J-V characteristics curve above the threshold voltage.

Table 3.2: Series resistance of solar cells treated with the different ligand are shown under dark and under solar illumination.

Ligand type	Series resistance under dark (Ωcm^{-2})	Series resistance under solar illumination (Ωcm^{-2})
PbS@MPA	12.06	7.12
PbS@TGA	18.76	11.84
PbS@TLA	57.64	17.10
PbS@CPT	24.64	16.12

The series resistance values of the solar cells are consistent with their hole mobility values as higher hole mobility results in lower series resistance in solar cells.

3.3.5 Cap-V analysis

It has been shown that carrier transport in QD solar cells is dominated by the drift motion over diffusion in determining their photovoltaic figure of merits.[45] Free carrier concentration and dielectric constant play important roles in the formation of depletion width across the *n-p* junction. This prompts us to determine depletion width and carrier concentration in the respective PbS films treated with various ligands as they fundamentally control the photocarrier extraction process. Capacitance measurements at varied applied bias in the low-frequency region have widely been used for this purpose to characterize QD solar cells.[5,7,12] Capacitance of an *n-p* heterojunction solar cell can be written as

$$C = \frac{\varepsilon_0 \varepsilon_r A}{W_d} \quad \text{----------} \quad (3.3)$$

Where 'C' is the junction capacitance, 'ε_0' permittivity of air, 'ε_r'relative dielectric constant of PbS layer (determined from photo-CELIV measurement), 'A' area of the device, and 'W_d' is depletion width inside PbS.

The activated doping density of different ligand exchanged PbS active layer was determined from the $\frac{1}{C^2}$ vs. V plot using the following equation.

$$N_a = \frac{2}{A^2 q \varepsilon_m \varepsilon_0 \frac{dC^{-2}}{dV}} \text{ ; considering } N_a \ll N_d \text{ ---------- (3.4)}$$

Where 'N_a' is the acceptor density of PbS layer, 'N_d' is the donor density of TiO_2 layer, and 'q'is electronic charge. Depletion widths at zero bias are determined from the C-V plots (Figure 3.7a) using equation 3.3, and the free carrier densities are determined from the slope of the $1/C^2$ vs. V plots (Figure 3.7b), implying equation 3.4.[7] Depletion width is the highest for MPA treated PbS layer (Figure 3.7c), indicating the highest contribution from drift mediated photocarrier extraction among the ligands.

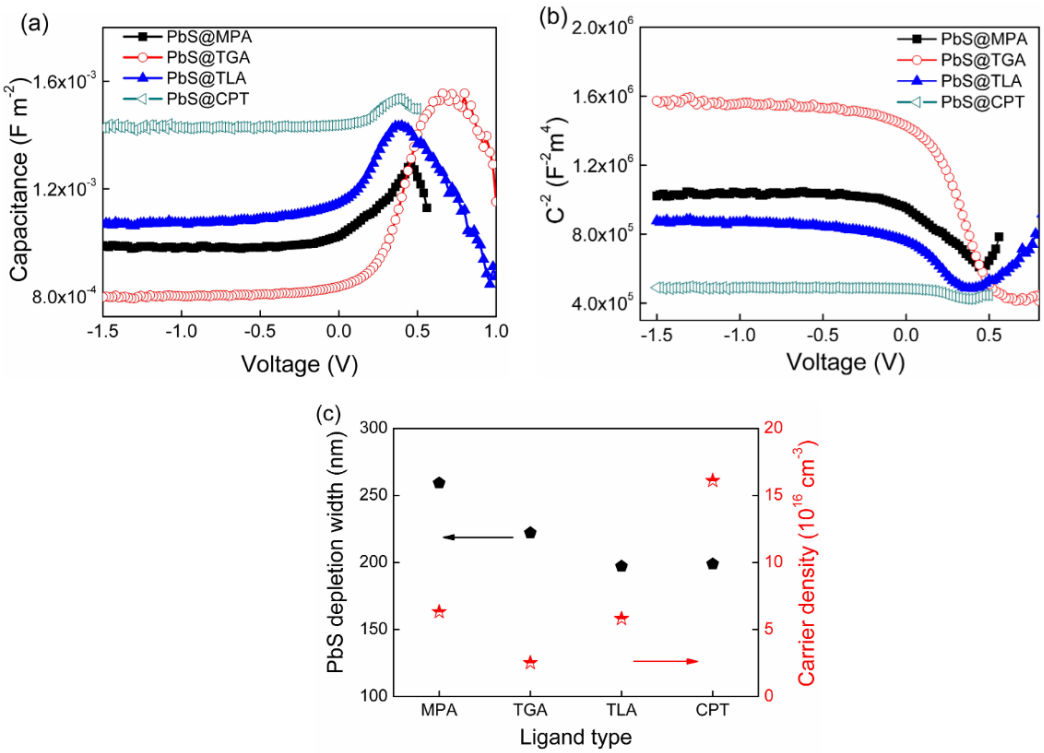

Figure 3.7: Capacitance-voltage (C-V) and $1/C^2$-V plots for solar cells treated with various ligands are shown in (a) and (b), respectively. Depletion width at zero bias and carrier density as determined from C-V and $1/C^2$-V plots for the PbS layers with different surface ligand types are shown in (c).

Maximum depletion width along with lowest carrier binding energy arising from the high dielectric constant of MPA treated PbS may have led to the highest short circuit current generation in their solar cell operation. On the other hand, TGA treated PbS layer shows the lowest free carrier density (Figure 3.7c), suggesting that TGA-treated PbS is the most

intrinsic in nature among the studied ligand types. The ascending order of carrier densities, as determined for PbS layers treated with various ligands (TGA<TLA<MPA<CPT), is in agreement with the trend in the open-circuit voltage generation for the respective solar cells (TGA>TLA>MPA>CPT). We surmise that incomplete/imperfect surface passivation leads to external doping and intermediate states in QD solid, which may result in Fermi energy pinning across the junction and loss in open-circuit voltage in solar cells.

3.3.6 Transient photovoltage and photocurrent study

Considering the incompetence of CPT ligand in photovoltaic operations (high carrier density and low open-circuit voltage generation), we exclude it from further studies of recombination processes in solar cells. Transient photovoltage and photocurrent

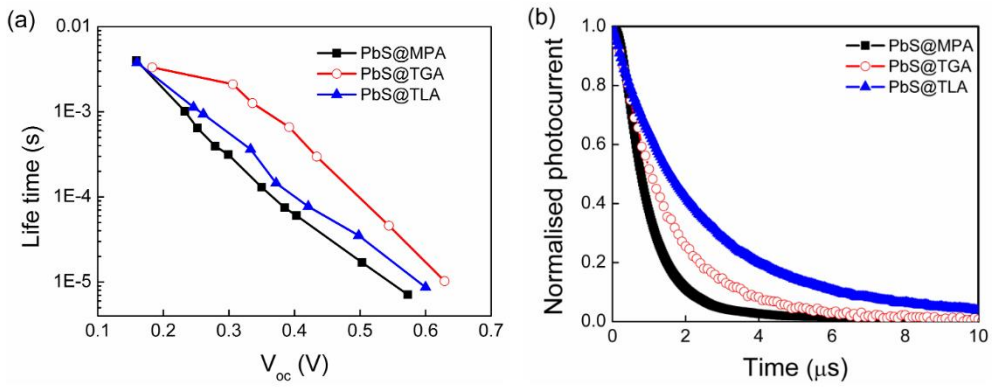

Figure 3.8: (a) Comparison of photocarrier lifetime for various ligand types as determined from transient photovoltage measurements. (b) Current transit times for various ligand types at short circuit condition.

measurements are employed to determine carrier lifetime and carrier transit time of solar cells to obtain a more vivid understanding of the underlying photovoltaic processes for the different ligands. Transient photovoltage measurements are carried out by biasing solar cells with white light to produce constant open-circuit voltage and simultaneously applying small perturbing light pulses to determine the charge carrier decay at open circuit condition.[2,22] Lifetime is determined by using the following equation,

$$\tau = -\frac{KT}{q}\frac{F_1}{\frac{dV_{oc}}{dt}} \quad \text{----------(3.5)}$$

Where 'τ' is photocarrier lifetime, 'K' is Boltzmann constant, 'T' is temperature, 'q' is the electronic charge, 'F_1' ranges between 1 at low injection and 2 at high injection. In this calculation, we used 'F_1' value one and T = 293 K. We have measured $\frac{dV_{oc}}{dt}$ from the initial linear slope of the voltage decay curve. Photocarrier lifetimes for MPA, TGA, and TLA treated PbS layers, as determined from open-circuit voltage decay measurements, are shown in Figure 3.8a. At any given V_{oc}, MPA or TLA treated PbS shows lower lifetime values compared to TGA treated PbS. This implies the recombination process is the slowest in TGA treated PbS layer. Carrier lifetime values determined from transient photovoltage measurements are consistent with the carrier density values from capacitance measurement as higher carrier density leads to faster recombination and lower lifetimes in QD solids. This further explains earlier observations that higher lifetimes generally yield higher open-circuit voltages in photovoltaic devices.[41] However, it is difficult to ascertain if the lifetime for different ligand types is limited by the bulk recombination inside the PbS layer or the interfacial recombination at the TiO_2-PbS interface. The knowledge of carrier lifetime, mobility, build-in potential, and depletion width as determined experimentally, enables us to estimate diffusion and drift lengths for PbS QD layers treated with different ligands (Table 3.3).[44] Carrier diffusion length (l_{diff}) under short-circuit condition is determined as

$$l_{diff} = \sqrt{\mu\tau KT/q} \quad (3.6)$$

where 'μ' is the hole mobility. We have calculated it at 0.9 sun illumination intensity.

The drift length (l_{drift}) is calculated by approximating the linearly varying electric field in the depletion region by its average value.

$$l_{drift} = \mu\tau V_{bi}/W \quad (3.7)$$

Where 'V_{bi}' is the built-in potential. V_{bi} is determined from the voltage at which J =(J_{light}-J_{dark}) =0. 'W' is the depletion at zero volt.

Both drift and diffusion length for MPA and TGA treated PbS layers are comparable, while the values are significantly low for TLA treated solar cells. Carrier transit times in photovoltaic devices are estimated from the transient photocurrent (TPC) decay measurements.[22] Transient photocurrent decay for the various ligand-based solar cells is shown in Figure 3.8b.

Table 3.3: Diffusion and drift lengths of PbS layer for different surface ligands.

Ligand type	Diffusion length (nm)	Drift length (µm)
PbS@MPA	105	1.3
PbS@TGA	105	1.35
PbS@TLA	38	0.19

Carrier transit times for MPA, TGA, and TLA are 1.1 µs, 1.7 µs, and 2.86 µs, respectively, in agreement with their respective mobility values. While high transport lengths facilitate photogenerated charge carrier extraction, high transit times increase the probability of photocarrier recombination inside solar cells. Drift length, diffusion length, and carrier transit time further explain similar short circuit current in MPA and TGA treated solar cells and lower current in TLA treated solar cells.

3.3.7 Intensity dependant J_{sc} & V_{oc} study

To elucidate the role of surface ligands on the charge generation-recombination process of solar cells, we have carried out incident photon intensity-dependent J_{sc} and V_{oc} generation of the studied photovoltaic devices. For the light intensity-dependent investigation, we have chosen monochromatic illumination at 635 nm. Photons at this wavelength have high penetration depth inside the PbS layer (extinction coefficient of PbS at long wavelength range is low) and are expected to excite the PbS thickness uniformly even at relatively lower intensities. In photovoltaic devices, the dependence of J_{sc} on light intensity (φ) is expressed as $J_{sc} \propto \varphi^p$, where p is the power exponent. p ~1 indicates generation limited current extraction, and p ~0.75 indicates space charge limited carrier extraction in solar cells.[46] Higher 'p' values (Figure 3.9a) in MPA (0.92) and TGA (0.93) treated devices indicate more balanced transport of photo-generated electrons and holes, which may lead to superior charge extraction in those solar cells. Diode ideality factor (η) is also known to carry important information regarding the photocarrier recombination process in a solar cell. The value of η is unity when the recombination process is determined by band-to-band recombination of photogenerated carriers, whereas the involvement of intermediate states in carrier recombination dynamics makes η greater than unity ($1 < \eta < 2$).[22,41]

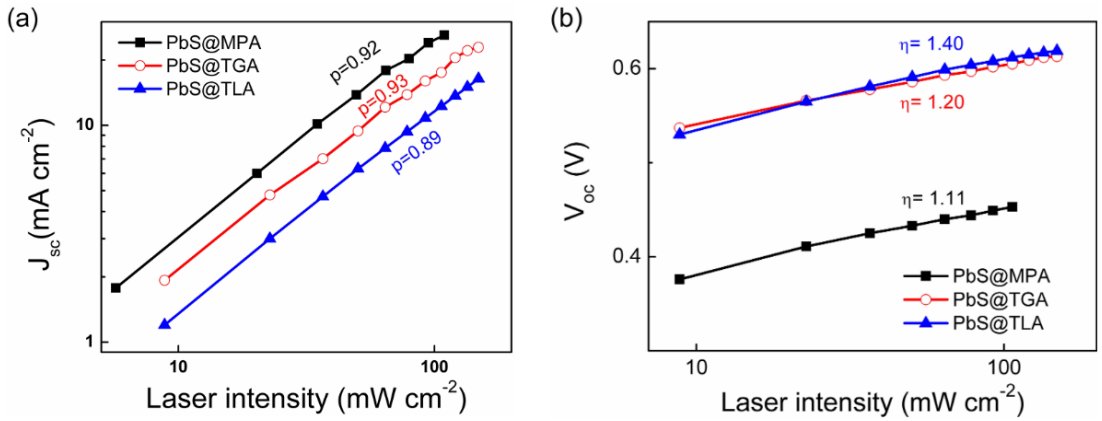

Figure 3.9: Intensity dependent (a) current density and (b) open-circuit voltage variation for solar cells treated with different ligands. Monochromatic illumination of 635 nm laser light is used for the intensity-dependent study.

Open circuit voltage of a solar cell depends with the light intensity through the following equation

$$V_{oc} = -\frac{p\eta KT}{q}\ln \emptyset + c \text{----------} (3.8)$$

Where $\emptyset$ is the light intensity, p is the power dependence of short circuit current density with light intensity ($J_{sc} \propto \varphi^p$), 'η' is the diode ideality factor, 'K' is Boltzmann constant, 'T' is temperature, 'q' is electronic charge and 'c' is the fitting parameter. From the slope of V_{oc} vs. ln ϕ, we determined the value of η at T=293K. Under 635 nm monochromatic laser illuminations, the estimated values of η are 1.11, 1.20, and 1.40 for MPA, TGA, and TLA treated photovoltaic devices, respectively (Figure 3.9b). This implies that trap-assisted recombination within the depletion layer of the PbS film is the lowest for MPA, intermediate for TGA, and the highest for TLA treated photovoltaic devices.

3.3.8 Temperature dependant V_{oc} study

Transient photovoltage measurement (Figure 3.8a) shows lower photocarrier lifetime for MPA treated solar cells as compared to TGA and TLA treated solar cells, despite the fact that MPA yields higher photocurrent. Photocarrier recombination in photovoltaic devices can happen in three possible regions inside the device, (i) recombination inside the bulk of the PbS layer, (ii) TiO_2-PbS interface recombination, and (iii) recombination inside TiO_2 and MoO_3 transport layers. We can ignore the lifetime contribution from the transport

layers due to the fact that they also act as filter layers for the hole and the electron (TiO_2 and MoO_3, respectively) and therefore are deprived of opposite charge carriers for recombination. However, interface recombination can play a critical role in determining the overall photocarrier lifetime in solar cells. In order to explicate the role of the TiO_2-PbS interface in the recombination process for the studied ligands, we have performed temperature-dependent characterization of J-V characteristics under illumination. In the case of a single thermally activated carrier generation-recombination mechanism, the open-circuit voltage of a solar cell can be expressed as[38,41,47]

$$V_{oc} = \frac{E_a}{q} - \frac{\eta KT}{q}\ln\left(\frac{J_{00}}{J_{sc}}\right) \quad (3.9)$$

where E_a is the activation energy, q is the electronic charge, J_{00} is the prefactor, and η is the diode ideality factor.

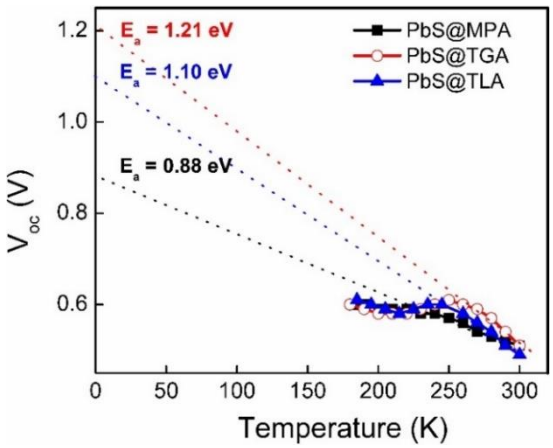

Figure 3.10: Temperature-dependent V_{oc} of photovoltaic devices for different ligand types measured at 1.5 A.M. solar illuminations is shown. Extrapolation of the high-temperature linear region of V_{oc} to determine E_a for various ligands are shown by dashed lines.

Two distinct regions are observed in the V_{oc} vs. T plots (Figure 3.10) for the solar cells. At the low-temperature range (<200 °K), open-circuit voltage seems to saturate with the decrease in temperature, whereas V_{oc} increases linearly with the decrease in temperature at the high-temperature range (>200 °K). The freezing of intermediate trap charges at low-temperature region could possibly make them ineffective to modulate quasi-Fermi levels of the PbS layer under illumination and therefore leads to saturation in V_{oc} generation.[41,47] At

the high-temperature range, where η, J_{00} and J_{sc} are independent of the temperature, extrapolation of V_{oc}-T plot to T= 0 K provides E_a. Activation energy bears a deep physical significance for the recombination processes in the solar cells. E_a, when equal to the band gap (E_g) of the PbS layer, implies dominance of band to band recombination, whereas lower values of the activation energy imply the significance of interfacial recombination.[38,41] As shown in Figure 3.10, $E_a$is 0.91 eV for MPA treated PbS layer, much lower than TGA and TLA ligands (1.18 eV). This suggests that high interfacial recombination of photocarriers at TiO_2 interface for MPA treated PbS possibly limits their lifetime values rather than the bulk of the PbS layer. Interfacial recombination at the TiO_2-PbS interface and the open-circuit voltage loss in TGA and TLA treated films are significantly lower. This result is crucial from the standpoint that open-circuit voltage loss has been reduced by smaller size passivating ligand.

3.3.9 Device stability

Further, while investigating the stability of different ligands in solar cell applications, it is observed that short-chain ligands show improved stability over MPA (Figure 3.11a).

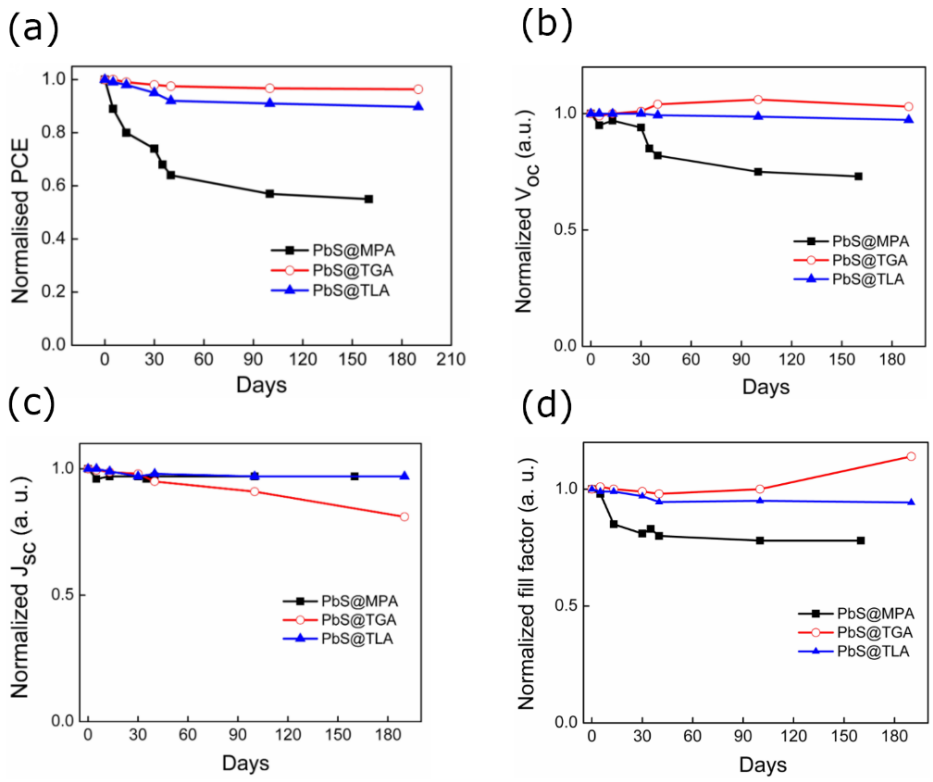

Figure 3.11: Stability of solar cells for different ligand passivation. (a) shows the evolution of normalized power conversion efficiency (PCE) with storing time for three ligands. Evolution of (b) V_{oc}, (c) J_{sc} and (d) fill factor (FF) with time is shown. V_{oc}, J_{sc}, and FF values are normalized for clear presentation.

During a period of 180 days, the power conversion efficiency of MPA treated samples reduced to 50% of its original value, whereas both TGA and TLA treated solar cells retain more than 90% of their pristine efficiency. The reduction of the individual parameter, V_{oc}, J_{sc}, and FF of solar cell devices are also presented in Figure 3.11 (b), (c), and (d), respectively.

3.3.10 XPS study

X-ray photoelectron spectroscopy (XPS) of PbS QD films passivated with the studied ligands has been carried out to better understand the surface properties. Since the ligands are anchored through the –SH group to the terminal Pb sites of the QD surface, we

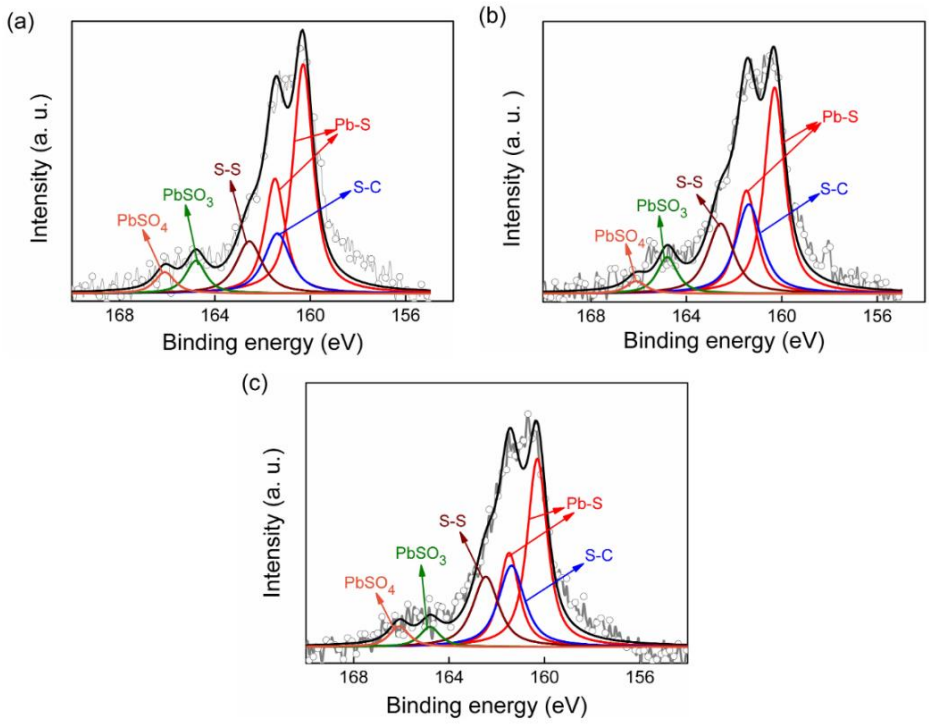

Figure 3.12: Comparison of XPS S 2p spectra for (a) MPA (b) TGA and (c) TLA passivated PbS QD films. Gray (scatter + line) represents the experimental data, and the black line represents the fitted experimental results. Peak positions corresponding to binding energy 160.30 eV and 161.48 eV are attributed (red) to the doublet splitting of S for PbS. Peaks at 161.38 eV (blue), 162.56 eV (wine line), 164.8 eV (olive), and 166.1 eV (orange) correspond to S-C bond, S-S bond, $PbSO_3$and $PbSO_4$ respectively.

focus on the S 2p XPS peaks to determine the surface properties. High-resolution XPS S 2p spectra for PbS QD films treated with MPA, TGA, and TLA are presented in Figure 3.12a-c, respectively. Deconvolution of S 2p spectra is carried out based on earlier published reports.[5,8,48] S 2p doublet peaks for Pb-S are fitted with a splitting energy difference of 1.18 eV and peak area ratio of 2:1. Further details of the XPS analysis are given in Table 3.4.

S-C and S-S peaks in the spectra arise from the bound thiol contribution of the surface ligands.[8] Thus, atomic percent determination of S-C and S-S would provide valuable

Table 3.4: XPS data analysis of S 2p spectra of PbS QD films treated with different ligands.

Ligand type	Species	Binding energy (eV)	Atomic %
PbS@MPA	Pb-S	160.3	63.3
	S-C	161.38	14.3
	S-S	162.56	12.4
	$PbSO_3$	164.8	6
	$PbSO_4$	166.1	3.9
PbS@TGA	Pb-S	160.3	54.7
	S-C	161.38	20.4
	S-S	162.56	16.1
	$PbSO_3$	164.8	6.4
	$PbSO_4$	166.1	2.2
PbS@TLA	Pb-S	160.3	54.3
	S-C	161.38	20.3
	S-S	162.56	17.5
	$PbSO_3$	164.8	3.9
	$PbSO_4$	166.1	3.9

information regarding surface coverage of different ligands on the PbS QD surface. Relative atomic percent of MPA, TGA, and TLA treated PbS films for S-C are 14.3%, 20.4%, and 20.3%, respectively, and that for S-S are 12.4%, 16.1%, and 17%, respectively. A Higher presence of S-C and S-S bond in PbS films for TGA and TLA ligands clearly suggests higher surface coverage for the ligands than MPA. Higher surface coverage could possibly originate from lower steric repulsion in the case of shorter ligands. XPS S 2p spectra also indicate the presence of $PbSO_3$ and $PbSO_4$ (or R-S=O) on PbS films. Relative atomic percent of the oxidative species for MPA, TGA, and TLA are 10%, 8.6%, and 7.8%, respectively, indicating higher oxidation in MPA-treated PbS samples. This is consistent with relative surface coverage (S-C and S-S) for the respective ligands, as higher coverage leads to better preservation and lower oxidation of PbS QD surface. This further explains higher stability

in TGA and TLA treated photovoltaic devices as higher ligand coverage inhibits degradation processes that originate from the ambient operation.

3.3.11 Thin film absorption & UPS study

It is observed and verified from complementary experimental techniques that shorter passivating ligands TGA and TLA yield higher open-circuit voltages than MPA.

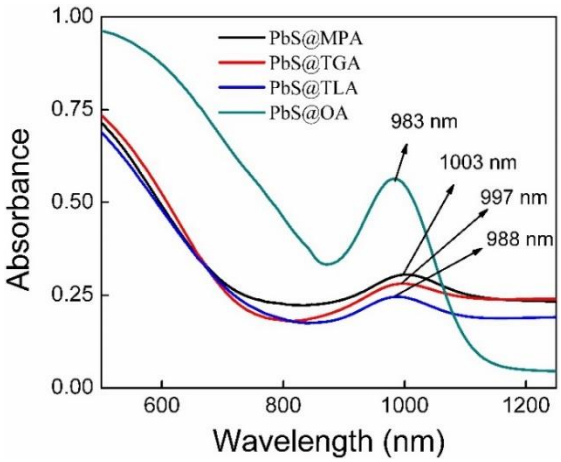

Figure 3.13: Absorption spectrums of PbS QD films treated with various surface ligands with as-synthesized oleic acid capped QDs.

Since the difference between the conduction band minimum of the *n*-type TiO_2 layer and the valence band maximum of the *p*-type PbS layer fundamentally controls the open-circuit voltage generation, we posit to determine the valance band and conduction band position of different ligand treated PbS QDs films from the absorption and ultraviolet photoelectron spectroscopic (UPS) studies. The thin-film absorption spectra for different ligands treated PbS QDs films are presented in Figure 3.13 for bandgap calculation. The full UPS spectra of different ligand treated films are shown in Figure 3.14a. The magnified portion of lower and higher binding energy ranges are shown in Figure 3.14b and 3.14c, respectively. The Fermi energy level (E_F) is calculated from the high binding-energy cut-off using the equation ($E_F = 21.22\ eV - E_{cut\ off}$). From the lower binding-energy cut-off, the difference between valance band edge and E_F is determined. Valance band position is then determined for different ligand treated PbS QDs. By implying the bandgap value from thin-film absorption spectroscopy, the conduction band position is also calculated. Figure 3.14d shows the conduction band and valence band position of PbS QD films treated with various

ligands. It can be seen that the valence band position of PbS QDs for different ligand types do not follow the trend of Voc generation in solar cell devices entirely; for example, TGA, despite having shallower valence band energy, produces higher V_{oc} than MPA. We attribute the V_{oc} generation to the interface (TiO_2/PbS) properties and electron trap formation in PbS QD film. Capacitance-voltage measurements and temperature-dependent V_{oc} results show MPA treated PbS possess the highest free carrier density and more pronounced trap mediated recombination at TiO_2/PbS interface. XPS study shows that MPA treated PbS film possess the highest amount of oxidative compounds in the form of $PbSO_3$ and $PbSO_4$ at its

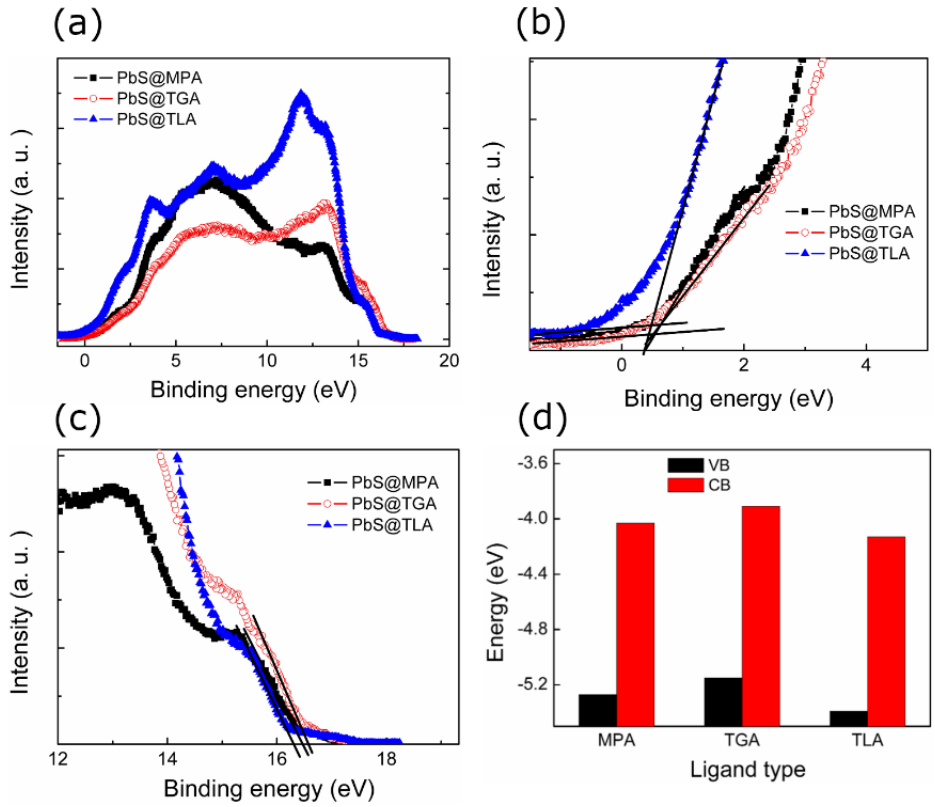

Figure 3.14: (a) shows the full energy range UPS spectra of PbS QD films for different ligands. (b) and (c) show the magnified view of secondary energy cut-off (SEC) and onset energy region, respectively. He-Iα radiation of energy 21.22 eV is used for the UPS measurement. (d) shows the valence band (VB) and conduction band (CB) positions as determined from absorption spectrum and UPS measurement.

surface, which is known to form electron trap states near the conduction band of PbS QD.[5] Therefore, we infer from the above observations that MPA treated films create the maximum

number of electron trap states, which limit the quasi-Fermi level splitting between electron and hole across the interface under illumination and results in the reduction in open-circuit voltage. The origin of photocurrent generation and fill factor for different ligand types have been explained by mobility, dielectric constant, depletion width, and diode ideality factor. The reason for the lower hole mobility and the lower dielectric constant of PbS QD films for short-chain ligands (TGA and TLA), as compared to MPA, however, is difficult to ascertain. Low hole mobility in TGA and TLA could possibly originate from higher hole trap density and trap energy distributions for holes (close to valence band) in their respective PbS QD films.[16,36] Shallow hole traps near the valence band edge may result in lowering the hole mobility due to continuous trapping and de-trapping and subsequent increase in carrier lifetime (Figure 3.8a). Observed dielectric constant values may be rooted in the different dielectric constant of the ligands and packing of QDs solids. Therefore, in designing new short-chain organic ligands, the relative dielectric constant of the ligand should be taken into consideration along with other prevailing factors.

3.4 Conclusion

In summary, we have investigated the photovoltaic figure of merits of PbS QD solar cells for various surface ligands with varied size and functionality. We have shown the non-trivial behavior of the decrease in hole mobility and dielectric constant with reduced ligand size for PbS QD solids. This underpins the importance of surface ligands in controlling the carrier transport properties of QD solids via trap state formation. We have shown shorter ligands can produce a higher open-circuit voltage in QD solar cells by diminishing surface oxidation and thereby eliminating electron trap states near the conduction band through a higher degree of surface passivation. Increased surface coverage for TGA and TLA leads to improve the stability of QD solar cells under ambient working conditions. Our study highlights the role of ligand chemistry to tune various electronic properties of QD solids like mobility, dielectric constant, and doping density through surface passivation, which would be valuable in designing new surface ligands for QD based electronic and optoelectronic applications.

3.5 References

(1) Luther, J. M.; Gao, J. B.; Lloyd, M. T.; Semonin, O. E.; Beard, M. C.; Nozik, A. J. Stability Assessment on a 3% Bilayer Pbs/Zno Quantum Dot Heterojunction Solar Cell. *Adv. Mater.* **2010**, *22*, 3704-3407.

(2) Ip, A. H.; Thon, S. M.; Hoogland, S.; Voznyy, O.; Zhitomirsky, D.; Debnath, R.; Levina, L.; Rollny, L. R.; Carey, G. H.; Fischer, A.; Kemp, K. W.; Kramer, I. J.; Ning, Z. J.; Labelle, A. J.; Chou, K. W.; Amassian, A.; Sargent, E. H. Hybrid Passivated Colloidal Quantum Dot Solids. *Nat. Nanotechnol.* **2012**, *7*, 577-582.

(3) Chuang, C. H. M.; Brown, P. R.; Bulovic, V.; Bawendi, M. G. Improved Performance and Stability in Quantum Dot Solar Cells through Band Alignment Engineering. *Nat. Mater.* **2014**, *13*, 796-801.

(4) Liu, M. X.; Voznyy, O.; Sabatini, R.; de Arquer, F. P. G.; Munir, R.; Balawi, A. H.; Lan, X. Z.; Fan, F. J.; Walters, G.; Kirmani, A. R.; Hoogland, S.; Laquai, F.; Amassian, A.; Sargent, E. H. Hybrid Organic-Inorganic Inks Flatten the Energy Landscape in Colloidal Quantum Dot Solids. *Nat. Mater.* **2017**, *16*, 258-263.

(5) Tang, J.; Brzozowski, L.; Barkhouse, D. A. R.; Wang, X. H.; Debnath, R.; Wolowiec, R.; Palmiano, E.; Levina, L.; Pattantyus-Abraham, A. G.; Jamakosmanovic, D.; Sargent, E. H. Quantum Dot Photovoltaics in the Extreme Quantum Confinement Regime: The Surface-Chemical Origins of Exceptional Air- and Light-Stability. *Acs Nano* **2010**, *4*, 869-878.

(6) Stavrinadis, A.; Pradhan, S.; Papagiorgis, P.; Itskos, G.; Konstantatos, G. Suppressing Deep Traps in Pbs Colloidal Quantum Dots Via Facile Iodide Substitutional Doping for Solar Cells with Efficiency >10%. *Acs Energy Lett.* **2017**, *2*, 739-744.

(7) Pattantyus-Abraham, A. G.; Kramer, I. J.; Barkhouse, A. R.; Wang, X. H.; Konstantatos, G.; Debnath, R.; Levina, L.; Raabe, I.; Nazeeruddin, M. K.; Gratzel, M.; Sargent, E. H. Depleted-Heterojunction Colloidal Quantum Dot Solar Cells. *Acs Nano* **2010**, *4*, 3374-3380.

(8) Cao, Y. M.; Stavrinadis, A.; Lasanta, T.; So, D.; Konstantatos, G. The Role of Surface Passivation for Efficient and Photostable Pbs Quantum Dot Solar Cells. *Nat. Energy* **2016**, *1*, 16035.

(9) Boles, M. A.; Ling, D.; Hyeon, T.; Talapin, D. V. The Surface Science of Nanocrystals. *Nat. Mater.* **2016**, *15*, 141-153.

(10) Kagan, C. R.; Lifshitz, E.; Sargent, E. H.; Talapin, D. V. Building Devices from Colloidal Quantum Dots. *Science* **2016**, *353*, 5523.

(11) Wang, R. L.; Shang, Y. Q.; Kanjanaboos, P.; Zhou, W. J.; Ning, Z. J.; Sargent, E. H. Colloidal Quantum Dot Ligand Engineering for High Performance Solar Cells. *Energy Environ. Sci.* **2016**, *9*, 1130-1143.

(12) Yuan, M. J.; Zhitomirsky, D.; Adinolfi, V.; Voznyy, O.; Kemp, K. W.; Ning, Z. J.; Lan, X. Z.; Xu, J. X.; Kim, J. Y.; Dong, H. P.; Sargent, E. H. Doping Control Via Molecularly Engineered Surface Ligand Coordination. *Adv. Mater.* **2013**, *25*, 5586-5592.

(13) Yuan, M. J.; Liu, M. X.; Sargent, E. H. Colloidal Quantum Dot Solids for Solution-Processed Solar Cells. *Nat. Energy* **2016**, *1*, 16016.

(14) Voznyy, O.; Zhitomirsky, D.; Stadler, P.; Ning, Z. J.; Hoogland, S.; Sargent, E. H. A Charge-Orbital Balance Picture of Doping in Colloidal Quantum Dot Solids. *Acs Nano* **2012,** *6*, 8448-8455.

(15) Zherebetskyy, D.; Scheele, M.; Zhang, Y. J.; Bronstein, N.; Thompson, C.; Britt, D.; Salmeron, M.; Alivisatos, P.; Wang, L. W. Hydroxylation of the Surface of Pbs Nanocrystals Passivated with Oleic Acid. *Science* **2014**, *344*, 1380-1384.

(16) Jeong, K. S.; Tang, J.; Liu, H.; Kim, J.; Schaefer, A. W.; Kemp, K.; Levina, L.; Wang, X. H.; Hoogland, S.; Debnath, R.; Brzozowski, L.; Sargent, E. H.; Asbury, J. B. Enhanced Mobility-Lifetime Products in Pbs Colloidal Quantum Dot Photovoltaics. *Acs Nano* **2012**, *6*, 89-99.

(17) Brown, P. R.; Kim, D.; Lunt, R. R.; Zhao, N.; Bawendi, M. G.; Grossman, J. C.; Bulovic, V. Energy Level Modification in Lead Sulfide Quantum Dot Thin Films through Ligand Exchange. *Acs Nano* **2014**, *8*, 5863-5872.

(18) Ning, Z. J.; Voznyy, O.; Pan, J.; Hoogland, S.; Adinolfi, V.; Xu, J. X.; Li, M.; Kirmani, A. R.; Sun, J. P.; Minor, J.; Kemp, K. W.; Dong, H. P.; Rollny, L.; Labelle, A.; Carey, G.; Sutherland, B.; Hill, I. G.; Amassian, A.; Liu, H.; Tang, J.; Bakr, O. M.; Sargent, E. H. Air-Stable N-Type Colloidal Quantum Dot Solids. *Nat. Mater.* **2014**, *13*, 822-828.

(19) Sytnykt, M.; Yakunin, S.; Schofberger, W.; Lechner, R. T.; Burian, M.; Ludescher, L.; Killilea, N. A.; YousefiAmin, A.; Kriegner, D.; Stangl, J.; Groiss, H.; Heiss, W. Quasi-Epitaxial Metal-Halide Perovskite Ligand Shells on Pbs Nanocrystals. *Acs Nano* **2017**, *11*, 1246-1256.

(20) Tang, J. A.; Sargent, E. H. Infrared Colloidal Quantum Dots for Photovoltaics: Fundamentals and Recent Progress. *Adv. Mater.* **2011**, *23*, 12-29.

(21) Ning, Z. J.; Ren, Y.; Hoogland, S.; Voznyy, O.; Levina, L.; Stadler, P.; Lan, X. Z.; Zhitomirsky, D.; Sargent, E. H. All-Inorganic Colloidal Quantum Dot Photovoltaics Employing Solution-Phase Halide Passivation. *Adv. Mater.* **2012**, *24*, 6295-6299.

(22) Pradhan, S.; Stavrinadis, A.; Gupta, S.; Bi, Y.; Di Stasio, F.; Konstantatos, G. Trap-State Suppression and Improved Charge Transport in Pbs Quantum Dot Solar Cells with Synergistic Mixed-Ligand Treatments. *Small* **2017**, *13*, 1700598.

(23) Wang, H. I.; Lu, H.; Nagata, Y.; Bonn, M.; Cánovas, E. Dipolar Molecular Capping in Quantum Dot-Sensitized Oxides: Fermi Level Pinning Precludes Tuning Donor–Acceptor Energetics. *ACS Nano* **2017**, *11*, 4760-4767.

(24) Shim, M.; Guyot-Sionnest, P. N-Type Colloidal Semiconductor Nanocrystals. *Nature* **2000**, *407*, 981-983.

(25) Oh, S. J.; Kim, D. K.; Kagan, C. R. Remote Doping and Schottky Barrier Formation in Strongly Quantum Confined Single Pbse Nanowire Field-Effect Transistors. *ACS Nano* **2012**, *6*, 4328-4334.

(26) Kirmani, A. R.; Kiani, A.; Said, M. M.; Voznyy, O.; Wehbe, N.; Walters, G.; Barlow, S.; Sargent, E. H.; Marder, S. R.; Amassian, A. Remote Molecular Doping of Colloidal Quantum Dot Photovoltaics. *Acs Energy Lett.* **2016**, *1*, 922-930.

(27) Choi, J. J.; Bealing, C. R.; Bian, K. F.; Hughes, K. J.; Zhang, W. Y.; Smilgies, D. M.; Hennig, R. G.; Engstrom, J. R.; Hanrath, T. Controlling Nanocrystal Superlattice Symmetry and Shape-Anisotropic Interactions through Variable Ligand Surface Coverage. *J. Am. Chem. Soc.* **2011**, *133*, 3131-3138.

(28) Giansante, C.; Infante, I.; Fabiano, E.; Grisorio, R.; Suranna, G. P.; Gigli, G. "Darker-Than-Black" Pbs Quantum Dots: Enhancing Optical Absorption of Colloidal Semiconductor Nanocrystals Via Short Conjugated Ligands. *J. Am. Chem. Soc.* **2015**, *137*, 1875-1886.

(29) Debellis, D.; Gigli, G.; Brinck, S.; Infante, I.; Giansante, C. Quantum-Confined and Enhanced Optical Absorption of Colloidal Pbs Quantum Dots at Wavelengths with Expected Bulk Behavior. *Nano Lett.* **2017**, *17*, 1248-1254.

(30) Liu, Y.; Gibbs, M.; Puthussery, J.; Gaik, S.; Ihly, R.; Hillhouse, H. W.; Law, M. Dependence of Carrier Mobility on Nanocrystal Size and Ligand Length in PbSe Nanocrystal Solids. *Nano Lett.* **2010**, *10*, 1960-1969.

(31) Klem, E. J. D.; Shukla, H.; Hinds, S.; MacNeil, D. D.; Levina, L.; Sargent, E. H. Impact of Dithiol Treatment and Air Annealing on the Conductivity, Mobility, and Hole Density in PbS Colloidal Quantum Dot Solids. *Appl. Phys. Lett.* **2008**, *92*, 212105.

(32) Koh, W. K.; Saudari, S. R.; Fafarman, A. T.; Kagan, C. R.; Murray, C. B. Thiocyanate-Capped Pbs Nanocubes: Ambipolar Transport Enables Quantum Dot Based Circuits on a Flexible Substrate. *Nano Lett.* **2011**, *11*, 4764-4767.

(33) Scheele, M.; Hanifi, D.; Zherebetskyy, D.; Chourou, S. T.; Axnanda, S.; Rancatore, B. J.; Thorkelsson, K.; Xu, T.; Liu, Z.; Wang, L.-W.; Liu, Y.; Alivisatos, A. P. Pbs Nanoparticles Capped with Tetrathiafulvalenetetracarboxylate: Utilizing Energy Level Alignment for Efficient Carrier Transport. *ACS Nano* **2014**, *8*, 2532-2540.

(34) Zhitomirsky, D.; Voznyy, O.; Levina, L.; Hoogland, S.; Kemp, K. W.; Ip, A. H.; Thon, S. M.; Sargent, E. H. Engineering Colloidal Quantum Dot Solids within and Beyond the Mobility-Invariant Regime. *Nat. Commun.* **2014**, *5*, 3803.

(35) Zhang, J.; Tolentino, J.; Smith, E. R.; Zhang, J.; Beard, M. C.; Nozik, A. J.; Law, M.; Johnson, J. C. Carrier Transport in Pbs and Pbse Qd Films Measured by Photoluminescence Quenching. *J. Phys. Chem. C* **2014**, *118*, 16228-16235.

(36) Chang, J.; Ogomi, Y. H.; Ding, C.; Zhang, Y. H.; Toyoda, T.; Hayase, S.; Katayama, K.; Shen, Q. Ligand-Dependent Exciton Dynamics and Photovoltaic Properties of Pbs Quantum Dot Heterojunction Solar Cells. *Phys. Chem. Chem. Phys.* **2017**, *19*, 6358-6367.

(37) Tang, J.; Kemp, K. W.; Hoogland, S.; Jeong, K. S.; Liu, H.; Levina, L.; Furukawa, M.; Wang, X. H.; Debnath, R.; Cha, D. K.; Chou, K. W.; Fischer, A.; Amassian, A.; Asbury, J. B.; Sargent, E. H. Colloidal-Quantum-Dot Photovoltaics Using Atomic-Ligand Passivation. *Nat. Mater.* **2011**, *10*, 765-771.

(38) Rath, A. K.; de Arquer, F. P. G.; Stavrinadis, A.; Lasanta, T.; Bernechea, M.; Diedenhofen, S. L.; Konstantatos, G. Remote Trap Passivation in Colloidal Quantum Dot Bulk Nano-Heterojunctions and Its Effect in Solution-Processed Solar Cells. *Adv. Mater.* **2014**, *26*, 4741-4747.

(39) Mandal, D.; Goswami, P. N.; Rath, A. K. Colossal Photo-Conductive Gain in Low Temperature Processed TiO_2 Films and Their Application in Quantum Dot Solar Cells. *Appl. Phys. Lett.* **2017**, *110*, 123902.

(40) Ip, A. H.; Kiani, A.; Kramer, I. J.; Voznyy, O.; Movahed, H. F.; Levina, L.; Adachi, M. M.; Hoogland, S.; Sargent, E. H. Infrared Colloidal Quantum Dot Photovoltaics Via Coupling Enhancement and Agglomeration Suppression. *Acs Nano* **2015**, *9*, 8833-8842.

(41) Chuang, C.-H. M.; Maurano, A.; Brandt, R. E.; Hwang, G. W.; Jean, J.; Buonassisi, T.; Bulović, V.; Bawendi, M. G. Open-Circuit Voltage Deficit, Radiative Sub-Bandgap States, and Prospects in Quantum Dot Solar Cells. *Nano Lett.* **2015**, *15*, 3286-3294.

(42) Law, M.; Beard, M. C.; Choi, S.; Luther, J. M.; Hanna, M. C.; Nozik, A. J. Determining the Internal Quantum Efficiency of Pbse Nanocrystal Solar Cells with the Aid of an Optical Model. *Nano Lett.* **2008**, *8*, 3904-3910.

(43) Mozer, A. J.; Sariciftci, N. S.; Lutsen, L.; Vanderzande, D.; Osterbacka, R.; Westerling, M.; Juska, G. Charge Transport and Recombination in Bulk Heterojunction Solar Cells Studied by the Photoinduced Charge Extraction in Linearly Increasing Voltage Technique. *Appl. Phys. Lett.* **2005**, *86*, 112104.

(44) Johnston, K. W.; Pattantyus-Abraham, A. G.; Clifford, J. P.; Myrskog, S. H.; Hoogland, S.; Shukla, H.; Klem, J. D.; Levina, L.; Sargent, E. H. Efficient Schottky-Quantum-Dot Photovoltaics: The Roles of Depletion, Drift, and Diffusion. *Appl. Phys. Lett.* **2008**, *92*, 122111.

(45) Lan, X. Z.; Masala, S.; Sargent, E. H. Charge-Extraction Strategies for Colloidal Quantum Dot Photovoltaics. *Nat. Mater.* **2014**, *13*, 233-240.

(46) Zhao, N.; Osedach, T. P.; Chang, L. Y.; Geyer, S. M.; Wanger, D.; Binda, M. T.; Arango, A. C.; Bawendi, M. G.; Bulovic, V. Colloidal PbS Quantum Dot Solar Cells with High Fill Factor. *Acs Nano* **2010**, *4*, 3743-3752.

(47) Speirs, M. J.; Dirin, D. N.; Abdu-Aguye, M.; Balazs, D. M.; Kovalenko, M. V.; Loi, M. A. Temperature Dependent Behaviour of Lead Sulfide Quantum Dot Solar Cells and Films. *Energy Environ. Sci.* **2016**, *9*, 2916-2924.

(48) Castner, D. G.; Hinds, K.; Grainger, D. W. X-Ray Photoelectron Spectroscopy Sulfur 2p Study of Organic Thiol and Disulfide Binding Interactions with Gold Surfaces. *Langmuir* **1996**, *12*, 5083-5086.

Chapter 4

Butylamine catalyzed 2D matrix engineering on quantum dot surface for solar cell application

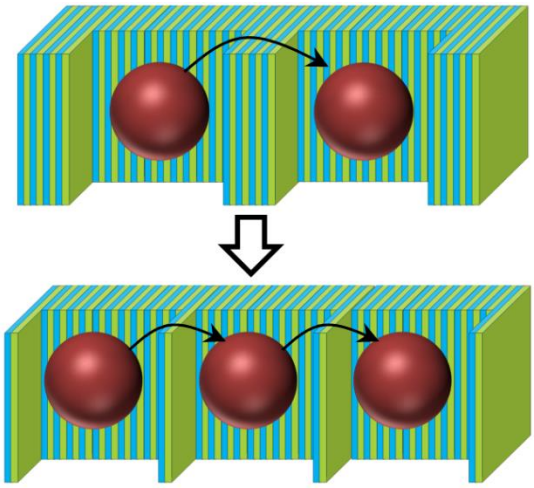

Abstract:

Colloidal quantum dots (QDs) have emerged as a promising material to harness panchromatic solar light, owing to their size-tunable optoelectronic properties. Advancements in surface passivation strategy and processing techniques have contributed immensely to their developments in photovoltaic applications. Recently, surface passivation using halometallate ligands is shown to form a protective shell layer in reducing the structural and energetic disorder in the QD solid. In this chapter, we report lead sulfide (PbS) QDs coupled to oriented two-dimensionally (2D) confined crystalline matrix by using halometallate ligand. The QDs undergo surface reconstruction during the ligand treatment process, which leads to change in shape, size, and axis length of PbS QDs. We show that the 2D matrix is a combination of two distinct crystalline layers consists of crystalline Pb-amine complex and 2D perovskite layer. The thickness of the matrix layer is modulated further by adjusting counter cation, which results in the enhancement in charge carrier mobility, carrier recombination lifetime, and diffusion length in QD solid. 2D passivated QDs are implemented to fabricate the photovoltaic devices with a high-power conversion efficiency of 9.1%.

4.1 Introduction

Size-tunable energy bandgap and monodispersity of colloidal QDs make them promising building blocks for the development of solar cells.[1-4] The power conversion efficiency (PCE) of QD solar cells has grown steadily over time due to advancements in device engineering[2,3,5], and surface chemistry.[6-9] In view of the high surface to volume ratio in nano-dimension materials, the surface plays a pivotal role in determining the electronic properties of the QDs.[10] The unsaturated terminal atoms are vulnerable to QD fusion, which would compromise the monodispersity to increase the energy disorder in solid films.[4,10] The under-coordinated surface atoms often lead to intermediate trap states inside the QD bandgap via oxidation or dangling bond formation.[11,12] Surface passivation using long-chain ligands or core/shell formation helps to attain monodispersity and clean energy band gap at the cost of charge carrier transport in QD films.[13] Post-processing of QD films using short-chain ligand exchange process enhances the conductivity by orders of magnitude[14] which have been implemented to develop photovoltaic devices using layer by layer (LBL) film growth process.[15-17] Besides the fact that LBL is a time-consuming and wasteful process for QDs and solvents, it further promotes in-homogeneity in QD films through random packing and heterogeneous aggregation. The inhomogeneous QD diffusion leads to site energy disorder, which inhibits the carrier transport process and limits the open-circuit voltage generation in QD solar cells.[18-20] The solution-based ligand exchange using halometallate ($MAPbI_3$, $KPbI_3$ $CsPbI_3$, PbI_3^-) ligands[21-24] has attracted significant attention in the recent past as it provides homogeneous surface passivation,[25] improved packings,[7] and deposition of thick conducting QD film from the one-step spin-coating process.[7,21] Striking progress of methylammonium lead iodide ($MAPbI_3$) perovskite material in solar cells,[26,27] acts as a catalyst for their implementation as the first halometallate ligand[21] to passivate the QD surface. It is shown that both $MAPbI_3$ and PbS quantum dots possess similar crystal structure (tetragonal and cubic respectively), comparable axis length ($MAPbI_3$: a= 6.26 Å; PbS: a= 5.94 Å), and low interfacial energy (10 meV $Å^{-2}$) which allow the room temperature epitaxial growth of 3D $MAPbI_3$ on PbS QD surface.[25,28] Counter cations ($CH_3NH_3^+$ and Cs^+), compatible to form 3D perovskite with lead iodide (PbI_2) have been tested to develop hybrid ($MAPbI_3$) and inorganic ($CsPbI_3$) perovskite protecting shell layer for PbS QD.[21,24] It is, however, shown that high bandgap perovskite shell forms type-I band alignment with the QD.[24] Therefore, a thick shell layer is likely to deter the carrier transport in QD film. This could be a reason for the low short circuit current in $MAPbI_3$[21] (21.8 mA cm^{-2}) and $CsPbI_3$[24]

(24.5 mA cm^{-2}) shelled PbS QD solar cells. Significant improvement in solar cell performance is achieved when the PbS QD surface is passivated by $[PbX_3]^-/[PbX]^+$ (X-halide) with the aid of a small amount of ammonium acetate.[7] Not many efforts have been dedicated to controlling the perovskite shell growth until recently, where a 2D layer matrix has been formed by using a longer chain hybrid–amine mixture to achieve a record PCE of 12% and short circuit current of 30 mA cm^{-2} in PbS QDs based solar cells.[8] It is reported widely in the literature[21,24,25,28] that the structure and growth of perovskite crystals are critically dependent on the size of the counter cation. In general, 3D Pb halide perovskite is represented by formula ($APbX_3$), where A- is the counter cation and X is a halide anion. The size of the A cation should be such that it fits in the space created by metal halide octahedral. The formation of perovskite crystal is governed by the Goldschmidt tolerance factor (t), as give below,

$$(R_A+R_X) = t\sqrt{2}\,(R_{Pb} + R_X)$$

R_A, R_{Pb} are radii of A and Pb Cation, R_X is the Radii of the halide anion.

Typically, the value of 't' should be close to 1 for a stable perovskite structure. In this regard, the A-site cation can be either inorganic (Cs, Rb, etc.) or organic (methylammonium, formamidinium, etc.). Typically, in a 3-dimensional networked (3DN) perovskite structure, all corners are connected or shared within the $[PbX_6]^{4-}$ octahedra and extends overall dimensions. The A-site cation occupies the space created by the Pb halide octahedra (provides overall negative charge) with appropriate valence state and upholds the structure with strong electrostatic interaction within themselves. Increasing the cationic size with suitable organic ammonium ion can lead to disconnection in the octahedral connections and subsequently generates lower-dimensional organic-inorganic hybrid perovskite. When the linear chain amine (like butylamine, hexylamine) is introduced, those amine does not fit in the space created by $[PbX_6]^{4-}$octahedra due to their high 't' values. As a result, the 3DN are broken along specific crystallographic planes to produce lower dimensional perovskite crystals. Long-chain linear amines (BA or HA) are reported to form 2D perovskite network. The 2D confinement prevents the thick shell growth from improving the QD packing and carrier transport properties to record the highest reported efficiency in QD solar cells to date. Therefore, we believe that further investigation on the halometallate passivation and shell growth strategy would be beneficial for the development of QD solar cells.

We reason that favorable Goldschmidt tolerance factor for MA^+ ion (t= 0.88) facilitate thick 3D $MAPbI_3$ perovskite shell growth over PbS QDs.[25,27] By replacing MA^+ (ionic radius=2.17 Å) with smaller ammonium ion (NH_4^+) (ionic radius= 1.43 Å) will reduce the tolerance factor to 0.72 which may prevent the 3D growth of the perovskite layer. Further, the AI would be more favorable than the MAI in the removal of the longer chain oleic acid from the QD surface due to its more reactive ammonium proton.[29] The ligand exchange process for the QDs is carried out with the subtle modifications of the earlier reported process of 3D perovskite shelling[21] (please see the experimental section for details). Typically, ligand exchange is a two-step process. In the first step, lead halide (3:1 combination of PbI_2 and $PbBr_2$) and ammonium iodide (AI) (or MAI) are dissolved in equimolar ratios (0.1mol/L) in DMF. The octane solution of oleic acid (OA) capped PbS QDs (15 mg/mL) are mixed with the ligand solution and shake for few minutes until the QDs are transferred to the DMF phase. This is followed by the precipitation of QDs from the DMF phase using solvent-anti solvent approach by toluene. In the second step, the isolated QDs are re-dispersed in volatile butylamine (BA) solvent to form concentrated QD ink for one step film deposition. Finally, the deposited films are annealed at 70°C for fifteen minutes for their optimum solar cell performance.

Herein, we show the photovoltaic application of the PbS QDs coupled to the 2D crystalline matrix. The halometallate ligand use for the solution-phase ligand exchange leads to the surface reconstruction of PbS QDs; size, shape, and axis length alters notably as a result. The amine solvent (BA in this case) used for the final dispersion of the halometallate treated QDs, plays an active role in the 2D confinement of the matrix layer during the film solidification process. The matrix layer is shown to consist of two 2D crystalline components, which are identified to be Pb-amine complex and $(BA)_2PbI_4$ perovskite layer. Both the components show long-range crystal ordering in the QD film. Multilayer growth of the 2D matrix along z-direction is strongly influenced by the choice of the counter cation. Replacing MAI with AI in the ligand exchange process deters the thick shell growth to improve QD packing in thin films. Subsequently, carrier transport in QDs coupled to the thinner 2D matrix increases to yield higher performances in solar cells. Since the lead halide is common for both the ligand treatments, AI and MAI are represented for the lead halide + AI, and lead halide + MAI treated PbS QDs for the rest of the report.

4.2 Experimental Details

4.2.1 ZnO nanocrystals preparation:

ZnO nanocrystals were synthesized following a previously reported method.[5] 2.95 gm zinc acetate dihydrate was dissolved in 125 mL methanol under stirring, and the reaction temperature was set at 60°C. In the meantime, in a separate beaker, 1.48 g KOH was dissolved in 65 mL methanol, and then the prepared KOH solution was added dropwise to the zinc acetate and methanol solution for a period of 10 minutes. The reaction conditions were remained unchanged for 2.5 hours. After completion of the reaction, the solution was allowed to cool down gradually to room temperature. Then ZnO nanocrystals solution was directly centrifuged at 4500 rpm for 5 min. The supernatants were discarded, and some amount of methanol was added and centrifuged again. This procedure was followed another three times and finally dispersed in 10% butylamine toluene mixture (100mg/mL) for deposition of the electron transporting layer.

4.2.2 Synthesis of Colloidal PbS QDs

Oleic acid capped PbS QDs were synthesized by the previously reported method with slight modification.[5] Octadecene was degassed under vacuum for 12 hrs prior to use in synthesis. PbO (0.45gm, 2mmol), 1.5 mL oleic acid (4.75mmol), and 3mL Octadecene were mixed in 3 neck flask and kept under vacuum at 95°C for 16 hours using a standard Schlenk line. After degassing, the lead oleate complex was formed, and the reaction condition was changed from vacuum to Ar Atmosphere. The reaction temperature was changed from 95°C to 120°C. 210µL $(TMS)_2S$ (1mmol) in 10 mL Octadecene was injected, and the solution color was immediately changed to brown. The reaction bath was allowed to cool down to 35°C naturally for approximately two hours. QDs were precipitated by injecting 30 mL acetone and centrifuged at 3500RPM. The nanocrystals were dispersed in toluene, again precipitated by acetone, centrifuged, and redissolved by anhydrous octane (15mg/mL) for ligand exchange to make *n*-type QD ink. For *p*-type PbS, QD was further cleaned approximately six to seven times by methanol and finally dispersed in octane (45mg/mL).

4.2.3 Ligand exchange of PbS QDs:

The QD solution (15mg/mL) was prepared in anhydrous octane for halometallate ligand treatment. The solution-phase ligand exchange process developed for $MAPbI_3$ was modified for the QD treatment in this study.[21] Typically, 0.1M NH_4I (or 0.1M CH_3NH_3I),

0.075M PbI_2 and 0.025M $PbBr_2$ are added to 5mL of DMF to get a clear transparent yellow color ligand solution. 5mL of PbS QDs solution was mixed with the DMF solution and vortexed for two minutes to transfer the PbS QDs from octane to DMF phase. Within two minutes, PbS QDs were transferred from octane to DMF phase. The top octane supernatant layer was discarded, and the QD solution was cleaned another three times using octane. The ligand exchanged QDs were precipitated from the DMF phase by adding 2.5 mL toluene and collected by centrifugation at 3500 RPM. The precipitated QDs were dried under vacuum for 20 minutes and finally disperse in BA (200mg/mL) for film fabrication.

4.2.4 Device Fabrication

ITO substrates were cleaned before ZnO NCs deposition by following the previously mentioned procedure in section 2.2.4.

Pre-synthesized ZnO NCs (100 mg/mL) were spin-coated from 10% butylamine: 90% toluene mixture solution on top of cleaned ITO substrates at 3500 RPM, and the substrates were heated at 250°C for 40 minutes. The BA solution of QD ink was spin-coated on the ZnO substrate for the deposition of a thick QD layer. The rotation and the acceleration speed were varied to change the film thickness from 180 nm to 360 nm. The films were then annealed at 70°C for fifteen minutes inside an argon glove box. For the hole transport layer formation, two layers of 1,2 ethanedithiol (EDT) treated PbS QD films were deposited using the layer-by-layer approach. Typically, OA-capped PbS QD solution (45 mg/mL) from octane was spin-coated (2500 RPM) followed by soaking in EDT solution (0.02 vol% in acetonitrile) for the 20s and washing two times using acetonitrile under rotation. 8 nm of MoO_3, 30 nm of Au, and 100 nm of Ag were deposited sequentially using a thermal evaporator (HHV BC-300) at the base pressure of 1 x 10^{-6} Torr.

4.2.5 Materials Characterization Techniques

Optical absorption measurements were carried out using a Shimadzu UV-Vis-NIR-3600 Plus spectrophotometer. Total absorption of thin films was measured with the help of an integrating sphere (ISR-603) attached to the instrument. Steady-state photoluminescence measurements were performed utilizing a spectrofluorometer FS5, Edinburgh Instruments. IR absorption spectra of the solution were recorded on an FTIR spectrometer (Vertex-70, Bruker) with 2 cm^{-1} resolution at room temperature. ATR-FTIR spectra of thin films were obtained on a Perkin Elmer Spectrum Two-Spectrophotometer, in the 4000–400 cm^{-1}

wavelength range with a resolution of 4 cm^{-1}. XRD profiles were recorded on an X'pert Pro model PANalytical diffractometer from Philips PANalytical instruments operated at a voltage of 40 kV and a current of 30 mA with Cu Kα (1.5418 Å) radiation. The QDs and ligand samples were scanned for the 2θ range of 4° to 60° with a scan rate of 0.4° per minute. The XPS was carried out using the thermo scientific K-Alpha+ spectrometer in ultrahigh vacuum condition (10^{-9} mbar). XPS measurements were performed with a monochromatic Al Kα X-ray source (1486.6 eV) with a pass energy of 50 eV for individual core levels. The XPS spectras were calibrated to the C1s peak at a binding energy of 284.8 eV. The fitting of the XPS spectra was performed using Casa XPS software. All the measurements were carried out using an electron flood gun source for surface charge neutralization. Cross-sectional and surface images of the device were taken by field emission scanning electron microscope (FESEM NNS 450). High-resolution images of QDs were captured by high resolution transmitted electron microscope (HRTEM, JEOL JEM 2200FES).

4.2.6 Device Characterization Techniques

J-V, EQE, and transient measurements (TPV and TPC) were followed by previously reported methods in sections 2.2.6.1, 2.2.6.3, and 3.2.4.4.

4.2.6.1 Bias dependant Transient Photocurrent measurement

Charge carrier mobility was determined by bias dependent photocurrent transient technique. A pulse laser diode (Newport LQA658-30C) controlled through a function generator (Tektronics, AFG 3021C) was used to create the light pulse of 500 ns. The device under test was excited by the short pulses at the light bias of one sun (solar simulator PEC-L01). Different electrical bias was applied to the device through the in-built function generator of the oscilloscope (Tektronics, MDO 3104). The transient signal from the device was measured across a 50Ω resistance using the same oscilloscope.

4.3 Results and Discussions

4.3.1 XRD analysis

X-ray diffraction (XRD) pattern of AI and MAI treated PbS QD films annealed at 70°C (represented as AI-70°C and MAI-70°C, respectively) are shown in Figure 4.1. The XRD peaks at 2θ value 25.45° and 29.48° are originated from (111) and (200) planes, confirms the presence of PbS QDs in the film.[30,31] In addition to PbS diffraction peaks, multiple sharp peaks are visible in their XRD pattern.

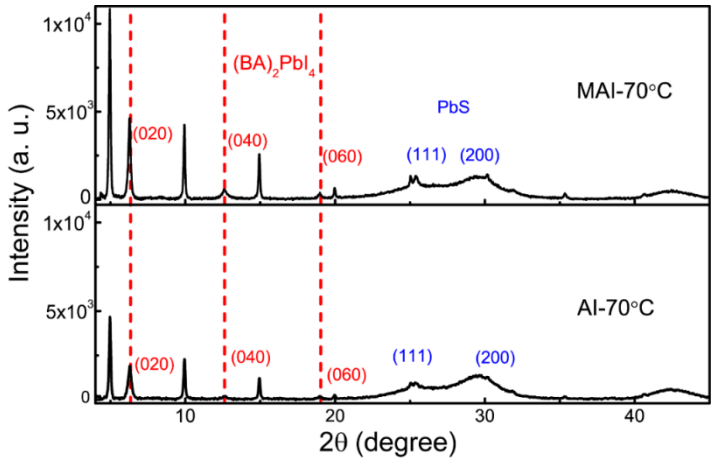

Figure 4.1: XRD pattern of the annealed (70°C) PbS QD film treated with AI and MAI. The peak positions correspond to PbS and $(BA)_2PbI_4$ are marked in blue and red color, respectively.

A closer look reveals that there are two sets of equidistant peaks with the repetition of 4.99° and 6.35° 2θ values run through their XRD spectrums. The equidistant sharp peaks are the signature of the 2D confined crystalline matrix. In Figure 4.1, the peak intensity for the PbS (200) planes is normalized for AI-70°C and MAI-70°C films for their ready comparison. Peak intensities correspond to 2D layer structures are more than two times higher in MAI-70°C, implying that for a fixed PbS QD film thickness, 2D matrix thickness in MAI-70°C film is higher than AI-70°C film. Surprisingly, the equidistant peaks with the repetition of 6.35° identically match with the 2D $(BA)_2PbI_4$ perovskite orthorhombic crystal structure and are assigned in the plot.[32,33] However, the origin of the pattern with the repetition of 4.99° is elusive and could not be ascertained from the literature reports. But it is quite clear that the formation of the 2D matrix on QDs surface is due to the reaction between butylamine and ligands. For QDs ink preparation, butylamine not only acts as a volatile solvent but also stays in the film as a 2D ligand matrix. To understand the ligand matrix formation and structure, we probe the reaction between BA+$Pb(Ac)_2$, BA+PbI_2, BA+PbI_2+NH_4I, and PbI_2+BA+MAI mixture. First, we try to find the origin of the repetition of the 4.99° peak on QDs surface. We assume that these repetitive 4.99° peaks may originate from the layer structure of PbI_2-amine or Pb-amine complex formation. However, before going into the detailed study of those BA+ligand reaction mixtures, we first check with the XRD of pure PbI_2 and $Pb(Ac)_2$ XRD spectrum (Figure 4.2). XRD spectrum of pure PbI_2 and $Pb(Ac)_2$ do not match with any pattern of the 2D matrix.

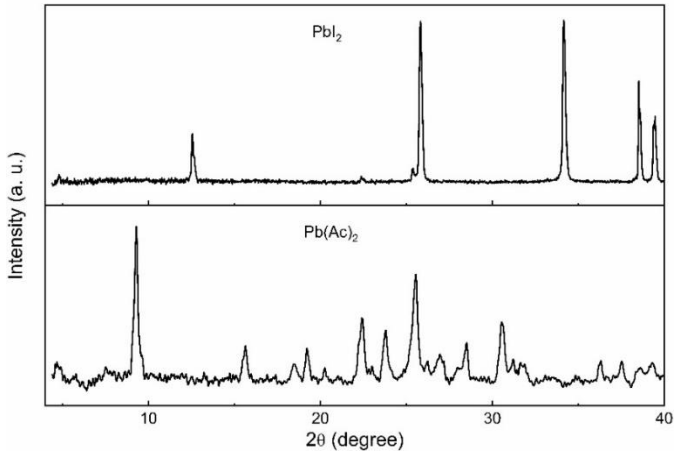

Figure 4.2: XRD spectrum of PbI_2 and $PbAc_2$ powder.

The XRD spectrums of different BA+ligand mixtures are shown in Figure 4.3. Interestingly, the XRD spectrum of lead acetate ($PbAc_2$) and BA mixture film (Figure 4.3) shows similar equidistant sharp peaks at identical positions with the repetition rate of 4.99°, which are observed in QDs films. This suggests that the pattern could be due to the 2D Pb-amine complex and eliminates the contribution from the PbI_2-amine complex. Due to the absence of iodide anion, BA+$Pb(Ac)_2$ mixture does not form $(BA)_2PbI_4$ complex. More interestingly, the XRD patterns of the BA+PbI_2 ligand film show exactly two similar equidistant types of peaks (repetitive 4.99° and 6.35°) as observed in ligand passivated QD films (Figure 4.3).

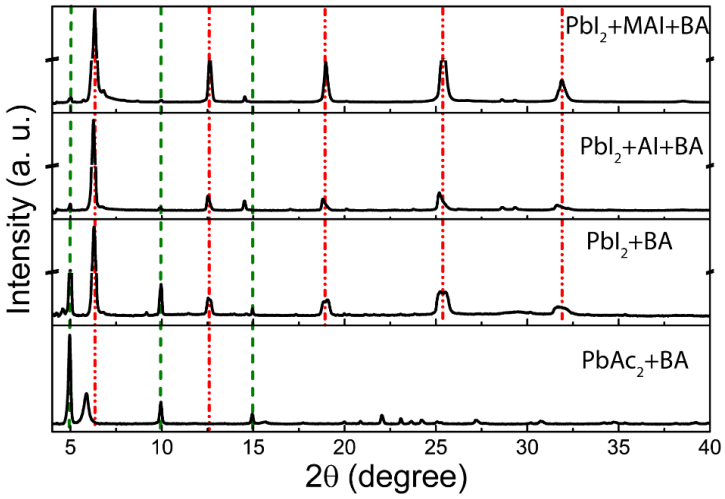

Figure 4.3: XRD spectrum for different ligands. Olive and red lines indicate the equidistant peaks correspond to the 2D Pb-amine complex and $(BA)_2PbI_4$ perovskite, respectively.

So, we designate the repetitive 6.35° peak for $(BA)_2PbI_4$ complex (marked by red color in Figure 4.3) and 4.99° peak for Pb-amine complex (marked by olive color in Figure 4.3). When AI or MAI is added to the PbI_2+BA ligand, the Pb-amine complex peak intensities reduce, and the $(BA)_2PbI_4$ peak intensities increase significantly. For all PbI_2 based ligands, $(BA)_2PbI_4$ perovskite peak intensities are much stronger than the Pb-amine complex, suggesting a favored condition for the 2D perovskite growth. In the presence of the QDs, however, Pb-amine complex peaks are significantly stronger than $(BA)_2PbI_4$ perovskite peaks (Figure 4.1). This indicates the critical role of the QD surface for the preferential growth of the 2D Pb-amine complex over $(BA)_2PbI_4$.

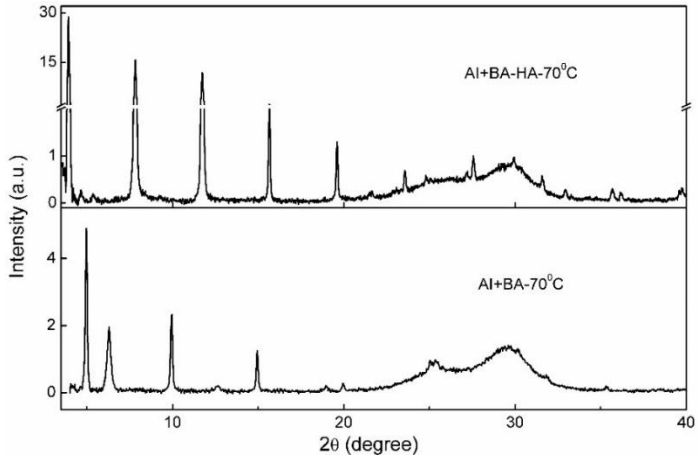

Figure 4.4: Comparison of the XRD spectrum of AI treated PbS QDs films deposited from 4:1 BA: HA mixed solvent and only BA.

It is further found that the 2D confinement of the matrix layer is true for longer chain hexylamine (HA) as well. In the case of BA+HA (4:1) mix solvent equidistant sharp peaks are also observed (Figure 4.4). Only one set of equidistant sharp peaks with repetition of 3.9° (2θ value) appear in the BA-HA mixture films, which are identified to be from the 2D Pb-HA complex. No peak related to 2D $(HA)_2PbI_4$ perovskite formation (which are reported in previous literature to have the repetition of 5.4° in the XRD spectrum [34]) are observed. In the case of PbS QDs films deposited from BA, both Pb-BA complex and $(BA)_2PbI_4$ perovskite are present as identified from the two sets of equidistant peaks, which we have discussed earlier.

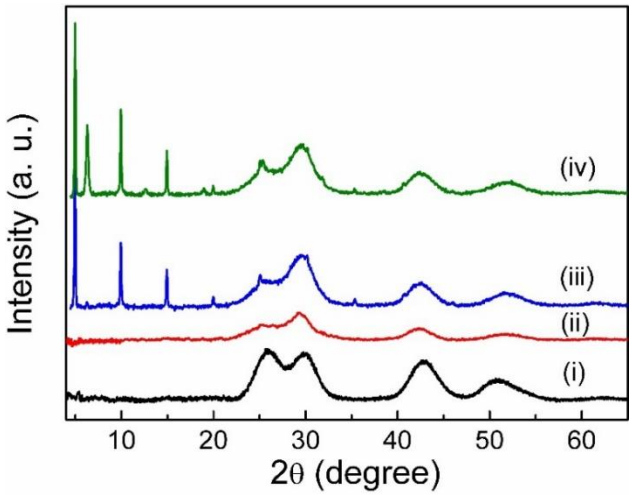

Figure 4.5: Evolution of XRD pattern at various stages of the AI ligand exchange process. Thin films of PbS QDs are measured (i) pristine OA caped, (ii) intermediate stage of ligand exchange in DMF, (iii) deposited from BA but not annealed, and (iv) deposited from BA and annealed at 70°C.

We note that for both AI and MAI, the ligand exchange process causes notable surface reconstruction of PbS QDs. The case study for AI ligand at different processing stages is shown in Figure 4.5. For the pristine OA capped PbS QDs, the peak intensity for the PbS (111) planes is stronger than the (200) planes; however, in the case of AI treated QDs, the peak intensity of the (111) planes is lower than the (200) planes in all processing stages. The PbS QDs (dia.~ 3nm) are terminated by (111) and (200) facets at their surface,[10,35], making the planes prudent to determine the size from XRD measurement. The magnified view of the XRD spectrum pertaining to the (111) and (200) planes of PbS QD is shown in Figure 4.6a. Particle size estimation from Debye-Scherrer equation[36] shows that (Figure 4.6b) there is a reduction in PbS diameter along (111) plane at the intermediate DMF stage, which recovers partially in the BA room temperature (BA-RT) stage, and finally increases in the annealed sample (BA-70°C). Particle size determined from the FWHM of the (200) plane shows that size increases systematically in each processing stage of the AI ligand treatment. We also note that along with the varied FWHM, the XRD peak positions for the (111) and (200) planes are also varied at different processing stages (Figure 4.6c), indicating different crystal strain at different stages of the ligand exchange process.[37]

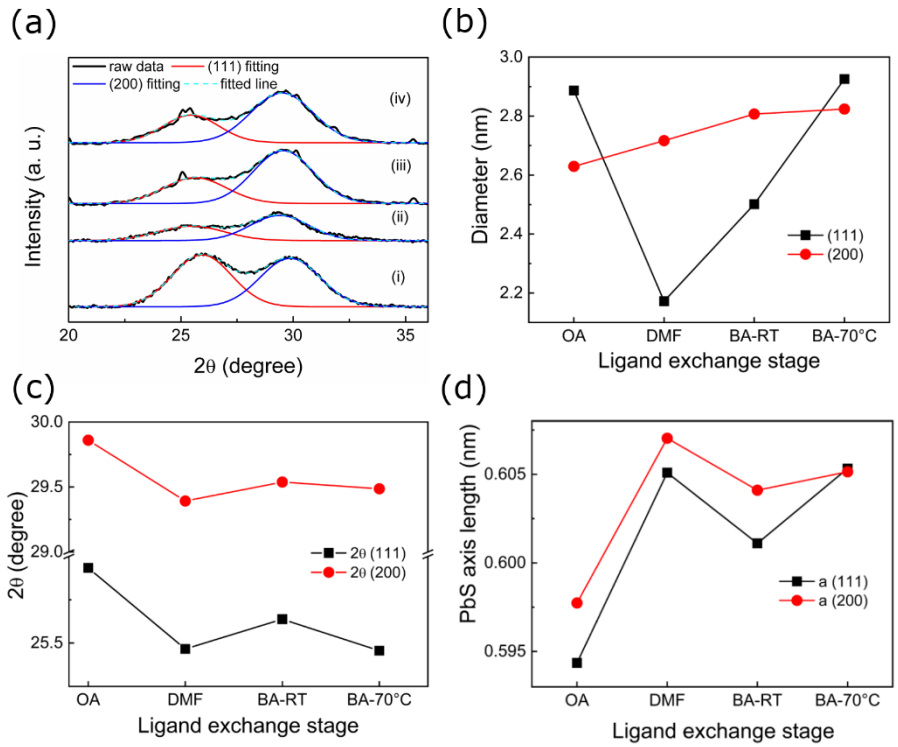

Figure 4.6: (a) Magnified view of the XRD peaks of PbS QDs at various stages of the AI ligand exchange process. XRD spectrum of QDs is shown for (i) pristine OA caped, (ii) intermediate stage of ligand exchange in DMF, (iii) deposited from BA but not annealed, and (iv) deposited from BA and annealed at 70°C. The peaks are fitted using Gaussian fitting. (b) Evolution of QDs size, (c) Change in 2θ value and (d) PbS axis length at different stages of the ligand exchange process for both (111) and (200) planes.

The axis length of the rock-salt PbS crystals determines from the diffraction peak position of the (111) and (200) planes at different stages of the ligand exchange process are shown in Figure 4.6d. The (111) facets of the PbS QDs are terminated by unsaturated lead atoms making the surface polar, whereas the (200) surfaces are charge-neutral, terminated by alternating lead and sulfur atoms.[10,35] Due to dissimilar surface chemistry, the interaction of ligand to these surfaces is different, which could be the origin for facet dependent surface strain. It is interesting to note that the QD size and the axis length determined from the (111) and (200) planes are similar for the annealed PbS QD films. This suggests that in the annealed films, PbS QDs are more spherical and have a similar surface strain in both (111) and (200) facets.

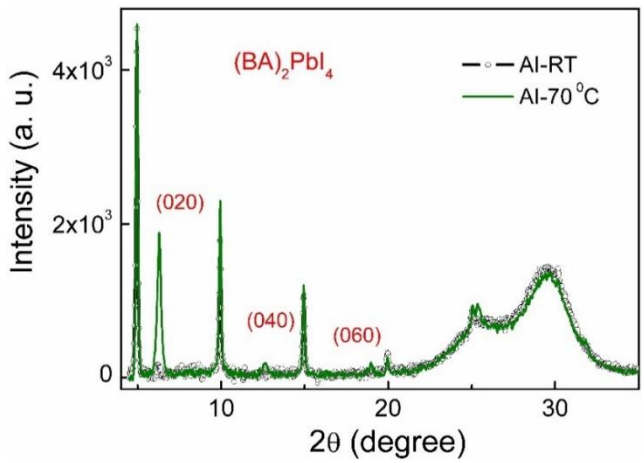

Figure 4.7: Comparison of the XRD spectrum for AI treated QD films for non-annealed and annealed films. 2D BA_2PbI_4 peak intensities (as marked in the plot) increases in the annealed sample.

Comparison of the XRD spectrum of the annealed and room temperature processed AI treated PbS QD films (Figure 4.5 and Figure 4.7) shows significant increases in 2D $(BA)_2PbI_4$ perovskite peak intensities in annealed samples, implying annealing helps long-range ordering of 2D $(BA)_2PbI_4$ perovskite crystals. The schematic view of the PbS QD size and shape progression at different stages of the ligand exchange process is deconstructed from the XRD results and shown in Figure 4.8. The crystal facets with the higher surface energy undergo selective etching under harsh ligand attack ($[PbI_3]^-$) in DMF solvent, which reduces the size along the (111) direction and increases the exposed surface area of the (111) facets.[38]

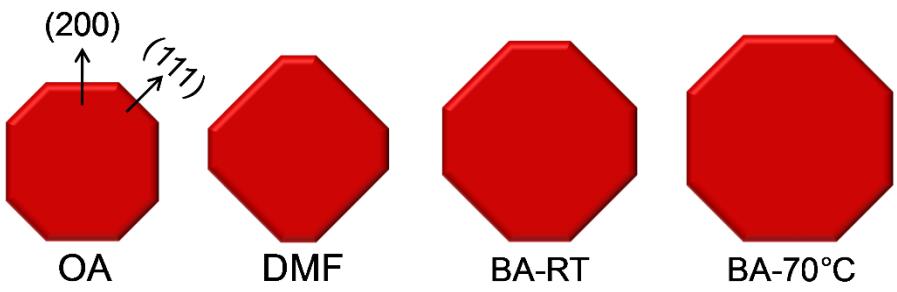

Figure 4.8: The schematic illustration of the change in QD size and shape at different stages of the ligand exchange process is deconstructed from the XRD results.

Non-annealed and annealed PbS QD films from BA show a progressive increase in the QD size along with both the directions, while the increase along the (111) direction is much

higher. We surmise that at the DMF phase, aggressive $[PbI_3]^-$ ions may etch some Pb atoms from the (111) facets and eventually passivates the (111) facets at the equilibrium.[38,39] In the presence of BA, the interaction of the $[PbI_3]^-$ ligand with the QD surface is relatively relaxed due to the formation of bulkier $[BAPbI_4]^-$ anion, which leads to the re-growth of the QDs along with the highly reactive (111) facets. The neutral Pb-amine complex may act as 'L' type ligand, which would coordinate with the neutral (200) facets of PbS QDs.[10] This is supported by the fact that the growth of the 2D Pb-amine complex is favorable in the presence of QDs, while only ligand films favored 2D $(BA)_2PbI_4$ perovskite formation.

4.3.2 Absorption and PL study

The absorption spectra of as-synthesized oleic acid capped QDs are shown in Figure 4.9. The absorption peak position of oleic acid capped QDs appears at 895 nm.

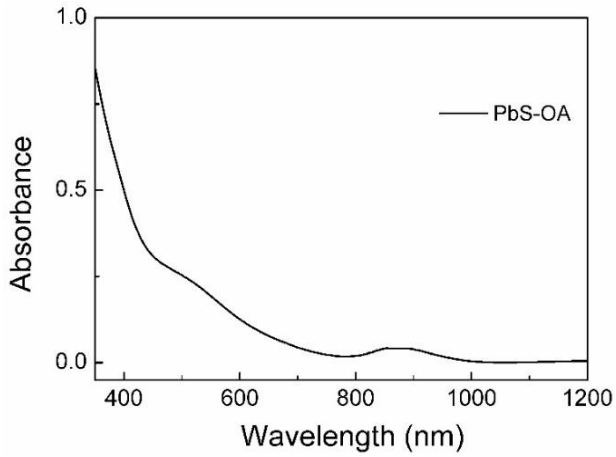

Figure 4.9: Absorption spectrum of the oleic acid capped PbS QD film.

After ligand exchange with MAI and AI, the absorption spectra are further studied to probe the 2D matrix layers in thin films. The absorption profiles for AI and MAI treated films are normalized to PbS excitonic peak position to illustrate the absorption contribution of the matrix layer (Figure 4.10a). The hump in absorption spectrums around 530 nm (as shown by the shaded region) could be originated from the 2D $(BA)_2PbI_4$ perovskite absorption. Further, the absorption spectrum of the ligand films is carried out as the control experiment and shown in Figure 4.10b. It is found that both PbI_2+AI+BA and PbI_2+MAI+BA ligand films show the strong excitonic feature of 2D $(BA)_2PbI_4$ perovskite peak at around (480 nm) whereas, for the PbI_2+BA film, the excitonic feature is less significant.[8,33]

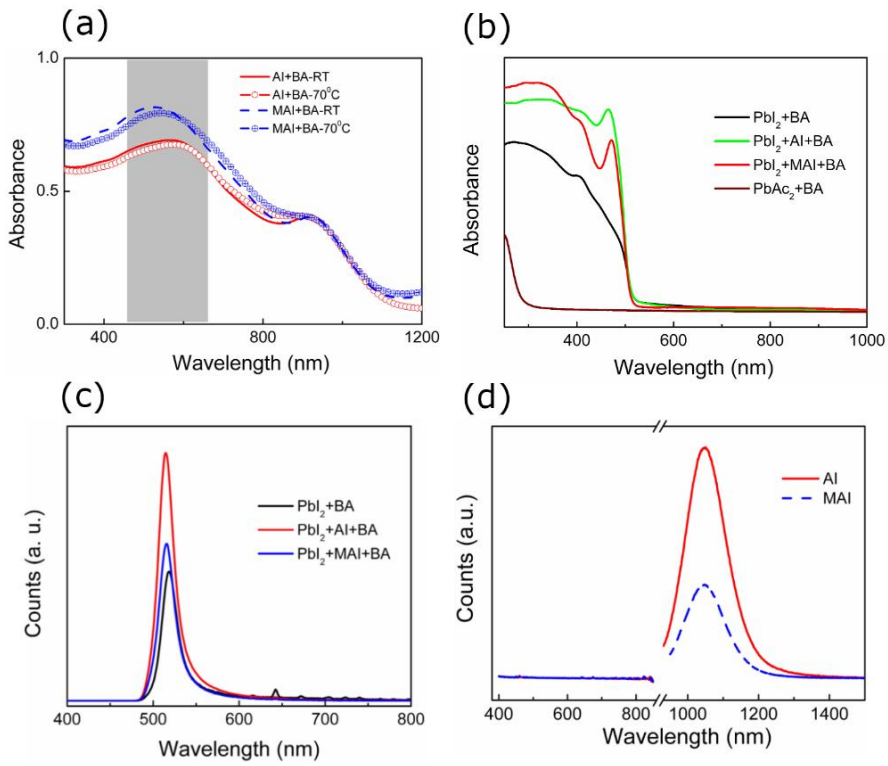

Figure 4.10: Spectroscopic characterization of the 2D crystalline matrix. (a) absorption spectra of AI and MAI treated non-annealed and annealed PbS QD films. (b) absorption and (c) PL spectra of the thin films of the ligands deposited on the quartz substrate. (d) PL spectra of QD films on a quartz substrate. The excitation wavelength is 380 nm.

The absorption spectrum of the $Pb(Ac)_2$+BA film shows no absorbance within the wavelength range. Further, narrow FWHM (~20 nm) of the photoluminescence (PL) spectrum (Figure 4.10c) of the ligand films supports the formation of 2D $(BA)_2PbI_4$ perovskite.[8,33] The PL spectrum of the QD films (Figure 4.10d) shows no peak for the ligand emission and shows the only band edge emission from the PbS QDs.[40] The absorbance peak of only $(BA)_2PbI_4$ redshifts by ~50 nm in QD films. The complete quenching of PL emission and redshift in absorbance of $(BA)_2PbI_4$ perovskite in QD films strongly suggests that the perovskite matrix does not form in isolation but is strongly coupled to the QD surface.[40]

4.3.3 FT-IR study

We further study the FT-IR spectra of ligand exchanged QDs to check the presence of the N-H stretching feature of the 2D matrix layer on QDs surface. This will also directly prove that BA solvent does not evaporate from the films during spin coating; rather, it reacts to the surface ligands to form the 2D matrix layer. From XRD analysis, we determined two

types of 2D matrix layers on QDs surface. The presence of 2D $(BA)_2PbI_4$ perovskite is confirmed from XRD and UV spectra analysis, which are supported by earlier reports on 2D perovskite. However, the structure of the Pb-amine complex is still not understood.

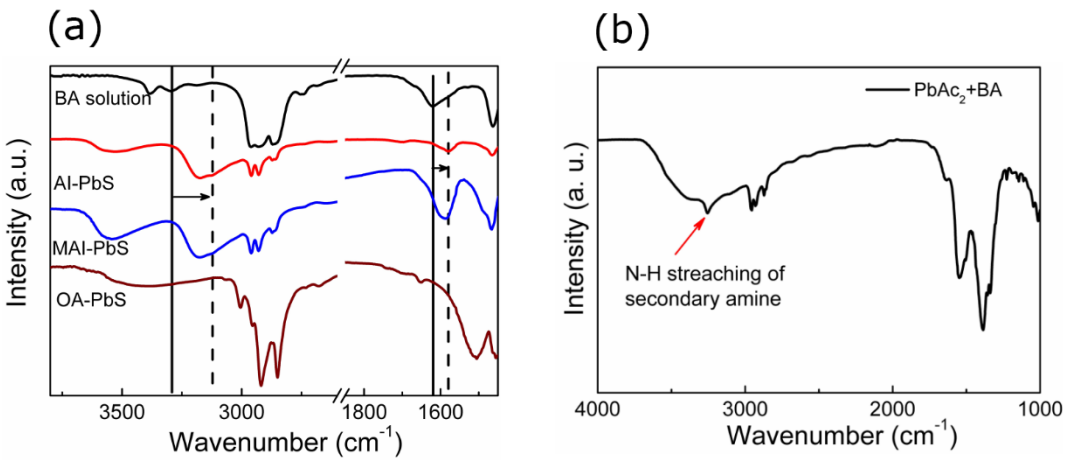

Figure 4.11: (a) ATR-FTIR spectroscopy of the QD film treated with different ligands (as marked in the plot) and FTIR spectrum of the pure BA in CCl_4 solution. The shift in the N-H stretching frequency and the N-H scissor mode frequency are shown in the plot. (b) ATR-FTIR spectra of $Pb(Ac)_2$+BA complex film. The appearance of a single N-H stretching peak indicates the formation of secondary amine.

Fourier transform infrared (FTIR) spectroscopy results show that the N-H stretching band (asymmetric and symmetric) of pure BA appears at 3384 cm^{-1} and 3295 cm^{-1} and shift to 3180 cm^{-1} and 3122 cm^{-1} in AI and MAI treated PbS QD film (Figure 4.11a). The N-H scissor mode vibration peak also shifts from 1620 cm^{-1} to 1580 cm^{-1} (Figure 4.11a). The shift might be due to the transformation of BA to BA^+ cation and the chemical coordination of the amine to PbI_4^{2-} anion in 2D $(BA)_2PbI_4$ perovskite matrix. As in ligand exchanged QDs and BA+PbI_2 ligand mixture, both have two types of 2D matrix layers; it is quite difficult to distinguish the nature of amine binding in the Pb-amine complex. We have probed the only Pb-amine complex synthesized from $Pb(Ac)_2$ + BA mixture. ATR-FTIR spectrum shows the single N-H stretching peak at 3255 cm^{-1} (Figure 4.11b) of the secondary amine in the case of Pb-amine complex from $Pb(Ac)_2$ + BA mixture. So, it suggests that the Pb-amine complex is composed of Pb and secondary amine binding.

4.3.4 Reaction Mechanism

It is interesting to note that for the equivalent QD excitonic absorption, the 2D $(BA)_2PbI_4$ ligand absorbance is higher in the case of MAI treated films, implying a higher proportion of the 2D perovskite. There is barely any change in absorption intensity of the $(BA)_2PbI_4$ in annealed and non-annealed samples. However, XRD data show that the diffraction peak intensity of the 2D $(BA)_2PbI_4$ perovskite increases significantly (Figure 4.5 and Figure 4.7) upon annealing. This implies that annealing improves the crystallinity and long-range ordering of the 2D $(BA)_2PbI_4$ perovskite, but the relative amount remains unchanged in the film. Further, there is no evidence of 3D $MAPbI_3$ perovskite formation from XRD, absorption, and PL data for both AI and MAI treated PbS QD films. We surmise that the deposition of QD films from the linear chain amine (BA or HA) confined the perovskite growth to the 2D. Based on the observations from XRD and spectroscopic results, we propose the following reaction mechanism for the Pb-amine complex and $(BA)_2PbI_4$ formation in the ligand exchange reaction.

<u>Case-I:</u> ($BA+PbI_2+NH_4I/MAI$)

$$2BA + 2NH_4PbI_3(/2MAPbI_3) \longrightarrow (BA)_2PbI_4 + PbI_2 + 2NH_3/CH_3NH_2\uparrow \quad \text{.....(i)}$$

$$nBA + nPbI_2 \longrightarrow (CH_3CH_2CH_2CH_2NH\ldots\ldots PbI)_n + nHI \quad \text{.....(ii)}$$

<u>Case-II:</u> ($BA+PbI_2$)

$$nBA + nPbI_2 \longrightarrow (CH_3CH_2CH_2CH_2NH\ldots\ldots PbI)_n + nHI \quad \text{.....(iii)}$$

$$nBA + nHI \longrightarrow nBA^+I^- \quad \text{.....(iv)}$$

$$2\,BA^+I^- + PbI_2 \longrightarrow (BA)_2PbI_4 \quad \text{.....(v)}$$

<u>Case-III:</u> ($BA+PbAc_2$)

$$nBA + nPbAc_2 \longrightarrow (CH_3CH_2CH_2CH_2NH\ldots\ldots PbAc)_n + nAcOH \quad \text{.....(vi)}$$

In Case-I, the mixture of PbI_2 and AI (or MAI) are taken in BA solution; AI (or MAI) protonates the BA to form BA^+ (butylammonium), which favors the formation of $(BA)_2PbI_4$ as shown in equation (i).[41] The excess PbI_2 can further react with BA to form the Pb-amine complex, as shown in equation (ii). Case-II, in the absence of AI (or MAI) in the reaction mixture, the intermediate 'HI' can protonate BA to form the $(BA)_2PbI_4$ as shown in

equations (iii), (iv) & (v) successively. When $PbAc_2$ is taken instead of PbI_2 (Case-III) in BA solvent only Pb-amine complex is formed (vi). It is interesting to note here that for all the Pb-amine complexes, the amine is a secondary amine that is supported by $Pb(Ac)_2$+BA ligand ATR-FT-IR result.

4.3.5 XPS analysis

X-ray photoelectron spectroscopy (XPS) of Pb4f shows that the atomic percent for Pb-ligand contribution (Pb-I, Pb-amine, etc.) is 12.14 % and 21.4%, respectively for AI and MAI treated PbS films (Figure 4.12a, 4.12b and Table 4.1). Higher Pb-ligand atomic percentage suggests a thicker ligand matrix for MAI treated PbS QD films.

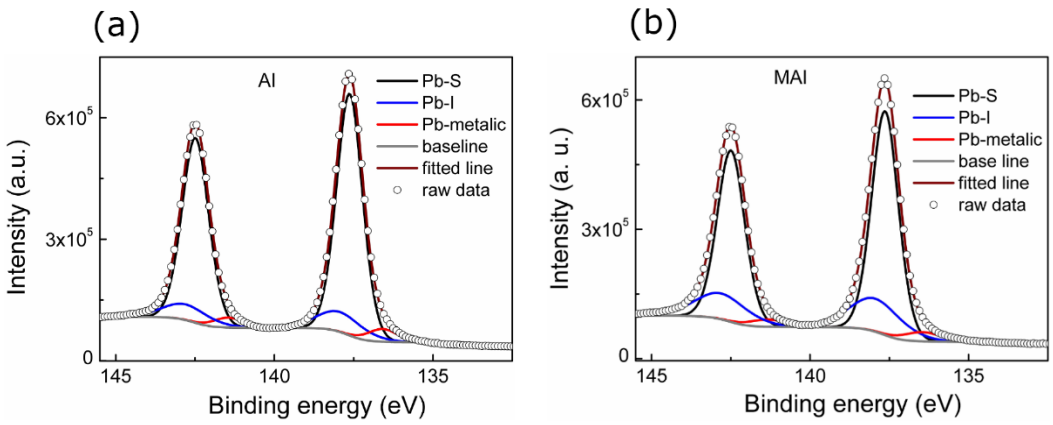

Figure 4.12: (a) and (b) shows the Pb4f XPS signal of AI and MAI treated QDs, respectively. The Pb4f signal is deconvoluted to Pb-ligand, Pb-S, and Pb-metallic signals to fit the spectrum.

Table 4.1: Atomic percent of different components determined from Pb4f XPS spectrum of AI and MAI treated PbS QDs shown in Figure 4.12 (a) and (b).

Name of ligand	Pb-S (%)	Pb-ligand (%)	Pb-metallic (%)
AI	82.94	12.14	4.98
MAI	74.6	21.22	4.18

Comparison of the S2p XPS spectrum shows that the S2p3/2 and S2p1/2 peaks are narrower in the case of AI treated QDs (Figure 4.13a) than MAI treated QDs (Figure 4.13b).

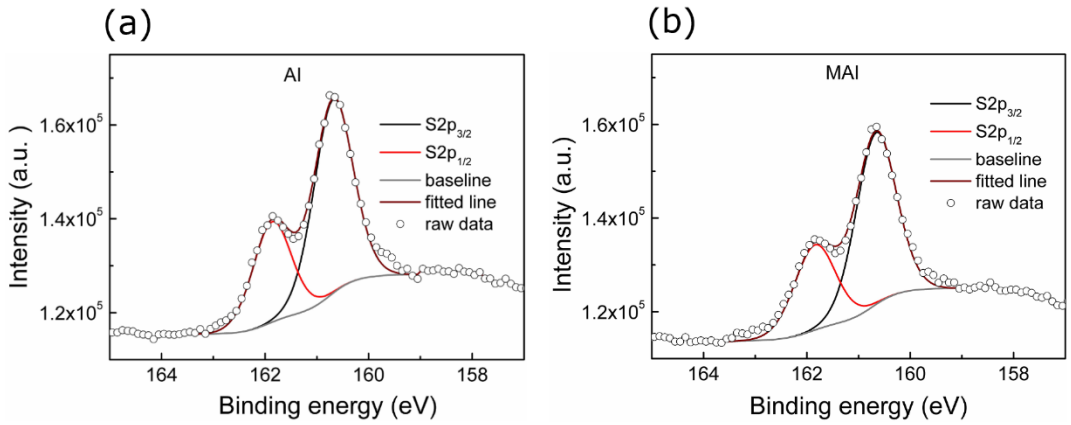

Figure 4.13: XPS spectrum of S2p orbital of PbS QD film treated with (a) AI and (b) MAI ligand. The fitting parameters for the $S2p_{3/2}$ and $S2p_{1/2}$ signals are summarized in Table 4.2.

The fitting parameters and quantitative analysis of S 2p spectra are tabulated in Table 4.2.

Table 4.2: Fitting parameters and quantitative analysis of S2p spectra of AI and MAI treated PbS QD film as shown in Figure 4.13 (a) and (b).

Name of ligand	element	Peak position	FWHM	Atomic ratio after R.S.F. correction (%)
AI	$S2p_{3/2}$	160.66	0.89	50
	$S2p_{1/2}$	161.84	0.88	50
MAI	$S2p_{3/2}$	160.66	0.92	50
	$S2p_{1/2}$	161.84	0.94	50

Considering the fact that under-coordinated surface 'S' atoms have different XPS signature than fully coordinated 'S' atoms in the bulk of PbS QDs, the narrowing in the S2p spectrum may be due to higher-order replacement of under-coordinated surface sulfur atoms by iodine.[16]

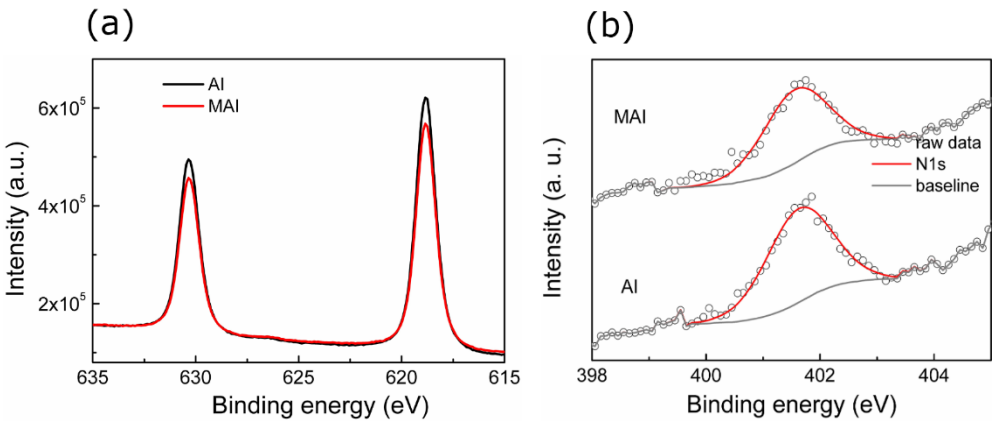

Figure 4.14: (a) XPS signal of I3d orbital of AI and MAI treated PbS QDs, respectively. (b) XPS signal of N1s orbital AI and MAI treated PbS QDs.

The I/Pb and I/S ratios for AI treated film (0.55 and 0.90 respectively) are higher than MAI (I/Pb=0.49, I/S=0.85) treated QD film (Figure 4.14a). The higher proportion of iodine in AI-treated QDs is likely to provide better surface passivation. The XPS spectrum of N1s shows the peak at ~402 eV (Figure 4.14b), indicating the transformation of amine to ammonium.[25]

4.3.6 TEM image analysis

The high-resolution transmission electron microscope (HRTEM) images show the individual particles in the case of OA and AI ligand, whereas PbS QDs are connected together by the matrix layer when the MAI ligand is used (Figure 4.15 a, b, and c). Careful analysis of the lattice fringes reveals that the lattice spacing of 0.34 nm is overwhelmingly observed in all three cases, which corresponds to {111} plane spacing of cubic PbS. The crystal fringes of the matrix layer could not be separated from the QDs, probably due to lattice matching and coherent growth of the ligand on the QD surface.[21] In comparison to AI-treated QDs, the higher amount of matrix is clearly visible in MAI treated sample. This further validates the observation of higher matrix presence in MAI treated PbS QDs.[21, 34]

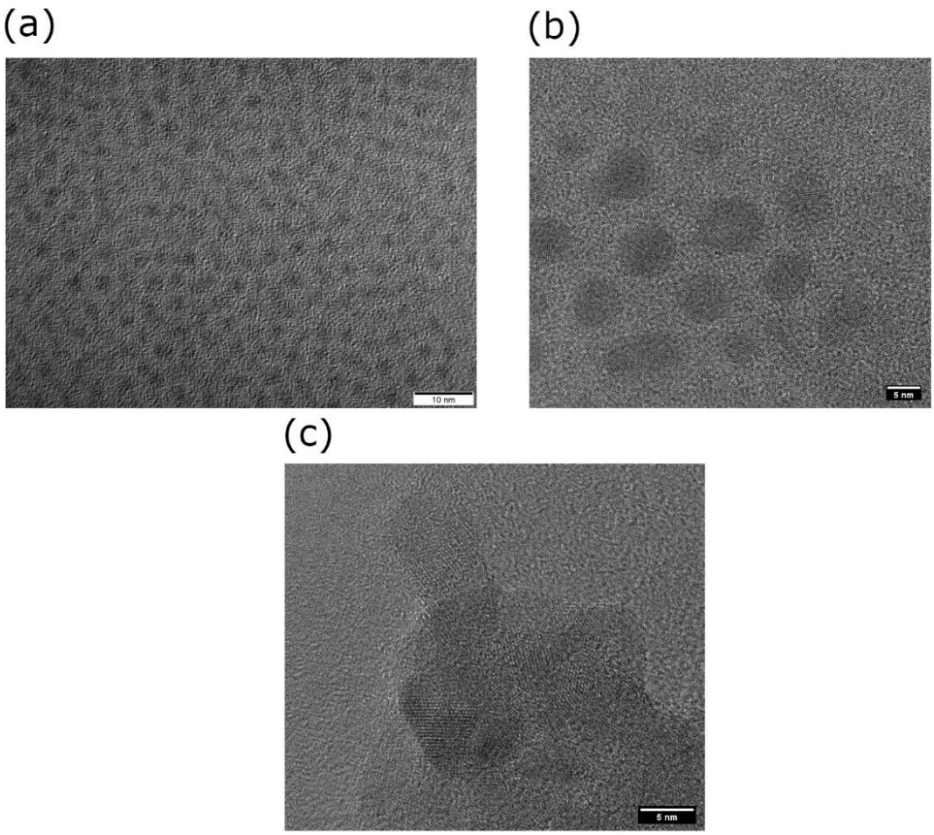

Figure 4.15: The high-resolution TEM images of (a) oleic acid capped PbS QDs, (b) AI, and (c) MAI treated PbS QDs deposited from BA and annealed at 70°C.

4.3.7 Cross-sectional SEM image of solar cell

To understand the impact of 2D matrix thickness on QDs surface, we further fabricate solar cells using ligand (MAI or AI) exchanged QDs as light-harvesting material.

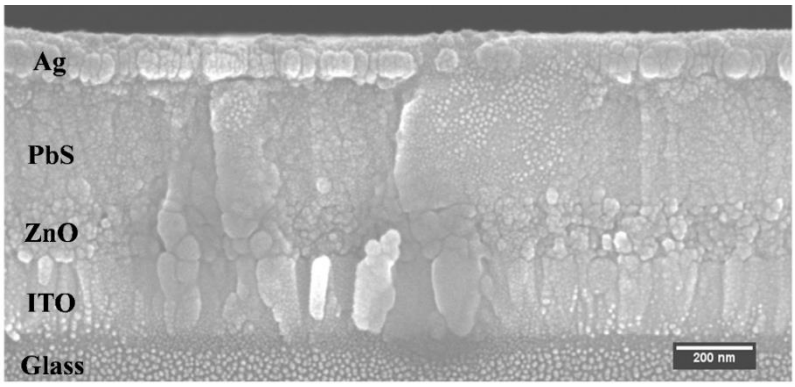

Figure 4.16: The cross-section SEM image of a representative solar cell device structure.

The devices are made with the following structure: ITO/ZnO (ETL,80-100nm)/ PbS QDs ink (AI or MAI treated)/PbS-EDT (HTL, 50-70 nm)/MoO_3 (8 nm)/Au (30 nm)/Ag (100 nm). The cross-sectional SEM of the typical solar cell is shown in Figure 4.16, where all the active layers are identified.

4.3.8 J-V characteristics

The optimized solar cell performance based on AI and MAI treated PbS QDs under AM 1.5 (100 mW cm^{-2}) simulated solar illumination is shown in Figure 4.17.

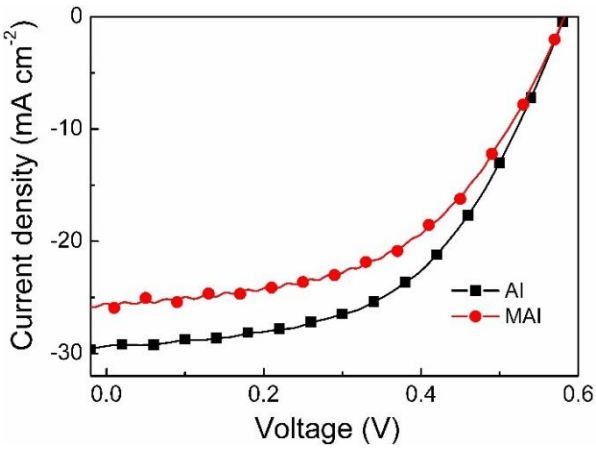

Figure 4.17: J-V characteristics (under reverse scan) of the solar cells under AM1.5 simulated solar illumination.

Short circuit current (J_{sc}) increases significantly from 25.3 mA cm^{-2} (in MAI-PbS) to 29.29 mA cm^{-2} in AI treated solar cells.

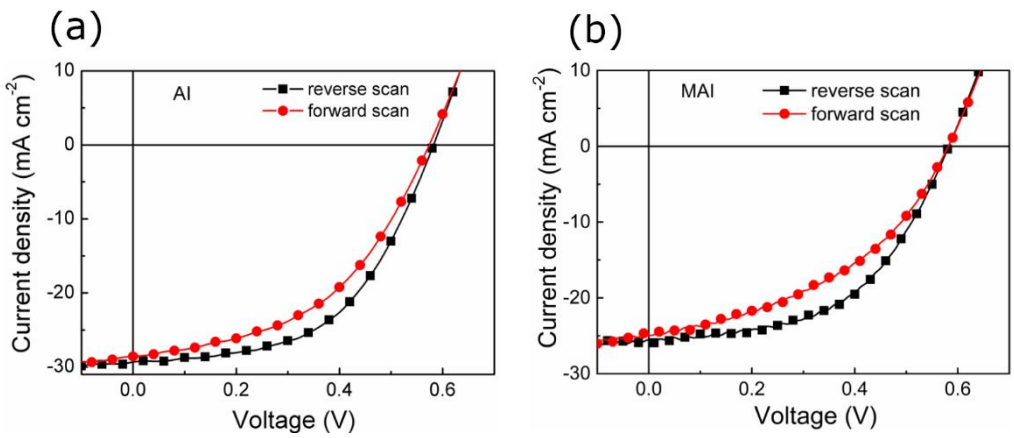

Figure 4.18: J-V characteristics show hysteresis under forward and reverse scan for a) AI and b) MAI treated solar cells.

Table 4.3: Photovoltaic parameters of AI and MAI treated PbS QD solar cells.

Name of the ligand	Scan direction	J_{sc} (mA cm^{-2})	V_{oc} (V)	FF (%)	PCE (%)
AI	reverse	29.29	0.58	53.6	9.10
	forward	28.57	0.58	47.2	7.82
MAI	reverse	25.37	0.58	53	7.80
	forward	25	0.58	43.1	6.24

Open circuit voltage (V_{oc}) remains unchanged (0.58 V) while the fill factor (FF) raises a little to increase the power conversion efficiency (PCE) from 7.80% to 9.10% in AI treated solar cells. Both the solar cells show hysteresis in their J-V characteristics (Figure 4.18). The photovoltaic parameters are summarized in Table 4.3 for comparison.

4.3.9 EQE spectrum

The external quantum efficiency (EQE) for the solar cells is determined for the wavelength range of 360 nm to 1200 nm for both AI and MAI treated solar cells.

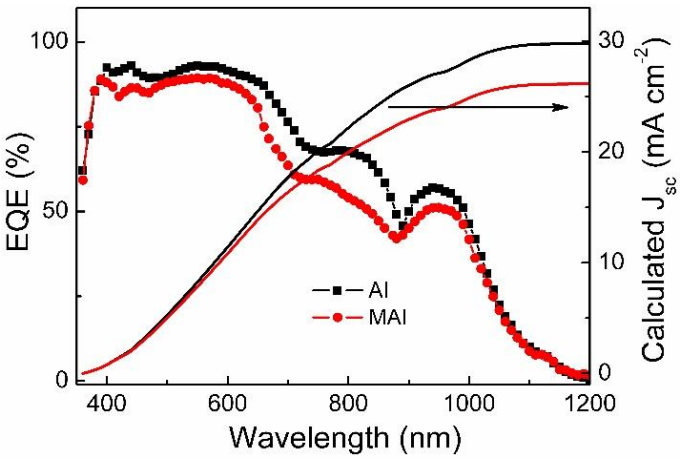

Figure 4.19: The full-spectrum EQE of AI and MAI treated solar cells. The axis on the right-hand side shows the calculated J_{sc} from the EQE under simulated solar illumination.

The calculated J_{sc} from the EQE spectrum matched well with the measured J_{sc} for the solar cells, as shown in Figure 4.19.

4.3.10 Statistical distribution of PCE

The average PCE of ten batches of solar cells for both AI and MAI treated solar cells are compared in Figure 4.20. In each batch, ten devices are made, so the PCE of a total 100 devices for both AI and MAI treated QDs are analyzed.

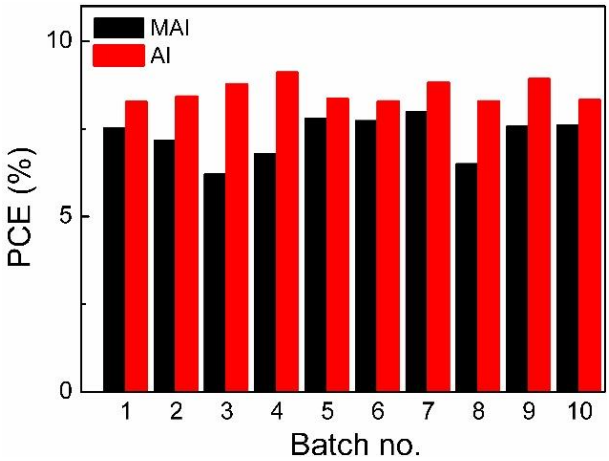

Figure 4.20: Batch to batch variation in solar cell PCE for AI and MAI treated solar cells.

Solar cells based on AI treated QDs show consistently high performance and little batch to batch variation as observed for ten batches of devices.

4.3.11 Thickness optimization of device

The thickness-dependent study shows that optimal thickness for the AI-treated solar cell is around 320 nm (J_{sc}=29.29 mA cm^{-2}, FF%=53.6, PCE%=9.1), whereas for MAI treated solar cell, the optimal thickness is around 250 nm (J_{sc} = 25.37 mA cm^{-2}, FF% = 53, PCE% = 7.80).

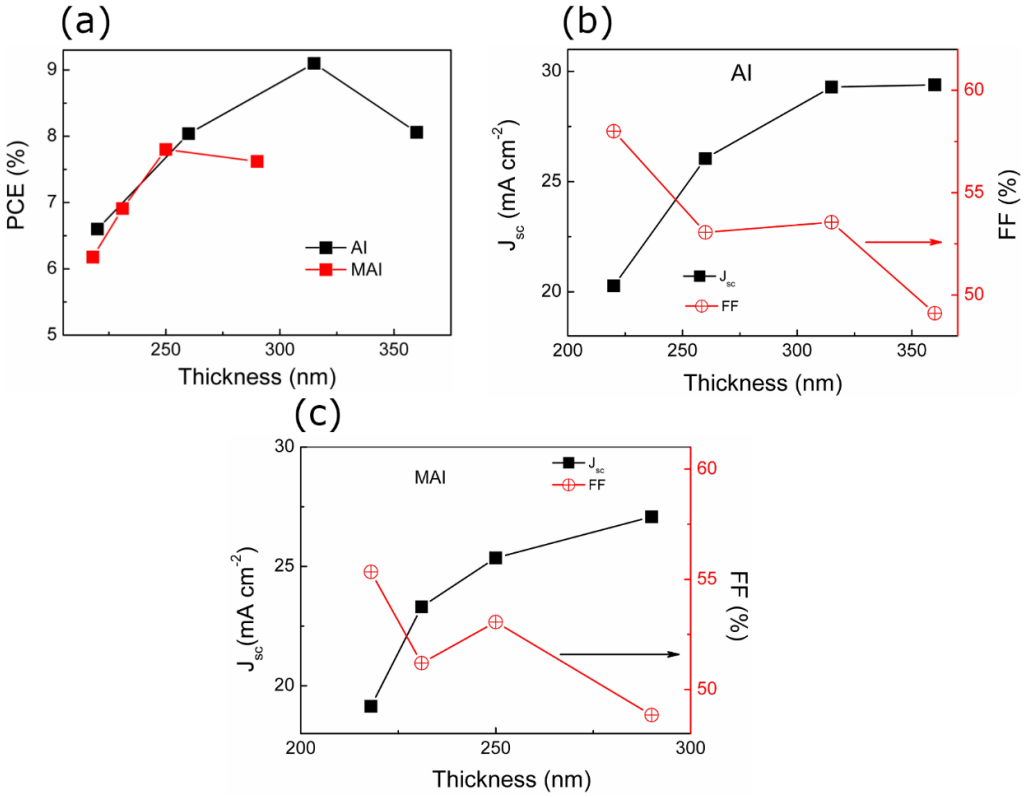

Figure 4.21: (a) Change of PCE with thickness for AI and MAI treated solar cells. (b) and (c) represents the variation of J_{sc} and FF with thickness for AI and MAI treated solar cells, respectively.

The change of PCE with thickness is shown in (Figure 4.21a). Here the thickness of the active layer (AI or MAI treated PbS QDs) is only varied, and the thickness of other layers (ETL and HTL) is kept constant. The change in J_{sc} and FF with active layer thickness are also presented in Figure 4.21b for AI treated, and 4.21c for MAI treated solar cells.

4.3.12 Carrier lifetime and DOS calculation

We further calculate the carrier lifetime and trap states distribution at different V_{oc} values for both AI, and MAI ligand treated solar cells. The photocarrier lifetime is measured from the transient photovoltage (TPV) decay technique at different open-circuit voltages.[42] For TPV measurement, solar cells are kept under solar simulator white light bias as well as with short light pulse. The intensity of the short light pulse is varied to get less than 10% perturbation of the V_{oc} values. V_{oc} is varied by tuning the intensity of solar simulator white light. The pulse width of the light pulse is maintained to 2 µs for all the measurements. A typical TPV decay profile is shown in Figure 4.22a.

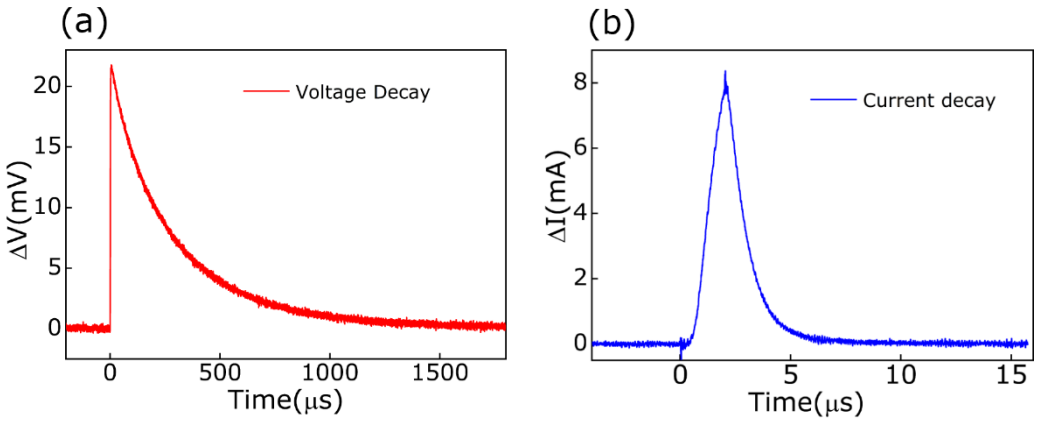

Figure 4.22: (a) represents a characteristics photovoltage decay profile and (b) shows a characteristics photocurrent decay profile.

The carrier lifetime calculation details are discussed in the third chapter of section 3.3.6. Intermediate band trap density is estimated from TPV decay and transient photocurrent (TPC) decay measurements.[43,44] To calculate the total number of charge carriers generated by the light pulse, TPC is measured by switching off the white light bias. The integration of the area under the TPC curve gives us the number of charge carriers (ΔQ) generated by the light pulse. A TPC decay profile is represented in Figure 4.22b. The density of states 'n' that need to be filled to generate a given V_{oc} is determined by equation 4.1.

$$n = \frac{1}{Aqd}\int_0^{V_{oc}} C dV \quad (4.1)$$

Where q is the electronic charge, and A and d are the area and thickness of the solar cell. The differential capacitance C is determined from $C = \frac{\Delta Q}{\Delta V_{oc}}$; where ΔV_{oc} is the change in V_{oc}

due to the light pulse measured from TPV data. The density of trap states can be expressed as $\frac{dn}{dV_{oc}}$.

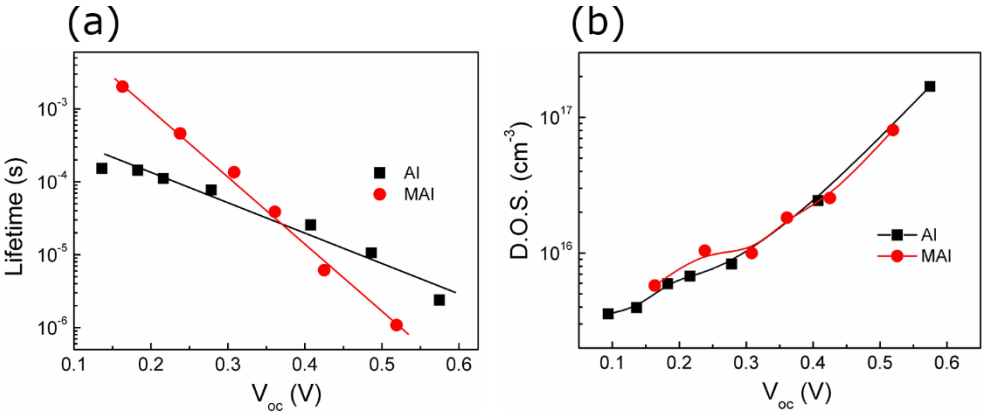

Figure 4.23: (a) Carrier lifetime measured from TPV at different V_{oc}. The V_{oc} has been varied by changing the illumination intensity of the solar simulator. (b)The density of intermediate trap states at different open-circuit voltages for AI and MAI treated solar cells.

Both the solar cells follow the general trend of decrease in carrier lifetime with the increase in light intensity (or V_{oc}),[42,43]; however, the slopes are different, as shown in Figure 4.23a. In higher light bias conditions (close to 1 sun), the carrier lifetime for AI treated solar cells is higher, allowing greater leverage for the carrier transportation. The plot of $\frac{dn}{dV_{oc}}$ vs V_{oc} is shown in Figure 4.23b. We find very little difference in intermediate trap distribution of PbS QDs, suggesting analogous trap distribution for both the ligand treatments.

4.3.13 Bias dependant transient time study

The carrier transit time (τ_{tr}) is determined from the photocurrent decay, which corresponds to the time required to decay 1/e of the maximum current value.[45,46] The photocurrent decay at varied applied biases for AI and MAI treated solar cells are shown in Figure 4.24a and 4.24b, respectively. Carrier mobility (μ) is determined using the formula $\mu = \frac{d^2}{\tau_{tr} \times V}$; where d is the film thickness and V is the applied bias. From the slope of the $\frac{d^2}{\tau_{tr}}$ vs. V plot (Figure 4.24c), μ is determined to be 1.63 x 10^{-3} $cm^2V^{-1}s^{-1}$, and 6.4 x 10^{-4} $cm^2V^{-1}s^{-1}$, respectively for AI and MAI treated solar cells. The higher carrier mobility in AI treated PbS QD films may be rooted in their lower 2D matrix thickness in comparison to MAI.

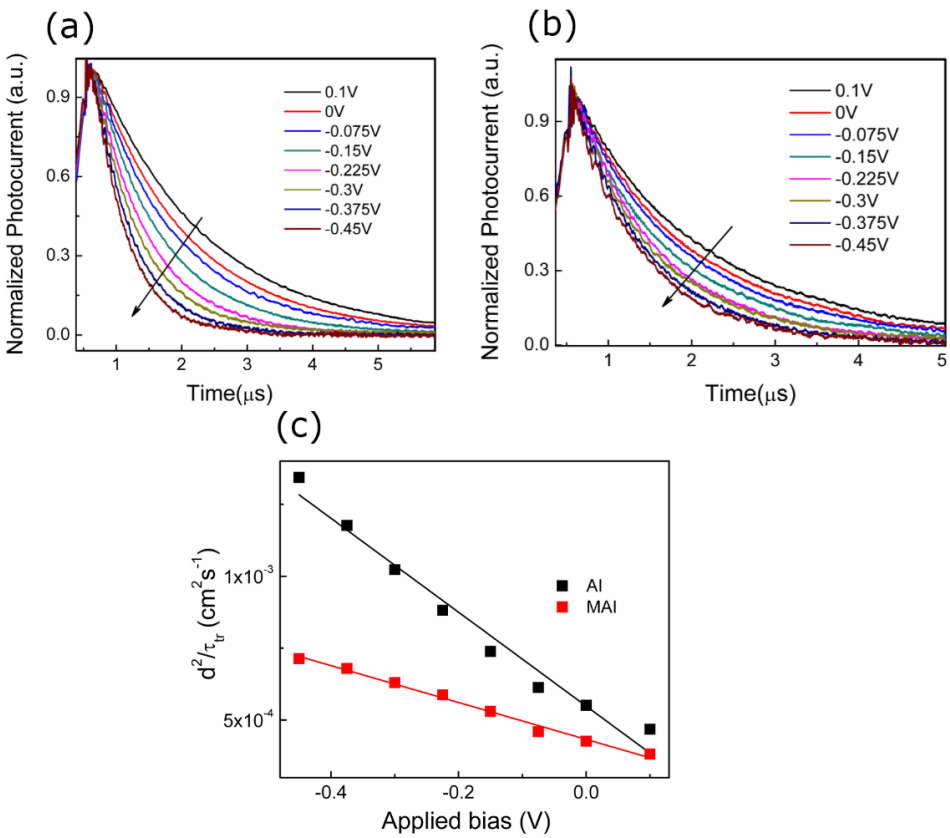

Figure 4.24: Photocurrent transients at a different applied bias of (a) AI and (b) MAI treated photovoltaic devices. (c) The charge carrier mobility is estimated from the slope of $\frac{d^2}{\tau_{tr}}$ vs. applied bias plot (where d is film thickness and τ_{tr} is the carrier transit time).

Further, diffusion width L_D is estimated using the formula, $L_D = \sqrt{\mu(KT)\tau/q}$;[46] K - Boltzmann constant, T-temperature (300 K), τ -carrier lifetime, and q -electronic charge. The L_D is calculated to be 100 nm and 42 nm for AI and MAI treated solar cells under one sun operating condition. Higher diffusion length in AI treated solar cells would allow more efficient carrier collection from the thicker QD films. This result further supports the higher optimized thickness of AI treated solar cells (320nm) than MAI treated solar cells (250 nm). These impact the enhancement of J_{sc} in AI treated solar cells without compromising the FF.

4.4 Conclusion

In summary, we have shown PbS QDs in the oriented 2D matrix by subjecting the halometallate treated QDs to linear chain amines like BA and HA. The halometallate ligand treatment is found to modify the size, shape, and axis length of PbS QDs through surface reconstruction. The 2D layer matrix is shown to consist of two 2D components in the form of a Pb-amine complex and $(BA)_2PbI_4$ perovskite layer. The choice of the counter cation influences the growth of the 2D matrix layer in PbS QD films. The enhancement in photovoltaic performances in AI treated QD films is correlated to the increase in carrier mobility, carrier lifetime, and diffusion length of the solar cells. Our study shows a general approach to develop the 2D matrix passivated QD film, which could be beneficial for the wide range of optoelectronic applications, such as the printable solar cell, tandem cell, photodetector, and light-emitting diodes.

4.5 References

1. McDonald, S. A.; Konstantatos, G.; Zhang, S. G.; Cyr, P. W.; Klem, E. J. D.; Levina, L.; Sargent, E. H., Solution-processed PbS Quantum Dot Infrared Photodetectors and Photovoltaics. *Nat. Mater.* **2005**, *4* (2), 138-142.

2. Luther, J. M.; Gao, J. B.; Lloyd, M. T.; Semonin, O. E.; Beard, M. C.; Nozik, A. J., Stability Assessment on a 3% Bilayer PbS/ZnO Quantum Dot Heterojunction Solar Cell. *Adv. Mater.* **2010**, *22* (33), 3704-3707.

3. Chuang, C. H. M.; Brown, P. R.; Bulovic, V.; Bawendi, M. G., Improved Performance and Stability in Quantum Dot Solar Cells Through Band Alignment Engineering. *Nat. Mater.* **2014**, *13* (8), 796-801.

4. Kagan, C. R.; Lifshitz, E.; Sargent, E. H.; Talapin, D. V., Building Devices From Colloidal Quantum Dots. *Science* **2016**, *353* (6302), aac5523 (1-11).

5. Pradhan, S.; Stavrinadis, A.; Gupta, S.; Konstantatos, G., Reducing Interface Recombination through Mixed Nanocrystal Interlayers in PbS Quantum Dot Solar Cells. *ACS Appl. Mater. Interfaces* **2017**, *9* (33), 27390-27395.

6. Lan, X. Z.; Voznyy, O.; de Arquer, F. P. G.; Liu, M. X.; Xu, J. X.; Proppe, A. H.; Walters, G.; Fan, F. J.; Tan, H. R.; Liu, M.; Yang, Z. Y.; Hoogland, S.; Sargent, E. H., 10.6% Certified Colloidal Quantum Dot Solar Cells via Solvent Polarity-Engineered Halide Passivation. *Nano ett.* **2016**, *16* (7), 4630-4634.

7. Liu, M. X.; Voznyy, O.; Sabatini, R.; de Arquer, F. P. G.; Munir, R.; Balawi, A. H.; Lan, X. Z.; Fan, F. J.; Walters, G.; Kirmani, A. R.; Hoogland, S.; Laquai, F.; Amassian, A.; Sargent, E. H., Hybrid Organic-inorganic Inks Flatten the Energy Landscape in Colloidal Quantum Dot Solids. *Nat. Mater.* **2017**, *16* (2), 258-263.

8. Xu, J. X.; Voznyy, O.; Liu, M. X.; Kirmani, A. R.; Walters, G.; Munir, R.; Abdelsamie, M.; Proppe, A. H.; Sarkar, A.; de Arquer, F. P. G.; Wei, M. Y.; Sun, B.; Liu, M.; Ouellette, O.; Quintero-Bermudez, R.; Li, J.; Fan, J.; Quan, L. N.; Todorovic, P.; Tan, H. R.; Hoogland, S.; Kelley, S. O.; Stefik, M.; Amassian, A.; Sargent, E. H., 2D Matrix Engineering for Homogeneous Quantum Dot Coupling in Photovoltaic Solids. *Nat. Nanotechnol.* **2018**, *13* (6), 456-462.

9. Jumabekov, A. N.; Cordes, N.; Siegler, T. D.; Docampo, P.; Ivanova, A.; Fominykh, K.; Medina, D. D.; Peter, L. M.; Bein, T., Passivation of PbS Quantum Dot Surface with L-Glutathione in Solid-State Quantum-Dot-Sensitized Solar Cells. *ACS Appl. Mater. Interfaces* **2016**, *8* (7), 4600-4607.

10. Boles, M. A.; Ling, D.; Hyeon, T.; Talapin, D. V., The Surface Science of Nanocrystals. *Nat. Mater.* **2016**, *15* (2), 141-153.

11. Tang, J.; Brzozowski, L.; Barkhouse, D. A. R.; Wang, X. H.; Debnath, R.; Wolowiec, R.; Palmiano, E.; Levina, L.; Pattantyus-Abraham, A. G.; Jamakosmanovic, D.; Sargent, E. H., Quantum Dot Photovoltaics in the Extreme Quantum Confinement Regime: The Surface-Chemical Origins of Exceptional Air- and Light-Stability. *Acs Nano* **2010**, *4* (2), 869-878.

12. Bakulin, A. A.; Neutzner, S.; Bakker, H. J.; Ottaviani, L.; Barakel, D.; Chen, Z. Y., Charge Trapping Dynamics in PbS Colloidal Quantum Dot Photovoltaic Devices. *Acs Nano* **2013**, *7* (10), 8771-8779.

13. Guyot-Sionnest, P., Electrical Transport in Colloidal Quantum Dot Films. *J. Phys. Chem. Lett.* **2012**, *3* (9), 1169-1175.

14. Talapin, D. V.; Murray, C. B., PbSe Nanocrystal Solids for n- and p-Channel Thin Film Field-Effect Transistors. *Science* **2005**, *310* (5745), 86-89.

15. Luther, J. M.; Law, M.; Beard, M. C.; Song, Q.; Reese, M. O.; Ellingson, R. J.; Nozik, A. J., Schottky Solar Cells Based on Colloidal Nanocrystal Films. *Nano Lett.* **2008**, *8* (10), 3488-3492.

16. Lan, X. Z.; Voznyy, O.; Kiani, A.; de Arquer, F. P. G.; Abbas, A. S.; Kim, G. H.; Liu, M. X.; Yang, Z. Y.; Walters, G.; Xu, J. X.; Yuan, M. J.; Ning, Z. J.; Fan, F. J.; Kanjanaboos,

P.; Kramer, I.; Zhitomirsky, D.; Lee, P.; Perelgut, A.; Hoogland, S.; Sargent, E. H., Passivation Using Molecular Halides Increases Quantum Dot Solar Cell Performance. *Adv. Mater.* **2016**, *28* (2), 299-304.

17. Zhang, X. L.; Santra, P. K.; Tian, L.; Johansson, M. B.; Rensmo, H.; Johansson, E. M. J., Highly Efficient Flexible Quantum Dot Solar Cells with Improved Electron Extraction Using MgZnO Nanocrystals. *Acs Nano* **2017**, *11* (8), 8478-8487.

18. Zhitomirsky, D.; Kramer, I. J.; Labelle, A. J.; Fischer, A.; Debnath, R.; Pan, J.; Bakr, O. M.; Sargent, E. H., Colloidal Quantum Dot Photovoltaics: The Effect of Polydispersity. *Nano Lett.* **2012**, *12* (2), 1007-1012.

19. Erslev, P. T.; Chen, H. Y.; Gao, J. B.; Beard, M. C.; Frank, A. J.; van de Lagemaat, J.; Johnson, J. C.; Luther, J. M., Sharp Exponential Band Tails in Highly Disordered Lead Sulfide Quantum Dot Arrays. *Phys. Rev. B* **2012**, *86* (15), 155313 (1-5).

20. Chuang, C. H. M.; Maurano, A.; Brandt, R. E.; Hwang, G. W.; Jean, J.; Buonassisi, T.; Bulovic, V.; Bawendi, M. G., Open-Circuit Voltage Deficit, Radiative Sub-Bandgap States, and Prospects in Quantum Dot Solar Cells. *Nano Lett.* **2015**, *15* (5), 3286-3294.

21. Yang, Z. Y.; Janmohamed, A.; Lan, X. Z.; de Arquer, F. P. G.; Voznyy, O.; Yassitepe, E.; Kim, G. H.; Ning, Z. J.; Gong, X. W.; Comin, R.; Sargent, E. H., Colloidal Quantum Dot Photovoltaics Enhanced by Perovskite Shelling. *Nano Lett.* **2015**, *15* (11), 7539-7543.

22. Dirin, D. N.; Dreyfuss, S.; Bodnarchuk, M. I.; Nedelcu, G.; Papagiorgis, P.; Itskos, G.; Kovalenko, M. V., Lead Halide Perovskites and Other Metal Halide Complexes As Inorganic Capping Ligands for Colloidal Nanocrystals. *J. Am. Chem. Soc.* **2014**, *136* (18), 6550-6553.

23. Zhang, H.; Jang, J.; Liu, W. Y.; Talapin, D. V., Colloidal Nanocrystals with Inorganic Halide, Pseudohalide, and Halometallate Ligands. *Acs Nano* **2014**, *8* (7), 7359-7369.

24. Zhang, X. L.; Zhang, J. D.; Phuyal, D.; Du, J.; Tian, L.; Oberg, V. A.; Johansson, M. B.; Cappel, U. B.; Karis, O.; Liu, J. H.; Rensmo, H.; Boschloo, G.; Johansson, E. M. J., Inorganic CsPbI3 Perovskite Coating on PbS Quantum Dot for Highly Efficient and Stable Infrared Light Converting Solar Cells. *Adv. Energy Mater.* **2018**, *8* (6), 1702049 (1-11).

25. Ning, Z. J.; Gong, X. W.; Comin, R.; Walters, G.; Fan, F. J.; Voznyy, O.; Yassitepe, E.; Buin, A.; Hoogland, S.; Sargent, E. H., Quantum-Dot-in-Perovskite Solids. *Nature* **2015**, *523* (7560), 324-328.

26. Burschka, J.; Pellet, N.; Moon, S. J.; Humphry-Baker, R.; Gao, P.; Nazeeruddin, M. K.; Gratzel, M., Sequential Deposition As a Route to High-Performance Perovskite-Sensitized Solar Cells. *Nature* **2013**, *499* (7458), 316-319.

27. Leijtens, T.; Eperon, G. E.; Noel, N. K.; Habisreutinger, S. N.; Petrozza, A.; Snaith, H. J., Stability of Metal Halide Perovskite Solar Cells. *Adv. Energy Mater.* **2015**, *5* (20), 1500963 (1-23).

28. Sytnykt, M.; Yakunin, S.; Schofberger, W.; Lechner, R. T.; Burian, M.; Ludescher, L.; Killilea, N. A.; YousefiAmin, A.; Kriegner, D.; Stangl, J.; Groiss, H.; Heiss, W., Quasi-epitaxial Metal-Halide Perovskite Ligand Shells on PbS Nanocrystals. *Acs Nano* **2017**, *11* (2), 1246-1256.

29. Balazs, D. M.; Dirin, D. N.; Fang, H. H.; Protesescu, L.; ten Brink, G. H.; Kooi, B. J.; Koyalenko, M. V.; Loi, M. A., Counterion-Mediated Ligand Exchange for PbS Colloidal Quantum Dot Super lattices. *Acs Nano* **2015**, *9* (12), 11951-11959.

30. Bakueva, L.; Gorelikov, I.; Musikhin, S.; Zhao, X. S.; Sargent, E. H.; Kumacheva, E., PbS Quantum Dots With Stable Efficient Luminescence in the Near-IR Spectral Range. *Adv. Mater.* **2004**, *16* (11), 926-929.

31. Bertolotti, F.; Dirin, D. N.; Ibanez, M.; Krumeich, F.; Cervellino, A.; Frison, R.; Voznyy, O.; Sargent, E. H.; Kovalenko, M. V.; Guagliardi, A.; Masciocchi, N., Crystal Symmetry Breaking and Vacancies in Colloidal Lead Chalcogenide Quantum Dots. *Nat. Mater.* **2016**, *15* (9), 987-994.

32. Mitzi, D. B., Synthesis, Crystal Structure, and Optical and Thermal Properties of $(C_4H_9NH_3)_2MI_4$ (M = Ge, Sn, Pb). *Chem. Mater.* **1996**, *8* (3), 791-800.

33. Cao, D. H.; Stoumpos, C. C.; Farha, O. K.; Hupp, J. T.; Kanatzidis, M. G., 2D Homologous Perovskites as Light-Absorbing Materials for Solar Cell Applications. *J. Am. Chem. Soc.* **2015**, *137* (24), 7843-7850.

34. Yang, Z. Y.; Voznyy, O.; Walters, G.; Fan, J. Z.; Liu, M.; Kinge, S.; Hoogland, S.; Sargent, E. H., Quantum Dots in Two-Dimensional Perovskite Matrices for Efficient Near-Infrared Light Emission. *Acs Photonics* **2017**, *4* (4), 830-836.

35. Zherebetskyy, D.; Scheele, M.; Zhang, Y. J.; Bronstein, N.; Thompson, C.; Britt, D.; Salmeron, M.; Alivisatos, P.; Wang, L. W., Hydroxylation of the Surface of PbS Nanocrystals Passivated with Oleic Acid. *Science* **2014**, *344* (6190), 1380-1384.

36. Patterson, A. L., The Scherrer Formula for X-Ray Particle Size Determination. *Phys. Rev.* **1939**, *56* (10), 978-982.

37. Norton, C. S. M. G., *X-Ray Diffraction: Apractical Approach*. Plenum Press: New York, USA, 1998.

38. Wang, Z. N.; Yang, G.; Zhang, Z. R.; Jin, M. S.; Yin, Y. D., Selectivity on Etching: Creation of High-Energy Facets on Copper Nanocrystals for CO2 Electrochemical Reduction. *Acs Nano* **2016**, *10* (4), 4559-4564.

39. Xia, Y. N.; Xiong, Y. J.; Lim, B.; Skrabalak, S. E., Shape-Controlled Synthesis of Metal Nanocrystals: Simple Chemistry Meets Complex Physics? *Angew. Chem. Int. Ed.* **2009**, *48* (1), 60-103.

40. Hyun, B. R.; Zhong, Y. W.; Bartnik, A. C.; Sun, L. F.; Abruna, H. D.; Wise, F. W.; Goodreau, J. D.; Matthews, J. R.; Leslie, T. M.; Borrelli, N. F., Electron Injection from Colloidal PbS Quantum Dots into Titanium Dioxide Nanoparticles. *Acs Nano* **2008**, *2* (11), 2206-2212.

41. Lin, Y.; Bai, Y.; Fang, Y. J.; Chen, Z. L.; Yang, S.; Zheng, X. P.; Tang, S.; Liu, Y.; Zhao, J. J.; Huang, J. S., Enhanced Thermal Stability in Perovskite Solar Cells by Assembling 2D/3D Stacking Structures. *J. Phys. Chem. Lett.* **2018**, *9* (3), 654-658.

42. Zhao, N.; Osedach, T. P.; Chang, L. Y.; Geyer, S. M.; Wanger, D.; Binda, M. T.; Arango, A. C.; Bawendi, M. G.; Bulovic, V., Colloidal PbS Quantum Dot Solar Cells with High Fill Factor. *Acs Nano* **2010**, *4* (7), 3743-3752.

43. Pradhan, S.; Stavrinadis, A.; Gupta, S.; Bi, Y.; Di Stasio, F.; Konstantatos, G., Trap-State Suppression and Improved Charge Transport in PbS Quantum Dot Solar Cells with Synergistic Mixed-Ligand Treatments. *Small* **2017**, *13* (21), 1700598 (1-9).

44. Ip, A. H.; Thon, S. M.; Hoogland, S.; Voznyy, O.; Zhitomirsky, D.; Debnath, R.; Levina, L.; Rollny, L. R.; Carey, G. H.; Fischer, A.; Kemp, K. W.; Kramer, I. J.; Ning, Z. J.; Labelle, A. J.; Chou, K. W.; Amassian, A.; Sargent, E. H., Hybrid Passivated Colloidal Quantum Dot Solids. *Nat. Nanotechnol.* **2012**, *7* (9), 577-582.

45. Li, Z.; Gao, F.; Greenham, N. C.; McNeill, C. R., Comparison of the Operation of Polymer/Fullerene, Polymer/Polymer, and Polymer/Nanocrystal Solar Cells: A Transient Photocurrent and Photovoltage Study. *Adv. Funct. Mater.* **2011**, *21* (8), 1419-1431.

46. Bi, Y.; Pradhan, S.; Gupta, S.; Akgul, M. Z.; Stavrinadis, A.; Konstantatos, G., Infrared Solution-Processed Quantum Dot Solar Cells Reaching External Quantum Efficiency of 80% at 1.35 µm and J(sc) in Excess of 34 mA cm(-2). *Adv. Mater.* **2018**, *30* (7), 1704928 (1-6).

Chapter 5

Hybrid passivated quantum dot ink attains thinner shell growth and clean energy bandgap for photovoltaic application

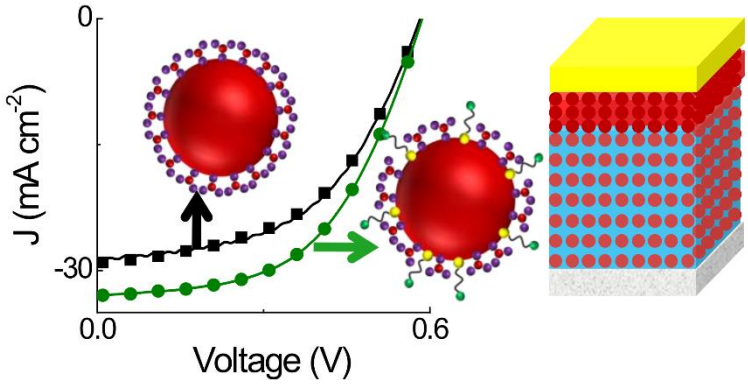

Abstract:

Tunable band gap colloidal QDs is a potential building block to harvest the wide energy solar spectrum. The solution-phase surface passivation with lead halide based halometallate ligands has remarkably simplified the processing of quantum dots (QDs) and enabled the proficient use of materials for the development of solar cells. It is, however, shown that the halometallate ligand passivated QD ink allows the formation of a thick crystalline shell layer, which limits the carrier transport in QD solids. Organic thiols have long been used to develop QD solar cells using a solid-state ligand exchange approach. However, their use is limited in solution-phase passivation due to poor dispersity of thiol treated QDs in common solvents. In this chapter, a joint passivation strategy using thiol and halometallate ligand is developed to prepare the QD ink. The mutually passivated QDs show a 50% reduction in shell thickness, reduced trap density, and improved monodispersity in their solid films. These improvements lead to a four-time increase in carrier mobility and doubling of the diffusion length, which enables the carrier extraction from a much thicker absorbing layer. The photovoltaic devices show the high efficiency of 10.3% and reduced hysteresis effect. The improvement in surface passivation leads to reduced oxygen doping and improved ambient stability of the solar cells.

5.1 Introduction

The quantum confinement effect of inorganic semiconductors has opened up the renewed possibility for the low bandgap semiconductors, which were earlier deemed unfit for the single-junction solar cell applications.[1,2] Widen material scope, solution-phase processability, and unique optical properties have established the quantum dots (QDs) as one of the promising candidates for the low cost, high-efficiency third-generation photovoltaic technology. Lead sulfide(PbS) based QDs are at the forefront of QD based solar cell research due to their wide bandgap tunability, low-temperature processability, and ambient stability.[3] Since their inception, the performance of PbS solar cells has shown steady improvements and recently reached the respectable efficiency of 12.4% in single-junction solar cells.[4-9] Tunable and deep NIR coverage of low bandgap PbS QDs find useful application to boost the performance of silicon and perovskite-based solar cells in the tandem configuration.[10-12] The long perused solid-state layer-by-layer ligand exchange strategy[13-15] has lately been substituted by solution-phase ligand exchange[13,16,17] to develop production compatible QD ink for large-area manufacturing. The ease of processing in solution-phase ligand exchange also facilitates regular arrangement and reduced energy disorder of QDs in solid films to attain record photovoltaic performance.[18]

Due to the aforementioned processing advantages and superior electronic properties, the solution-phase ligand exchange process has gained significant research attention lately.[9,10,16,19,20] In solution-phase ligand exchange, the surfactants are required to passivate the surface states of the QDs, alongside; they should enable the dispersion of QDs in a volatile organic solvent for thin film deposition. Lead halides in conjugation with different organic and inorganic halide salts (CH_3NH_3I, NH_4I, CsI, and $CH_3CH_2COONH_4$) have been used as surfactants to perform the solution-based ligand exchange in dimethylformamide (DMF). In DMF solution, the surfactants dissociate to form $[PbI_3]^-$ and $[X]^+$ (X= CH_3NH_3, NH_4, Cs); where the halometallate anions bind to the unsaturated Pb atoms of the PbS QD and the $[X]^+$ cations form a diffusive layer to provide colloidal stability and charge balance to the QD surface.[18] However, deposition of thick QD film using spin-coating from DMF solution is challenging due to its high boiling point and viscosity, as discussed in the previous chapter. Volatile butylamine (BA) or mix-amine (BA and a small proportion of hexylamine) are used as solvents to deposit thick QD films using spin-coating.[9,18] In the previous chapter, it is shown that BA (or HA) reacts with $[PbI_3]^-$ $[X]^+$ ligands to form thick

shell layer on the QD surface.[9,20] In solid films, the QDs are shown to be embedded in the 2D matrix of BA_2PbI_4 perovskite[9] and Pb-amine complex.[20,21] The matrix layer is shown to form lattice matching solder between the PbS QDs.[19,22] The carrier transport in such QD solids is, however, sensitive to the thickness of the shell layer, from the perspective both of electronic tunnelling and of resonance energy transfer. Control over the matrix growth would be beneficial for the efficient transport of the photocarriers in photovoltaic devices. In the earlier chapter, the use of NH_4I instead of CH_3NH_3I reduces the shell thickness of PbS QDs, which leads to higher carrier mobility and greater photovoltaic performance.[20] Small chain organic molecules with thiol as anchoring group have been studied widely to passivate the QD surface and used extensively in layer-by-layer solar cell building.[23,24] A monolayer of thiol molecules can proficiently passivate the QD surface. However, the thin films deposited using the layer-by-layer process suffer from inhomogeneous ligand exchange, QD aggregation, and leftover organic residue, which limit their charge transport.[24] Poor dispersity of small thiol molecule passivated QDs in organic solvents, so far renders their use in solution-phase ligand exchange.[25] Mutual passivation of QD surface using thiol and halide ligands have been achieved in the past, using the layer-by-layer approach,[26,27] where dispersity of the QDs was not a concern. Such hybrid passivation enabled higher ligand loading on the QD surface, reduce trap states, and improve carrier mobility to boost the solar cell performance.[26-28] Earlier reports on solution-phase ligand exchange use the combination of lead halide and organic salts (CH_3NH_3I, NH_4I, and $CH_3CH_2COONH_4$), but the organic part does not participate directly to passivate the terminal QD surface sites.[9,16,20] Iodine atoms are shown to passivate the unsaturated metal atoms of the QD surface while the role of the organic part is limited to provide colloidal stability and charge balance to the QD.[29] We envisage that solution-phase hybrid passivation of QDs using halometallate and thiol molecule would be rewarding in providing more excellent surface coverage to attain cleaner energy bandgap QDs solids.

In this chapter, we showcase a hybrid passivation strategy, compatible with solution-phase ligand exchange, where the PbS QD surface is passivated mutually by 3-Chloro-1-propanethiol (CPT) and lead halide-NH_4I based halometallate ligand. Only PbI_2 +AI treated QDs are presented as AI in the rest of the chapter. The hybrid passivation is carried out in two steps; after partial ligand exchange with CPT ligand of as-synthesized QDs, the AI+PbI_2 ligand treatment is further carried out in the DMF solution phase. The hybrid passivation is

demonstrated in the rest of the chapter as CPT+AI. To the best of our knowledge, this was the first report on the all solution-phase hybrid passivation of QDs using inorganic halometallate and organic thiol ligands. The hybrid passivation gives rise to a high solar cell performance of 10.3% under simulated solar illumination. The optical and electronic properties of PbS QDs improved considerably due to an increase in monodispersity and reduced electronic trap states in the case of hybrid passivation. The most significant impact of hybrid passivation is realized in matrix shell layer growth, which is reduced by 50%, enabling a four times increase in carrier transport. Improved carrier mobility and reduced trap states allow the efficient collection of photocarriers from a much thicker QD absorber layer, leading to the enhancement in J_{sc} and PCE of the photovoltaic devices. The hybrid passivation also reduces the oxygen doping to the light-absorbing QD layer to improve the stability of the un-encapsulated solar cells under ambient operation.

5.2 Experimental Details

Synthesis of ZnO and PbS NCs were followed earlier mentioned methods in section 4.2.1 and 4.2.2.

5.2.1 Partial Ligand exchange of PbS QDs:

The as-synthesized QDs solution was transferred to a glovebox without any cleaning step being performed. 1mmol CPT in 2.5 ml ODE was injected into the PbS QDs solution and stirred for half an hour at 70°C. Then the mixture was allowed to settle to room temperature and cleaned two times by acetone precipitation and toluene dispersion. Finally, CPT treated PbS QDs were dispersed in octane for halometallate ligand exchange.

5.2.2 Halometallate Ligand exchange of PbS QDs:

In 5 mL of DMF, 0.1M NH_4I and 0.075M PbI_2 and 0.025M $PbBr_2$ were mixed to get a clear transparent yellow color solution. 5mL of PbS QDS (15mg/mL) was added with DMF ligand precursor and mixed vigorously for two minutes. Within two-minute PbS QDs were transferred from octane to DMF phase. The top octane layer was discarded, and the DMF phase was cleaned another two times by the addition of octane. The ligand exchange QDs were precipitated by toluene addition and collected by centrifugation. The QDs were then dried under vacuum for 20 minutes and finally dispersed in BA (250mg/mL) for film deposition. The aforementioned procedure was followed to treat the CPT treated QDs for mutual passivation, and OA capped QDs for only halometallate passivation.

5.2.3 Device Fabrication

ITO substrates were cleaned before by following the previously mentioned method in section 2.2.4.

Pre-synthesized ZnO NCs were deposited on top of cleaned ITO by spin coating at 3000RPM, and substrates are heated around 250°C for 40 minutes. On top of the ZnO substrate, the QDs ink was spin coated. The films were then transferred to a glovebox to anneal at 70°C for 15 minutes. By changing acceleration and rotation speed, device thickness was varied from 160 nm to 500nm. The hole transport layer (60 nm) was deposited using 1,2 ethanedithiol (EDT) treated PbS QDs following the reported layer by layer method. To complete the device fabrication, electrode deposition was carried out by a thermal evaporator (HHV BC-300) at the base pressure of 1×10^{-6} Torr; 8 nm of MoO_3, 30 nm of Au, and 100 nm of Ag were deposited sequentially.

5.2.4 Materials Characterization Techniques

Optical absorption measurements were carried out by Shimadzu UV-Vis-NIR (UV-3600 Plus) spectrophotometer. Thin-film absorption was measured with the help of an integrating sphere (ISR-603), attached to Shimadzu UV-3600 Plus spectrophotometer. Steady-state photoluminescence measurements were performed utilizing Spectrofluorometer FS5, Edinburgh instruments. XPS was carried out using the thermo scientific K-Alpha$^+$ spectrometer in ultrahigh vacuum condition (10^{-9} mbar). XPS measurements were performed with a monochromatic Al Kα x-ray source (1486.6 eV) with pass energy 50 eV for individual core levels. The XPS spectra were calibrated to the C 1s peak at a binding energy of 284.8 eV. The fitting of the XPS spectra was performed by casa XPS software. All the measurements were carried out using an electron flood gun source for surface charge neutralization. UPS measurement was also carried out by the same instrument. He-Iα radiation of energy 21.22 eV was used for the UPS measurement. Cross-sectional and surface images of the device were taken by field emission scanning electron microscope (FESEM NNS 450). High-resolution images of QDs were captured by high resolution transmitted electron microscope (HRTEM, JEOL JEM 2200FES).

5.2.5 Device Characterization Techniques

J-V, EQE, Cap-V, Photo-CELIV, and Transient measurements (TPV, TPC) measurements were carried out, and all the measurements procedures were followed by

already mentioned methods in section 2.2.6.1, 2.2.6.3, 2.2.6.4, 3.2.4.3, and 3.2.4.4, respectively.

5.3 Results and Discussions

5.3.1 XPS analysis

The hybrid passivation with CPT and halometallate ligand has been carried out in two steps. In the first step, the as-synthesized oleic acid (OA) passivated PbS QDs are partially ligand-exchanged with CPT (See Experimental section 5.2.3). In the partial ligand exchange step, some of the OA ligands are replaced by CPT molecules; however, a critical number of OA ligands remain on the QD surface to disperse them in organic non-polar solvents. The QDs are then cleaned and taken in octane for halometallate (lead halide and ammonium iodide) ligand treatment, following the previous chapter 4 to prepare the QD ink. The particular halometallate ligand treatment is known to form $[PbI_3]^-$ Stern layer on the QD surface while the cationic component $[NH_4]^+$ forms the diffuse layer to provide the charge balance and colloidal dispersity to the QDs in DMF solvent.[18] It is imperative to check whether the CPT passivation survives the halometallate ligand treatment. We carried out X-ray photoelectron spectroscopy (XPS) for the CPT+AI and only AI treated PbS QDs. For the XPS study, thin films of PbS QDs are deposited from their BA dispersion on Au coated silicon substrates.

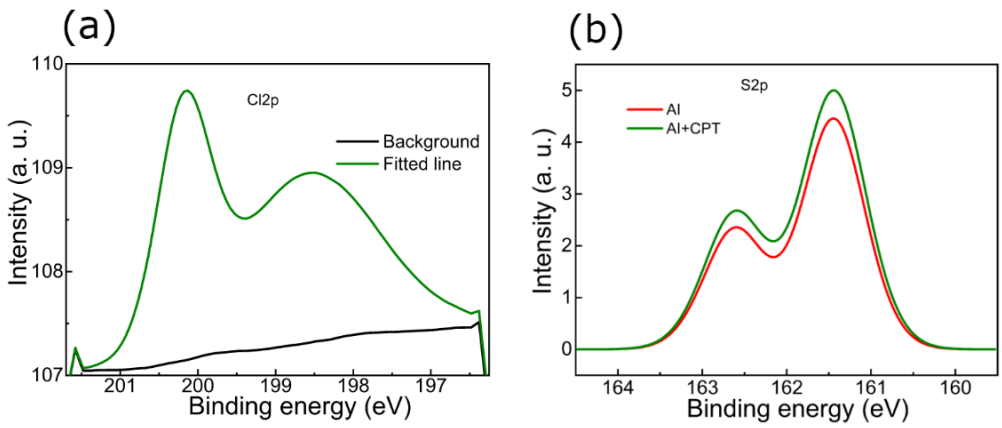

Figure 5.1: (a) High-resolution XPS spectrum of Cl2p orbital of CPT+AI treated PbS QD film. (b) XPS spectrum of S2p orbital, indicating an increase in intensity and broadening of $S2p_{3/2}$ and $S2p_{1/2}$ peaks for CP+AI treated QD films. The background signal has been subtracted for the presentation.

The Cl2p orbital peaks ($Cl2p_{3/2}$ and $Cl2p_{1/2}$) are found in the CPT+AI treated QD film (Figure 5.1a), implying the presence of CPT molecule on the QD surface. No Cl2p peaks are observed in only AI treated films. The atomic percentage of different atoms (Cl, S, Pb, I, N, O, and C) calculated from XPS analysis are compared for both AI and CPT+AI treated films in Table 5.1.

Table 5.1: Atomic ratio of different elements for AI and CPT+AI treated PbS QDs from XPS.

Name of ligand	Atomic ratio (%)						
	Cl	O	I	Pb	N	S	C
AI	0	0.899	23.570	35.694	1.416	22.423	15.997
CPT+AI	1.387	0.618	19.588	36.271	0.711	24.005	17.419

The analysis of the XPS spectrum shows that the atomic contribution (%) of S increases in CPT-AI film due to thiol attachment, compared to AI film (Figure 5.1b and Table 5.1).

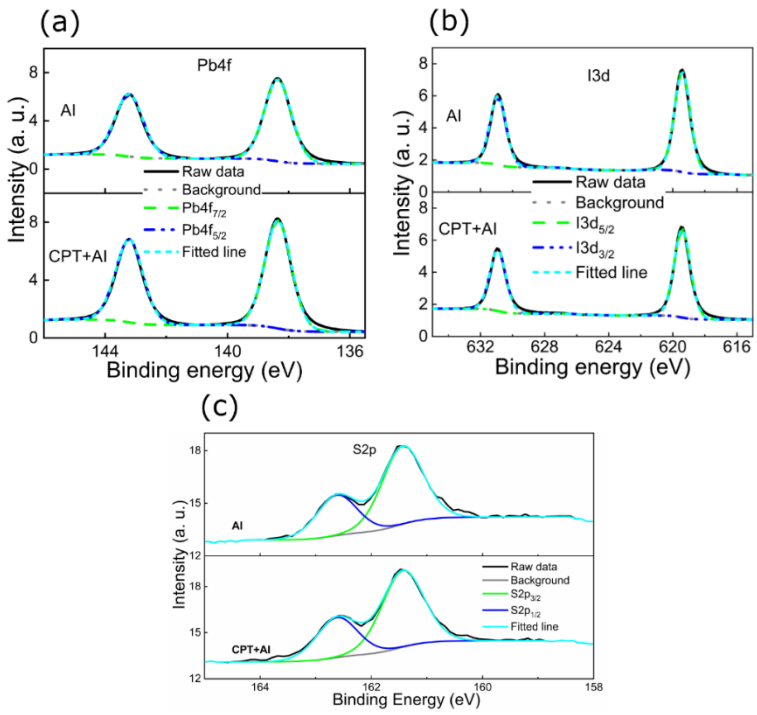

Figure 5.2: Deconvoluted high-resolution XPS spectrum of (a) Pb4f, (b) I3d, and (c) S2p binding energies for AI and CPT+AI treated QD films. The splitting of orbital energies is fitted using CASA XPS software.

Deconvolution of Pb4f, I3d, and S2p binding energy spectra for AI and CPT+AI treated QDs are shown in Figure 5.2a, b, and c, respectively. With respect to AI treated PbS film, the FWHM increases for $S2p_{3/2}$ (0.87 eV to 0.89 eV) and $S2p_{1/2}$ (0.85 eV to 0.87 eV) binding energies in the case of CPT+AI film. This could be due to the fact that the surface-bound thiol molecules have different binding energy than the Pb-S bond of PbS QDs. The attachment of the thiol molecule to the under-co-ordinate surface Pb atoms, therefore, leads to the broadening of the S2p binding energies. The XPS data clearly suggests that the Pb-thiol bond is robust enough to endure the assault of halometallate ligand treatment.

It is very important to study the amount of oxygen doping in QDs films as oxygen is known to form intermediate trap states inside the bandgap of PbS QDs. The unpassivated sites of PbS QDs can be easily oxidized by atmospheric oxygen during processing in ambient condition. Compact surface passivation restricts the surface oxidation of QDs.

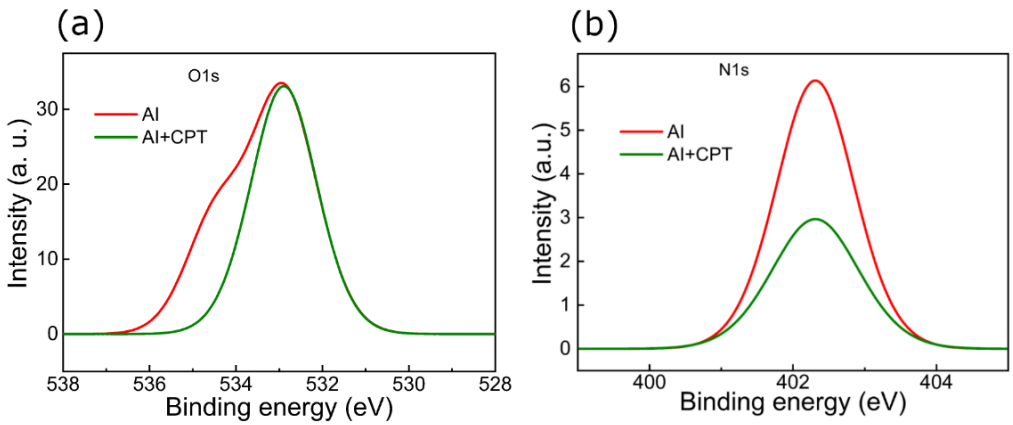

Figure 5.3: (a) High-resolution XPS spectrum of O1s orbital and (b) N1s orbital for AI and CPT+AI treated PbS QD films.

In this study, the oxygen content in AI treated films is much higher than the AI+CPT treated films. The comparison of high-resolution O1s XPS spectrum shows one peak for CPT+AI, and two peaks for AI treated PbS QDs (Figure 5.3a). The peak at 532.5 eV is attributed to the hydroxyl peak (Pb-OH), which is commonly present at the PbS (111) surface[30]; however, the peak at higher energy (534.1 eV) is attributed to the oxygen adsorption (in the form of COO- and CO_2) at the QD surface.[31] In the previous chapter, we have shown that the growth of the 2D matrix layer on QDs surface during the dispersion in BA solvent of AI ligand treated QDs. The 2D matrix is composed of $(BA)_2PbI_4$ and Pb-amine complex. As the 2D matrix contains an amine compound, so the atomic percentage of N signifies the 2D matrix

layer thickness. Higher the N content denotes the formation of a thicker 2D matrix. The atomic ratio of N (and I), which constitutes the shell layer, is found to be higher in the case of AI treated QDs (Table 5.1 and Figure 5.3b). In the case of hybrid passivation, the organic CPT ligand restricts the growth of the 2D matrix.

5.3.2 UPS study

The effect of hybrid passivation is evident in the electronic landscape of the QDs, as observed through the ultraviolet photoelectron spectroscopy (UPS) measurement.

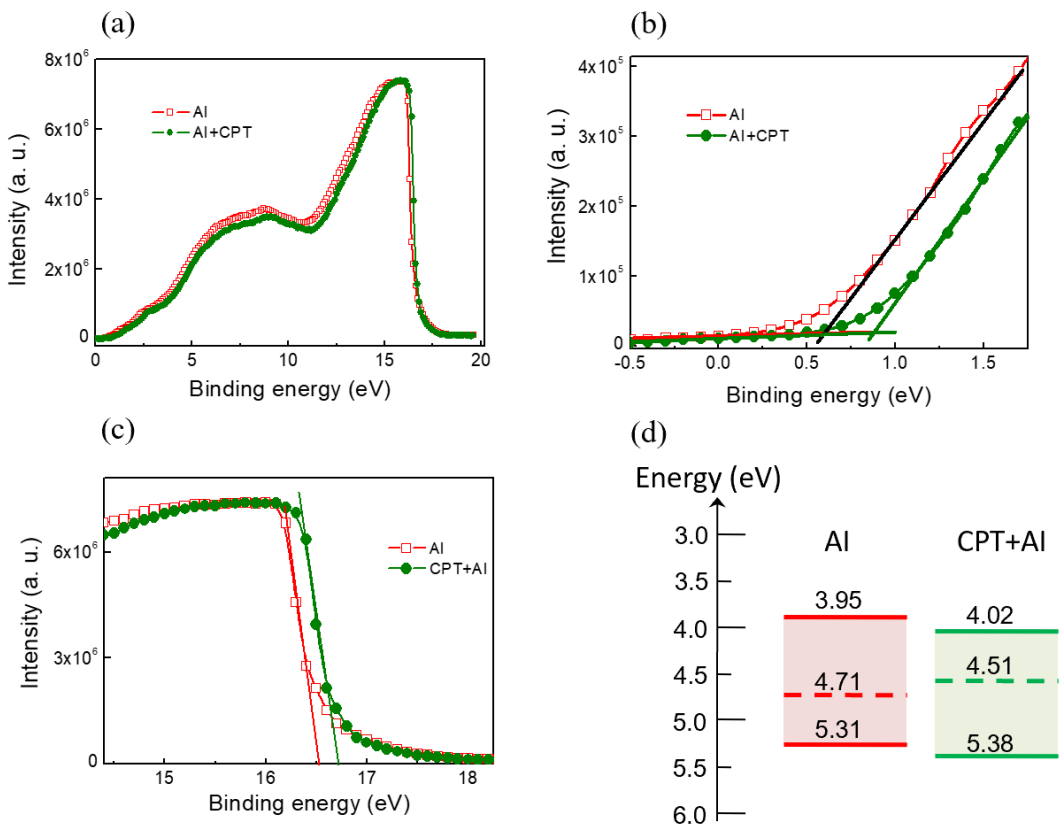

Figure 5.4: (a) Full-scale UPS spectrum of AI and CPT+AI treated PbS QD films. (b) and (c) shows the magnified view of the UPS spectrum to illustrate the valance band onset (low binding energy) and secondary cutoff regions (high binding energy), respectively. (d) The energy band positions of PbS QDs for different surface passivation are deduced from their UPS and absorption measurements.

The full rage UPS spectrums are shown in Figure 5.4a, and the magnified portion of low and high binding energy regions are shown in Figure 5.4b and 5.4c, respectively. The Fermi energy is determined from the high binding energy cut off using equation[32] ($E_F =$

$21.22\ eV - E_{cut\ off}$); and the difference between the valance band edge and Fermi energy is determined from the low energy threshold as shown in Figure 5.4b.[31] The energy band gap for the PbS QDs, determined from the first excitonic peak position (Figure 5.10), is 1.36 eV.[33] The energy band edges, as determined from UPS and absorbance data for AI and CPT+AI treated PbS QDs, are shown for comparison in Figure 5.4d. It is interesting to note here that the conduction band edge and valence band edge values are deeper by 0.07 eV while the Fermi energy is 0.2 eV shallower in CPT+AI treated PbS QDs. This may appear to be in contrast with the established knowledge that thiol passivation leads to shallower energy band values and *p*-type doping, whereas iodine passivation leads to deeper band edge positions and *n*-type doping to the PbS QDs.[32] A closer look at the XPS data (Table 5.1) shows that the oxygen content to the AI treated films are much higher compared to CPT+AI treated QDs, when processed in ambient condition. As oxygen is known as *p*-type dopant[34-36] to the PbS QDs, the higher oxygen content in AI treated film may lead to the *p*-type doping (deep Fermi energy) and shallow band edge values.

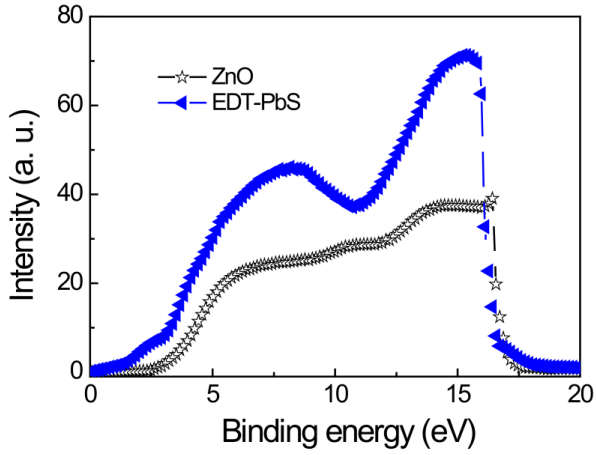

Figure 5.5: Full-scale UPS spectrum of ZnO (ETL) and EDT-PbS (HTL) layer.

Further, the UPS measurements for ZnO -electron transport layer and 1,2 ethanedithiol treated PbS QDs-hole transport layer is performed to determine their band alignment with the active PbS QD layer (Figure 5.5). We calculate the valance band, conduction band, and fermi energy level of individual layers of photovoltaic devices to understand the carriers transport mechanism.

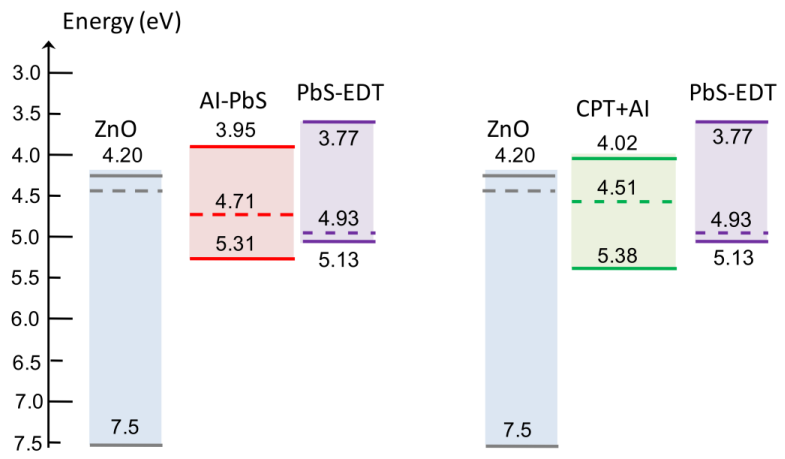

Figure 5.6: Valance band, Fermi energy, and conduction band position of different layers used in solar cells, determined from UPS and absorbance measurements. The layers are shown as per their arrangement in photovoltaic devices.

The energy band positions of the constituent layers used in the photovoltaic device fabrication are shown in Figure 5.6. Both the cases show favorable band alignment for the solar cell application, but deeper energy band positions of the CPT+AI layer would facilitate higher voltage generations in the solar cells.

5.3.3 Ligand structure characteristics

It is shown that the halometallate treated PbS QDs spin-coated from volatile BA forms a crystalline matrix in their solid films where the matrix layer consists of 2D $(BA)_2PbI_4$ perovskite[9] and 2D Pb-amine complex.[20] In order to probe the matrix layer, the ligand solution (one molar solution of PbI_2 and NH_4I in BA solvent) is spin-coated on glass substrates for the formation of the matrix layer. The XRD spectrum of the ligand film shows two sets of equidistant peaks with 2θ repetition of 4.99° and 6.26°, pertaining to 2D Pb-amine complex and 2D $(BA)_2PbI_4$ perovskite respectively as reported earlier (Figure 5.7a).[20] The absorption characteristic of the ligand film shows the 1st excitonic peak at 465 nm and a narrow band-edge emission peak centered at 515nm, which further supports the formation of the BA_2PbI_4 perovskite phase (Figure 5.7b).[9,20]

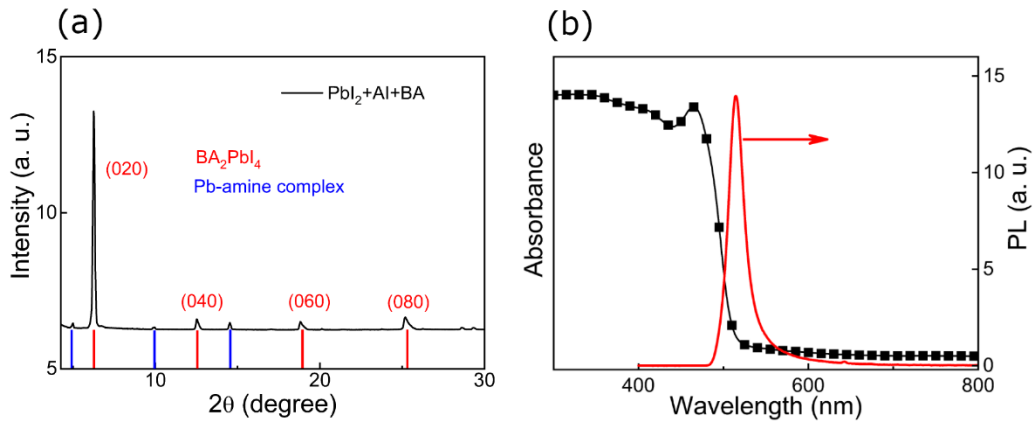

Figure 5.7: (a) XRD spectrum of PbI_2+AI+BA ligand film deposited on the glass substrate. The parallel peaks pertaining to BA_2PbI_4 and Pb-amine complex are shown by red and blue lines, respectively. (b) Absorbance and emission spectrum of the PbI_2+AI+BA ligand film deposited on the glass substrate. The excitation wavelength is 380 nm.

Further, we study crystal fringe analysis of only ligand (AI+PbI_2+BA) from HRTEM image (Figure 5.8). The d-spacing of the only ligand matrix as observed from the HRTEM image is 3.12±0.03 Å.

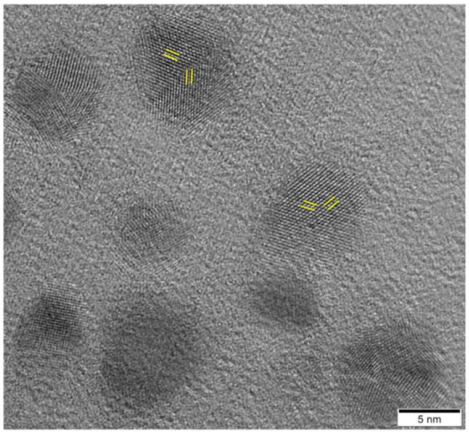

Figure 5.8: HRTEM image of the (PbI_2+AI+BA) ligand.

5.3.4 Absorption and PL study

First, we probe the change in the absorbance of PbS QDs due to the partial ligand exchange of oleic acid ligands by CPT ligands. The first excitonic peak of OA capped PbS QD is redshifted by 10 nm due to CPT partial ligand exchange (Figure 5.9a), indicating a small increase in PbS QD size due to thiol binding. Then we further study the optical

properties of both AI and CPT+AI ligand exchanged QDs. In the DMF solution, the relative emission intensity of the CPT+AI treated QD is three times higher than AI treated QDs (Figure 5.9b) for the fixed QD concentration.

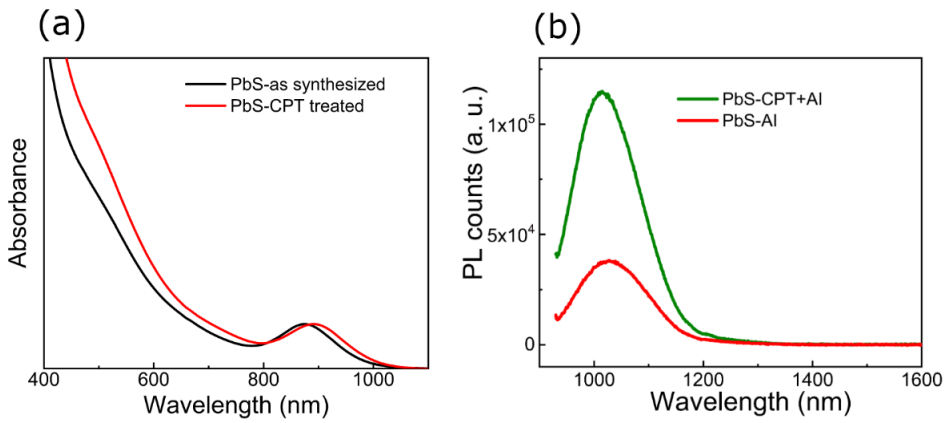

Figure 5.9: (a) The absorbance spectrum of OA capped PbS QDs and partially ligand-exchanged with CPT in toluene. (b) PL emission spectra of PbS QDs for different ligands in DMF solution. The concentration (0.16 mg/mL) and the excitation wavelength (550nm) are kept constant for both the ligands.

An increase in PL intensity implies superior QD surface properties in the case of hybrid passivation. Absorbance and photoluminescence (PL) measurements for AI and CPT+AI

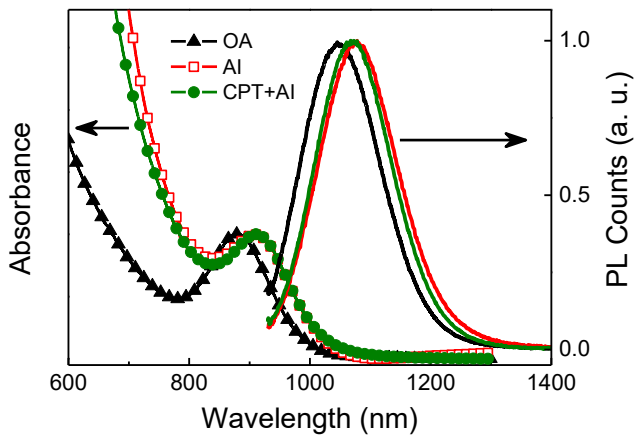

Figure 5.10: Normalized absorption and photoluminescence of PbS QD films treated with different surface ligands. The emission spectra are recorded for the excitation wavelength of 550 nm.

passivation are carried out on the thin films of PbS QDs, spin-coated from BA solution, for their resemblance with the solar cells (Figure 5.10).

Table 5.2. Absorbance and emission properties of PbS QD films for different surface passivation.

Ligand name	1st excitonic peak position (nm)	FWHM [absorbance] (nm)	PL peak position (nm)	FWHM [PL] (nm)	Stokes shift (nm)
OA	874	141	1057	155	183
AI	898	158	1080	155	182
CPT+AI	902	149	1072	150	170

The as-synthesized OA capped PbS QD film (formed from octane) is used as the reference. The 1st excitonic and PL peak intensities for OA, AI, and CPT+AI passivated PbS QD films are normalized for their comparison (Figure 5.10 and Table 5.2). The absorbance and the PL peaks are fitted with Gaussian type fitting to determine their full-width half maxima (FWHM).

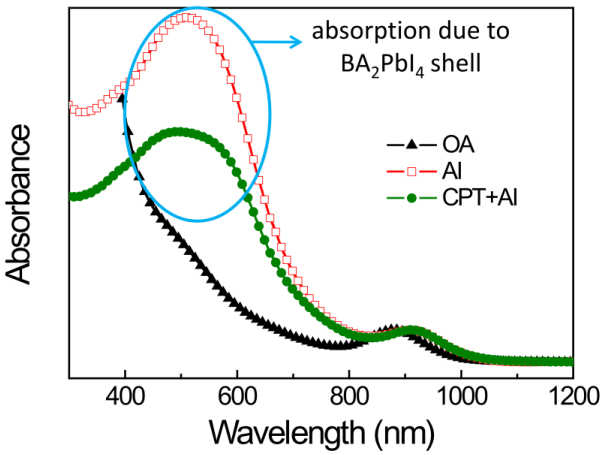

Figure 5.11: The absorbance spectra of PbS QD films treated with different ligands for the entire wavelength range of absorption. AI and CPT+AI treated PbS QDs films are deposited from their BA solution. The peak at 500 nm (as marked) is attributed to BA_2PbI_4 perovskite shell absorption.

With respect to AI passivation, hybrid passivation reduces the FWHM of absorbance (9 nm) and PL (5 nm) peaks. Further, the Stokes shift is minimum in the case of CPT+AI treated

QDs. Narrow absorbance and emission peak and less stokes shift suggest higher monodispersity of PbS QDs in the case of CPT+AI ligand passivation.[32] The full wavelength range absorption characteristic of PbS QD films for different ligand passivation (the magnified view is shown in Figure 5.10), is shown in Figure 5.11. In addition to the PbS excitonic peak (~910 nm), a broad hump centered around 500 nm is observed due to the perovskite shell formation in AI and CPT+AI treated QD films. Stronger absorption by the perovskite shell layer indicates higher shell thickness in the case of AI treated solar cells. The broadening and the redshift in the perovskite hump are attributed to the strong coupling and interfacial strain of the perovskite shell with the PbS QD core.[20] The high bandgap shell layer (~2.1 eV) forms type-I band alignment with the core PbS QD (~1.36 eV). Hence, a thicker shell layer is likely to deter carrier transport in solid films.[20]

5.3.5 TEM image analysis

The TEM image of OA capped PbS QDs is shown in Figure 5.12a. The average diameter of the OA capped PbS QDs is 3 nm (Figure 5.12b). It is calculated from the statistical distribution of particles.

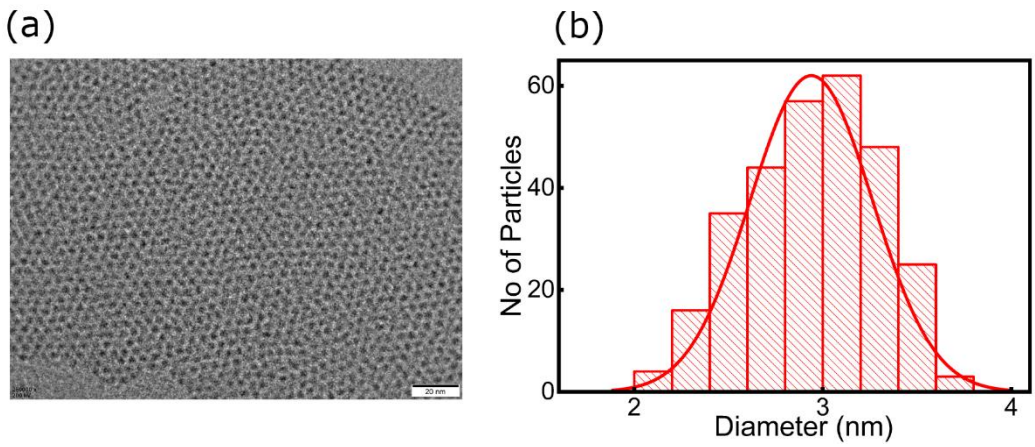

Figure 5.12: (a) TEM image and (b) particle size distribution of oleic acid capped QDs.

The TEM images of the PbS QDs treated with AI and CPT+AI are shown in Figure 5.13a & 5.13b, respectively. The average diameter of PbS QD plus the crystalline ligand shell in the case of AI ligand is 9.8 nm and for CPT+AI is 6.5 nm. The distribution of the size for the core-shell particles (PbS QD core and ligand shell) is shown in Figure 5.13c. The absorption data (Figure 5.10) suggests that the excitonic peak of OA capped PbS QDs redshifts by (~25 nm) when treated with AI or CPT+AI ligands. The redshift could be due

to the diffusion of Pb and S atoms during the ligand exchange process. The absorbance redshift would account for approximately 0.12 nm increases in QD diameter due to the quantum confinement effect. Therefore, the excess increase in diameter in the case of AI

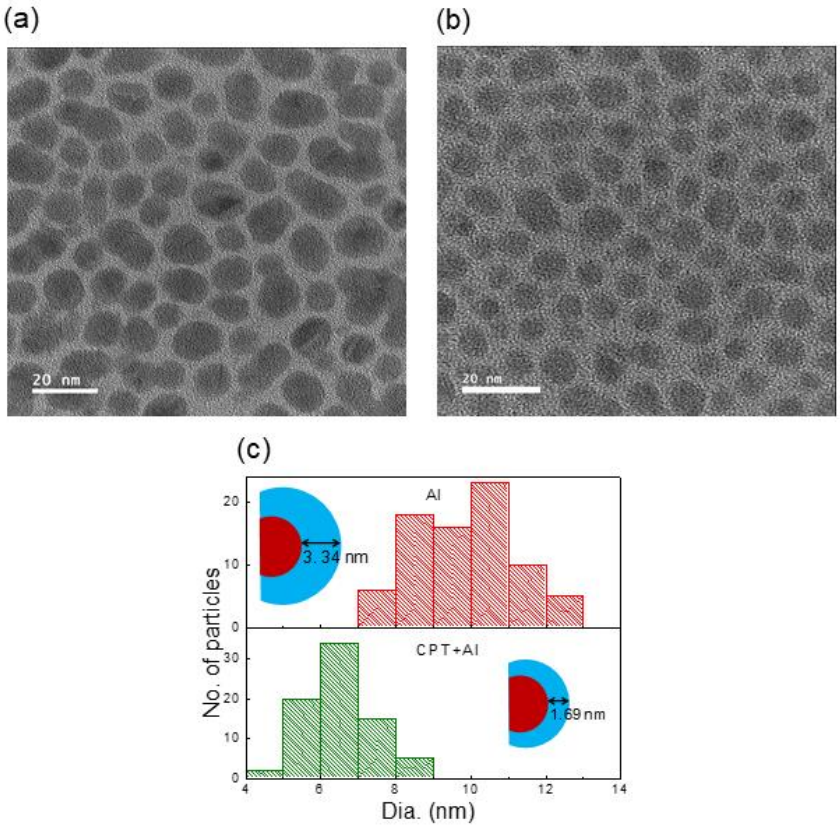

Figure 5.13: TEM images of (a) AI and (b) CPT+AI passivated PbS QDs. (c) shows the distribution of particle size (PbS core and ligand shell) for different ligand treatments. The average shell thicknesses for the respective ligands are shown at the inset.

and CPT+AI treated QDs as observed in TEM images are attributed to the thickness of the ligand shell. The situation is depicted schematically at the inset of Figure 5.13c, where the respective shell thickness for AI (3.34 nm) and CPT+AI (1.69 nm) is marked. The higher shell thickness of AI exchanged QDs further corroborated with the previously discussed XPS results. The atomic ratio of N, which presents in the shell layer, is found to be higher in the case of AI-treated QDs than hybrid passivated QDs (Table 5.1 and Figure 5.3b). The crystal fringes for AI and CPT+AI treated PbS QDs have shown in Figure 5.14a and 5.14b, respectively. The interplanar spacing in both cases is found to be 3.15±0.03 Å. The d-spacing of the only ligand matrix as observed from the HRTEM image (Figure 5.8) matches identically with the d-spacing spacing of AI and CPT+AI treated PbS QDs. Further, the d-

spacing of the oleic acid capped PbS QDs (111) plane is 3.40Å (Figure 5.14c), which comes close to the interplanar spacing of the matrix layer, which may enable the quasi-epitaxial growth of the shell layer on the PbS QD surface.

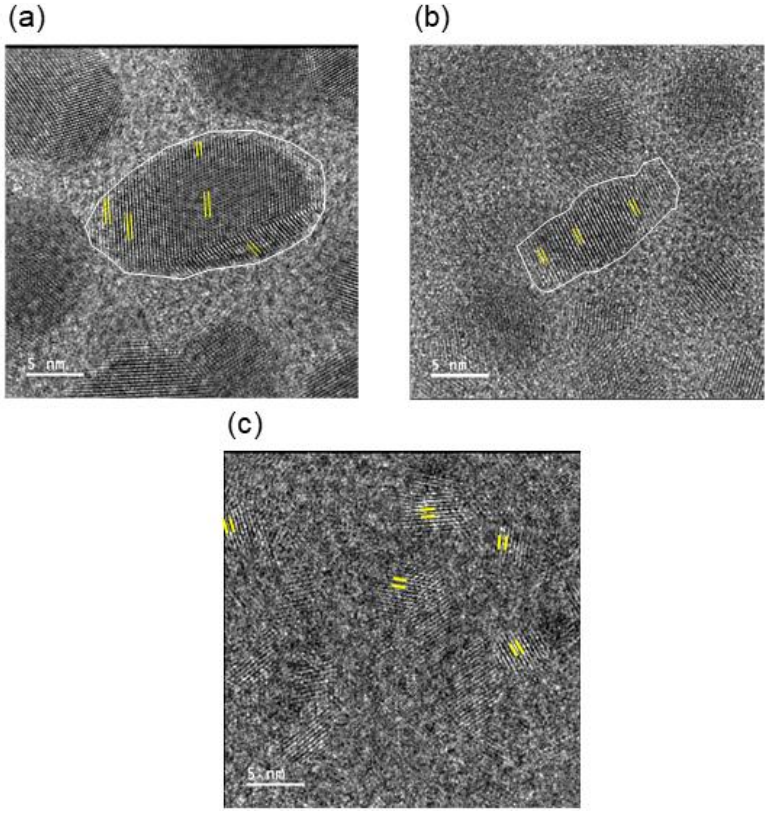

Figure 5.14: Magnified HRTEM images of (a) AI and (b) CPT+AI passivated and (c) oleic acid capped PbS QDs.

TEM study clearly suggests that in the case of mutual passivation, the shell thickness is reduced by 50%. This could be due to the fact that the addition of the CPT ligand reduces the nucleation centers ($[PbI_3]^-$) and increases inhomogeneity at the QD surface, which deters the growth of the thick perovskite shell layer. It is envisaged that the thinner shell layer would decrease the inter-dot distances and benefit the carrier transport in mutually passivated films.

5.3.6 Surface SEM and AFM image

SEM images of AI-treated QD films show some uneven texture which might be due to the growth of the 2D matrix. This leads to the formation of nanostructures at their surface whereas, the hybrid passivated films are smoother and free from such nanostructure formation (Figure 5.15). The hybrid passivation restricts the growth of 2D layers on QDs

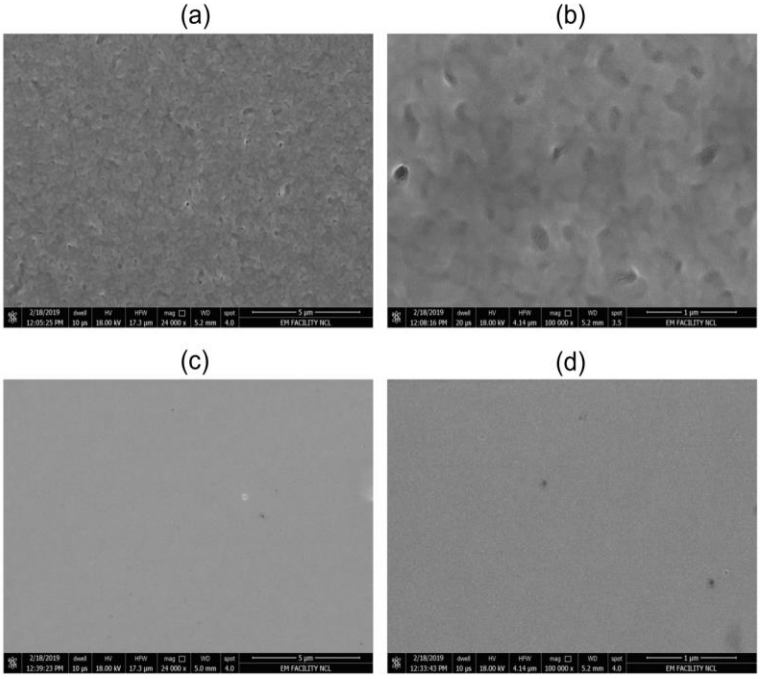

Figure 5.15: The SEM images of AI (a & b) and CPT+AI (c & d) treated PbS QD films for different magnifications (5µm and 1µm).

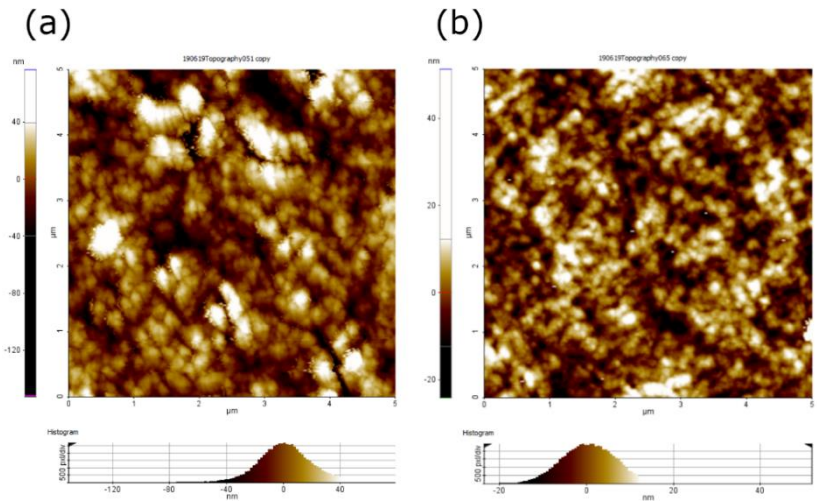

Figure 5.16: The AFM images of (a) AI treated and (b) CPT+AI treated PbS QD films. The average roughness for AI and CPT+AI treated film are found to be 15 nm and 5 nm, respectively.

surface due to the CPT attachment and maintain the QDs shape and size. We have also collected the AFM images of both AI treated, and hybrid passivated films (Figure 5.16). Bigger size grains are observed in the AFM image of AI treated QD film; as a result, the

average roughness in AI treated film (15 nm) is much higher than CPT+AI treated (5 nm) QD film.

5.3.7 Cross-sectional SEM image of device

The solar cells are fabricated with the following device structure: ITO/ ZnO (ETL-100 nm) /PbS-CPT+AI (/AI)/ PbS-EDT (HTL-60 nm)/ MoO_3 (8 nm)/ Au (30 nm)/Ag (100 nm).

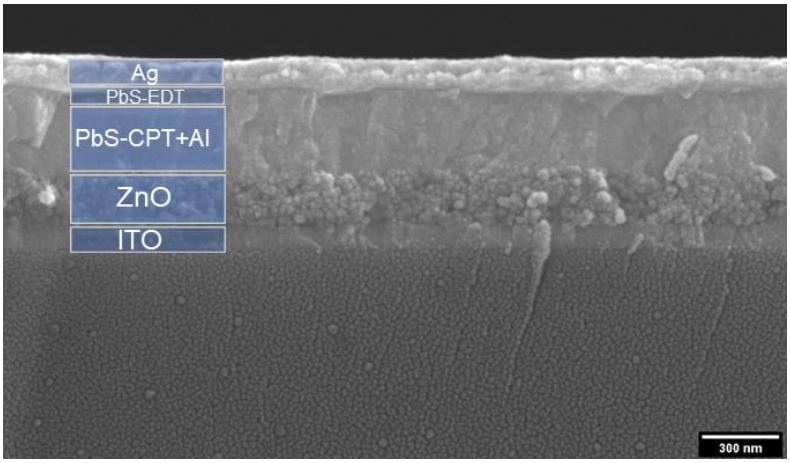

Figure 5.17: The cross-sectional image of a solar cell indicating distinguishable different layers.

The cross-section image of a typical solar cell, indicating all the layers, is shown in Figure 5.17. For device thickness optimization, the PbS-CPT+AI active layer thickness is varied by changing the spin speed.

5.3.8 J-V characteristics

To check the impact of hybrid passivation, solar cell devices were fabricated. The PCE of both AI and AI+CPT treated solar cells are measured from their J-V curves (Figure 5.18). The solar cell made of CPT+AI treated QDs shows lower hysteresis and higher J_{sc} in their J-V characteristics compared to AI treated QDs. AI treated QDs integrated solar cells show a significantly higher hysteresis effect while changing the scanning direction. Photovoltaic parameters for the representative optimized solar cells for AI and CPT+AI passivation are shown in Table 5.3 for their comparison. The PCE of hybrid passivated QDs integrated solar cell has reached 10.3%, whereas the only halometallate passivated QDs fabricated solar cell has shown 8.7% PCE.

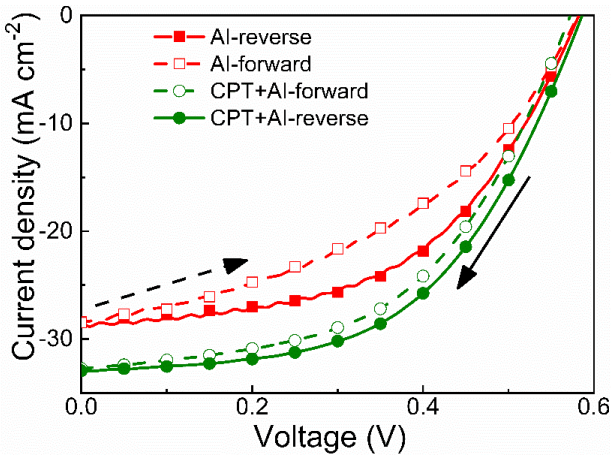

Figure 5.18: Reverse and forward scan J-V characteristics (scan rate 0.1V s^{-1}) for AI and CPT+AI treated solar cells under AM1.5 simulated solar illumination.

Table 5.3. Photovoltaic parameters for optimized solar cells.

Name of the ligand	Scan direction	J_{sc} (mA cm^{-2})	V_{oc} (V)	FF (%)	PCE (%)
AI	reverse	28.43	0.58	53.06	8.74
	forward	28.4	0.58	43.01	7.08
CPT+AI	reverse	32.94	0.59	53.07	10.31
	forward	32.68	0.57	52.06	9.71

The PCE and corresponding photovoltaic parameters (Voc, Jsc, and FF) are probed for different batches of devices. The statistical variation of all the photovoltaic parameters and overall PCE for different batches of both AI and CPT+AI treated solar cells are presented in Figure 5.19.

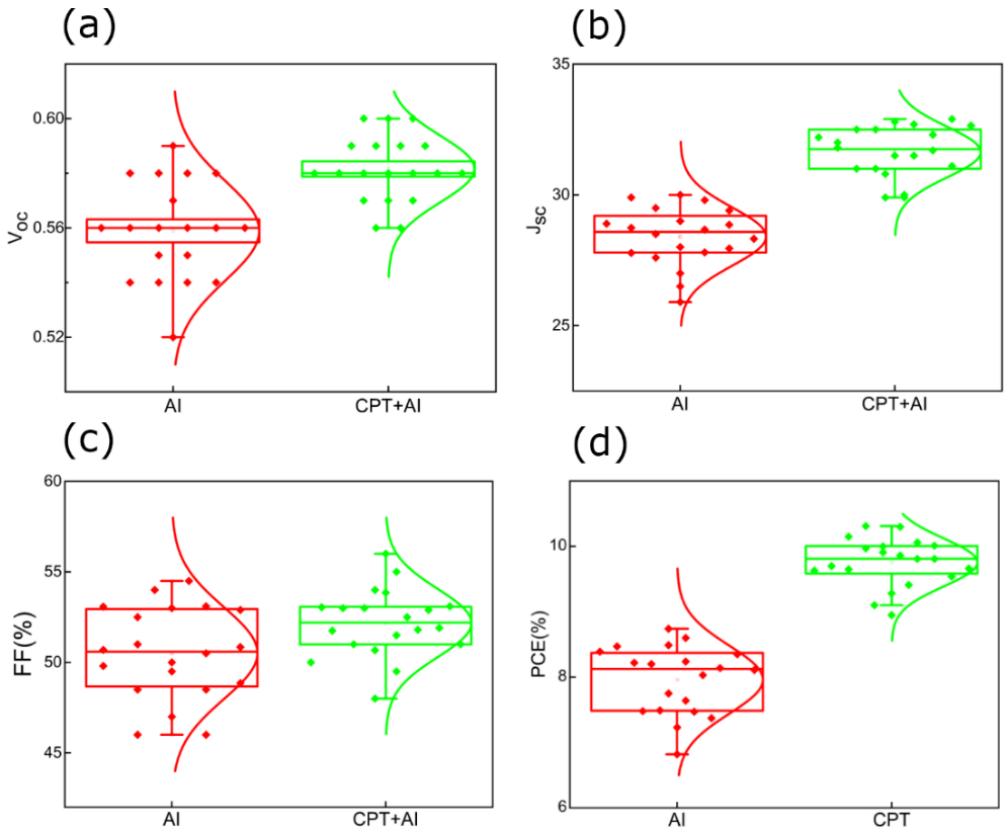

Figure 5.19: The statistical variation of (a) V_{oc}, (b) J_{sc}, (c) FF%, and (d) PCE% for different batches of AI and CPT+AI treated solar cells.

The data shows a clear improvement in PCE in the case of hybrid passivation compared to only halometallate treatment.

5.3.9 Device Thickness optimization

The active layer (PbS-AI/PbS-AI+CPT) thickness-dependent J-V curves for AI and CPT+AI treated solar cells are given in Figure 5.20. From the above study, the optimum thicknesses for the PbS QD layer for CPT+AI and AI passivation are found to be 430 nm and 310 nm, respectively.

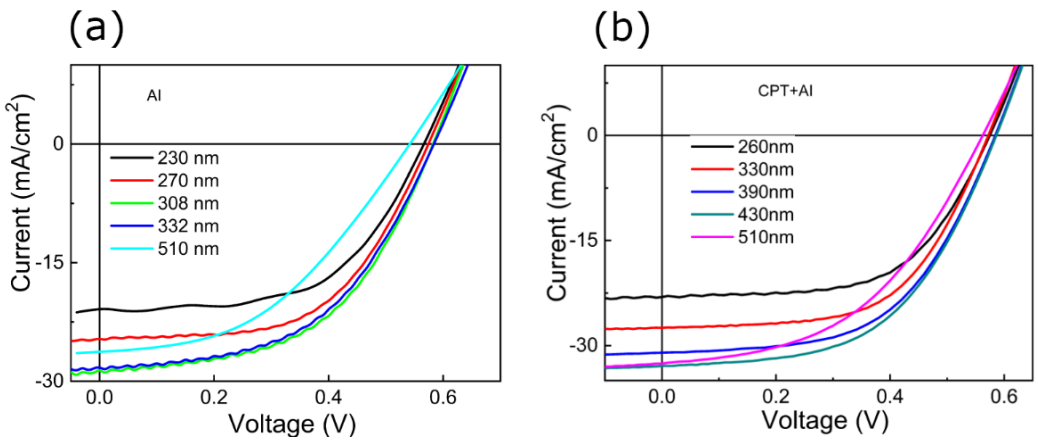

Figure 5.20: Thickness dependent J-V curves for (a) AI and (b) CPT+AI treated solar cells.

The active layer thickness vs. PCE is compared in Figure 5.21. Higher absorber layer thickness in the case of CPT+AI treated solar cells leads to the increase in J_{sc} without significant reduction in the FF.

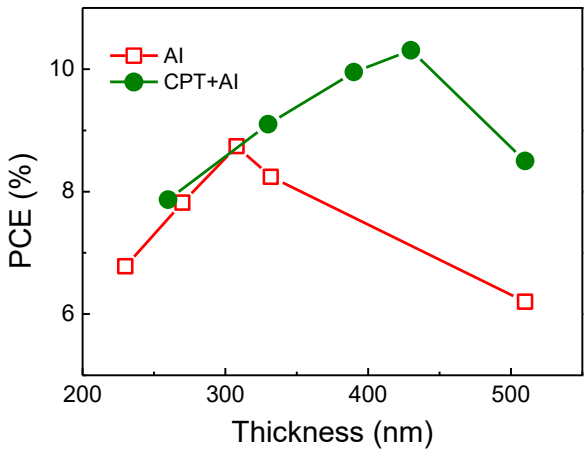

Figure 5.21: The evolution of PCE of the solar cells with active absorber layer thickness for (a) AI and (b) CPT+AI ligand passivation.

5.3.10 EQE spectrum

The external quantum efficiency (EQE (%)) data clearly indicates the enhancement in the NIR photoconversion efficiency (Figure 5.22). The integrated Jsc from the EQE spectrum (shown in the right axis of Figure 5.22) for the individual solar cells matches closely with their experimentally measured J_{sc} under simulated solar illumination.

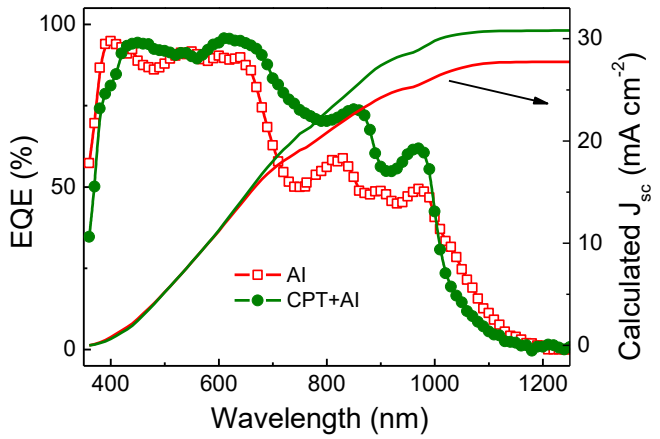

Figure 5.22: EQE (%) of AI and CPT+AI ligand treated the solar cells. The axis on the right side indicates the predicted J_{sc} under simulated solar illumination from the EQE spectrums.

5.3.11 Cap-V analysis

Carrier depletion width is determined from the capacitance-voltage characteristics, measured at the dark condition (Figure 5.23). The CPT+AI treated solar cell shows depletion

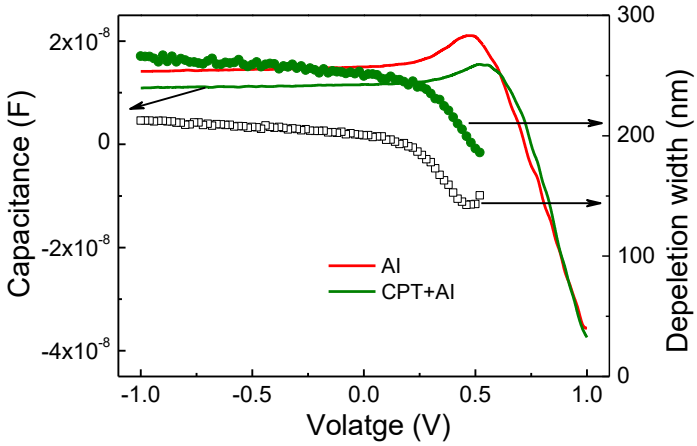

Figure 5.23: Capacitance-voltage characteristics of the solar cells measured at 1K Hz at a scan rate of 0.1V s^{-1}. The depletion widths for the respective solar cells (right-hand axis) at different voltages are shown.

width of 250 nm and 230 nm respectively at zero bias and at maximum power point respectively, in comparison to 200 nm and 180 nm for AI treated solar cells. Higher depletion width facilitates the efficient carrier collection from thicker QD layer in the case of CPT+AI treated solar cells.

5.3.12 Power dependant V_{oc} study

Diode ideally factor for the solar cells are determined using the intensity-dependent generation of V_{oc}, using the equation[37] $V_{oc} = \frac{\eta KT}{q} \ln(\phi)$; where η -diode ideality factor, K-Boltzman constant, T-temperature, q-electronic charge and ϕ-photon flux.

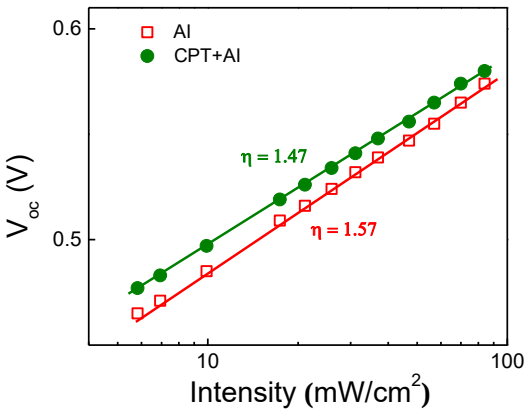

Figure 5.24: Change of V_{oc} at varied light intensity (ϕ). From the slope of the V_{oc} vs. ln(ϕ) plot, the diode ideality factor (η) is determined for the solar cells.

Lower η value of CPT+AI treated solar cell implies lesser trap recombination in CPT+AI than AI treated solar cells (Figure 5.24).[38]

5.3.13 Device stability

The stability of the AI and CPT+AI treated un-encapsulated solar cells is further studied, at different time intervals. The solar cells are exposed to ambient condition for

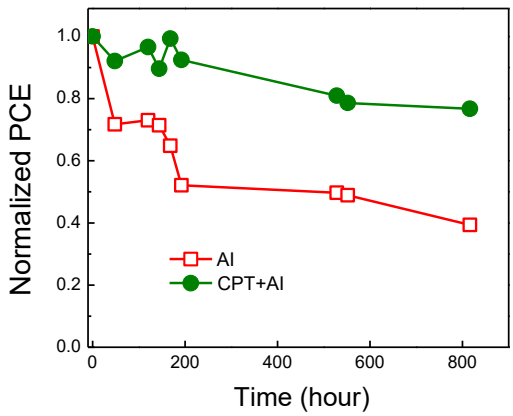

Figure 5.25: Stability data for the un-encapsulated solar cells stored in Argon glove box and measured at different time intervals in ambient air.

studies, at different time intervals. The solar cells are exposed to ambient condition for the performance testing, otherwise stored in an Ar-glove box. After 800 hours, the CPT+AI treated solar cells retain 80% when AI passivation loses 50% of their initial performance (Figure 5.25).

5.3.14 Photo-CELIV analysis

It is envisaged that the reduced shell thickness would impact favorably on the carrier transport properties of the QD solid. Charge carrier mobility is determined using the photo-induced carrier extraction by linearly increasing voltage (photo-CELIV) technique for solar cell devices.[23,39] Initially, a short light pulse is applied to the solar cell to create photocarriers.

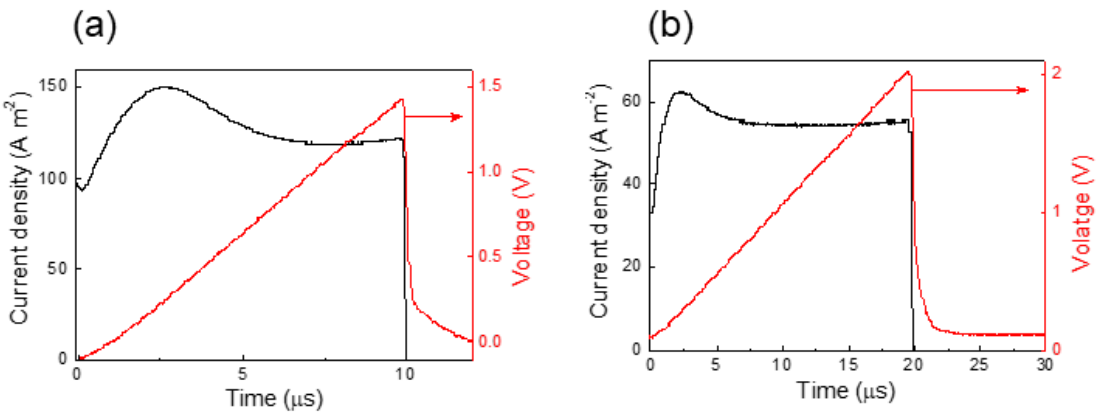

Figure 5.26: Photo-CELIV measurement of (a) AI and (b) CPT+AI treated solar cells. The evolution of solar cell current under the influence of linearly increasing voltage pulse is shown.

After a few microseconds of time delay, a linearly increasing voltage pulse with a suitable voltage ramp is applied in reverse bias to extract the free carriers from the solar cell (details of photo-CELIV measurement is given in the experimental section). The evolution of current under the influence linearly increasing voltage pulse for AI and CPT+AI treated PbS QD solar cells are shown in Figure 5.26a and 5.26b, respectively. Charge carrier mobility is estimated using the equation[39] $\mu_h = \frac{2d^2}{3At_{max}^2\left(1+0.36\frac{\Delta J}{J_d}\right)}$; where A -is voltage ramp rate, t_{max} -is the time for the transient current signal to reach its maximum value, ΔJ -is the maximum drift current, and J_d -is the displacement current, and d is the PbS QD layer thickness. The QD layer thicknesses of 420 nm and 593 nm are used for AI and CPT+AI, respectively, for the photo-CELIV study. The carrier mobility for AI and CPT+AI treated solar cells are

found to be 1.10x10^{-3} cm^{2}V^{-1}s^{-1} and 4.38x10^{-3} cm^{-2}V^{-1}s$^{-1,}$ respectively, indicating a four times increase in carrier mobility in hybrid passivated QD solid. The average shell thickness of CPT+AI treated QDs (1.69 nm) is 50% lower than AI treated QDs (3.34 nm), as shown in Figure 5.13c, which leads to four times increase in carrier mobility in the hybrid passivated QDs. The carrier extraction depth in solar cells is controlled by the product of carrier mobility and lifetime.

5.3.15 Carrier lifetime and DOS calculation

We cared to measure the photocarrier lifetime using transient photovoltage measurement at different light biases.[23,35] The carrier lifetime in the case of CPT+AI is found to be marginally higher than AI treated solar cells at all open-circuit voltages (Figure 5.27a). At full solar illumination, the carrier diffusion length for AI and CPT+AI solar cells is estimated to be 95 nm and 200 nm, respectively, from the carrier mobility and lifetime values.[23] The density of trap state is further determined using the transient photovoltage and transient photocurrent measurements as discussed in the fourth chapter of section 4.3.12.[20,26,40] The density of trap states at any given V_{oc} is found to be lower in CPT+AI treated devices than AI passivated devices (Figure 5.27b).

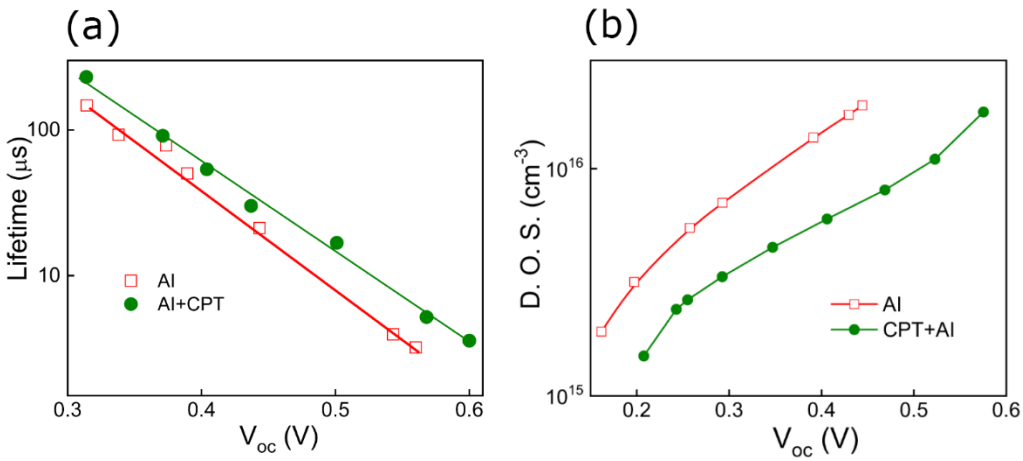

Figure 5.27: (a) Photo carrier lifetime and (b) density of trap states at different V_{oc} of AI and CPT+AI treated solar cells.

Lower trap density and thinner shell layer would jointly responsible for higher carrier mobility and lifetime values for the mutually passivated QDs. The higher trap density of AI treated QDs is further correlated with the amount of oxygen contents on the QDs surface. Oxygen is known to form intermediate trap states inside the bandgap of PbS QDs.[41,42] The

excess oxygen doping in AI-treated QDs, as shown in Figure 5.3a, would likely the reason for their higher trap density (Figure 5.27b) and deeper Fermi energy (Figure 5.4d). From the above results, it can be inferred that some of the surface sites of PbS QDs are left unpassivated by the halometallate ligands, which are vulnerable to the oxygen attack. The implementation of mutual passivation covers the surface sites more efficiently to protect the QDs from oxidation and improve their size selectivity in solid films. Further, the mutual passivation leads to the formation trap deprived QDs solids with high carrier mobility, which helps to reduces recombination and enhance carrier collection to increase the solar cell performance.

5.4 Conclusion

In summary, a hybrid passivation scheme has been commenced to decorate the PbS QD surface with thiol and halometallate ligands. The passivation strategy is compatible with the solution-phase ligand exchange process and allows developing quantum dot ink for the one-step deposition of thick and conducting QD film. Advancement in surface engineering enables higher monodispersity and lower trap density in QD solids. Mutually passivated QDs show lower shell growth and reduced oxygen doing, which helps to attain a four times increase in carrier mobility, doubles the diffusion length, and cleaner energy band bap in solid films. As a result, the photovoltaic devices show higher PCE% and lower hysteresis in their *J-V* characteristics. Thiol passivation is particularly useful to passivate the surface sites which are otherwise inaccessible to halometallate ligands to improve resilience towards oxygen attack and prolong the lifetime of the solar cells. We envisage that the developed mutual passivation strategy can be extended to other organic and inorganic ligand combinations as well and would be beneficial to the development of QD based optoelectronic devices like light-emitting diodes and tandem solar cells.

5.5 References

(1) Carey, G. H.; Abdelhady, A. L.; Ning, Z. J.; Thon, S. M.; Bakr, O. M.; Sargent, E. H. Colloidal Quantum Dot Solar Cells. *Chem. Rev.* **2015**, *115* (23), 12732-12763.

(2) Yuan, M. J.; Liu, M. X.; Sargent, E. H. Colloidal Quantum Dot Solids for Solution-Processed Solar Cells. *Nat. Energy* **2016**, *1*, 16016.

(3) Kramer, I. J.; Sargent, E. H. The Architecture of Colloidal Quantum Dot Solar Cells: Materials to Devices. *Chem. Rev.* **2014**, *114* (1), 863-882.

(4) McDonald, S. A.; Konstantatos, G.; Zhang, S. G.; Cyr, P. W.; Klem, E. J. D.; Levina, L.; Sargent, E. H. Solution-Processed PbS Quantum Dot Infrared Photodetectors and Photovoltaics. *Nat. Mater.* **2005**, *4* (2), 138-142.

(5) Luther, J. M.; Gao, J. B.; Lloyd, M. T.; Semonin, O. E.; Beard, M. C.; Nozik, A. J. Stability Assessment on a 3% Bilayer PbS/ZnO Quantum Dot Heterojunction Solar Cell. *Adv. Mater.* **2010**, *22* (33), 3704-3707.

(6) Rath, A. K.; Bernechea, M.; Martinez, L.; de Arquer, F. P. G.; Osmond, J.; Konstantatos, G. Solution-Processed Inorganic Bulk Nano-Heterojunctions and Their Application to Solar Cells. *Nat. Photonics* **2012**, *6* (8), 529-534.

(7) Chuang, C. H. M.; Brown, P. R.; Bulovic, V.; Bawendi, M. G. Improved Performance and Stability in Quantum Dot Solar Cells Through Band Alignment Engineering. *Nat. Mater.* **2014**, *13* (8), 796-801.

(8) Lan, X. Z.; Voznyy, O.; de Arquer, F. P. G.; Liu, M. X.; Xu, J. X.; Proppe, A. H.; Walters, G.; Fan, F. J.; Tan, H. R.; Liu, M.; Yang, Z. Y.; Hoogland, S.; Sargent, E. H. 10.6% Certified Colloidal Quantum Dot Solar Cells via Solvent Polarity-Engineered Halide Passivation. *Nano Lett.* **2016**, *16* (7), 4630-4634.

(9) Xu, J. X.; Voznyy, O.; Liu, M. X.; Kirmani, A. R.; Walters, G.; Munir, R.; Abdelsamie, M.; Proppe, A. H.; Sarkar, A.; de Arquer, F. P. G.; Wei, M. Y.; Sun, B.; Liu, M.; Ouellette, O.; Quintero-Bermudez, R.; Li, J.; Fan, J.; Quan, L. N.; Todorovic, P.; Tan, H. R.; Hoogland, S.; Kelley, S. O.; Stefik, M.; Amassian, A.; Sargent, E. H. 2D Matrix Engineering for Homogeneous Quantum Dot Coupling in Photovoltaic Solids. *Nat. Nanotechnol.* **2018**, *13* (6), 456-462.

(10) Kim, T.; Firdaus, Y.; Kirmani, A. R.; Liang, R. Z.; Hu, H. L.; Liu, M. X.; El Labban, A.; Hoogland, S.; Beaujuge, P. M.; Sargent, E. H.; Amassian, A. Hybrid Tandem Quantum Dot/Organic Solar Cells with Enhanced Photocurrent and Efficiency via Ink and Interlayer Engineering. *Acs Energy Lett.* **2018**, *3* (6), 1307-1314.

(11) Karani, A.; Yang, L.; Bai, S.; Futscher, M. H.; Snaith, H. J.; Ehrler, B.; Greenham, N. C.; Di, D. W. Perovskite/Colloidal Quantum Dot Tandem Solar Cells: Theoretical Modeling and Monolithic Structure. *Acs Energy Lett.* **2018**, *3* (4), 869-874.

(12) Bi, Y.; Pradhan, S.; Gupta, S.; Akgul, M. Z.; Stavrinadis, A.; Konstantatos, G. Infrared Solution-Processed Quantum Dot Solar Cells Reaching External Quantum Efficiency of 80% at 1.35 mu m and J(sc) in Excess of 34 mA cm(-2). *Adv. Mater.* **2018**, *30* (7), 1704928.

(13) Kagan, C. R.; Lifshitz, E.; Sargent, E. H.; Talapin, D. V. Building Devices From Colloidal Quantum Dots. *Science* **2016**, *353* (6302), aac5523.

(14) Lu, K. Y.; Wang, Y. J.; Liu, Z. K.; Han, L.; Shi, G. Z.; Fang, H. H.; Chen, J.; Ye, X. C.; Chen, S.; Yang, F.; Shulga, A. G.; Wu, T.; Gu, M. F.; Zhou, S. J.; Fan, J.; Loi, M. A.; Ma, W. L. High-Efficiency PbS Quantum-Dot Solar Cells with Greatly Simplified Fabrication Processing via "Solvent-Curing". *Adv. Mater.* **2018**, *30* (25), 180166.

(15) Zhang, X. L.; Johansson, E. M. J. Reduction of Charge Recombination in PbS Colloidal Quantum Dot Solar Cells at the Quantum Dot/ZnO Interface by Inserting a MgZnO Buffer Layer. *J. Mater. Chem. A* **2017**, *5* (1), 303-310.

(16) Yang, Z. Y.; Janmohamed, A.; Lan, X. Z.; de Arquer, F. P. G.; Voznyy, O.; Yassitepe, E.; Kim, G. H.; Ning, Z. J.; Gong, X. W.; Comin, R.; Sargent, E. H. Colloidal Quantum Dot Photovoltaics Enhanced by Perovskite Shelling. *Nano Lett.* **2015**, *15* (11), 7539-7543.

(17) Zhang, X. L.; Oberg, V. A.; Du, J.; Liua, J. H.; Johansson, E. M. J. Extremely Lightweight and Ultra-Flexible Infrared Light-Converting Quantum Dot Solar Cells With High Power-Per-Weight Output Using a Solution-Processed Bending Durable Silver Nanowire-Based Electrode. *Energy Environ. Sci.* **2018**, *11* (2), 354-364.

(18) Liu, M. X.; Voznyy, O.; Sabatini, R.; de Arquer, F. P. G.; Munir, R.; Balawi, A. H.; Lan, X. Z.; Fan, F. J.; Walters, G.; Kirmani, A. R.; Hoogland, S.; Laquai, F.; Amassian, A.; Sargent, E. H. Hybrid Organic-Inorganic Inks Flatten the Energy Landscape in Colloidal Quantum Dot Solids. *Nat. Mater.* **2017**, *16* (2), 258-263.

(19) Zhang, X. L.; Zhang, J. D.; Phuyal, D.; Du, J.; Tian, L.; Oberg, V. A.; Johansson, M. B.; Cappel, U. B.; Karis, O.; Liu, J. H.; Rensmo, H.; Boschloo, G.; Johansson, E. M. J. Inorganic CsPbI3 Perovskite Coating on PbS Quantum Dot for Highly Efficient and Stable Infrared Light Converting Solar Cells. *Adv. Energy Mater.* **2018**, *8* (6), 1702049.

(20) Mandal, D.; Rath, A. K. Quantum Dots Coupled to an Oriented Two-Dimensional Crystalline Matrix for Solar Cell Application. *ACS Appl. Mater. Interfaces* **2018**, *10* (45), 39074-39082.

(21) Yang, Z. Y.; Voznyy, O.; Walters, G.; Fan, J. Z.; Liu, M.; Kinge, S.; Hoogland, S.; Sargent, E. H. Quantum Dots in Two-Dimensional Perovskite Matrices for Efficient Near-Infrared Light Emission. *Acs Photonics* **2017**, *4* (4), 830-836.

(22) Ning, Z. J.; Gong, X. W.; Comin, R.; Walters, G.; Fan, F. J.; Voznyy, O.; Yassitepe, E.; Buin, A.; Hoogland, S.; Sargent, E. H. Quantum-dot-in-perovskite solids. *Nature* **2015**, *523* (7560), 324-328.

(23) Goswami, P. N.; Mandal, D.; Rath, A. K. The Role of Surface Ligands in Determining the Electronic Properties of Quantum Dot Solids and Their Impact on Photovoltaic Figure of Merits. *Nanoscale* **2018**, *10* (3), 1072-1080.

(24) Tang, J. A.; Sargent, E. H. Infrared Colloidal Quantum Dots for Photovoltaics: Fundamentals and Recent Progress. *Adv. Mater.* **2011**, *23* (1), 12-29.

(25) Fischer, A.; Rollny, L.; Pan, J.; Carey, G. H.; Thon, S. M.; Hoogland, S.; Voznyy, O.; Zhitomirsky, D.; Kim, J. Y.; Bakr, O. M.; Sargent, E. H. Directly Deposited Quantum Dot Solids Using a Colloidally Stable Nanoparticle Ink. *Adv. Mater.* **2013**, *25* (40), 5742--5749.

(26) Ip, A. H.; Thon, S. M.; Hoogland, S.; Voznyy, O.; Zhitomirsky, D.; Debnath, R.; Levina, L.; Rollny, L. R.; Carey, G. H.; Fischer, A.; Kemp, K. W.; Kramer, I. J.; Ning, Z. J.; Labelle, A. J.; Chou, K. W.; Amassian, A.; Sargent, E. H. Hybrid Passivated Colloidal Quantum Dot Solids. *Nat. Nanotechnol.* **2012**, *7* (9), 577-582.

(27) Pradhan, S.; Stavrinadis, A.; Gupta, S.; Bi, Y.; Di Stasio, F.; Konstantatos, G. Trap-State Suppression and Improved Charge Transport in PbS Quantum Dot Solar Cells with Synergistic Mixed-Ligand Treatments. *Small* **2017**, *13* (21), 1700598..

(28) Hong, J.; Hou, B.; Lim, J.; Pak, S.; Kim, B. S.; Cho, Y.; Lee, J.; Lee, Y. W.; Giraud, P.; Lee, S.; Park, J. B.; Morris, S. M.; Snaith, H. J.; Sohn, J. I.; Cha, S.; Kim, J. M. Enhanced Charge Carrier Transport Properties in Colloidal Quantum Dot Solar Cells via Organic and Inorganic Hybrid Surface Passivation. *J. Mater. Chem. A* **2016**, *4* (48), 18769-18775.

(29) Dirin, D. N.; Dreyfuss, S.; Bodnarchuk, M. I.; Nedelcu, G.; Papagiorgis, P.; Itskos, G.; Kovalenko, M. V. Lead Halide Perovskites and Other Metal Halide Complexes As Inorganic Capping Ligands for Colloidal Nanocrystals. *J. Am. Chem. Soc.* **2014**, *136* (18), 6550-6553.

(30) Zherebetskyy, D.; Scheele, M.; Zhang, Y. J.; Bronstein, N.; Thompson, C.; Britt, D.; Salmeron, M.; Alivisatos, P.; Wang, L. W. Hydroxylation of the Surface of PbS Nanocrystals Passivated With Oleic Acid. *Science* **2014**, 344 (6190), 1380-1384.

(31) Cao, Y. M.; Stavrinadis, A.; Lasanta, T.; So, D.; Konstantatos, G. The Role of Surface Passivation for Efficient and Photostable PbS Quantum Dot Solar Cells. *Nat. Energy* **2016**, *1*, 16035.

(32) Brown, P. R.; Kim, D.; Lunt, R. R.; Zhao, N.; Bawendi, M. G.; Grossman, J. C.; Bulovic, V. Energy Level Modification in Lead Sulfide Quantum Dot Thin Films through Ligand Exchange. *Acs Nano* **2014**, *8* (6), 5863-5872.

(33) Moreels, I.; Lambert, K.; Smeets, D.; De Muynck, D.; Nollet, T.; Martins, J. C.; Vanhaecke, F.; Vantomme, A.; Delerue, C.; Allan, G.; Hens, Z. Size-Dependent Optical Properties of Colloidal PbS Quantum Dots. *Acs Nano* **2009**, *3* (10), 3023-3030.

(34) Yuan, M. J.; Zhitomirsky, D.; Adinolfi, V.; Voznyy, O.; Kemp, K. W.; Ning, Z. J.; Lan, X. Z.; Xu, J. X.; Kim, J. Y.; Dong, H. P.; Sargent, E. H. Doping Control Via Molecularly Engineered Surface Ligand Coordination. *Adv. Mater.* **2013**, *25* (39), 5586-5592.

(35) Zhao, N.; Osedach, T. P.; Chang, L. Y.; Geyer, S. M.; Wanger, D.; Binda, M. T.; Arango, A. C.; Bawendi, M. G.; Bulovic, V. Colloidal PbS Quantum Dot Solar Cells with High Fill Factor. *Acs Nano* **2010**, *4* (7), 3743-3752.

(36) Kirmani, A. R.; Sheikh, A. D.; Niazi, M. R.; Haque, M. A.; Liu, M. X.; de Arquer, F. P. G.; Xu, J. X.; Sun, B.; Voznyy, O.; Gasparini, N.; Baran, D.; Wu, T.; Sargent, E. H.; Amassian, A. Overcoming the Ambient Manufacturability-Scalability-Performance Bottleneck in Colloidal Quantum Dot Photovoltaics. *Adv. Mater.* **2018**, *30* (35), 1801661.

(37) Chuang, C. H. M.; Maurano, A.; Brandt, R. E.; Hwang, G. W.; Jean, J.; Buonassisi, T.; Bulovic, V.; Bawendi, M. G. Open-Circuit Voltage Deficit, Radiative Sub-Bandgap States, and Prospects in Quantum Dot Solar Cells. *Nano Lett.* **2015**, *15* (5), 3286-3294.

(38) Speirs, M. J.; Dirin, D. N.; Abdu-Aguye, M.; Balazs, D. M.; Kovalenko, M. V.; Loi, M. A. Temperature Dependent Behaviour of Lead Sulfide Quantum Dot Solar Cells and Films. *Energy Environ. Sci.* **2016**, *9* (9), 2916-2924.

(39) Mozer, A. J.; Sariciftci, N. S.; Lutsen, L.; Vanderzande, D.; Osterbacka, R.; Westerling, M.; Juska, G. Charge Transport and Recombination in Bulk Heterojunction Solar Cells Studied by the Photoinduced Charge Extraction in Linearly Increasing Voltage Technique. *Appl. Phys. Lett.* **2005**, *86* (11), 112104.

(40) Shuttle, C. G.; O'Regan, B.; Ballantyne, A. M.; Nelson, J.; Bradley, D. D. C.; de Mello, J.; Durrant, J. R. Experimental Determination of the Rate Law for Charge Carrier Decay in a Polythiophene: Fullerene Solar Cell. *Appl. Phys. Lett.* **2008**, *92* (9), 093311.

(41) Tang, J.; Brzozowski, L.; Barkhouse, D. A. R.; Wang, X. H.; Debnath, R.; Wolowiec, R.; Palmiano, E.; Levina, L.; Pattantyus-Abraham, A. G.; Jamakosmanovic, D.; Sargent, E. H. Quantum Dot Photovoltaics in the Extreme Quantum Confinement Regime: The Surface-Chemical Origins of Exceptional Air- and Light-Stability. *Acs Nano* **2010**, *4* (2), 869-878.

(42) Boles, M. A.; Ling, D.; Hyeon, T.; Talapin, D. V. The Surface Science of Nanocrystals. *Nat. Mater.* **2016**, *15* (2), 141-153.

Chapter 6

Control over ligand ratio on thiol, halometallate mediated one-step hybrid passivation of quantum dots for photovoltaics

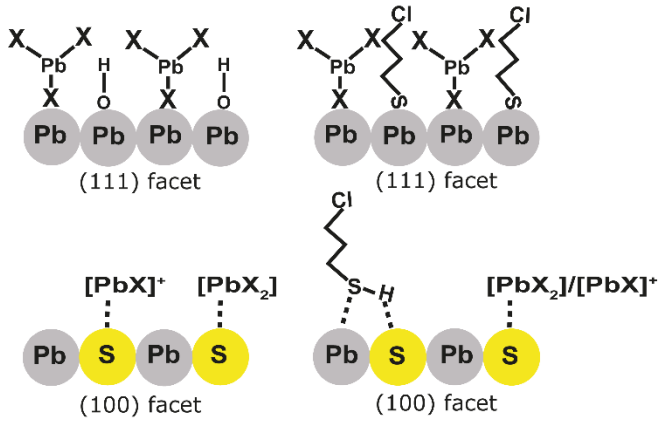

Abstract:

Tuning the electronic properties in semiconductor materials is crucial for optoelectronic device applications. Carrier doping in colloidal quantum dots (CQDs) can be controlled by the surface passivating ligands. Recent's advancements in halometallate ligand passivation facilitate a one-step deposition of thick QD films to build solar cells, but it has certain limitations like poor dispersibility, inhomogeneous QDs fusion, imperfect passivation, and thick cell layer formation on QDs surface. In this chapter, we introduce a one-step hybrid passivation of QD surface using halometallate and thiol ligands. The developed passivation strategy allows to tune loading of organic thiol ligands on QDs surface, which has been shown to control the optical and electronic properties of QDs. The hybrid passivated QDs show stable band to band photoluminescence (PL) emission, narrower excitonic absorption, and improved dispersion in solution phase. The hybrid passivation leads to 1.7 times higher carrier mobility, an increase in carrier depletion width and diffusion length, reduction of trap density, and higher carrier lifetime than the only halometallate passivated QDs. The photovoltaic devices attain 10.62% PCE with a negligible hysteresis effect, which is 20% higher PCE compared to the only halometallate passivated solar cells.

6.1 Introduction

Colloidal quantum dots (CQDs) possess interesting properties like their size-tunable bandgap, solution processing, controllable carrier type, and ambient stability.[1-3] These characteristics make them attractive for thin-film optoelectronic applications such as light-emitting diodes,[4-5] transistors,[6-7] lasers,[8] photodetectors,[9-10,] and photovoltaics (PV).[11-13] Research progresses in CQDs devices have been achieved through improvements in CQDs synthesis,[14] progress in surface chemistry,[13,15] and advancements in device engineering.[11,16-17] The combined effect of these improvements has helped to realize the certified power conversion efficiency of 12.3% in single-junction PbS QDs solar cells.[18]

The CQDs are synthesized by using long-chain insulating ligands such as oleic acid (OA) and oleylamine. For the development of optoelectronic devices, these long-chain insulating ligands need to be replaced with shorter ligands to enhance carrier transport in CQDs films. During the initial stage of CQD device developments, a layer-by-layer (LBL) solid-state ligand exchange process has been employed to fabricate CQD device.[11,19-20] However, the LBL ligand exchange leads to QD agglomeration and inhomogeneous ligand exchange, which deteriorates the energy landscape of QDs. LBL ligand exchange is also not compatible with large scale manufacturing, and it is a highly wasteful process for valuable chemicals.[21-23]

Solution phase ligand exchange (SPLE) processes have been developed to overcome these issues, where a single step smooth crack-free film was deposited with 100% utilization of materials.[13,16-18,24-28] High quality CQDs inks are developed using lead halide (X=Br, I) ligands, and their colloidal stability is maintained through electrostatic interactions. The lead halide exchanged QDs are passivated by X-type halide or PbX_3^- ligand, and their corresponding counter cation PbX^+,[13,16-17] MA^+,[24] Na^+,[26] K^+,[27] Cs^+,[28] NH_4^+ [29] form a diffusive layer to preserve colloidal stability and charge balance of the QDs surface during SPLE. Although these advancements promote homogeneous packing, reduced energy disorder, and single-step thick layer formation of CQDs films than the LBL approach, there are certain limitations to this approach that need to be sorted out for further improvements in PCE. Recent reports show that QDs passivated by lead halide ligands form a thick shell layer in their solid films.[30] Depending on the type of counter cation, thick perovskite shell layers of $MAPbI_3$, [24] $CsPbI_3$[28] grow on the surface of QDs. In chapters 4 and 5, we have shown that butylamine solvent used to disperse the QDs for thin film deposition, also reacts

with the lead iodide ligands to form 2D shell layer on the QD surface. We have shown that the 2D shell is a combination of $(BA)_2PbI_4$ and Pb-amine complex and improved PCE by tunning the matrix thickness on the QDs surface.[29]

To restrict the growth of the shell layer on the QDs surface, modification of atomic ligand passivation will be an alternative way forward. PbS QDs are exposed to polar (111) facets and neutral (200) facets. PbS (111) facets are composed of unsaturated Pb atoms which are passivated by X-type ligand ($RCOO^-$, X^-, PbX_3^-, RS^-, etc.). The charge-neutral PbS (200) facets are consisted of alternate Pb and S atoms. These Pb and S atoms are passivated by electrostatic interaction with the neutral donor (RCOOH, RSH, RNH_2, etc.) and neutral acceptor ($CdCl_2$, PbX_2, $Pb(RCOO)_2$, etc.), respectively.[31] In PbI_2 passivated QDs inks, PbS (111) facets are passivated by PbI_3^- and S atoms of PbS (100) facets are protected by electrostatic interaction with neutral PbI_2. Due to the bigger size of halometallate ion, all the Pb atoms of (111) facets are not terminated, and Pb atoms of the PbS (200) surface remain unpassivated. In chapter 5, we proposed a two-step hybrid passivation strategy, in which as synthesized oleic acid capped QDs were treated first with a 3-chloro-1-propane thiol (CPT) ligand. In the second step, halometallate ligand passivation was carried out.[32] Due to the introduction of CPT, 2D matrix shell thickness was reduced to 50%, and QDs stability was also enhanced significantly as CPT was electronically bound to unpassivated Pb atoms of (111) facets and electrostatically passivated Pb atoms of (200) facets.[32] But, in this process, we had limitations of thiol loading on QDs surface (only 0.18mM CPT for 70mg PbS QDs), and as it was a two-step (time-consuming) process, we wasted a lot of materials after CPT treatment due to poor solubility of QDs in the nonpolar solvent.

In this chapter, we develop a one-step hybrid passivation strategy in the DMF solution to develop QDs ink with almost 100% utilization of materials. Here we achieved control over CPT (from 0.1mM to 0.3M for 70mg PbS QDs) loading on the QDs surface. Due to control over thiol loading, optical properties of hybrid passivated QDs in the DMF solvent phase as well as in thin films have improved significantly (enhanced dispersity, narrower excitonic absorption, and PL emission, higher PL intensity, lower stokes shift) than the only halometallate passivation. Hybrid passivated QDs retains their band to band thin-film emission for 36 hours in ambient condition while halometallate passivated thin films degrade within 30 minutes. The optimized hybrid passivation leads to a 70% reduction of shell thickness. Hybrid passivated QDs integrated solar cells show higher carrier mobility,

higher carrier lifetime, and reduced trap density. This allows photocarriers extraction from thicker QDs films, leading to the enhancement in J_{sc} of solar cells. The improvement of open-circuit voltage is around 50mV, which is attributed to lesser stokes shift in PL spectra of hybrid passivated QDs. Combining all these factors, the PCE of hybrid passivated QDs made solar cells reach 10.6%, which is 20% higher than the halometallate passivated QDs solar cells. The hybrid passivation also improves the unencapsulated solar cells' stability in ambient conditions.

6.2 Experimental Details

The synthesis procedure of ZnO and PbS NCs were followed earlier mentioned methods in section 4.2.1 and 4.2.2.

6.2.1 Ligand exchange of PbS QDs:

For halometallate ligand precursor preparation, 0.75M NH_4I, 0.075M PbI_2, and 0.025M $PbBr_2$ were mixed in 5 mL of DMF to get a clear transparent yellow color solution. In the case of hybrid ligand passivation, CPT ligand was added to the 5mL halometallate precursor solution. The CPT ligand concentration was varied from very low to very high in the range of 0.1mM to 0.3M systematically. For a standard ligand exchange process, 5mL of PbS QDS (15mg/mL) was mixed with DMF ligand precursor solution and mixed it vigorously for two minutes (30 seconds for hybrid ligand exchange). PbS QDs were then transferred from octane to the DMF phase. The top octane layer was discarded, and the DMF phase was cleaned another two times by octane solvent. The ligand exchange QDs were precipitated by toluene and collected by centrifugation. The collected QDs were dried under vacuum for 20 minutes and finally dispersed in butylamine (250mg/mL) for a one-layer spin coating.

6.2.2 Device Fabrication

Before ZnO NCs deposition, ITO substrates were cleaned by following the previously mentioned method in section 2.2.4. Pre-synthesized ZnO NCs were then deposited on top of cleaned ITO by spin coating at 3000 RPM, and substrates were heated around 230°C for 40 minutes. On top of the ZnO substrate, ligand exchange QDs inks were spin coated. Then the films were transferred inside Glovebox to anneal at 70°C for 15 minutes. By changing acceleration and rotation speed, device thickness was varied from 160 nm to 680 nm. For the deposition of the hole transport layer, 60 nm of 1,2 ethanedithiol

(EDT) treated PbS QD layer was deposited using the reported layer by layer method. To complete the device fabrication, electrode deposition was carried out by a thermal evaporator (HHV BC-300) at the base pressure of 1×10^{-6} Torr; 8 nm of MoO_3, 25 nm of Au, and 100 nm of Ag were deposited sequentially.

6.2.3 Materials Characterization Techniques

The ^{1}H NMR spectra were recorded at Bruker 400 MHz NMR spectrometer instrument. The chemical shift values for ^{1}H (TMS as internal standard) were recorded in $CDCl_3$. IR absorption spectra of the solution were recorded on an FTIR spectrometer (Vertex-70, Bruker) with 2 cm^{-1} resolution at room temperature. Optical absorption measurements were carried out by Shimadzu UV-Vis-NIR (UV-3600 Plus) spectrophotometer. Thin-film absorption was measured with the help of an integrating sphere (ISR-603) attached to the Shimadzu UV-3600 Plus spectrophotometer. Steady-state photoluminescence measurements were performed utilizing Spectrofluorometer FS5, Edinburgh instruments. Cross-sectional and surface images of the device were taken by field emission scanning electron microscope (FESEM NNS 450). High-resolution images of QDs were captured by a high-resolution transmitted electron microscope (HRTEM, JEOL JEM 2200FES).

6.2.4 Device Characterization Techniques

J-V, EQE, Cap-V, Photo-CELIV, Transient measurements (TPV and TPC), and bias dependent transient photocurrent measurements were carried out, and the measurements procedure was followed by already mentioned methods in section 2.2.6.1, 2.2.6.3, 2.2.6.4, 3.2.4.3, 3.2.4.4, and 4.2.6.1, respectively.

6.3 Results and Discussions

6.3.1 NMR Study

For one-step hybrid passivation, we mix CPT, PbI_2, and NH_4I precursors in DMF solvent to proceed SPLE process, and conventional halometallate passivation is carried out in the presence of only PbI_2 and NH_4I. As synthesized PbS CQDs are capped with long-chain insulating oleic acids and dispersed in nonpolar octane solvent. During the SPLE process, octane dispersed oleic acid capped QDs are added to the DMF solution of ligand precursor; after 2-3 minutes of vigorous mixing (for mixed CPT+$NH_4^+PbI_3^-$ ligand within 30 seconds), the QDs are transferred to the DMF phase. The insulating oleic acid molecules are replaced by PbI_3^- and CPT ligands on the QDs surface, and the colloidal stability and charge balance in the DMF phase are achieved by the formation of the diffusive layer of NH_4^+ ion. However, metals like palladium, nickel, mercury, and lead are highly reactive towards thiol; they easily form metal thiolate(M-SR) complex.[33] Before hybrid ligand (CPT + $NH_4^+PbI_3^-$) treatment on QDs, we probe -SH peak in the presence of PbI_2+NH_4I in DMF solvent through a ^{1}H NMR experiment.

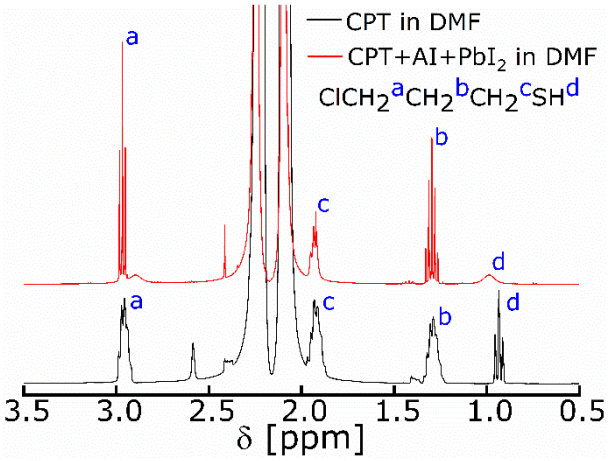

Figure 6.1: NMR spectra of CPT ligand in DMF and presence of NH_4I+PbI_2 precursor in DMF solvent. A small amount of $CDCl_3$ is used as a reference solvent for standardization.

During NMR studies, CPT concentration is kept lower than the PbI_2 concentration to inquest the -SH reactivity. The ^{1}H NMR data suggest that the -SH functional group remains intact in the presence of PbI_2+NH_4I in DMF solvent (Figure 6.1). The chemical shift of -SH proton is up-field in the presence of DMF solvent (δ_{S-H} -0.95-0.91ppm), as well as in the presence of PbI_2+NH_4I in DMF (δ_{S-H} -0.99 ppm) with reference to only $CDCl_3$ solvent (Figure 6.2).

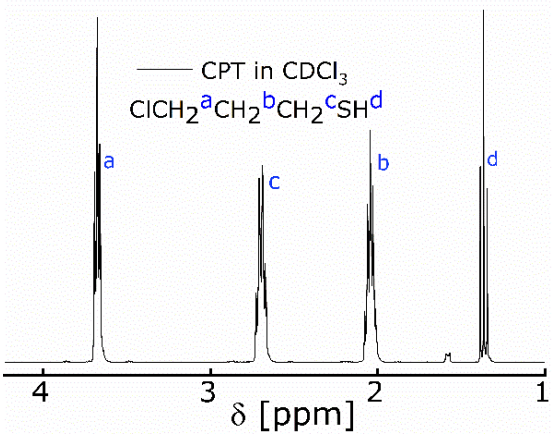

Figure 6.2: ^{1}H NMR spectrum of CPT ligand in $CDCl_3$ solvent.

This may be due to the enhancement of electron density around -SH group for the presence of high dielectric solvation environment of DMF. Although the -SH peak is broadened in the PbI_2+NH_4I mixture, but the integration of the area under the curve is close to one of the corresponding -SH single protons. The broadening of the peak may have arisen from the inhomogeneities in the magnetic field, which may have been caused by poor shimming in the sample.

6.3.2 FT-IR analysis

Solution phase FT-IR study also shows that the -S-H stretching band of CPT molecules appears at 2539 cm^{-1} in the presence of PbI_2+NH_4I, and for only CPT molecules at 2541cm^{-1} in DMF-D7 solvent (Figure 6.3).

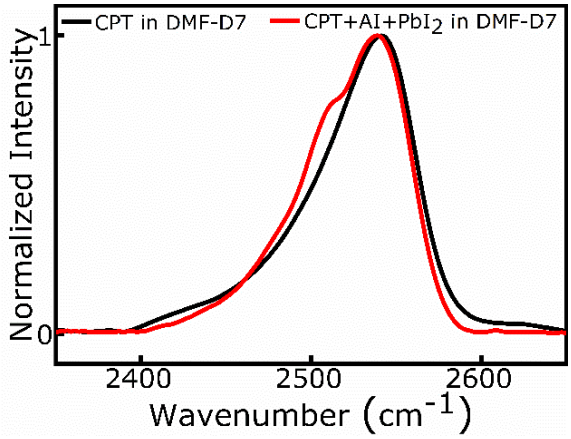

Figure 6.3: Solution phase FT-IR spectra of -SH functional group of CPT ligand in DMF-D7 and mixed solution of CPT+ NH_4I+PbI_2 precursor in DMF-D7 solvent.

This indicates that Pb-thiolate complex doesn't form when CPT is mixed with PbI_2+NH_4I mixture in DMF. We further probe the -SH stretching peak of CPT for different possible ligand combinations as shown in Figure 6.4.

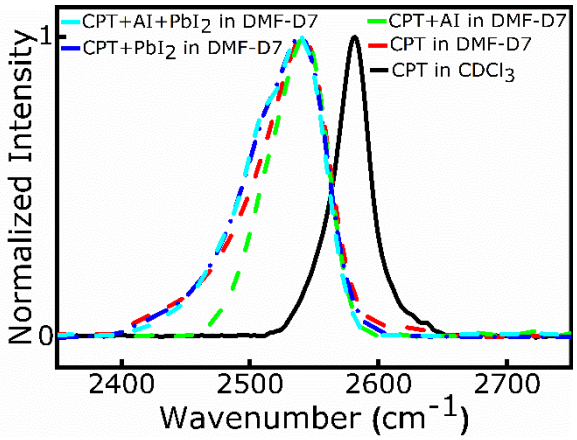

Figure 6.4: Solution phase FT-IR spectroscopy of -SH functional group of CPT ligand in $CDCl_3$ (2581cm^{-1}) and DMF-D7(2541cm^{-1}) solvent and in the presence of AI (2542 cm^{-1}), PbI_2 (2539 cm^{-1}), and both AI and PbI_2 (2539 cm^{-1}) in DMF D-7 solvent.

CPT molecules remain unreactive for all the possible scenarios; however, the -SH stretching peak has redshifted to 2539 cm^{-1} in DMF-D7 solvent compared to the $CDCl_3$ solvent (2581cm^{-1}). The reason for redshift could be due to the 'H' bonding interaction of -SH proton and the carbonyl group (-SH···O=CHNH$(Me)_2$) of DMF-D7 molecules, which weakens the -S-H bond strength.

6.3.3 Absorption and PL study

6.3.3.1 Solution Phase Absorption and PL study

After confirming that CPT ligands do not react to PbI_2+NH_4I precursor in DMF, we carry out a one-step hybrid SPLE of as-synthesized oleic acid capped QDs. In the DMF phase, the ligand exchanged QDs are analysed minutely through absorbance (Figure 6.5a) and PL (Figure 6.5b) spectroscopy. Due to the quantum confinement effect and high surface to volume ratio of QDs, the absorbance and emission properties of QDs are very sensitive to their size and surface properties. To check the colloidal stability as well as the impact of surface passivation, we have collected absorption and emission data after 30 minutes of each ligand exchanged process.

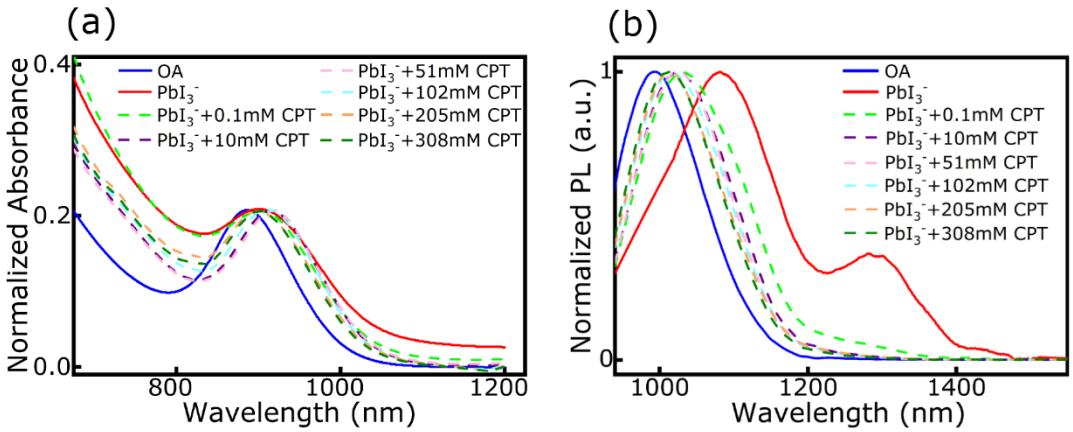

Figure 6.5: (a) Absorbance and (b) Photoluminescence (PL) spectra of PbS QDs in DMF solvent for different concentration of CPT ligand. All the spectral measurements are carried out after 30 minutes of ligand exchange in the DMF phase. The PL spectra are recorded at the 550 nm excitation wavelength. The absorbance spectra are normalized at excitonic peak position, and PL spectra are normalized at band edge emission peak for comparative study.

The absorbance and photoluminescence data are analysed to determine peak position, FWHM, and stokes shift and shown in Table 6.1. As synthesized octane dispersed, Oleic acid capped QDs have lower FWHM (138nm) and absorption peak at 886 nm. Only halometallate passivation leads to redshift in absorbance peak to 900 nm and enhancement in FWHM to 180 nm. The reason for the redshift in excitonic peak is due to the growth of QDs size, and the increase in FWHM indicates the polydispersity in the QDs size. For hybrid ($NH_4^+PbI_3^-$ + CPT) ligand passivation, we increase CPT ligand concentration sequentially from 0.1mM to 300 mM, and the halometallate concentration is fixed at 100 mM. With increasing CPT ligand concentration leads to the shift in excitonic peak position to longer wavelengths routinely[34] (Table 6.1).

Table 6.1: Tabular representation of absorption and PL spectral data of oleic acid capped PbS QDs in octane and PbS QDs for different ligands in DMF phase.

Ligand	excitonic peak position (nm)	FWHM [Absorbance] (nm)	PL peak position (nm)	FWHM [PL] (nm)	Stokes shift (nm)
OA-PbS	886	138	993	135	107
PbI_3^-	900	184	1085	232	185
PbI_3^- +0.1mM CPT	902	180	1032	228	130
PbI_3^- +10mM CPT	915	149	1025	154	110
PbI_3^- +51mM CPT	920	144	1024	149	103
PbI_3^- +102mM CPT	912	145	1017	151	105
PbI_3^- +205mM CPT	897	158	1015	148	118
PbI_3^- +308mM CPT	899	150	1012	148	113

However, when the thiol concentration is doubled (200 mM) than halometallate ligand concentration (100 mM), the excitonic peaks further shifted to shorter wavelengths, which might be due to the etching[35] of Pb atoms from the QDs surface. The FWHM of the excitonic peak reduces systematically with the increase in thiol concentration till 200 mM of CPT. Higher concentrations of CPT (more than 200 mM) than halometallate lead to an increase in FWHM (Table 6.1). The narrowing of FWHM signifies the reduction of polydispersity of QDs in the DMF phase after ligand exchange.

The corresponding PL spectra of those ligand exchanged QDs are also analysed rigorously. Emission properties of oleic acid capped QDs shows FWHM of 135nm, and stokes shift (107nm), and no trap emission. Halometallate exchanged QDs have shown two emission peaks. Band edge emission peak appears at 1085 nm with higher intensity, and the trap emission appears at 1290 nm with relatively lower intensity. The origin of trap emission of halometallate exchanged QDs might be due to the surface oxidation (Pb-O bond formation) mediated mid-gap state formation or QDs fusion through the unpassivated facets. The halometallate passivated QDs also have the highest FWHM (232nm) and stokes shift (185nm). With the introduction of CPT ligand for hybrid passivation, no such trap emission is observed, as well as the gradual decrease in FWHM and stokes shift is followed by a systematic increase in CPT concentration (Table 6.1). The higher value of FWHM signifies the inhomogeneous growth of QDs, which leads to a higher degree of polydispersity. Again, the polydispersed ensemble of QDs facilitates the energy transfer from higher bandgap QDs (smaller size QDs) to lower bandgap QDs (bigger size QDs); thus, the larger stokes shift is also observed.[36]

We have compared the band edge PL intensity for different ligand exchanged QDs in Figure 6.6. The PL intensity rises with increasing CPT concentration till saturation is reached for and above 50 mM of CPT. The large increase in the band-to-band PL intensity is due to the reduction of trap state density in between the bandgap of QDs.

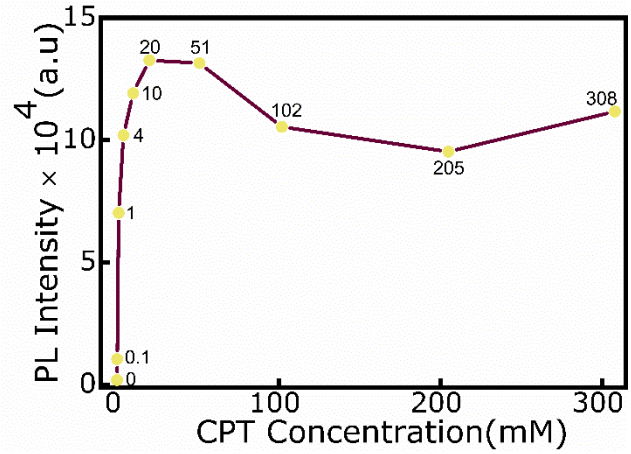

Figure 6.6: Shows the comparative PL intensity of PbI_3^- and hybrid PbI_3^- +CPT ligand exchanged PbS QDs. CPT ligand concentration is varied from 0.1mM to 300 mM for the fixed 100 mM PbI_3^- ligand. Throughout the measurements, the excitation and emission bandwidth of the fluorometer were kept constant, and all the measurements were carried out at 550 nm excitation wavelength.

6.3.3.2 Urbach energy calculation

We have calculated the Urbach energy of thin films to determine the band tail states of QDs. Urbach energy is estimated by converting reflectance data into absorbance (Figure 6.7) by using the Kubel-Munk equation.[37]

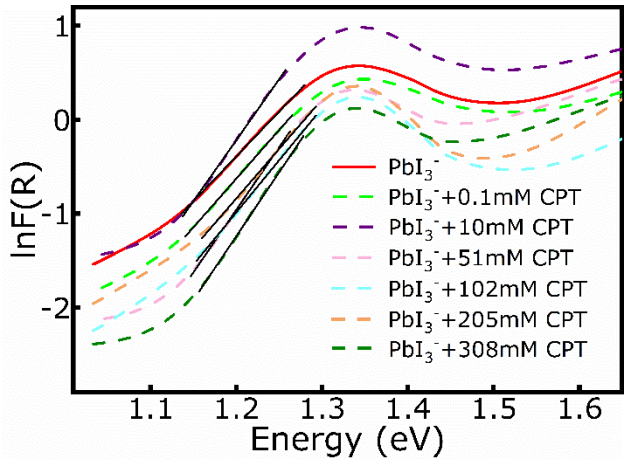

Figure 6.7: Urbach energy calculation from the conversion of diffuse reflectance of thin films into absorption spectra by implying Kubel-Munk function F(R).

The reflectance spectra can be converted to the corresponding absorption spectra by applying the Kubel-Munk function F(R),

$F(R) = \frac{K}{S} = \frac{(1-R)^2}{2R}$ ----------(6.1)

While 'K' and 'S' are the absorption and scattering coefficients, respectively. The Urbach energy is calculated from the following equation,

$\alpha = \alpha_0 + e^{\frac{hv}{E_u}}$ ----------(6.2)

where 'α' is the absorption coefficient, 'hv' is the photon energy and 'E_u's the Urbach energy. The Urbach energy is calculated from the 'ln (α)' vs. 'hv' plot. Since the absorption coefficient is proportional to absorbance '$F(R)$', then we have plotted 'ln $(F(R))$' vs. 'hv' in Figure 6.7 for all the samples. The reciprocal of the slope of the linear fit will be equal to the Urbach energy E_u,[37] which are tabulated in Table 6.2.

Table 6.2: Urbach energy calculation from Reflectance spectra of PbS QDs for different ligand passivation.

Ligand	Eμ (meV)
PbI_3^-	104.9
PbI_3^- +0.1mM CPT	96.52
PbI_3^- +10mM CPT	76.99
PbI_3^- +51mM CPT	75.06
PbI_3^- +102mM CPT	90.09
PbI_3^- +205mM CPT	94.72
PbI_3^- +308mM CPT	73.50

The Urbach energy for halometallate passivated QDs is 105 meV, in the case of hybrid passivated QDs reduced to 75 meV (varied from 96 meV to 73 meV with CPT concentration). Lower Urbach energy signifies the lower electronic tail states within the bandgap of QDs films.

6.3.4 TEM image analysis

TEM image of oleic acid capped QDs are shown in Figure 6.8a, and the HRTEM image is in Figure 6.8b.

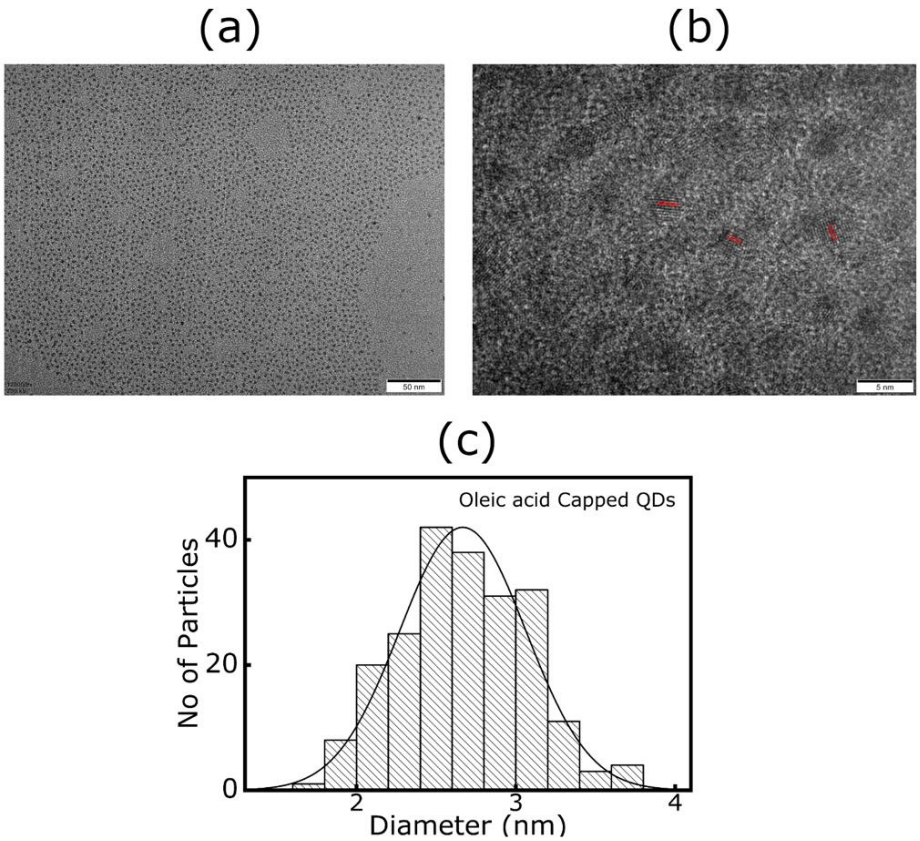

Figure 6.8: HRTEM images of oleic acid capped PbS QDs, (a) lower magnified image, (b) higher magnified image to show crystal fringes, and (c) particle size distribution of oleic acid capped QDs.

The d-spacing of the oleic acid capped PbS QDs is determined to be 3.38Å, which indicates the (111) planes. Oleic acid capped QDs are self-assembled through an ordered arrangement with a narrow particle size distribution (Figure 6.8c). The average QD size is 2.85 nm.

Figure 6.9a represents the TEM image of halometallate exchanged QDs, where marked particles signify the fused QDs, and Figure 6.9b represents the corresponding HRTEM. The interplanar spacing of halometallate treated QDs is found to be 3.15±0.03 Å. Halometallate ligand treated QDs have a broad distribution of particle size (Figure 6.9c), and their average particle size increased from 2.66 nm (OLA -PbS QDs) to 7.42 nm (PbI_3^- treated QDs). The enhancement in particle size (average size and distribution) might be due

to the growth of the 2D matrix shell on the QDs surface[18,29] and QDs fusion through unpassivated (200) facets. In the case of hybrid passivation, the CPT ligands passivation on

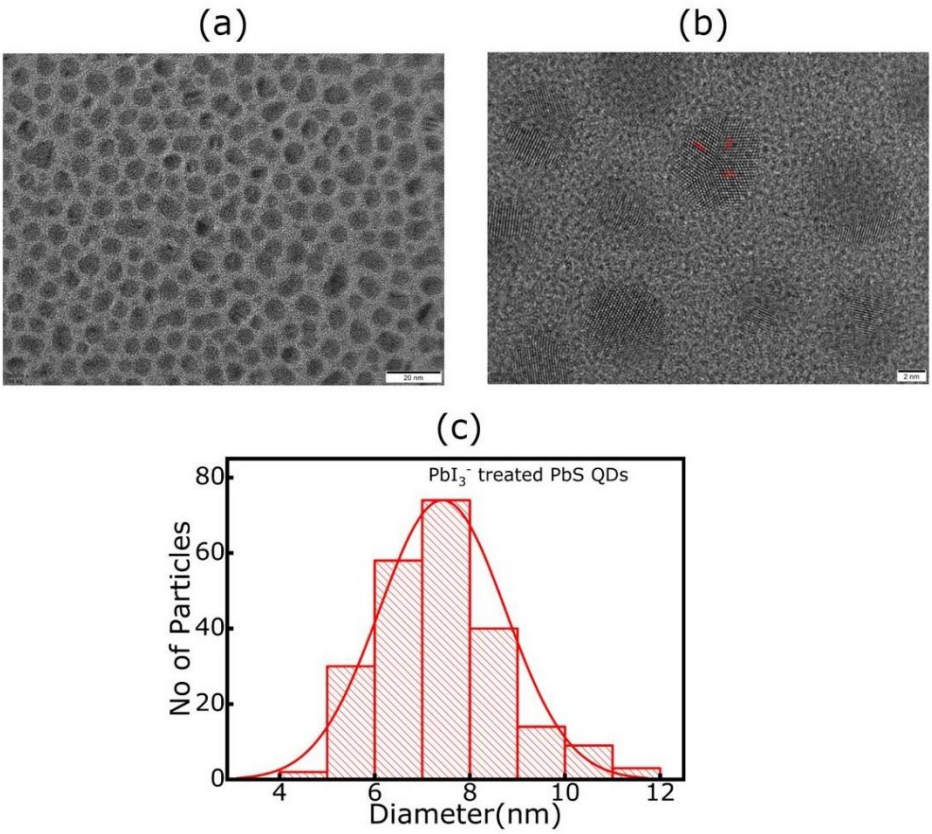

Figure 6.9: HRTEM images of halometallate treated PbS QDs, (a) lower magnified image, (b) higher magnified image to show crystal fringes, and (c) particle size distribution of halometallate treated QDs.

(111) facets hinder the growth of shell formation on the QDs surface, and electrostatic interaction on (200) facets restrict the fusion of QDs. No such fused QDs are observed in the TEM image (Figure 6.10a) of hybrid ligand exchanged QDs. The d-spacing for hybrid passivated QDs also have a similar value (3.15±0.03 Å) of halometallate passivated QDs (Figure 6.10b). It might be due to the growth of a similar type of 2D matrix layer on QDs surface. However, the average particle size (4.19nm) and width of size variation (Figure 6.10c) reduce significantly in the case of hybrid passivation. The 2D matrix shell thickness on the QDs surface reduces from 2.37 nm (halometallate exchanged QDs) to 0.76 nm (hybrid ligand exchanged QDs); this further impact the QD-to-QD distance in QD films.

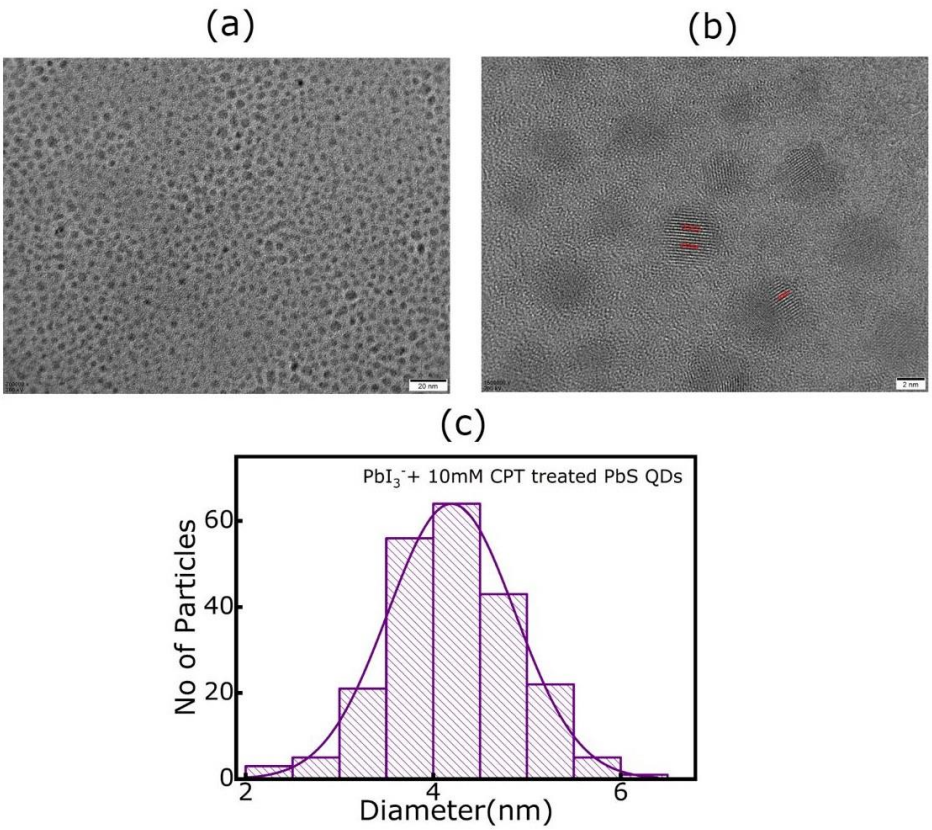

Figure 6.10: HRTEM image of PbI_3^-+10mM CPT treated QD PbS QDs, (a) lower magnified image, (b) higher magnified image to show crystal fringes, and (c) particle size distribution of PbI_3^-+10 mM CPT exchanged PbS QDs.

6.3.5 Surface SEM image

The scanning electron microscope image of halometallate exchanged QD films show some cracks (8.1nm diameter) marked by the yellow circle in the films (figure 6.11a). The hybrid ligand exchanged QDs mediated films are significantly smoother and don't have any such cracks or nanostructures on their surface (Figure 6.11b). The thinner shell layer of hybrid passivated QDs leads to form the compact films (Figure 6.11b), which will be beneficial for the charge carrier transports.

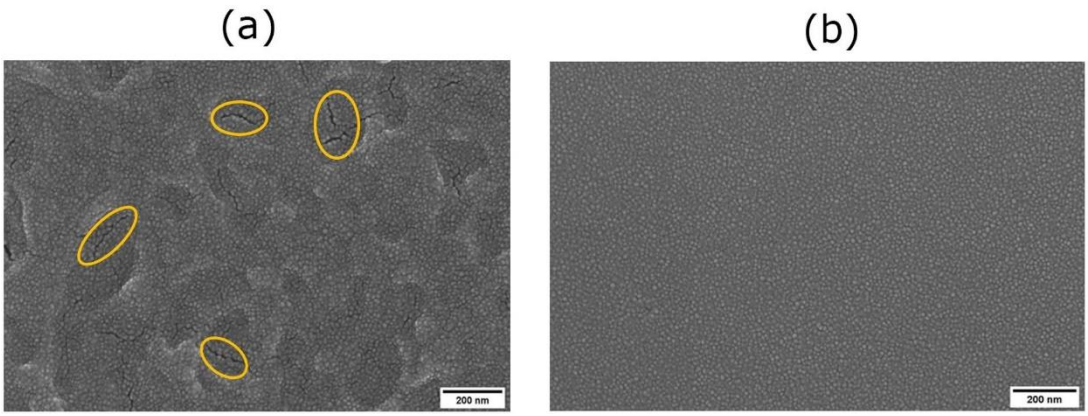

Figure 6.11: SEM image of (a) halometallate passivated QDs and (b) hybrid PbI_3^-+10mM CPT passivated QDs.

6.3.6 Cross-sectional SEM image of solar cell

We fabricate QDs solar cells to realize those advantages of hybrid passivation in photovoltaic performance. The solar cells are made up of the following device architecture ITO/ETL-ZnO (100 nm)/PbS QDs (PbI_3^-+CPT or PbI_3^- passivation)/HTL-PbS QDs (60 nm)-EDT ligand treated/MoO_3(8 nm)/Au (25 nm)/Ag (100 nm). The details of device fabrication have been discussed in the experimental section. The cross-sectional SEM image of a characteristic solar cell, indicating all the layers, is shown in Figure 6.12.

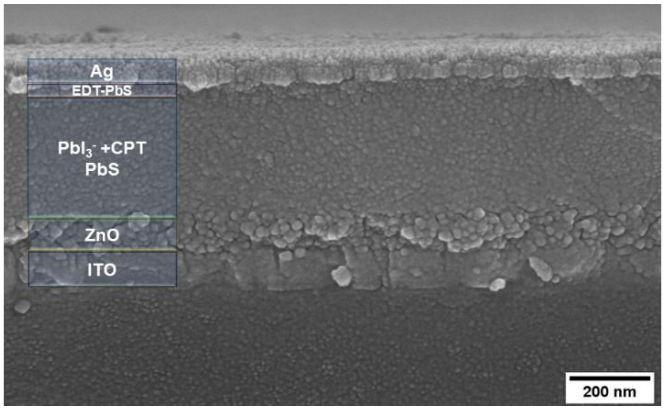

Figure 6.12: Cross-sectional image represents all the layers of integrated PbS QDs solar cell.

6.3.7 J-V characteristics

The current density (J) vs. voltage (V) curves for the different CPT ligand treated solar cells are shown in Figure 6.13a, and the corresponding photovoltaic outputs are tabulated in Table 6.3. The PCE of solar cells for the different amounts of CPT concentrations has shown in Figure 6.13b. The zero amount of CPT ligand signifies the only halometallate passivation.

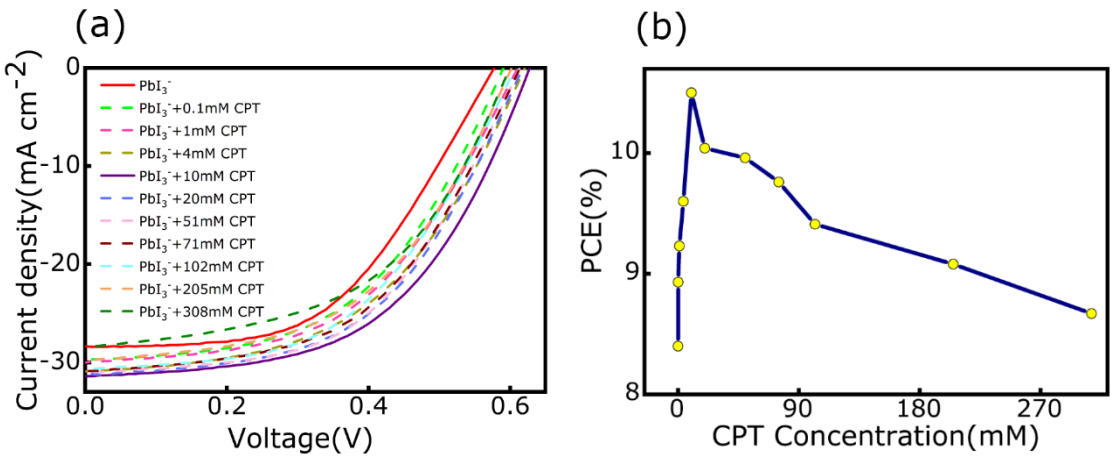

Figure 6.13: (a) J-V curves of solar cells under 1.5 AM illumination condition, and (b) Change of PCE with CPT ligand concentrations.

With the addition of CPT ligand along with halometallate ligand, the PCE increases gradually, and the solar cells made up with PbI_3^-+10mM CPT ligand treated QDs exhibits maximum PCE. Upon further increase in CPT concentration decreases the PCE as the J_{sc} and FF reduce significantly. The increase in solar cell PCEs is corroborated by the improvement in absorbance and PL properties of hybrid passivated QDs. However, for higher CPT concentration (more than 70mM CPT), the PCE of solar cells drops significantly, which might be due to the higher amount of thiol loading on the QD surface hinders the carrier transport in films. The J-V characteristics curves for the champion devices of the only PbI_3^- and hybrid PbI_3^-+10mM CPT ligand passivated QDs are shown in Figure 6.14, and their photovoltaic parameters are presented in Table 6.4.

Table 6.3: Tabular representation of solar cells device J-V curves parameters for different ligand treated PbS QDs thin film.

Name of the ligand	V_{oc} (V)	J_{sc} (mA cm^{-2})	FF (%)	PCE (%)
PbI_3^-	0.58	28.4	51	8.40
PbI_3^- + 0.1mM CPT	0.59	29.8	50.83	8.93
PbI_3^- + 1mM CPT	0.61	30	50.45	9.23
PbI_3^- + 4mM CPT	0.62	30.9	50.14	9.6
PbI_3^- + 10mM CPT	0.63	31.4	53.08	10.5
PbI_3^- + 20mM CPT	0.62	31.3	51.77	10.05
PbI_3^- + 51mM CPT	0.61	31	52.7	9.96
PbI_3^- + 71mM CPT	0.61	30.9	51.8	9.76
PbI_3^- + 102mM CPT	0.61	30.6	50.45	9.41
PbI_3^- + 205mM CPT	0.6	29.8	50.8	9.08
PbI_3^- + 308mM CPT	0.6	28.4	50.9	8.67

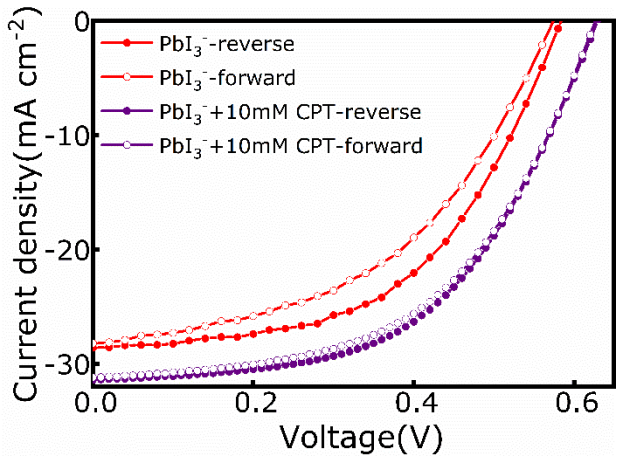

Figure 6.14: J-V characteristics (reverse and forward scan) of champion halometallate and hybrid halometallate+10mM CPT ligand exchanged QDs constructed device under AM 1.5 solar illumination.

Table 6.4: Photovoltaic parameters of optimized solar cells.

Name of the ligand	Scan direction	J_{sc} (mA cm^{-2})	V_{oc} (V)	FF (%)	PCE (%)
PbI_3^-+10mM CPT	reverse	31.4	0.63	53.65	10.6
	forward	31.2	0.63	52.48	10.3
PbI_3^-	reverse	28.6	0.58	53.17	8.82
	forward	28.2	0.58	47.19	7.71

Solar cells based on halometallate treated QDs show high hysteresis effect, while solar cells constructed with 10mM CPT+ PbI_3^- ligand treated QDs show negligible hysteresis effect. The statistical variation of photovoltaic parameters (V_{oc}, FF, and J_{sc} and PCE) for different batches of solar cells exhibit a distinct improvement in the case of PbI_3^-+10 mM CPT hybrid passivation than only halometallate passivation (Figure 6.15).

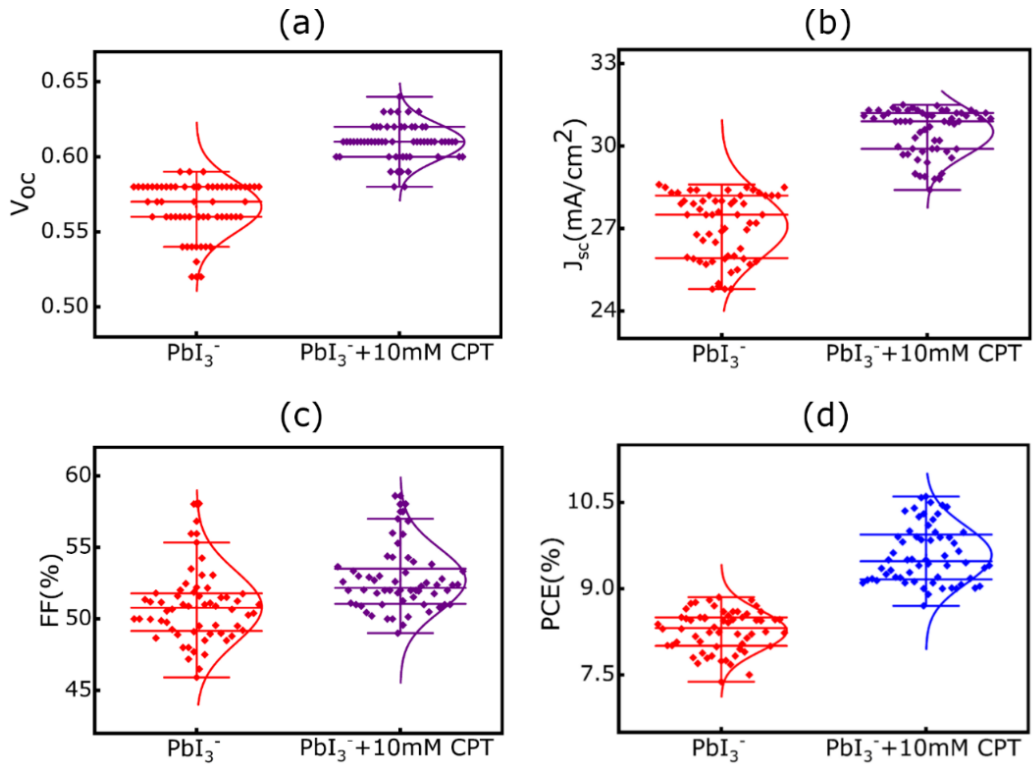

Figure 6.15: Statistical variation of photovoltaic parameters and PCE for different batches of PbI_3^- and PbI_3^-+10mM CPT ligand exchanged QDs solar cells, (a) V_{oc} (b) J_{sc} (c) FF% and (d) PCE%.

6.3.8 Device thickness optimization

The active layer thickness-dependent J-V curves for PbI_3^- and PbI_3^- +10mM CPT treated solar cells are shown in Figure 6.16, and their corresponding photovoltaic parameters tabulated in Table 6.5 (PbI_3^-) and Table 6.6 (PbI_3^- +10mM CPT).

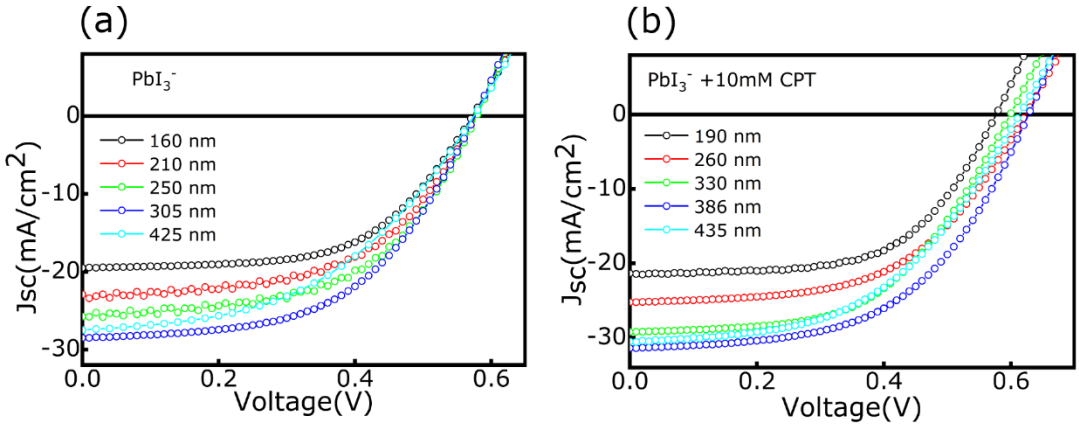

Figure 6.16: Thickness dependent J-V curves for (a) PbI_3^- and (b) PbI_3^-+10mM CPT treated solar cells.

Table 6.5: Photovoltaic parameters of active layer thickness varied PbI_3^- treated solar cells.

Thickness (nm)	V_{oc} (V)	J_{sc} (mA cm^{-2})	FF (%)	PCE (%)
160	0.57	19.5	58.3	6.5
210	0.58	23	55	7.34
250	0.58	25.8	54.2	8
305	0.58	28.5	53	8.8
425	0.58	27.5	46	7.37

Table 6.6: Photovoltaic parameters of thickness dependant studies of PbI_3^- +10mM CPT treated solar cells.

Thickness (nm)	V_{oc} (V)	J_{sc} (mA cm^{-2})	FF (%)	PCE (%)
190	0.58	21.3	59.06	7.3
260	0.62	25.2	54.38	8.5
330	0.6	29.2	53.34	9.35
386	0.63	31.4	53.08	10.5
435	0.61	30.8	49.9	9.37

The optimum thickness of the active PbS QDs layer (the QDs layer in between ETL and HTL) for PbI_3^- and hybrid PbI_3^-+10 mM CPT passivated solar cells are noticed to be 305 and 386 nm, respectively (Figure 6.17).

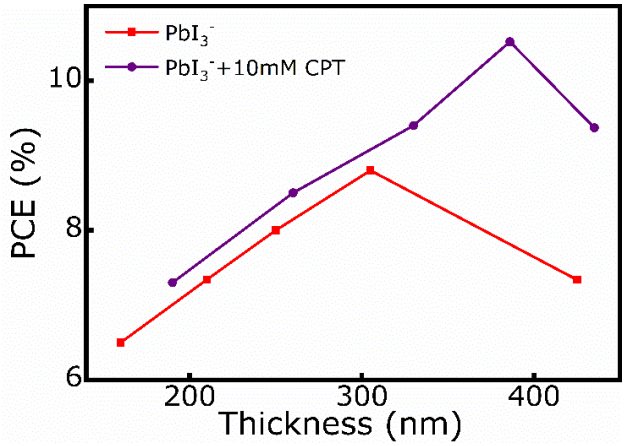

Figure 6.17: Comparison of PCE of the solar cell with active layer thickness for halometallate and hybrid halometallate+10mM CPT ligand exchanged QDs.

Due to the growth of a thicker active layer in the case of PbI_3^- +10mM CPT treated solar cells, the J_{sc} increases considerably without a notable reduction in FF.

6.3.9 Power dependant V_{oc} study

The diode ideality factors for the solar cells are calculated from the power dependant V_{oc} measurement, using the equation[23] $V_{oc} = \frac{\eta KT}{q} \ln(\phi)$, where η is the diode ideality factor,

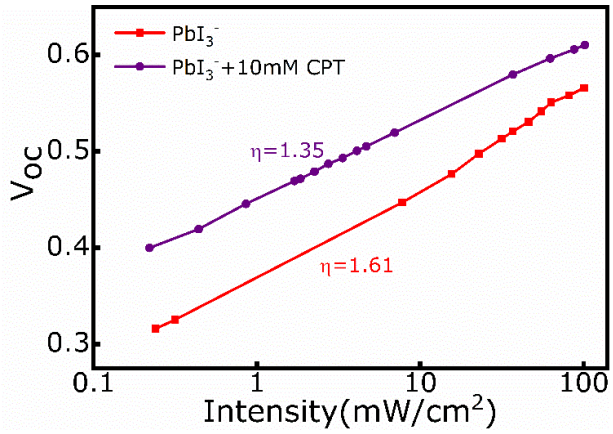

Figure 6.18: Light intensity(ϕ) dependant V_{oc} of the solar cells. The diode ideality factor (η) is calculated from the slope of the V_{oc} vs. $\ln(\phi)$ plot for the solar cells.

K is the Boltzmann constant, T is the temperature, q is the electronic charge, and ϕ is the photon flux. The η value reduces from 1.61 (PbI_3^- passivated solar cells) to 1.35 for PbI_3^- +10mM CPT treated solar cells, which implies the lesser trap recombination for hybrid passivated solar cells[38] (Figure 6.18).

6.3.10 Device stability

We have tested the stability of unencapsulated solar cells by measuring PCE at different time intervals; during PCE measurements, the solar cells are exposed to ambient conditions or else stored in Ar glovebox.

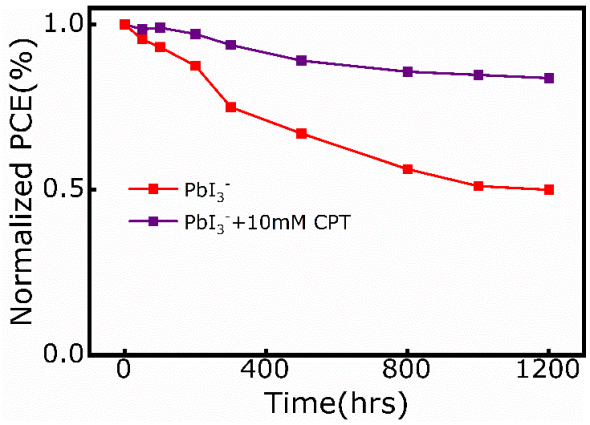

Figure 6.19: Device stability data of the unwrapped solar cells stored in Argon glovebox and measured in different time intervals.

After 1200 hours, the hybrid PbI_3^-+10mM CPT passivated solar cells retain 83% of PCE, while PbI_3^- treated solar cells drop 51% of their initial PCE (Figure 6.19).

6.3.11 Cap-V analysis

The capacitance of different ligand treated solar cells is measured to determine the depletion width at different voltage[19] (Figure 6.20). For depletion width calculation, we have first estimated dielectric constants using equation 3.2 from the photo-CELIV measurements (Figure 6.22), which were discussed later. Hybrid ligand (PbI_3^-+10mM CPT) treated QDs have a higher dielectric constant (27.58) than PbI_3^- treated QDs (23.15). The dielectric constant plays a crucial role in the formation of depletion width across the *n-p* junction. The carrier doping density calculated from Cap-V measurements decreases from 1.41×10^{23} m^{-3} (PbI_3^- treated solar cells) to 1.74×10^{22} m^{-3} (PbI_3^-+10mM CPT), 1.83×10^{22} m^{-3} (PbI3-+51mM CPT), and 1.76×10^{22} m^{-3} (PbI_3^-+71mM CPT). While the total depletion width of the device at zero bias condition increases from 237.6 nm (PbI_3^- treated solar cells) to 410 nm (PbI_3^- +10mM CPT), 415 nm (PbI_3^-+51mM CPT), and 418 nm (PbI_3^-+71mM CPT) hybrid ligand treated devices.

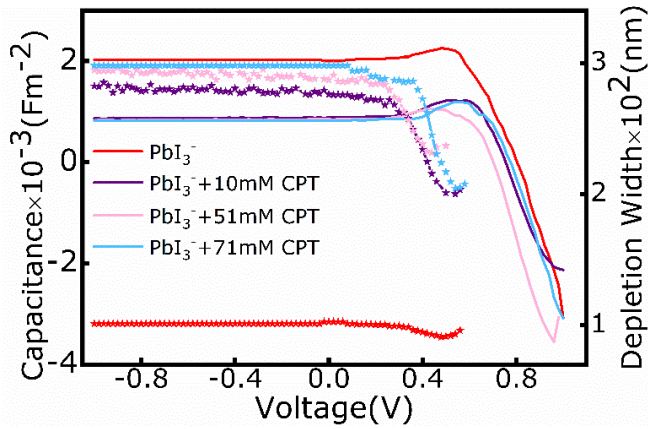

Figure 6.20: Capacitance- voltage characteristics of halometallate and mixed halometallate+CPT (for three different CPT ligand ratio) ligand treated QDs integrated device. The depletion width of the respective solar cells (left-hand axis) at different voltages are represented.

Higher depletion width enhances the efficient carrier collection from the thicker QDs layer of hybrid ligand treated solar cells.

6.3.12 Lifetime and DOS calculation

To understand the carrier recombination mechanism inside the solar cell, we further investigated the carrier lifetime and density of trap states from transient photovoltage and photocurrent measurements.[19,29,32] Carrier lifetime is measured from transient photovoltage measurements at different V_{oc}. Hybrid ligand treated (different CPT concentration) QDs integrated solar cells have a higher carrier lifetime than PbI_3^- treated solar cells (Figure 6.21a). Lower carrier lifetime signifies the fastest rate of carrier recombination within the solar cell. The density of trap states (DOS) is determined from the transient photovoltage (TPV) and transient photocurrent measurements (TPC); the details of TPV, TPC measurements, and calculation are described in section 4.312.[29,32,39] The DOS of hybrid ligand treated solar cells at any given V_{oc} is lower than halometallate passivated solar cells (Figure 6.21b). The DOS at different V_{oc} presents the distribution of trap states across the bandgap of light-absorbing QDs layer. The V_{oc} of a solar cell is estimated from the difference between the quasi-Fermi energy levels of electrons and holes under photo illumination.

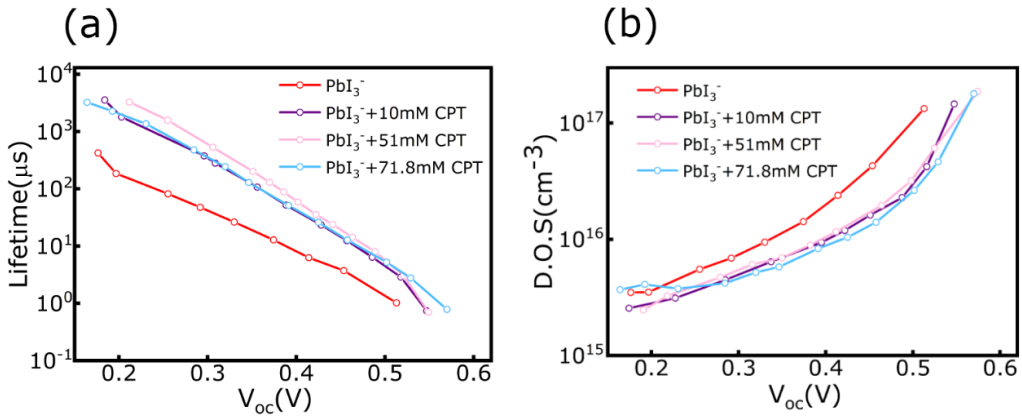

Figure 6.21: (a) Photocarrier lifetime and (b) density of trap states at different V_{oc} values for halometallate and mixed halometallate+CPT (three different CPT concentration) exchanged QDs constructed device.

So, higher DOS enhances the trap carriers density, which further limits the quasi-Fermi energy splitting for electrons and holes. Hybrid (PbI_3^- + CPT) ligand treated solar cells have lower DOS, which helps to produce higher photovoltage. The reduction of shell thickness and lower DOS would favorably affect the carrier transport properties of QDs solid.

6.3.13 Mobility calculation

Charge carrier mobility is calculated from the photoinduced carrier extraction from linearly increasing voltage (photo-CELIV) measurements of solar cells. [19,32,40] The mobility calculation details from the photo-CELIV measurement are discussed in section 3.3.3. The change of current under the influence of linearly increasing voltage pulse for PbI_3^- and PbI_3^- +10mM CPT treated solar cells are presented in Figure 6.22a and 6.22b. Solar cells having QD active layer thickness of 551 nm (PbI_3^-) and 679 nm (PbI_3^-+10mM CPT) are used for photo-CELIV measurements. The cross-sectional SEM image of the thick device is presented in Figure 6.23. The carrier mobility of PbI_3^- and PbI_3^-+10mM CPT treated solar cells are 2.51×10^{-3} and 3.54×10^{-3} cm^2 $V^{-1}s^{-1}$, respectively, indicating a 1.4 times increase in carrier mobility for hybrid ligand treated solar cells. The carrier mobility of PbI_3^- treated solar cells is increased 2.28 times than our previouus chapter report. The enhancement might be due to the reduction of shell thickness on the QDs surface from our previous reports using a lesser amount of NH_4^+ ion during the ligand exchange.[29,32]

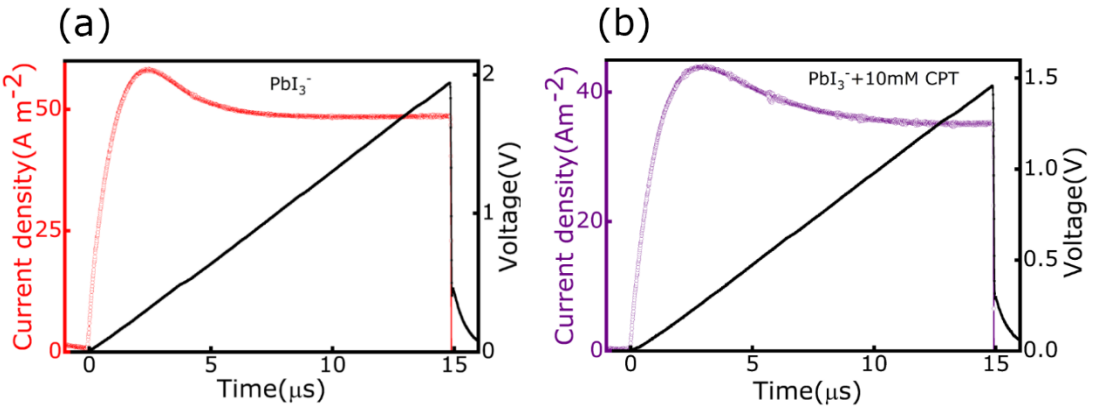

Figure 6.22: Photo-CELIV measurement of (a) PbI_3^- and (b) PbI_3^-+10mM CPT ligand treated solar cells. The change of solar cell current under the influence of linearly increasing voltage pulse is represented.

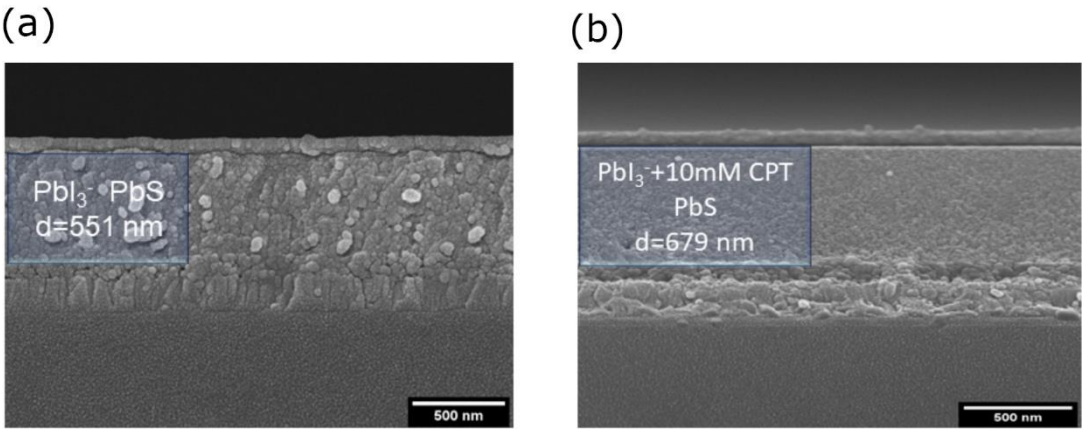

Figure 6.23: Cross-Sectional image of solar cells used for Photo-CELIV measurements, (a) PbX_3^- exchanged and (b) PbX_3^- +10mM CPT exchanged PbS QDs.

We have further measured the bias dependant photocurrent decay of solar cells to cross-check the carrier mobility values.[41,42] The photocurrent decay profile of PbI_3^- and PbI_3^- +10mM CPT treated solar cells are shown in figure 6.24.

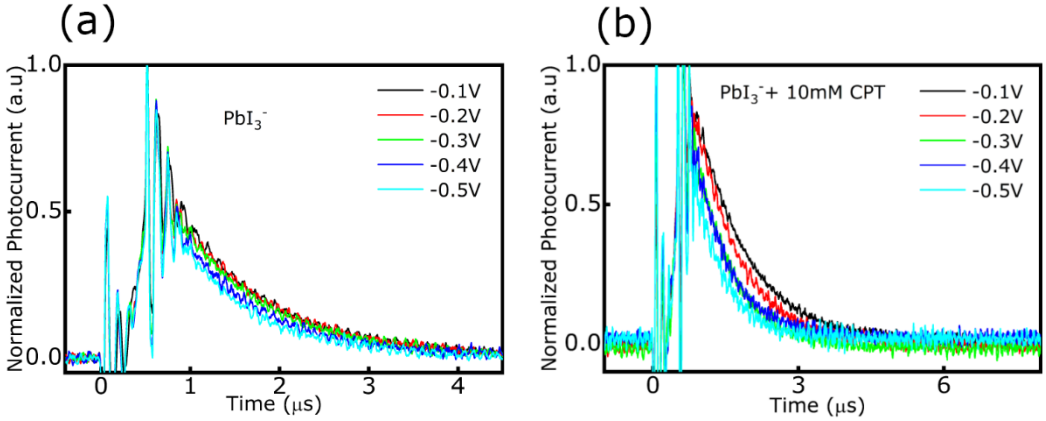

Figure 6.24: Bias dependent transient photocurrent decay profile of (a) PbI_3^- and (b) PbI_3^- +10mM CPT exchanged QDs solar cells. The carrier transit time changes with the application of different bias.

Carrier mobility (μ) is determined using the equation $\mu = \frac{d^2}{\tau_{tr} \times V}$, where d is the film thickness, τ_{tr} is the transient time (time is taken to decay 1/e times of the maximum current value of Figure 6.24), and V is the applied bias. The carrier mobility is determined from the slope of the V vs $\frac{d^2}{\tau_{tr}}$ plot (Figure 6.25), and the calculated mobility values are 2.38×10^{-3} and 3.54×10^{-3} $cm^2\ V^{-1}s^{-1}$ for PbI_3^- and PbI_3^-+10mM CPT treated solar cells, respectively.

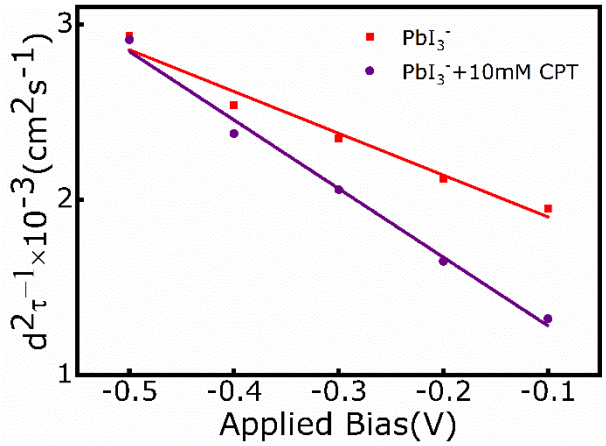

Figure 6.25: Charge carrier mobility is calculated from the slope of d^2/τ vs. applied bias plot for PbX_3^- and PbX_3^-+10mM CPT treated device.

The carrier mobility values from both the measurement techniques are almost matching to each other. We have further calculated the carrier diffusion length (L_D) by utilizing the carrier lifetime and carrier mobility data in the equation $L_d = \sqrt{\frac{\mu(KT)\tau}{q}}$, K -Boltzmann constant, T-temperature(300K),τ- carrier lifetime, and q-electronic charge. The carrier diffusion lengths of PbI_3^- and PbI_3^-+10mM CPT are 81 nm and 161 nm, respectively. The one-step hybrid ligand treatment of QDs leads to more compact surface passivation (size selectivity) and protection from air oxidation (PL stability) of thin films. As a result, hybrid ligand passivation prompts the formation of trap-deprived QDs solar cells with higher depletion width and higher diffusion length, which further helps to enhance V_{oc}, J_{sc}, FF, and overall PCE of solar cells.

6.4 Conclusion

In summary, we have developed a one-step thiol, halometallate ligand exchanged PbS QDs ink for the solar cell development. Thiols and halometallate ligands remain intact for facet specific passivation during the solution phase ligand exchange process. Conventional halometallate ligand treatments can not passivate all the Pb atoms of (111) facets and (200) facets, while the hybrid ligand engineering enables the passivation of the inaccessible sites of (111) facets and Pb atoms of (200) facets. The hybrid ligand passivation leads to higher monodispersity, reduces QDs fusion, decreases the matrix shell growth, and retains band edge emission. The photovoltaic devices built from hybrid ligand exchanged QDs have higher depletion width, higher carrier lifetime, lower number of trap states, higher

carrier mobility, and higher diffusion length, which results in higher PCE% with lower hysteresis effect in solar cells. By controlling the thiol loading on the QDs surface, we can tune the Fermi energy level of the QDs. This could be beneficial for the development of bulk heterojunction solar cells and other QDs based electronic devices like light-emitting diodes (LED), tandem solar cells, etc.

6.5 References

(1) McDonald, S. A.; Konstantatos, G.; Zhang, S. G.; Cyr, P. W.; Klem, E. J. D.; Levina, L.; Sargent, E. H. Solution-processed PbS quantum dot infrared photodetectors and photovoltaics. *Nat. Mater.* **2005**, *4* (2), 138-142.

(2) Semonin, O. E.; Luther, J. M.; Choi, S.; Chen, H. Y.; Gao, J. B.; Nozik, A. J.; Beard, M. C. Peak External Photocurrent Quantum Efficiency Exceeding 100% via MEG in a Quantum Dot Solar Cell. *Science* **2011**, *334* (6062), 1530-1533.

(3) Bae, W. K.; Joo, J.; Padilha, L. A.; Won, J.; Lee, D. C.; Lin, Q.; Koh, W. K.; Luo, H.; Klimov, V. I.; Pietryga, J. M. Highly Effective Surface Passivation of PbSe Quantum Dots through Reaction with Molecular Chlorine. *J. Am. Chem. Soc.* **2012**, *134* (49), 20160−20168.

(4) Wood, V.; Panzer, M. J.; Chen, J.; Bradley, M. S.; Halpert, J. E.; Bawendi, M. G.; Bulovic, V. Inkjet-Printed Quantum Dot–Polymer Composites for Full-Color AC-Driven Displays. *Adv. Mater.* **2009**, *21*, 2151-2155.

(5) Kwak, J.; Bae, W. K.; Lee, D.; Park, I.; Lim, J.; Park, M.; Cho, H.; Woo, H.; Yoon, D. Y.; Char, K.; Lee, S.; Lee, C. Bright and Efficient Full-Color Colloidal Quantum Dot Light-Emitting Diodes Using an Inverted Device Structure. *Nano Lett.* **2012**, *12* (5), 2362-2366.

(6) Jeong, S. Y.; Lim, S. C.; Bae, D. J.; Lee, Y. H.; Shin, H. J.; Yoon, S.-M.; Choi, J. Y.; Cha, O. H.; Jeong, M. S.; Perello, D. Photocurrent of CdSe Nanocrystals on Single-Walled Carbon Nanotube-Field Effect Transistor. *Appl. Phys. Lett.* **2008**, *92*, 243103.

(7) Yang, S. Y.; Zhao, N.; Zhang, L.; Zhong, H. Z.; Liu, R. B.; Zou, B. S. Field-Effect Transistor-Based Solution-Processed Colloidal Quantum Dot Photodetector with Broad Bandwidth into near-Infrared Region. *Nanotechnology* **2012**, *23*, 5826−5831.

(8) Lim, J.; Park, Y. S.; Klimov, V. I. Optical gain in colloidal quantum dots achieved with direct-current electrical pumping. *Nat. Mater.* **2018**, *17* (1), 42.

(9) Konstantatos, G.; Howard, I.; Fischer, A.; Hoogland, S.; Clifford, J.; Klem, E.; Levina, L.; Sargent, E. H. Ultrasensitive solution-cast quantum dot photodetectors. *Nature,* **2006**, *442*, 180.

(10) Lee, J. S.; Kovalenko, M. V.; Huang, J.; Chung, D. S.; Talapin, D. V. Band-like transport, high electron mobility and high photoconductivity in all-inorganic nanocrystal arrays. *Nat. Nanotechnol.* **2011**, *6*, 348.

(11) Chuang, C. H. M.; Brown, P. R.; Bulovic, V.; Bawendi, M. G. Improved performance and stability in quantum dot solar cells through band alignment engineering. *Nat. Mater.* **2014**, *13* (8), 796-801.

(12) Kagan, C. R.; Lifshitz, E.; Sargent, E. H.; Talapin, D. V. Building Devices From Colloidal Quantum Dots. *Science,* **2016**, *353*, 5523.

(13) Liu, M. X.; Voznyy, O.; Sabatini, R.; de Arquer, F. P. G.; Munir, R.; Balawi, A. H.; Lan, X. Z.; Fan, F. J.; Walters, G.; Kirmani, A. R.; Hoogland, S.; Laquai, F.; Amassian, A.; Sargent, E. H. Hybrid organic-inorganic inks flatten the energy landscape in colloidal quantum dot solids. *Nat. Mater.* **2017**, *16* (2), 258-263.

(14) Weidman, M. C.; Beck, M. E.; Hoffman, R. S.; Prins, F.; Tisdale, W. A. Monodisperse, air-stable PbS nanocrystals via precursor stoichiometry control. *ACS Nano,* **2014**, *8*, 6363–6371.

(15) Tang, J.; Kemp, K. W.; Hoogland, S.; Jeong, K. S.; Liu, H.; Levina, L.; Furukawa, M.; Wang, X. H.; Debnath, R.; Cha, D. K.; Chou, K. W.; Fischer, A.; Amassian, A.; Asbury, J. B.; Sargent, E. H. Colloidal-quantum-dot photovoltaics using atomic-ligand passivation. *Nat. Mater.* **2011**, *10* (10), 765-771.

(16) Choi, J.; Jo, J. W.; de Arquer, F. P. G.; Zhao, Y. B.; Sun, B.; Kim, J.; Choi, M. J.; Baek, S. W.; Proppe, A. H.; Seifitokaldani, A.; Nam, D. H.; Li, P.; Ouellette, O.; Kim, Y.; Voznyy, O.; Hoogland, S.; Kelley, S. O.; Lu, Z. H.; Sargent, E. H. Activated Electron-Transport Layers for Infrared Quantum Dot Optoelectronics. *Adv. Mater.* **2018**, *30*, 1801720.

(17) Biondi, M.; Choi, M.-J.; Ouellette, O.; Baek, S.-W.; Todorovic,́ P.; Sun, B.; Lee, S.; Wei, M.; Li, P.; Kirmani, A. R.; Sagar, L. K.; Richter, L. J.; Hoogland, S.; Lu, Z.-H.; de Arquer, F. P. G.; Sargent, E. H. AA Chemically Orthogonal Hole Transport Layer for Efficient Colloidal Quantum Dot Solar Cells. *Adv. Mater.* **2020**, *32*, 1906199.

(18) Xu, J. X.; Voznyy, O.; Liu, M. X.; Kirmani, A. R.; Walters, G.; Munir, R.; Abdelsamie, M.; Proppe, A. H.; Sarkar, A.; de Arquer, F. P. G.; Wei, M. Y.; Sun, B.; Liu, M.; Ouellette, O.; Quintero-Bermudez, R.; Li, J.; Fan, J.; Quan, L. N.; Todorovic, P.; Tan, H. R.; Hoogland,

S.; Kelley, S. O.; Stefik, M.; Amassian, A.; Sargent, E. H. 2D matrix engineering for homogeneous quantum dot coupling in photovoltaic solids. *Nat. Nanotechnol.* **2018**, *13* (6), 456.

(19) Goswami, P. N.; Mandal, D.; Rath, A. K. The Role of Surface Ligands in Determining the Electronic Properties of Quantum Dot Solids and Their Impact on Photovoltaic Figure of Merits. *Nanoscale* **2018**, *10*, 1072−1080.

(20) Azmi, R.; Oh, S.H.; Jang, S.Y. High-efficiency colloidal quantum dot photovoltaic devices using chemically modified heterojunctions. *ACS Energy Lett.* **2016**, *1*, 100–106.

(21) Zhitomirsky, D.; Kramer, I. J.; Labelle, A. J.; Fischer, A.; Debnath, R.; Pan, J.; Bakr, O. M.; Sargent, E. H. Colloidal Quantum Dot Photovoltaics: The Effect of Polydispersity. *Nano Lett.* **2012**, *12*, 1007−1012.

(22) Erslev, P. T.; Chen, H.-Y.; Gao, J.; Beard, M. C.; Frank, A. J.; van de Lagemaat, J.; Johnson, J. C.; Luther, J. M. Sharp Exponential Band Tails in Highly Disordered Lead Sulfide Quantum Dot Arrays. *Phys. Rev. B: Condens. Matter Mater. Phys.* **2012**, *86*, 155313 1−5.

(23) Chuang, C.-H. M.; Maurano, A.; Brandt, R. E.; Hwang, G. W.; Jean, J.; Buonassisi, T.; Bulović, V.; Bawendi, M. G. Open-Circuit Voltage Deficit, Radiative Sub-Bandgap States, and Prospects in Quantum Dot Solar Cells. *Nano Lett.* **2015**, *15*, 3286−3294.

(24) Yang, Z.; Janmohamed, A.; Lan, X.; de Arquer, F. P. G.; Voznyy, O.; Yassitepe, E.; Kim, G.-H.; Ning, Z.; Gong, X.; Comin, R.; Sargent, E. H. Colloidal Quantum Dot Photovoltaics Enhanced by Perovskite Shelling. *Nano Lett.* **2015**, *15*, 7539−7543.

(25) Aqoma, H.; Al Mubarok, M.; Hadmojo, W. T.; Lee, E.; Kim, T.; Ahn, T. K.; Oh, S.; Jang, S. High-efficiency photovoltaic devices using trap-controlled quantum-dot ink prepared via phase-transfer exchange. *Adv. Mater.* **2017**, *29*, 1605756.

(26) Kim, Y.; Che, F.; Jo, J. W.; Choi, J.; García de Arquer, F. P.; Voznyy, O.; Sun, B.; Kim, J.; Choi, M. J.; Quintero-Bermudez, R.; Fan, F.; Tan, C. S.; Bladt, E.; Walters, G.; Proppe, A. H.; Zou, C.; Yuan, H.; Bals, S.; Hofkens, J.; Roeffaers, M. B. J.; Hoogland, S.; Sargent, E. H. A Facet-specific quantum dot passivation strategy for colloid management and efficient infrared photovoltaics. *Adv. Mater.* **2019**, *31*, 1805580.

(27) Choi, J.; Choi, M.J.; Kim, J.; Dinic, F.; Todorovic, P.; Sun, B.; Wei, M.; Baek, S.W.; Hoogland, S.; Garcia de Arquer, F.P.; Voznyy, O.; Sargent, E. H. Stabilizing Surface Passivation Enables Stable Operation of Colloidal Quantum Dot Photovoltaic Devices at Maximum Power Point in an Air Ambient. *Adv. Mater.* **2020**, 1906497.

(28) Zhang, X.; Zhang, J.; Phuyal, D.; Du, J.; Tian, L.; Öberg, V. A.; Johansson, M. B.; Cappel, U. B.; Karis, O.; Liu, J.; Rensmo, H.; Boschloo, G.; Johansson, E. M. J. Inorganic $CsPbI_3$ Perovskite Coating on PbS Quantum Dot for Highly Efficient and Stable Infrared Light Converting Solar Cells. *Adv. Energy Mater.* **2018**, *8*, 1702049.

(29) Mandal, D.; Rath, A. K. Quantum Dots Coupled to an Oriented Two-Dimensional Crystalline Matrix for Solar Cell Application. *ACS Appl. Mater. Interfaces* **2018**, *10*, 39074−39082.

(30) Yang, Z. Y.; Voznyy, O.; Walters, G.; Fan, J. Z.; Liu, M.; Kinge, S.; Hoogland, S.; Sargent, E. H. Quantum Dots in Two-Dimensional Perovskite Matrices for Efficient Near-Infrared Light Emission. *ACS Photonics* **2017**, *4*, 830−836.

(31) Boles, M. A.; Ling, D.; Hyeon, T.; Talapin, D. V. The surface science of nanocrystals. *Nat. Mater.* **2016**, *15*, 141–153.

(32) Mandal, D.; Goswami, P. N.; Rath, A. K. Thiol and Halometallate, Mutually Passivated Quantum Dot Ink for Photovoltaic Application. *ACS Appl. Mater. Interfaces* **2019**, *11* (29), 26100-26108.

(33) Busupalli, B.; Kummara, S.; Kumaraswamy, G.; Prasad, B. L. V. Ultrathin sheets of metal or metal sulfide from molecularly thin sheets of metal thiolates in solution. *Chem. Mater.* **2014**, *26*, 3436−3442.

(34) Giansante, C.; Infante, I.; Fabiano, E.; Grisorio, R.; Suranna, G. P.; Gigli, G. "Darker-than-Black" PbS Quantum Dots: Enhancing Optical Absorption of Colloidal Semiconductor Nanocrystals via Short Conjugated Ligands. *J. Am. Chem. Soc.* **2015**, *137* (5), 1875-1886.

(35) Lin, Q.; Yun, H. J.; Liu, W.; Song, H. J.; Makarov, N. S.; Isaienko, O.; Nakotte, T.; Chen, G.; Luo, H.; Klimov, V. I.; Pietryga, J. M. Phase-Transfer Ligand Exchange of Lead Chalcogenide Quantum Dots for Direct Deposition of Thick, Highly Conductive Films. *J. Am. Chem. Soc.* **2017**, *139* (19), 6644−6653.

(36) Liu, Y.; Kim, D.; Morris, O. P.; Zhitomirsky, D.; Grossman, J. C. Origins of the Stokes Shift in PbS Quantum Dots: Impact of Polydispersity, Ligands, and Defects. *Acs Nano* **2018**, *12* (3), 2838-2845.

(37) Akshay, V. R.; Arun, B.; Mandal, G.; Vasundhara, M. Visible range optical absorption, Urbach energy estimation and paramagnetic response in Cr-doped TiO2 nanocrystals derived by a sol−gel method. *Phys. Chem. Chem. Phys.* **2019**, *21*, 12991−13004.

(38) Speirs, M. J.; Dirin, D. N.; Abdu-Aguye, M.; Balazs, D. M.; Kovalenko, M. V.; Loi, M. A. Temperature Dependent Behaviour of Lead Sulfide Quantum Dot Solar Cells and Films. *Energy Environ. Sci.* **2016**, *9*, 2916−2924.

(39) Shuttle, C. G.; O'Regan, B.; Ballantyne, A. M.; Nelson, J.; Bradley, D. D. C.; de Mello, J.; Durrant, J. R. Experimental Determination of the Rate Law for Charge Carrier Decay in a Polythiophene: Fullerene Solar Cell. *Appl. Phys. Lett.* **2008**, *92*, 093311.

(40) Mozer, A. J.; Sariciftci, N. S.; Lutsen, L.; Vanderzande, D.; Osterbacka, R.; Westerling, M.; Juska, G. Charge Transport and Recombination in Bulk Heterojunction Solar Cells Studied by the Photoinduced Charge Extraction in Linearly Increasing Voltage Technique. *Appl. Phys. Lett.* **2005**, *86*, 112104.

(41) Li, Z.; Gao, F.; Greenham, N. C.; McNeill, C. R. Comparison of the Operation of Polymer/Fullerene, Polymer/Polymer, and Polymer/Nanocrystal Solar Cells: A Transient Photocurrent and Photovoltage Study. *Adv. Funct. Mater.* **2011**, *21*, 1419−1431.

(42) Bi, Y.; Pradhan, S.; Gupta, S.; Akgul, M. Z.; Stavrinadis, A.; Konstantatos, G. Infrared Solution-Processed Quantum Dot Solar Cells Reaching External Quantum Efficiency of 80% at 1.35 μm and J(sc) in Excess of 34 mA cm^{-2}. *Adv. Mater.* **2018**, *30*, 1704928.

Chapter 7

Conclusion and future work

7.1 Conclusion of thesis findings

The main aim of this thesis has been to explore the use of PbS QDs in solar cell devices as the main light-absorbing materials. At first, we analysed the problems associated with the QDs solar cell for further improvement in the PCE and promotion in real market photovoltaic technology. The major challenge is the preservation of the optical properties of PbS QDs from synthesis to solar cell devices. During translation from as-synthesized QDs to solar cell device through surface ligand exchange process, the mid-gap trap states form inside the bandgap of QDs. These intermediate states trap the photogenerated charge carriers, reduce the carrier mobility, open-circuit voltage, and increase charge recombination rate in QD solar cells. PbS QDs show rock salt crystal structure, and surface facets are terminated by polar (100) and non-polar (111) crystal facets. In the case of polar (111) crystal facets, only Pb atoms are present and terminated by anionic ligands, whereas for non-polar (100) facets, both Pb and S atoms constitute terminal facets. PbS (100) facets are electronically neutral and protected by the electrostatic interaction of neutral ligands. So, both facets have different ligand passivation criteria to protect them from air oxidation and aggregation. This thesis provides various surface passivation strategies of QDs, which prohibit trap state formation and allow fast transportation of carriers in QDs solar cell devices. This section summarizes the overall research progress carried out in this thesis to improve the power conversion efficiency of PbS QD solar cells from 3.5% to 10.6%, through surface passivation of active layers, device engineering, and electron transport layer modification.

We have developed an energy-and cost-efficient process to build n-type TiO_2 layer used in QD solar cells. Nb-doped TiO_2 layer processed at lower temperatures (80˚c -150˚C) can act as an efficient n-type layer for QD solar cells when photodoped using solar light exposure. TiO_2 layers developed in this process is more efficient and cost-effective than the anatase phase TiO_2 layers processed at 500˚C. This photodoping effect leads to exceptional enhancement in electron densities, electron mobilities of TiO_2 layers, and ambient stability of QDs solar cell. PbS QDs are passivated by Z-type ligand $CdCl_2$ during synthesis, and MPA is used as an X-type ligand for the LBL ligand exchange process. The PCE of solar

cells increased from 3.5% in high temperature TiO_2 to 7.7% in the developed low-temperature processed TiO_2 based solar cells.

We have also investigated the impact of changes in size, shape, and functional groups of small chain organic thiols as X-type ligands for the LBL exchange process to modulate mobility, dielectric constant, and carrier doping density of lead sulfide quantum dot solids. We show the optimum criteria for X-type organic ligand selection. We have shown shorter ligands passivated QDs solar cells generate higher open-circuit voltage and improve ambient stability. However, shorter ligands passivated QDs solar cell do not exhibit higher short circuit current, which is quite unconventional as QD-to-QD distance reduces significantly and till this phenomenon is not well understood.

Next, we work on the development of QDs ink for one-step deposition of the thick active layer instead of LBL growth of QDs layer. Solution phase ligand exchange process is carried out to develop QDs ink, where halometallate anion and neutral lead halides are used as surface passivating ligands. Halometallate (PbX_3^-, X-Br, I) ion passivate polar (111) facets of QDs, and neutral PbX_2 protect S atoms of (100) facets through Z-type interaction. For the final one-step deposition of QDs, butylamine is used as a volatile solvent. However, we have shown that volatile butylamine solvent does not vaporize during film fabrication. Instead, it reacts with halometallate and lead halide ligands to form 2D crystalline matrix on QDs surface. As a result, a thick 2D matrix layer grows on QDs surface, which restricts the charge carrier transport in QDs solids and promotes the fusion of QDs through (100) facets. We have determined the composition of the 2D matrix layer for better understanding and further modifications. The 2D matrix is composed of two sets of complex Pb-amine and $(BA)_2PbI_4$ perovskite. Further, we have tuned the matrix layer thickness by changing counter cation of halometallate anion and achieved a maximum of 9% PCE in solar cells.

For further tuning the growth of the 2D matrix layer on QDs surface, we have introduced a two-step thiol, halometallate hybrid ligand passivation strategy. This is to reduce the matrix layer thickness and to attain atomically thin ligand shell. In the first step, an optimum amount of CPT ligand is added to as-synthesized oleic acid capped QDs, then proceed for halometallate ligand exchange to make QD ink. Due to the flexible nature of organic molecules, they can adjust in between two halometallate ions and bind to the unpassivated Pb atoms of PbS (111) facets. The lone pair electrons of sulfur atoms (from thiol ligands) interact electrostatically with charge neutral (100) facets of PbS QDs to

passivate the surface. The hybrid passivated QDs exhibit a 50% reduction in matrix shell thickness, reduced trap density, and improved monodispersity in solid films. These improvements allow a four-time increase in carrier mobility and doubling of the diffusion length, which permits the carrier extraction from a thicker QD absorbing layer. Solar cells made of hybrid passivated QDs show the high efficiency of 10.3% and reduced hysteresis effect. The advancements of surface passivation reduce oxygen doping and improve the ambient stability of the solar cells.

Next, we have advanced the thiol, halometallate hybrid passivation strategy to one step process for the preparation of QD ink. In this method, we have tuned CPT thiol ligand loading on QDs surface for a very wide range from very low to very high concentration along with halometallate ion. Due to the higher amount of thiol ligand loading along with halometallate ion, Pb atoms of PbS (111) facets are more compactly passivated, and Pb atoms of (100) facets are also protected by thiol molecules electrostatically. These mutually passivated QDs exhibit significant improvement in optoelectronic properties with preserving clean energy bandgap and maintaining their band-to-band emission for a longer period of time. This strategy restricts further the growth of the 2D matrix shell layer and reduces 70% of matrix shell thickness. A higher concentration of CPT thiol ligand has more favourable electrostatic interaction on PbS (100) facets to protect QDs from fusion and maintain their monodispersity. These photophysical improvements of QDs directly impact the PCE of solar cells. The photovoltaic devices of hybrid passivated QDs have shown remarkable improvement in open-circuit voltage as well as in short-circuit current and lesser hysteresis effect. Finally, we have achieved a maximum of 10.6% efficient solar cells made by mutually hybrid passivated QDs, and this is also the maximum reported efficiency in this thesis.

7.2 Future work

There is still plenty of room to improve the performance of PbS QDs solar cells. The facets selective surface ligand passivation of QDs lead to the enhancement in carrier mobility and longer carrier lifetime in QDs solids.[1,2] But to date, the carrier mobility of QDs solid films with excellent optical properties is significantly low (10^{-3} to 10^{-4} $cm^2V^{-1}s^{-1}$), which results in the reduction of charge extraction efficiency from thicker QDs films.[3,4] Low carrier mobility increases the carrier recombination rate inside the QDs films. These are the fundamental limitation for further improvement of PbS QDs solar cell PCE. Major advances

in improving the charge extraction efficiency have been attained through increasing the carrier diffusion length (L_D).[1,2,5] This strategy will result in extended carrier lifetimes, reduced recombination rates, and therefore longer carrier diffusion lengths in device.[6-8] To fabricate the bulk heterojunction solar cells *p*- and *n*-type semiconductors need to be mixed at the nanoscale level while maintaining the continuous charge transport network. There are few reports on CQDs bulk heterojunction solar cells made by CQDs/ polymer[7] blends and two different CQDs (*n*-type ZnO and *p*-type PbS QDs) mixture.[8]

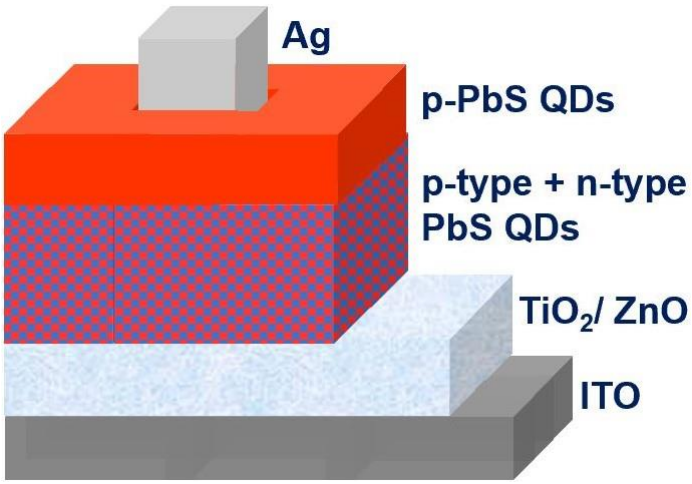

Figure 7.1: Schematic representation of bulk heterojunction device architecture.

In our last working chapter, we have developed a one-step hybrid (thiol+halometallate) passivated QDs ink with higher amount of thiol loading. Increase in thiol loading makes the QDs p-type, whereas halometallate only passivated QDs show n-type characteristics.

On the continuation of our last work, we can further construct a bulk heterojunction device by mixing both the p-type and n-type PbS QDs ink, as both the QDs are dispersed in a common butylamine solvent. In general, it is quite challenging to disperse two differently doped QDs in a common solvent. This p-type and n-type blended mixture of PbS QDs will exhibit a distinct potential difference in the device. This will increase the junction area of the solar cells. The blended network of the mixture will enforce efficient carriers extraction from the thicker devices. As a result, we assume that PbS QDs solar cell will achieve record PCE in this device architecture.

7.2 References

(1) Liu, M. X.; Voznyy, O.; Sabatini, R.; de Arquer, F. P. G.; Munir, R.; Balawi, A. H.; Lan, X. Z.; Fan, F. J.; Walters, G.; Kirmani, A. R.; Hoogland, S.; Laquai, F.; Amassian, A.; Sargent, E. H. Hybrid organic-inorganic inks flatten the energy landscape in colloidal quantum dot solids. *Nat. Mater.* **2017**, *16* (2), 258-263.

(2) Carey, G. H.; Levina, L.; Comin, R.; Voznyy, O.; Sargent, E. H. Record charge carrier diffusion length in colloidal quantum dot solids via mutual dot-to-dot surface passivation. *Adv. Mater.* **2015**, *27*, 3325–3330.

(3) Mandal, D.; Rath, A. K. Quantum Dots Coupled to an Oriented Two-Dimensional Crystalline Matrix for Solar Cell Application. *ACS Appl. Mater. Interfaces* **2018**, *10* (45), 39074−39082.

(4) Mandal, D.; Goswami, P. N.; Rath, A. K. Thiol and Halometallate, Mutually Passivated Quantum Dot Ink for Photovoltaic Application. *ACS Appl. Mater. Interfaces* **2019**, *11* (29), 26100-26108.

(5) Zhitomirsky, D.; Voznyy, O.; Levina, L.; Hoogland, S.; Kemp, K. W.; Ip, A. H.; Thon, S. M.; Sargent, E. H. Engineering Colloidal Quantum Dot Solids within and beyond the Mobility-Invariant Regime. Nat. Commun. **2014**, *5*, 3803.

(6) Kramer, I. J.; Zhitomirsky, D.; Bass, J. D.; Rice, P. M.; Topuria, T.; Krupp, L.; Thon, S. M.; Ip, A. H.; Debnath, R.; Kim, H.-C.; Sargent, E. H. Ordered Nanopillar Structured Electrodes for Depleted Bulk Heterojunction Colloidal Quantum Dot Solar Cells. Adv. Mater. **2012**, *24*, 2315−2319.

(7) Nam, M.; Park, J.; Kim, S.-W.; Lee, K. Broadband-Absorbing Hybrid Solar Cells with Efficiency Greater than 3% Based on a Bulk Heterojunction of PbS Quantum Dots and a Low-Bandgap Polymer. J. Mater. Chem. A **2014**, *2*, 3978.

(8) Rath, A. K.; Bernechea, M.; Martinez, L.; de Arquer, F. P. G.; Osmond, J.; Konstantatos, G. Solution-Processed Inorganic Bulk Nano-Heterojunctions and Their Application to Solar Cells. Nat. Photonics **2012**, *6*, 529−534.

ABSTRACT

Name of the Student: Debranjan Mandal **Registration No.:** 10CC17A26016
Faculty of Study: Chemical Sciences **Year of Submission:** 2021
AcSIR academic centre/CSIR Lab: NCL, Pune **Name of the Supervisor:** Dr. Arup K. Rath

Title of the thesis: Role of Surface Passivation and Doping on the Development of Quantum Dot Solar Cells

The work in this thesis is focused on the use of advanced nanotechnology for the development of next-generation solar cells. Noble processes are developed to harness the unique optoelectronic properties of quantum dots to improve the performance of solar cells. This thesis explores the use of lead sulfide (PbS) quantum dots (QDs) as the main light-absorbing material for the development of QD solar cells. Near-infrared active and earth-abundant PbS QDs have emerged as a viable alternative to conventional materials (like Si solar cell, CIZS solar cell, etc.) due to their many distinct advantages, like solution-phase facile processability, bandgap tenability, and low material cost. Despite significant breakthroughs over the years, low performance has remained the major roadblock for the commercialization of QD solar cells. It has been understood that the primary reasons for the underperformance of QD solar cells are originated from not so high carrier mobility, low open-circuit voltage, and high charge recombination rate in QDs based solar cells. We posited that most of these drawbacks could effectively be mitigated by a comprehensive surface passivation strategy which would prohibit trap state formation and allow fast transport of photo carriers through the QD solids.

In this thesis, by understanding the surface chemistry of PbS QDs in detail, we have strategically developed the surface passivation methods to improve the power conversion efficiency (PCE) of QD solar cells. A low-temperature processed TiO_2 layer (acts as an electron extracting layer in solar cell device) has been demonstrated to make QD solar cells on flexible substrates. The solvent induced 2D matrix layer has been tracked on the surface of QD ink. The 2D matrix layer thickness on the QD surface has been engineered to improve the PCE of QD solar cell. A two-step hybrid (organic and inorganic) ligand passivation strategy has been developed for the first time to make high quality QDs ink. Further, the one-step hybrid passivation method has been realized to develop QD solar cells. Through these strategic developments, in this thesis work, the PCE of PbS QD solar cell has been improved from 3.7% to 10.6%.

Lastly, based on the findings in this thesis work, possible future directions that could further improve the efficiency of QD solar cells are discussed.

List of Publication(s) in SCI Journal(s) Emanating from the Thesis Work

(I) **Mandal, D**.; Goswami, P. N.; Rath, A. K. Colossal photo-conductive gain in low temperature processed TiO_2 films and their application in quantum dot solar cells. *Appl. Phys. Lett*, **2017**, *110*, 123902.

(II) Goswami, P. N.; **Mandal, D**.; Rath, A. K. The role of surface ligands in determining the electronic properties of quantum dot solids and their impact on photovoltaic figure of merits. *Nanoscale*, **2018**, *10*, 1072-1080.

(III) **Mandal, D**.; Rath, A. K. Quantum Dots Coupled to an Oriented Two-Dimensional Crystalline Matrix for Solar Cell Application. *ACS Appl. Mater. Interfaces*, **2018**, *10*, 39074−39082.

(IV) **Mandal, D**.; Goswami, P. N.; Rath, A. K. Thiol and Halometallate, Mutually Passivated Quantum Dot Ink for Photovoltaic Application. *ACS Appl. Mater. Interfaces*, **2019**, *11*, 26100−26108.

List of papers with abstract presented (oral or poster) at national or international conferences/seminars.

(I) **"Science Day Celebration 2019"** held at CSIR National Chemical laboratory Pune. (Presented poster)

(II) **"Mumbai-Pune Semiconductor Conference 2019"** held at Indian Institute of Technology, Mumbai (IIT Mumbai). (Presented poster)

(III) **"Divisional day celebration 2017"** held at CSIR National Chemical laboratory Pune. (Delivered oral presentation)

(IV) **"Mumbai-Pune Semiconductor Conference 2017"** held at Tata Institute of Fundamental Research, Mumbai (TIFR-Mumbai). (Presented poster)

(V) **"Science day celebration 2017"** held at CSIR National Chemical laboratory Pune. (Presented poster)

Colossal photo-conductive gain in low temperature processed TiO_2 films and their application in quantum dot solar cells

Debranjan Mandal, Prasenjit N. Goswami, and Arup K. Rath

Citation: Appl. Phys. Lett. **110**, 123902 (2017); doi: 10.1063/1.4978766
View online: http://dx.doi.org/10.1063/1.4978766
View Table of Contents: http://aip.scitation.org/toc/apl/110/12
Published by the American Institute of Physics

Articles you may be interested in

Retraction: "Experimental techniques for imaging and measuring transient vapor nanobubbles" [Appl. Phys. Lett. 101, 264102 (2012)]
Appl. Phys. Lett. **110**, 129901129901 (2017); 10.1063/1.4978413

Observation of individual stacking faults in GaN microcrystals by x-ray nanodiffraction
Appl. Phys. Lett. **110**, 121905121905 (2017); 10.1063/1.4978870

Mechanical signatures of degradation of the photovoltaic perovskite CH3NH3PbI3 upon water vapor exposure
Appl. Phys. Lett. **110**, 121903121903 (2017); 10.1063/1.4978687

Localization crossover and phase coherent electron transport in a-InGaZnO4 thin films
Appl. Phys. Lett. **110**, 122101122101 (2017); 10.1063/1.4978530

Colossal photo-conductive gain in low temperature processed TiO_2 films and their application in quantum dot solar cells

Debranjan Mandal, Prasenjit N. Goswami, and Arup K. Rath[a)]
CSIR-National Chemical Laboratory, Dr. Homi Bhabha Road, Pune 411008, India

(Received 17 November 2016; accepted 6 March 2017; published online 20 March 2017)

Colloidal quantum dot (QD) solar cells have seen remarkable progress in recent past to reach the certified efficiency of 10.6%. Anatase titanium oxide (TiO_2) is a widely studied n-type widow layer for the collection of photogenerated electrons in QD solar cells. Requirement of high temperature (~500 °C) processing steps proved to be disadvantageous for its applications in flexible solar cells and roll to roll processing, and it also has adverse commercial implications. Here, we report that solar light exposure to low temperature processed (80 °C–150 °C) TiO_2 and niobium doped TiO_2 films leads to unprecedented enhancement in their electron densities and electron mobilities, which enables them to be used as efficient n-type layers in quantum dot solar cells. Such photoinduced high conducting states in these films show gradual decay over hours after the light bias is taken off and can be retrieved under solar illumination. On the contrary, TiO_2 films processed at 500 °C show marginal photo induced enhancements in their characteristics. In bilayer configuration with PbS QDs, photovoltaic devices based on low temperature processed TiO_2 films show improved performance over high temperature processed TiO_2 films. The stability of photovoltaic devices also improved in low temperature processed TiO_2 films under ambient working conditions. *Published by AIP Publishing.* [http://dx.doi.org/10.1063/1.4978766]

Titanium dioxide (TiO_2) has long been studied as a preferred n-type window layer in dye sensitised solar cells (DSSCs),[1,2] organic photovoltaics,[3,4] perovskites,[5,6] and quantum dot (QD) solar cells,[7,8] for its favourable optical and electronic properties. In order to implement TiO_2 in high performance solar cell applications, annealing over 500 °C is a crucial step to form the calcinated anatase phase TiO_2 layer of desired electronic properties.[7–9] Especially, for QD solar cells, the heterojunction between the TiO_2 and QD layers is of particular importance as the photocarrier extraction process is dominated by the drift motion of carriers rather than diffusion.[10,11] Preparation of an efficient n-type TiO_2 layer for a QD solar cell often involves multiple high temperature processing steps and sequential deposition of various sized TiO_2 nanoparticle layers.[7–9] High temperature annealing requirement has narrowed down the prospect of TiO_2 to be used in flexible solar cells, is incompatible with roll to roll processing, and has hindered the commercial prospect by increasing the processing cost. Although low temperature processed TiO_2 films (<200 °C) are desirable, they so far lead to poor electrical conductivity, unfavourable for fast electron extraction and electron transport in solar cells. However, low temperature processed TiO_2 has been used in solar cell application as a complementary hole blocking layer along with key n-type layers like PCBM or C_{60} in organic[12] and perovskite[13] solar cells. Synthesis of the TiO_2 layer at low temperatures with desirable electrical properties will therefore be a notable step forward. This would not only be advantageous from economic aspect but also add flexibility in terms of device engineering for the development of high performance solar cells.

Here, we report TiO_2 and niobium (Nb) doped TiO_2 thin films processed below 150 °C to be used as efficient n-type layers for QD solar cell applications. We show that solar light exposure for a brief period of time leads to a semi-sustainable increase in electron density and electron mobility of TiO_2 layers, which retains these enhancements for hours after switching of the light. This enables us to develop n-p junction solar cells utilizing low temperature processed TiO_2 or Nb doped TiO_2 as sole n-type layers with p-type PbS QDs.

Details of the synthesis process of TiO_2 and Nb doped TiO_2 films can be found in the experimental section of the supplementary material. Thin films consist of 0%, 2.5%, and 5% Nb doped TiO_2 layers, annealed at 150 °C, will be represented as TiO_2–150 °C, 2.5Nb/TiO_2–150 °C, and 5Nb/TiO_2–150 °C, respectively, and TiO_2 film annealed at 500 °C will be referred as TiO_2–500 °C, for the rest of the report. X-ray photoelectron spectroscopy is used to determine the chemical composition of studied films (S1, supplementary material). The fine spectrum of "Ti" 2 P orbital splitting confirms the formation of only "Ti^{4+}" oxidation state.[14] However, "Ti" to "O" atomic ratios in TiO_2–500 °C and TiO_2–150 °C samples are found to be 2.08 and 1.97, respectively, indicating mild oxygen deficiency in low temperature processed TiO_2 films (Table S2, supplementary material).[14] Measured concentrations of Nb doping in 2.5% and 5% doped samples are found to be 4.5% and 5.9%, respectively. The XRD pattern of TiO_2 films shows (S3, supplementary material) the formation of the anatase phase TiO_2 for samples annealed at 350 °C or higher temperatures, whereas no peak is observed for samples annealed below 350 °C.[15] However, crystal fringes are observed in TEM measurement of low temperature processed TiO_2 films (S4, supplementary material). Selected area electron diffraction measurement shows nice diffraction spots, suggesting towards the semi-crystalline nature and nanometer range grain size in TiO_2

[a)]Email: ak.rath@ncl.res.in

films processed at 150 °C. SEM images of the films show uniform film depositions with good surface coverage in all TiO_2 films (S5, supplementary material). Direct optical band gaps for TiO_2–500 °C, TiO_2–150 °C, 2.5Nb/TiO_2–150 °C, and 5Nb/TiO_2–150 °C films are 3.62 eV, 3.65 eV, 3.68 eV, and 3.73 eV, respectively, as determined from the Tauc plot[16] of absorption study, shown in Fig. S6 of the supplementary material. An increase in optical band gap with an increase in doping density could be due to the Burstein–Moss effect in semiconductors.[17] Cyclic voltammetry is used to determine the conduction band edge from the reduction potential of TiO_2 films (S7, supplementary material).[18] Measured values of the conduction band position for TiO_2–500 °C, TiO_2–150 °C, 2.5Nb/TiO_2–150 °C, and 5Nb/TiO_2–150 °C samples are 4.27 eV, 3.82 eV, 3.87 eV, and 4 eV, respectively.

Planer n-p heterojunction solar cells are prepared using TiO_2 as the n- type layer and PbS QDs as the p-type layer. The device structure is given as transparent conducting electrode (TCE)/n-type layer/PbS QD/MoO_3/Au/Ag. Figure 1(a) shows the current voltage characteristics of solar cells under the dark condition for before (lines) and after 20 min of light soaking (scatter+line) under 1.5 solar illumination. Light soaking under solar illumination is found to have a profound influence on the current voltage characteristics of solar cells, especially for low temperature processed TiO_2 layers. Solar cells based on TiO_2–150 °C, 2.5Nb/TiO_2–150 °C, and 5Nb/TiO_2–150 °C show approximately 10^4 times increase in forward bias current and rectification ratio at 0.8 V, whereas the TiO_2–500 °C based device shows moderate five times improvement due to photodoping. Figure 1(b) shows the evolution of short circuit current density (J_{sc}) with time for the solar cells. J_{sc} for low temperature processed TiO_2 based solar cells increases steadily with time and takes almost seventeen minutes to saturate, whereas TiO_2–500 °C based solar cells show very little increase in J_{sc} within initial 10s and continuous illumination over 100s leads to a monotonic decrease in J_{sc} with time. This could be due to stronger photocatalytic activity of the TiO_2–500 °C layer, which may lead to gradual degradation of the TiO_2/PbS QD junction.[19,20] Figure 1(c) shows the current density vs voltage plot for different solar cells under solar illumination at the saturated working condition. Comparison of solar cell performances is shown in Table I.

Comparative study of annealing temperatures and Nb doping optimizations are given in S8 and S9 of the supplementary material, respectively. It is found that the TiO_2 layer processed between 80 °C and 150 °C with 2.5% Nb doping is best suited for optimised photovoltaic performance. There are negligible differences in performances due to forward and reverse scans as shown in S10 (supplementary material). The statistical variations in performance for 2.5Nb/TiO_2–150 °C and TiO_2–150 °C based solar cells are shown in S11 (supplementary material). Figure 1(d) represents the external quantum efficiency plot (EQE %) of the studied devices. Low temperature processed TiO_2 layers show superior carrier extraction ability than TiO_2–500 °C based devices for almost entire wavelength range. The integrated short circuit current from EQE for TiO_2–500 °C, TiO_2–150 °C, 2.5Nb/TiO_2–150 °C, and 5Nb/TiO_2–150 °C solar cells is 14.1 mA/cm^2, 24.3 mA/cm^2, 25.8 mA/cm^2, and 21.4 mA/cm^2, respectively. Small discrepancies in measured and predicted short circuit current from EQE for the respective solar cells could be due to unsaturated photodoping due to low intensity white light biasing used during EQE measurements.

In order to elucidate the chemical doping and photodoping effect on constituent layers, we have carried out capacitance vs voltage (Cap-V)[9,21,22] study of solar cells. Capacitance (real part) of an n-p heterojunction solar cell can be written as[23]

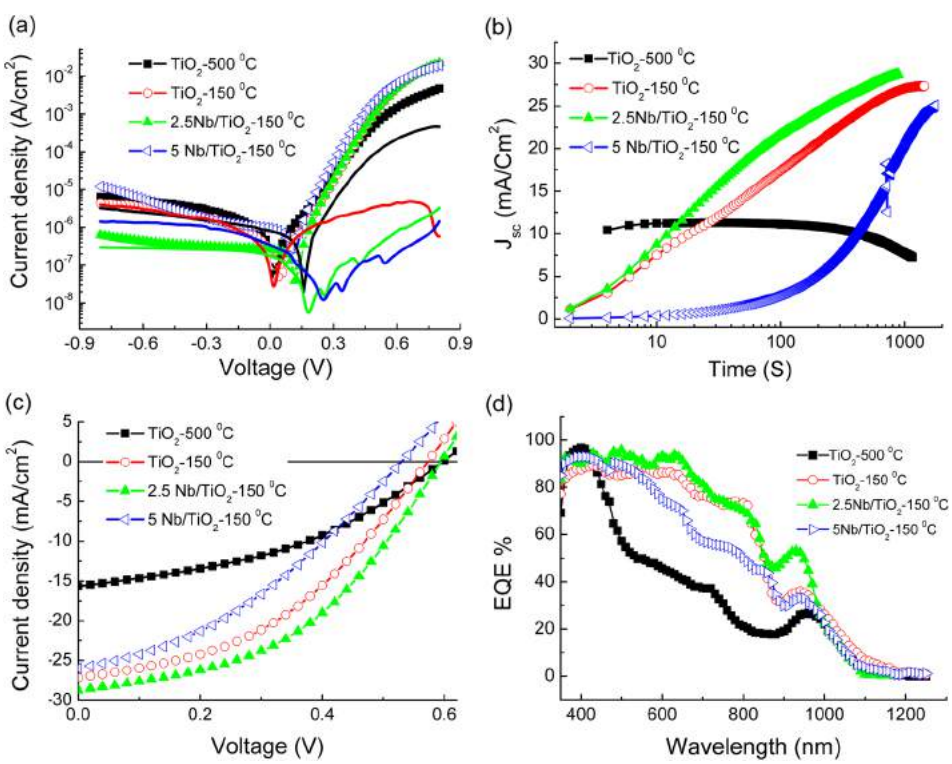

FIG. 1. (a) J-V characteristics of solar cells for different n-type layers under dark condition. Before and after photodoping situations are depicted by lines and scatter symbol+line, respectively. (b) J_{sc} Vs time for solar cells measured under continuous solar illumination. (c) J-V characteristics of solar cells under 1.5 AM illumination and (d) comparison of the EQE spectrum of solar cells for different n-type layers.

TABLE I. Comparison of solar cell performances for various TiO_2 layers at saturated photodoping condition.

Name	V_{oc} (V)	J_{sc} (mA/cm^2)	FF (%)	PCE (%)
ITO/TiO_2-500 °C/PbS/MoO_3/Au/Ag	0 .6V	15.66	39.4	3.70
ITO/TiO_2-150 °C/PbS/MoO_3/Au/Ag	0.58	27.18	41.52	6.54
ITO/2.5Nb/TiO_2-150 °C/PbS/MoO_3/Au/Ag	0.6	28.7	44.67	7.69
ITO/5Nb/TiO_2-150 °C/PbS/MoO_3/Au/Ag	0.6	25.98	37.01	5.77

$$C = \frac{\varepsilon_0 A}{\frac{X_p}{\varepsilon_p} + \frac{X_n}{\varepsilon_n}}, \quad (1)$$

where "C" is the junction capacitance, "ε_0" is the permittivity of air, "A" is the area of the device, "X_p" and "X_n" are the depletion widths for PbS and the n-type layer, and ε_p and ε_n are dielectric constants of PbS and the n-type layer. Figures 2(a) and 2(b) show Cap-V plots of solar cells before and after light soaking, respectively. It can be seen that for both conditions, capacitance of all the devices saturates at high reverse biases. This implies that either both PbS and TiO_2 layers or one of the layers is fully depleted under high reverse bias condition. Since PbS is relatively mildly doped than TiO_2, we can safely assume that, at −0.8 V reverse bias condition, the PbS layer is fully depleted.[9,21] Depletion widths of individual layers at different applied bias for before and after light soaking conditions are determined from the Cap-V results. Figure 2(c) represents the depletion width of PbS layers for before and after photodoping conditions. Clearly, photodoping has a minimal impact on the depletion width of PbS layers. This implies that free hole density of the PbS layers does not change due to photodoping. However, saturated depletion widths of different TiO_2 layers decrease quite significantly due to photodoping, as shown in Figure 2(d). The effects of photodoping on depletion widths for low temperature process TiO_2 layers are more prominent than the TiO_2–500 °C layer. Considering the abrupt p-n junction model,[23] we determine the electron density of different TiO_2 layers, which is shown in Table II (details of the analysis are given in S12 of the supplementary material). It can be seen that carrier density for the low temperature processed TiO_2 layers almost get doubled upon photodoping, whereas for the TiO_2–500 °C layer, it remains almost unchanged.

In order to have better insights into the underlying mechanism of light induced enhancements in low temperature processed TiO_2 layers, simulation of the current voltage characteristics has been carried out for the best performing solar cell using the SCAPS simulation.[24–26] Details of the simulation parameters are shown in S13 (supplementary material). As shown in Figure 3(a), at the saturated photodoping condition, simulation results show excellent

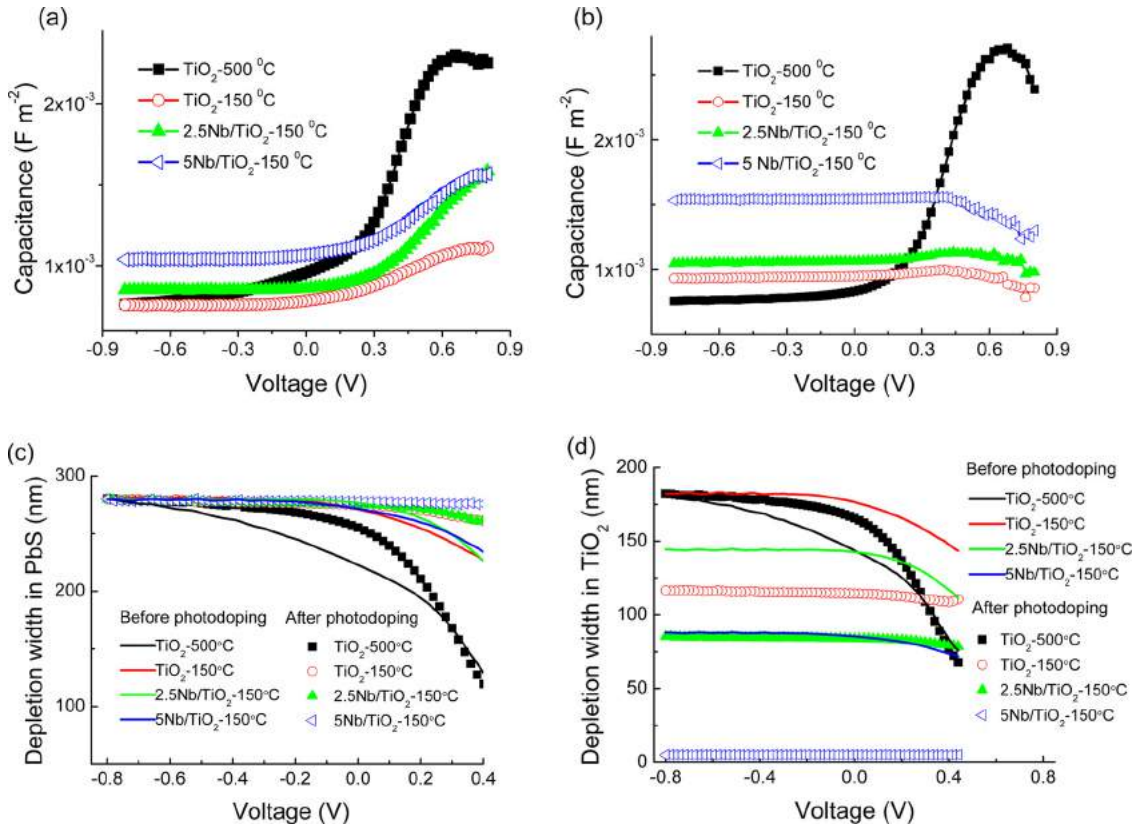

FIG. 2. Cap-V results of the photovoltaic devices measured under dark condition (a) before (b) after photodoping, respectively. Depletion width vs applied bias plots of (c) PbS layers and (d) n-type TiO_2 layers are shown. Colour lines and symbols correspond to depletion widths before light soaking and after photodoping conditions, respectively.

TABLE II. Electron density of various n-type layers for before and after light soaking conditions, from Cap-V measurement.

n-Type layer	Electron density before light soaking (cm^{-3})	Electron density after light soaking (cm^{-3})
TiO_2-500 °C	4.65×10^{16}	4.63×10^{16}
TiO_2-150 °C	4.62×10^{16}	7.21×10^{16}
2.5Nb/TiO_2-150 °C	5.83×10^{16}	1.03×10^{17}
5Nb/TiO_2-150 °C	9.65×10^{16}	1.66×10^{18}

agreements with measured J-V characteristics of the photodoped 2.5Nb/TiO_2–150 °C based solar cell, for both dark and illuminated conditions. In order to simulate the dark J-V characteristics of the solar cell before photodoping, we change the electron density to $5.9 \times 10^{16} cm^{-3}$ (as determined from Cap-V measurement (Table II)), while keeping the rest of the parameters unchanged. It is observed that simulated data do not follow the experimental dark J-V curve before photodoping. Since the electrical conductivity depends on carrier density as well as mobility, we sought to vary the electron mobility of the 2.5Nb/TiO_2–150 °C layer to simulate the experimental data. As shown in Figure 4(b), electron mobility is varied independently in between 10^{-3} and 10^{-9} $cm^2V^{-1}S^{-1}$. It is found that for the electron mobility in between 10^{-7} and 10^{-8} $cm^2V^{-1}S^{-1}$, simulated results corroborate well with the dark experimental J–V results. Therefore, simulation suggests that in addition to electron density, electron mobility of the 2.5Nb/TiO_2–150 °C layer must increase upon photodoping to justify the increase in solar cell performance.

In order to probe the mobility of low temperature processed TiO_2 layers, we have fabricated metal-semiconductor-metal (MSM) devices, where the TiO_2 layer is sandwiched between two metal contacts.[27] Single carrier, electron only devices based on 2.5Nb/TiO_2–150 °C layer and 5Nb/TiO_2–150 °C layer are prepared using ITO as the bottom electrode and Ag as the top electrode. At constant applied bias of 0.3 V, the current of the devices is probed against time under dark and continuous solar illumination. As illustrated in Figure 4(a), current of the devices remains constant under dark probing, but under continuous solar illumination, current of the devices increases monotonically with time. It can be noted that unlike photovoltaic devices, current

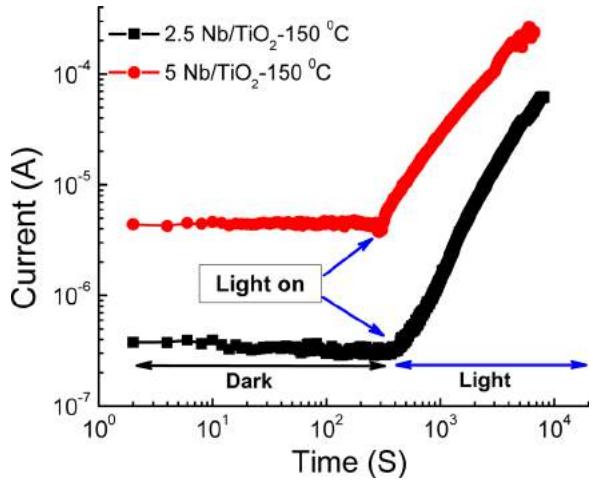

FIG. 4. Current vs time plot for MSM devices made of 2.5Nb/TiO_2-150 °C and 5Nb/TiO_2-150 °C layer, measured under dark and solar illumination. "Light on" position is marked to guide the eye.

saturation in these devices is not attained even after two hours of light exposure. In the low injection regime, current for ohmic conduction can be expressed by $J = \mu nqE$,[28] where J is the current density, μ is the carrier mobility, n is the electron density, q is the electronic charge, and E is the applied electric field. It is found that for the above measurement range, carrier mobility increases to ~100 times for the 2.5Nb/TiO_2–150 °C layer and ~5 times for the 5Nb/TiO_2–150 °C layer due to light soaking (S14, supplementary material). Therefore, experimental results from MSM devices do support the simulation prophecy of increase in electron mobility of low temperature processed TiO_2 layers upon light exposure. Further, electron mobility before light exposure for the 2.5Nb/TiO_2–150 °C layer is determined to be 4.46×10^{-8} $cm^2V^{-1}S^{-1}$, which is in good agreement with the simulation findings. Free electrons of TiO_2 layers can be trapped due to adsorption organic components from starting materials and ambient gas molecules such as O_2, NO_2, and CO on TiO_2 surfaces.[22] When exposed to high energy light, electrons from the valence band jump to the conduction band, which helps to dissociate the surface absorbents and thereby reduce trap states and enhance free electron density and mobility in TiO_2 films.[29,30] In photovoltaic devices, photoelectron transfer from PbS to TiO_2 layer would increase the electron density in the conduction band significantly.

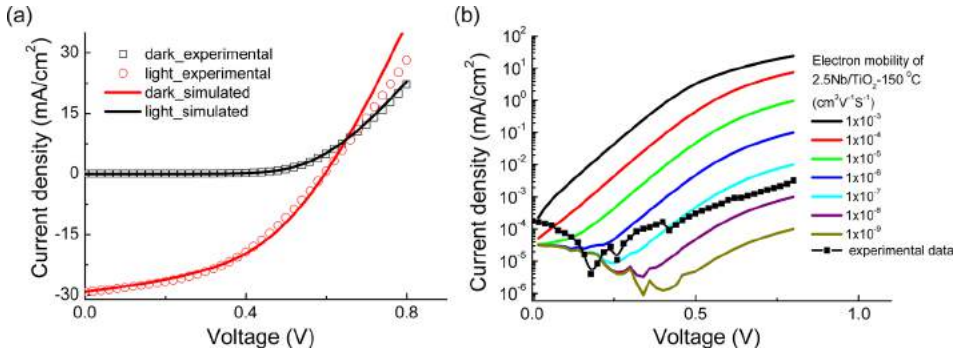

FIG. 3. (a) The experimental (scatter) and simulated (line) J-V plots for 2.5Nb/TiO_2-150 °C based photovoltaic device under dark and 1.5 AM illumination for the saturated photodoping condition. (b) Simulated dark J-V response of the device for varied electron mobility of the 2.5Nb/TiO_2-150 °C layer. Black symbol+line in (b) represents the experimental dark J-V curve of the device measured before photodoping.

This would further facilitate the dissociation of absorbents from the TiO_2 surface and thereby may help to attain faster current saturation.

In summary, we demonstrate that TiO_2 and Nb doped TiO_2 processed below 150 °C could be used as excellent electron accepting layers for QD solar cells. Light induced enhancements in electron concentration and electron mobility of low temperature processed TiO_2 layers are confirmed by both the experiment and simulation. For this work, we have opted to use organic ligand passivated p-type PbS QDs, in order to furnish the electron excepting properties of low temperature processed TiO_2 layers. Further improvement in solar cell performance would be possible by adopting advance inorganic passivation scheme in PbS QDs processing.

See supplementary material for experimental details, material characterizations, and additional device characterization details.

The authors acknowledge financial support from GAIL India Limited and CSIR-NCL start up grant to carry out the research work. The authors thank Dr. C. S. Gopinath from NCL for extending the XPS measurement facility.

[1]S. Mathew, A. Yella, P. Gao, R. Humphry-Baker, B. F. E. Curchod, N. Ashari-Astani, I. Tavernelli, U. Rothlisberger, M. K. Nazeeruddin, and M. Gratzel, Nat. Chem. **6**(3), 242–247 (2014).
[2]M. Durr, A. Bamedi, A. Yasuda, and G. Nelles, Appl. Phys. Lett. **84**(17), 3397–3399 (2004).
[3]C. Goh, S. R. Scully, and M. D. McGehee, J. Appl. Phys. **101**(11), 114503 (2007).
[4]J. A. Chang, J. H. Rhee, S. H. Im, Y. H. Lee, H. J. Kim, S. I. Seok, M. K. Nazeeruddin, and M. Gratzel, Nano Lett. **10**(7), 2609–2612 (2010).
[5]M. M. Lee, J. Teuscher, T. Miyasaka, T. N. Murakami, and H. J. Snaith, Science **338**(6107), 643–647 (2012).
[6]A. Guerrero, E. J. Juarez-Perez, J. Bisquert, I. Mora-Sero, and G. Garcia-Belmonte, Appl. Phys. Lett. **105**(13), 133902 (2014).
[7]H. Liu, J. Tang, I. J. Kramer, R. Debnath, G. I. Koleilat, X. H. Wang, A. Fisher, R. Li, L. Brzozowski, L. Levina, and E. H. Sargent, Adv. Mater. **23**(33), 3832–3837 (2011).
[8]L. Etgar, T. Moehl, S. Gabriel, S. G. Hickey, A. Eychmuller, and M. Gratzel, ACS Nano **6**(4), 3092–3099 (2012).
[9]A. G. Pattantyus-Abraham, I. J. Kramer, A. R. Barkhouse, X. H. Wang, G. Konstantatos, R. Debnath, L. Levina, I. Raabe, M. K. Nazeeruddin, M. Gratzel, and E. H. Sargent, ACS Nano **4**(6), 3374–3380 (2010).
[10]J. P. Clifford, K. W. Johnston, L. Levina, and E. H. Sargent, Appl. Phys. Lett. **91**(25), 253117 (2007).
[11]K. W. Johnston, A. G. Pattantyus-Abraham, J. P. Clifford, S. H. Myrskog, S. Hoogland, H. Shukla, J. D. Klem, L. Levina, and E. H. Sargent, Appl. Phys. Lett. **92**(12), 122111 (2008).
[12]J. Y. Kim, K. Lee, N. E. Coates, D. Moses, T. Q. Nguyen, M. Dante, and A. J. Heeger, Science **317**(5835), 222–225 (2007).
[13]P. Docampo, J. M. Ball, M. Darwich, G. E. Eperon, and H. J. Snaith, Nat. Commun. **4**, 2761 (2013).
[14]M. Z. Atashbar, H. T. Sun, B. Gong, W. Wlodarski, and R. Lamb, Thin Solid Films **326**(1–2), 238–244 (1998).
[15]L. Li, P. Zhang, W. M. Wang, H. T. Lin, A. B. Zerdoum, S. J. Geiger, Y. C. Liu, N. Xiao, Y. Zou, O. Ogbuu, Q. Y. Du, X. Q. Jia, J. J. Li, and J. J. Hu, Sci. Rep. **5**, 13832 (2015).
[16]N. Ghobadi, Int. Nano Lett. **3**(1), 2 (2013).
[17]A. V. Emeline, Y. Furubayashi, X. T. Zhang, M. Jin, T. Murakami, and A. Fujishima, J. Phys. Chem. B **109**(51), 24441–24444 (2005).
[18]D. Mandal and T. W. Hamann, ACS Appl. Mater. Interfaces **8**(1), 419–424 (2016).
[19]T. Leijtens, G. E. Eperon, S. Pathak, A. Abate, M. M. Lee, and H. J. Snaith, Nat. Commun. **4**, 2885 (2013).
[20]C. Y. Fan, C. Chen, J. Wang, X. X. Fu, Z. M. Ren, G. D. Qian, and Z. Y. Wang, J. Mater. Chem. A **2**(38), 16242–16249 (2014).
[21]A. K. Rath, M. Bernechea, L. Martinez, and G. Konstantatos, Adv. Mater. **23**(32), 3712–3717 (2011).
[22]S. M. Willis, C. Cheng, H. E. Assender, and A. A. R. Watt, Nano Lett. **12**(3), 1522–1526 (2012).
[23]C. M. Wolfe, N. Holonyak, and G. E. Stillman, *Physical Properties of Semiconductors* (Prentice Hall, 1989).
[24]A. H. Ip, S. M. Thon, S. Hoogland, O. Voznyy, D. Zhitomirsky, R. Debnath, L. Levina, L. R. Rollny, G. H. Carey, A. Fischer, K. W. Kemp, I. J. Kramer, Z. J. Ning, A. J. Labelle, K. W. Chou, A. Amassian, and E. H. Sargent, Nat. Nanotechnol. **7**(9), 577–582 (2012).
[25]M. X. Liu, F. P. G. de Arquer, Y. Y. Li, X. Z. Lan, G. H. Kim, O. Voznyy, L. K. Jagadamma, A. S. Abbas, S. Hoogland, Z. H. Lu, J. Y. Kim, A. Amassian, and E. H. Sargent, Adv. Mater. **28**(21), 4142–4148 (2016).
[26]A. Niemegeers and M. Burgelman, J. Appl. Phys. **81**(6), 2881–2886 (1997).
[27]K. C. Kao and W. Hwang, *Electrical Transport in Solids: With Particular Reference to Organic Semiconductors* (Pergamon Press, 1981).
[28]F. C. Chiu, Adv. Mater. Sci. Eng. 578168 (2014).
[29]O. Carp, C. L. Huisman, and A. Reller, Prog. Solid State Chem. **32**(1–2), 33–177 (2004).
[30]D. A. H. Hanaor and C. C. Sorrell, J. Mater. Sci. **46**(4), 855–874 (2011).

Nanoscale

PAPER

View Article Online
View Journal | View Issue

Published on 04 December 2017. Downloaded by National Chemical Laboratory, Pune on 4/9/2021 8:24:04 AM.

Check for updates

Cite this: *Nanoscale*, 2018, **10**, 1072

The role of surface ligands in determining the electronic properties of quantum dot solids and their impact on photovoltaic figure of merits†

Prasenjit N. Goswami, Debranjan Mandal and Arup K. Rath *

Received 17th August 2017,
Accepted 4th December 2017

DOI: 10.1039/c7nr06116a

rsc.li/nanoscale

Surface chemistry plays a crucial role in determining the electronic properties of quantum dot solids and may well be the key to mitigate loss processes involved in quantum dot solar cells. Surface ligands help to maintain the shape and size of the individual dots in solid films, to preserve the clean energy band gap of the individual particles and to control charge carrier conduction across solid films, in turn regulating their performance in photovoltaic applications. In this report, we show that the changes in size, shape and functional groups of small chain organic ligands enable us to modulate mobility, dielectric constant and carrier doping density of lead sulfide quantum dot solids. Furthermore, we correlate these results with performance, stability and recombination processes in the respective photovoltaic devices. Our results highlight the critical role of surface chemistry in the electronic properties of quantum dots. The role of the size, functionality and the surface coverage of the ligands in determining charge transport properties and the stability of quantum dot solids have been discussed. Our findings, when applied in designing new ligands with higher mobility and improved passivation of quantum dot solids, can have important implications for the development of high-performance quantum dot solar cells.

1. Introduction

The solution processed inorganic semiconductor quantum dot based solar cells have shown steady improvements over the years to emerge as a promising contender for next generation solar cell technology.[1–4] Control over synthesis techniques,[5] advancements in post-synthesis processing[2,6] and maneuver over a passivation strategy[3,4,7,8] have contributed critically to their progress in photovoltaic and other optoelectronic applications. A large proportion of surface atoms along with the associated minuscule volume of quantum dot (QD) particles introduce surface dominance in determining the electronic properties of QD solids. Unsaturated surface atoms often result in the formation of dangling bonds, leading to the creation of intermediate states of varying energies across their band gaps.[9,10] This may give rise to a range of phenomena in QD solids, namely, the formation of band tails, uncontrolled doping, and the formation of midgap trap states. Trap states are detrimental to both current and voltage generation as they reduce charge carrier mobility, decrease band edge carrier lifetime, and increase photocarrier recombination by providing alternate pathways through midgap states.[9] Moreover, degradation of interfacial properties by means of Fermi energy pinning and reduction of built-in potential across a junction also make the intermediate states unfavorable in photovoltaic applications.[8,11] Surface chemistry plays a crucial role in eliminating the formation of intermediate states in QDs by passivation of surface atoms through appropriate ligands. Surface ligation pushes the intermediate states deep inside the valence band[12] or the conduction band[9] and thus produces a cleaner band gap QD solid.

Lead sulfide (PbS) QDs have dominated the spectrum of QD solar cells due to their wide band gap tunability, solution phase processability, ambient stability, and high performance.[13] The as-synthesized PbS QDs are off-stoichiometric (band gap ~1.3 eV), where the (111) crystal facets are terminated by Pb atoms and the (100) facets constitute both Pb and S atoms.[14,15] The surface ligands are thus designed such that they interact with the empty orbitals of the electron deficient metal atoms of the QD surface. A plethora of surface ligands, that includes small chain organic molecules with suitable anchoring groups,[16,17] atomic size halide ligands[3,18] and the most recent organic–inorganic halometallate ligands,[4,19] have been studied for effective passivation of the QD surface to develop high-performance photovoltaic devices. Among the various groups tested so far (SH, COOH, CN, and NH_2), thiol (SH) has turned out to be the most suitable anchoring group

CSIR-National Chemical Laboratory, Dr. Homi Bhabha Road, Pune, 411008, India. E-mail: ak.rath@ncl.res.in

†Electronic supplementary information (ESI) available. See DOI: 10.1039/c7nr06116a

This journal is © The Royal Society of Chemistry 2018

Published on 04 December 2017. Downloaded by National Chemical Laboratory, Pune on 4/9/2021 8:24:04 AM.

for PbS QD solar cells.[4,20] Thiol terminated organic ligands generally result in p-type doping,[12] whereas iodine[18] and halometallate[4] passivation yield n-type doping to PbS QDs. Organic ligands generally yield low mobility QD solids ($<10^{-2}$ cm^2 V^{-1} S^{-1}) which have been attributed to their longer dot-to-dot distance and high tunnelling barrier for charge carrier transportation, thereby limiting their performance in QD solar cells.[11] In comparison with inorganic ligand passivated QD solar cells, organic ligand passivation has, however, reported to yield higher open circuit voltage[8,21,22] and shown improved resilience over ambient degradation.[3,4] To date, the highest performance has been obtained by interfacing an n-type PbS QD layer passivated by an inorganic ligand PbI_3^- with a 1,2-ethanedithiol (organic ligand) capped p-type PbS QD layer.[4] A better understanding of the ligand induced modulation of the electronic properties of QDs may inspire designing novel organic ligands that would lead to higher mobility and superior preservation of the QD surface.

Different aspects of the role of surface ligands in the electronic properties of QDs have been revealed in previously published reports.[8,9,11] Changes in the anchoring group and the dipole moment of the surface ligands have been shown to shift the positions of the valence and the conduction bands of QD solids,[17,23] which enables the modulation of the interfacial properties in photovoltaic applications. The introduction of electron accepting and electron donating functional groups into the surface ligands has been used for remote doping of QD films.[24–26] Control over surface coverage and facet selective steric properties of QDs has led to the formation of superstructures with long-range translational and orientational orders in QD solids.[27] Recently, the use of π-conjugated ligands has shown bulk like optical absorption and broad band optical absorption enhancement in colloidal QDs.[28,29] The use of thiophenol derivatives as the ligand in PbS QDs has been reported to result in up to 300% improvement in absorption over bulk values.[28] The drastic increase in the absorption coefficient has been attributed to the mixing of the ground state ligand orbitals leading to a subsequent increase in the density of states of the QDs. The charge carrier mobility of QD solids has been reported to increase exponentially with a decrease in the ligand size when the dielectric constant of the environment is maintained.[30] The mobility of the QD solid, however, strongly depends on the anchoring groups[31,32] and the energy levels (HOMO/LUMO) of the surface ligands.[33] Surface ligands which only produce high mobility QD solids are not necessarily the best suitable for photovoltaic applications;[34] effective passivation of the QD surface to create clean band gap is also a desirable quality that is deemed from a good ligand.[11] It has been found that longer ligands show a high photoluminescence quantum yield, an indication of clean band gap due to the reduction in dot-to-dot coupling, but leads to inefficient carrier mobility; the opposite is true for shorter ligands.[16,35,36] In the case of the asymmetric ligands having different terminal anchoring groups, the correlation between the charge carrier mobility with the ligand size and anchoring groups has not been well understood to date. For example, it has been reported that 3-mercaptopropionic acid (MPA) capped PbS QDs show almost an order of magnitude higher mobility than 1,2-ethanedithiol passivated PbS QD films, despite the fact that the latter ligand is a shorter MPA.[16,37] It is safe to say that achieving both the desirable high electrical mobility and clean band gap is not mutually exclusive and could be attained through a better understanding of the role of ligand mediated phenomena in QD solids. A detailed study on the impact of various ligand types on the electronic properties of QD solids is, therefore, necessary to develop novel ligands for high-performance solar cell applications.

Given the aforementioned complexities in the choice of surface ligands, we posit to study a series of ligands, chosen judiciously with varied sizes and functionalities, to understand the overall impact of the ligands on the photovoltaic figure of merits. Among the various ligands used in this study, MPA has been extensively studied in quantum dot solar cell development and has reported the highest efficiency to date among organic ligands.[2,7,38,39] The other organic ligands studied here, namely thioglycolic acid (TGA),[36] thiolactic acid (TLA) and 3-chloro-1-propanethiol (CPT),[40] however, have rarely been explored in previous reports. TGA and TLA are particularly interesting due to the fact that they possess similar terminal anchoring groups such as SH and COOH to MPA, but they are ~1.54 Å shorter than MPA.[36] General notion suggests that smaller ligands would reduce the dot-to-dot separation and thereby increase the compactness, carrier mobility and dielectric constant of the QD solid. Higher mobility and higher dielectric constant are of significant importance in solar cells for fast carrier transport and dielectric screening of Coulomb attraction between the photo-generated carriers for their efficient delocalization. Our results suggest that PbS QD films, passivated using TGA and TLA, give rise to lower mobility and lower dielectric constant than those of MPA treated PbS QD films. The photovoltaic performance of MPA passivated photovoltaic devices shows higher photocurrent whereas TGA and TLA passivated solar cells show higher open circuit voltage and superior stability in their solar cell performance. Through a series of optoelectronic characterization studies namely photo-CELIV, transient photocurrent, transient photovoltage, light intensity dependent short circuit current and open circuit voltage measurements, temperature dependent study and XPS measurements, we provide a detailed electronic and physical understanding of ligand mediated properties of PbS QD solids and corroborate our results to explain their performances in solar cell devices.

2. Results and discussion

Photovoltaic devices are fabricated by utilizing a layer by layer solid state ligand exchange approach as reported previously.[2] The device fabrication process is given in detail in the Experimental section (ESI†). In a typical process, a thin layer of oleic acid capped PbS QDs is deposited by a spin coating

Published on 04 December 2017. Downloaded by National Chemical Laboratory, Pune on 4/9/2021 8:24:04 AM.

process. A ligand solution is applied to the PbS thin film for a brief period of time for complete removal of oleic acid and passivation of the PbS QD surface by the applied ligand. Successful completion of the ligand exchange process is confirmed from the attenuated total reflectance (ATR) mode Fourier transform infrared spectroscopy (FT-IR) study (Fig. S1†).

A schematic representation of the photovoltaic device architecture is shown in Fig. 1a. In order to probe ligand mediated solar cell performance, we have selected MPA, TGA, TLA, and CPT as organic ligands (respective molecular structures are shown in Fig. 1a) to passivate the PbS QD surface. TGA, TLA, and MPA possess thiol and carboxylic acid as terminal anchoring groups. TGA has one carbon atom less than MPA (straight chain) and TLA (branched), however, the effective distance between the anchoring groups in both TGA and TLA is one carbon length (~1.54 Å) shorter than MPA. CPT consists of the same number of backbone carbon atoms as MPA while the terminal acid functional group has been replaced by chlorine. From here on, we would refer to both TGA and TLA as short chain ligands due to their shorter inter-anchoring-group distances. The cross-sectional image (Fig. 1b) shows the relative thickness of each layer for an optimized MPA ligand based solar cell. Optimized solar cell performances for various ligand passivated PbS QD films are shown in Fig. 1(c) and the comparison of solar cell performances under 1.5 A.M. illumination is given in Table 1. MPA and TGA treated devices show comparable performances whereas TLA and CPT treated solar cells show much lower efficiencies. MPA shows the highest short circuit current density (J_{sc}), however, it is interesting to note that the short chain ligands (TGA and TLA) give rise to higher open circuit voltages (V_{oc}) than the longer chain ligands (MPA and CPT). This is of crucial importance due to the fact that QD solar cells suffer from higher open circuit voltage loss (0.55–0.75 V for 1.1 to 1.4 eV band gap)[41] compared to CIGS (0.35 V for 1.1 eV), c-Si (0.38 V for 1.12 eV band gap) and hybrid perovskite (0.4 V for 1.5 eV band gap) solar cells.[22] Therefore any reduction in open circuit voltage loss is considered critical for QD solar cell development. Furthermore, while investigating the stability of different ligands in solar cell applications, it is observed that short chain ligands show

Table 1 Comparison of photovoltaic performances

Ligand type	V_{oc} (V)	J_{sc} (mA cm^{-2})	FF (%)	PCE (%)
PbS@MPA	0.576	24.00	47.4	6.55
PbS@TGA	0.629	22.56	44.1	6.25
PbS@TLA	0.610	14.22	40.3	3.50
PbS@CPT	0.526	21.43	38.2	4.31

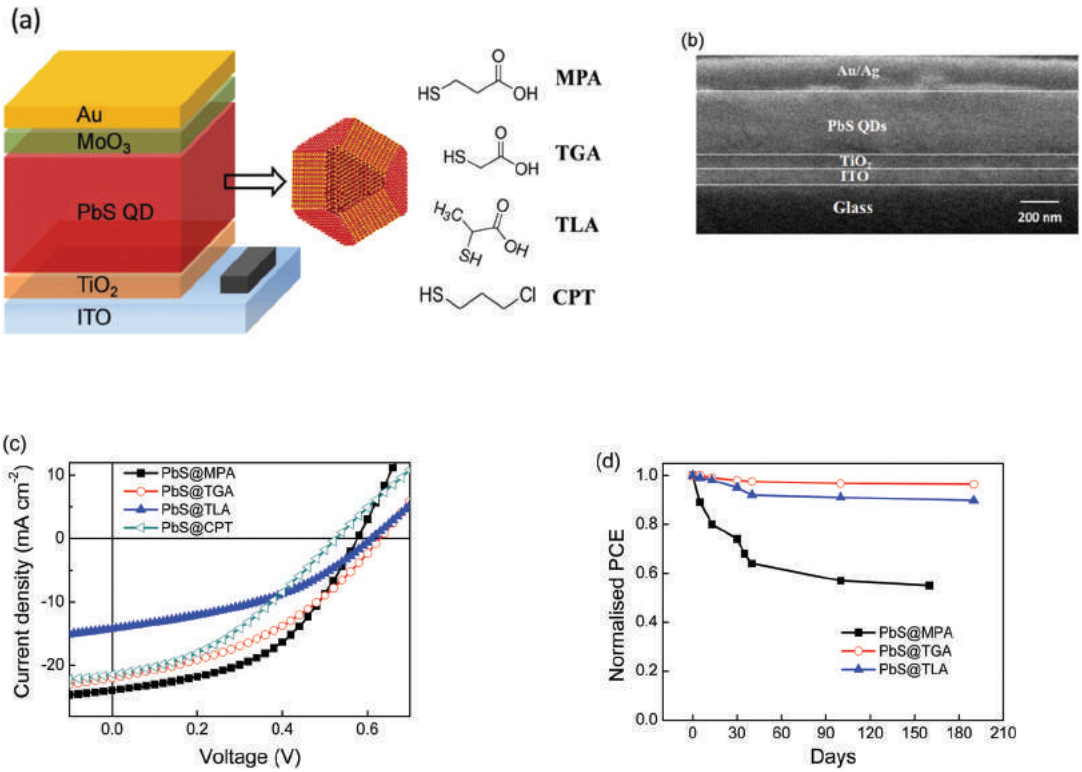

Fig. 1 Schematic of the solar cell device architecture and the molecular structures of the studied ligands are shown in (a). Cross-sectional image of a prepared solar cell with the scale bar is shown in (b). Current density *vs.* voltage characteristics of PbS QD based solar cells, treated with various ligands, are shown in (c). Colour codes for the respective ligands are shown as legend. (d) depicts the stability test and shows the evolution of normalized power conversion efficiency (PCE) with storing time for the three ligands.

 This journal is © The Royal Society of Chemistry 2018

Published on 04 December 2017. Downloaded by National Chemical Laboratory, Pune on 4/9/2021 8:24:04 AM.

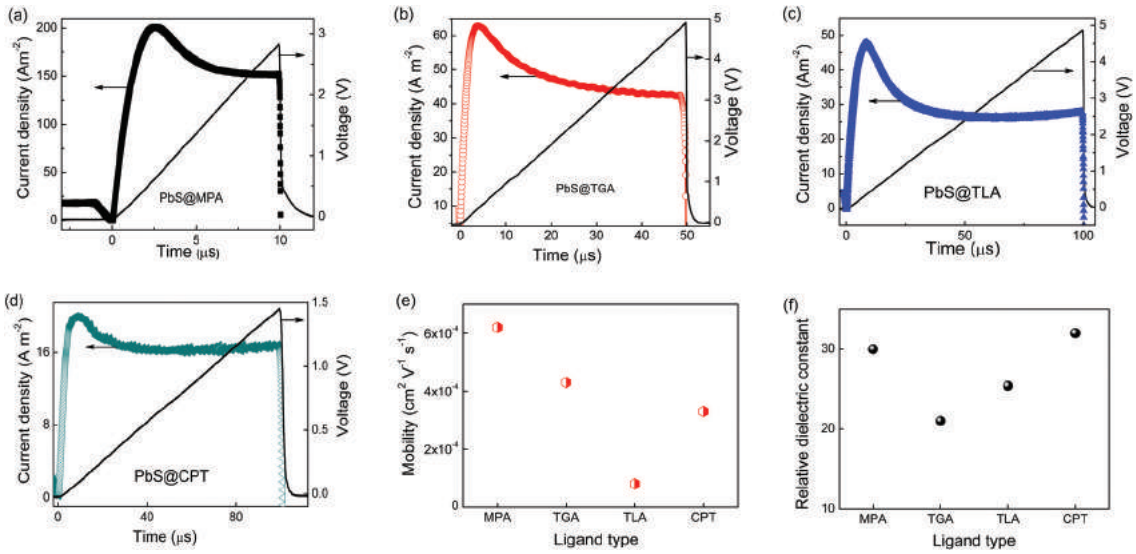

Fig. 2 (a)–(d) represent the photo-CELIV measurements for MPA, TGA, TLA and CPT treated PbS QD solar cells respectively. Current evolution and the applied voltage pulse, as a function of time, are shown in the same plots for the respective devices. (e) and (f) show the variations in hole mobility and dielectric constant of PbS QD layers treated with various ligands (details of the data analysis are given in Fig. S3†).

improved stability over MPA (Fig. 1d). During a period of 180 days, the power conversion efficiency of MPA treated sample reduced to 50% of its original value, whereas both TGA and TLA treated solar cells retain more than 90% of their pristine efficiency (stability data for V_{oc}, J_{sc}, and FF are given in Fig. S2†).

Competition between the carrier transit time and carrier recombination time gives rise to the photocurrent generation in solar cells. The carrier transit time in a solar cell is inversely proportional to mobility ($t_{\text{transit}} = \frac{d^2}{\mu V}$; d: device thickness, μ: mobility, and V: applied voltage). In our studied device structure of n–p junction solar cells, the n-type layer (TiO_2) acts as a transparent window layer. Under panchromatic solar illumination, a gradient of photo-generated carriers is created across the PbS QD layer thickness where a majority of the carriers are created close to the junction.[42] In such a scenario, the majority of the photo-generated electrons can easily reach the n-type layer, whereas the photo-generated holes need to travel across the full PbS QD layer thickness to reach the counter electrode. Therefore determination of hole mobility may provide valuable insights into the photocurrent generation process for the studied ligands. Photo-CELIV, a powerful technique to determine majority carrier mobility (hole, in our case), has been used widely for QD and other thin film solar cells.[43,44] We utilize the photo-CELIV technique to determine hole mobility of PbS films treated with various surface ligands. Details of the experimental procedure are given in the Experimental section (ESI†). Applied offset voltage, as well as the time delay between the light pulse and the voltage pulse, are kept constant during the measurements, while the voltage ramp for the devices is varied to maintain the condition of lower extraction current as compared to capacitive displacement current.[43] The PbS QD layer thickness is kept in between 220 nm and 450 nm for the photo-CELIV study. The current evolution and the voltage ramp for various surface ligand treated photovoltaic devices are shown in Fig. 2a–d. PbS QD solids treated with longer ligands (MPA and CPT) show higher dielectric constant and hole mobility as compared to shorter ligand (TGA and TLA) passivation (Fig. 2e and f). These observations are in stark contrast to the common notion that shorter ligands would generate higher mobility and higher dielectric constant by reducing the dot-to-dot separation. Furthermore, hole mobility determined from photo-CELIV experiments are consistent with the forward bias J–V characteristics (S4†) and the series resistance results (Table S1†) of the respective photovoltaic devices, both in the dark and under illumination. A high mobility results in low series resistance in solar cells for the respective ligand types.

It has been shown that the carrier transport in QD solar cells is dominated by the drift motion over diffusion in determining their photovoltaic figure of merits.[45] Free carrier concentration and dielectric constant play important roles in the formation of depletion width across the n–p junction. This prompts us to determine depletion width and carrier concentration in the respective PbS films treated with various ligands as they fundamentally control the photocarrier extraction process. Capacitance measurements at varied applied biases in the low-frequency region have widely been used for this purpose to characterize QD solar cells.[5,7,12] Depletion widths at zero bias are determined from the C–V plots (Fig. 3a) and the free carrier densities are determined from the slope of the $1/C^2$ *vs.* V plots (Fig. 3b, details of the data analysis are shown in S5†).[7] Depletion width is the highest for MPA treated PbS layers (Fig. 3c), indicating the highest contribution from drift mediated photo-carrier extraction among the ligands. The maximum depletion width along with the lowest carrier

Published on 04 December 2017. Downloaded by National Chemical Laboratory, Pune on 4/9/2021 8:24:04 AM.

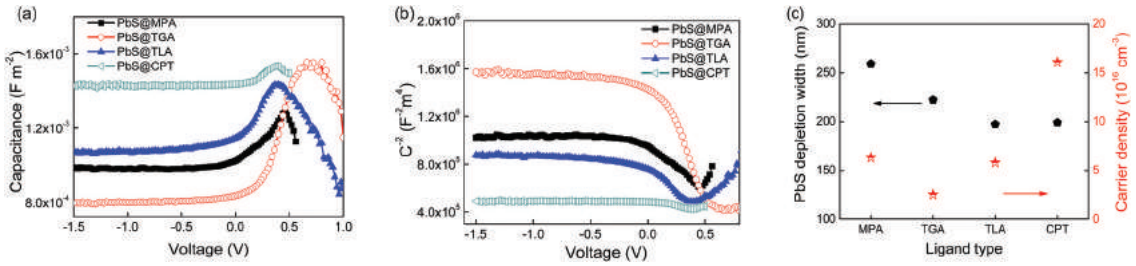

Fig. 3 Capacitance–voltage (C–V) and $1/C^2$–V plots for solar cells treated with various ligands are shown in (a) and (b) respectively. Depletion width at zero bias and carrier density as determined from the C–V and $1/C^2$–V plots for the PbS layers with different surface ligand types are shown in (c).

binding energy arising from the high dielectric constant of MPA treated PbS may have led to the highest short circuit current generation in their solar cell operation. On the other hand, the TGA treated PbS layer shows the lowest free carrier density (Fig. 3c) suggesting that TGA treated PbS is the most intrinsic in nature among the studied ligand types. The ascending order of carrier densities, as determined for PbS layers treated with various ligands (TGA < TLA < MPA < CPT), is in agreement with the trend in the open circuit voltage generation for the respective solar cells (TGA > TLA > MPA > CPT). We surmise that incomplete/imperfect surface passivation leads to external doping and intermediate states in the QD solid, which may result in Fermi energy pinning across the junction and loss in open circuit voltage in solar cells.

Considering the incompetence of the CPT ligand in photovoltaic operations (high carrier density and low open circuit voltage generation) we exclude it from further studies of recombination processes in solar cells. Transient photovoltage and photocurrent measurements are employed to determine the carrier lifetime and carrier transit time of solar cells to obtain a more vivid understanding of the underlying photovoltaic processes for the different ligands. Transient photovoltage measurements are carried out by biasing solar cells with white light to produce constant open circuit voltage and simultaneously applying small perturbing light pulses to determine the charge carrier decay under open circuit conditions (details of the data analysis are shown in S6†).[2,22] Photocarrier lifetimes for MPA, TGA, and TLA treated PbS layers, as determined from open circuit voltage decay measurements, are shown in Fig. 4a. At any given V_{oc}, MPA or TLA treated PbS shows lower lifetime values compared to TGA treated PbS. This implies that the recombination process is the slowest in the TGA treated PbS layer. Carrier lifetime values determined from transient photovoltage measurements are consistent with the carrier density values from capacitance measurement as higher carrier density leads to faster recombination and lower lifetimes in QD solids. This further explains previous observations that higher lifetimes generally yield higher open circuit voltages in photovoltaic devices.[41] However, it is difficult to ascertain if the lifetime for different ligand types is limited by the bulk recombination inside the PbS layer or the interfacial recombination at the TiO_2–PbS interface. The knowledge of carrier lifetime, mobility, built-in potential and depletion width as determined experimentally, enables us to estimate drift and diffusion lengths for PbS QD layers treated with different ligands (Table 2).[44]

Diffusion and drift lengths for the hole (Table 2) are determined under 0.9 sun illumination (refer to S6† for more details). Both drift and diffusion lengths for MPA and TGA treated PbS layers are comparable while the values are signifi-

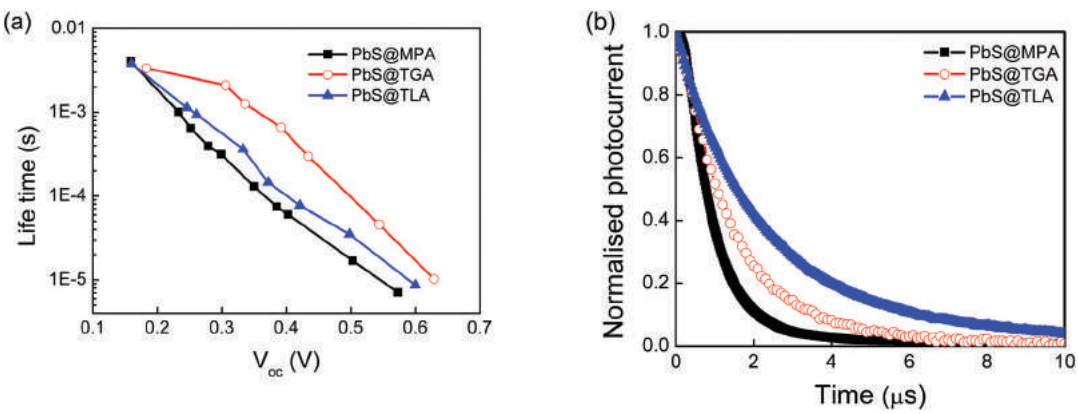

Fig. 4 (a) Comparison of photocarrier lifetimes for various ligand types as determined from transient photovoltage measurements. (b) Current transit times for various ligand types under short circuit conditions.

 This journal is © The Royal Society of Chemistry 2018

Published on 04 December 2017. Downloaded by National Chemical Laboratory, Pune on 4/9/2021 8:24:04 AM.

Table 2 Diffusion and drift lengths of a PbS layer for different surface ligands

Ligand type	Diffusion length (nm)	Drift length (μm)
PbS@MPA	105	1.3
PbS@TGA	105	1.35
PbS@TLA	38	0.19

cantly low for TLA treated solar cells. Carrier transit times in photovoltaic devices are estimated from the transient photocurrent (TPC) decay measurements.[22] Transient photocurrent decay for the various ligand based solar cells is shown in Fig. 4b. Carrier transit times for MPA, TGA and TLA are 1.1 μs, 1.7 μs and 2.86 μs, respectively, in agreement with their respective mobility values. While high transport lengths facilitate photo-generated charge carrier extraction, high transit times increase the probability of photocarrier recombination inside solar cells. Drift length, diffusion length and carrier transit time further explain similar short circuit current in MPA and TGA treated solar cells and lower current in TLA treated solar cells.

To elucidate the role of surface ligands in the charge generation–recombination process of solar cells, we have studied incident photon intensity dependent J_{sc} and V_{oc} generation of the studied photovoltaic devices. For the light intensity dependent investigation, we have chosen monochromatic illumination at 635 nm. Photons at this wavelength have high penetration depth inside the PbS layer (extinction coefficient of PbS in a long wavelength range is low) and are expected to excite the PbS thickness uniformly even at relatively lower intensities. In photovoltaic devices, the dependence of J_{sc} on light intensity (φ) is expressed as $J_{sc} \propto \varphi^p$, where p is the power exponent. $p \sim 1$ indicates generation limited current extraction and $p \sim 0.75$ indicates space charge limited carrier extraction in solar cells.[46] Higher 'p' values (Fig. 5a) of MPA (0.92) and TGA (0.93) treated devices indicate a more balanced transport of photo-generated electrons and holes which may lead to superior charge extraction in those solar cells. The diode ideality factor (η) is also known to carry important information regarding the photocarrier recombination process in a solar cell. The value of η is unity when the recombination process is determined by band-to-band recombination of photo-generated carriers, whereas the involvement of intermediate states in carrier recombination dynamics makes η greater than unity ($1 < \eta < 2$).[22,41] Under 635 nm monochromatic laser illumination, the estimated values of η are 1.11, 1.20 and 1.40 for MPA, TGA and TLA treated photovoltaic devices, respectively (Fig. 5b, details of the data analysis are given in S7†). This implies that trap assisted recombination within the depletion layer of the PbS film is the lowest for MPA, intermediate for TGA and the highest for TLA treated photovoltaic devices. The qualitative density of trap state estimation for the respective ligand types, as predicted from the values of η, corroborates well with photocurrent generation under solar cell operation (Fig. 1c) and intensity dependent J_{sc} values under monochromatic illumination (Fig. 5a).

Transient photovoltage measurement (Fig. 4a) shows lower photocarrier lifetimes for MPA treated solar cells as compared to TGA and TLA treated solar cells, despite the fact that MPA yields higher photocurrent. Photocarrier recombination in photovoltaic devices can occur in three possible regions inside the device: (i) recombination inside the bulk of the PbS layer, (ii) TiO_2–PbS interface recombination and (iii) recombination inside TiO_2 and MoO_3 transport layers. We can ignore the lifetime contribution from the transport layers due to the fact that they also act as filter layers for the holes and the electrons (TiO_2 and MoO_3, respectively) and therefore are deprived of opposite charge carriers for recombination. However, interface recombination can play a critical role in determining the overall photocarrier lifetime in solar cells. In order to explicate the role of the TiO_2–PbS interface in the recombination process for the studied ligands, we have performed temperature dependent characterization of J–V characteristics under illumination. In the case of a single thermally activated carrier generation–recombination mechanism, open circuit voltage of a solar cell can be expressed as $V_{oc} = \frac{E_a}{q} - \frac{\eta KT}{q}\ln\left(\frac{J_{00}}{J_{sc}}\right)$,[38,41,47] where E_a is the activation energy, q is the electronic charge, J_{00} is the prefactor and η is the diode ideality factor. Two distinct regions are observed in the V_{oc} *vs.* T plots (Fig. 5c) for the solar cells. In the low-temperature range (<200 K) open circuit voltage seems to saturate with the decrease in temperature,

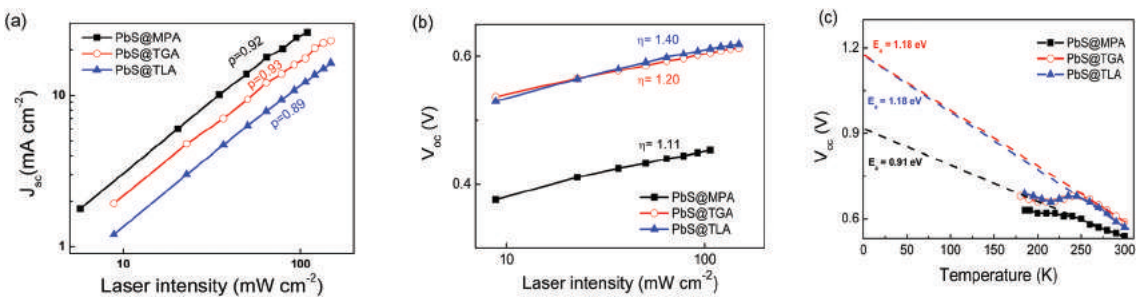

Fig. 5 Intensity dependent (a) current density and (b) open circuit voltage variation for solar cells treated with different ligands. Monochromatic illumination of 635 nm laser light is used for the intensity dependent study. (c) Temperature dependent V_{oc} of photovoltaic devices for different ligand types measured at 1.5 A.M. solar illumination is shown. Extrapolation of the high-temperature linear region of V_{oc} to determine E_a for various ligands are shown by the dashed lines.

Published on 04 December 2017. Downloaded by National Chemical Laboratory, Pune on 4/9/2021 8:24:04 AM.

whereas V_{oc} increases linearly with the decrease in temperature in the high-temperature range (>200 K). The freezing of intermediate trap charges in the low-temperature region could possibly make them ineffective to modulate the quasi Fermi levels of the PbS layer under illumination and therefore leads to saturation in V_{oc} generation.[41,47] In the high-temperature range, where η, J_{00} and J_{sc} are independent of the temperature, extrapolation of the V_{oc}–T plot at T = 0 K provides E_a. Activation energy bears a deep physical significance for the recombination processes in the solar cells. E_a, when equal to the band gap (E_g) of the PbS layer, implies the dominance of band to band recombination, whereas the lower values of the activation energy imply the significance of interfacial recombination.[38,41] As shown in Fig. 5c, E_a is 0.91 eV for the MPA treated PbS layer, much lower than TGA and TLA ligands (1.18 eV). This suggests that high interfacial recombination of photocarriers at the TiO_2 interface for MPA treated PbS possibly limits their lifetime values rather than the bulk of the PbS layer. Considering that the first excitonic peak position for PbS QDs (Fig. S8(a)†) is 1.24 eV, the observed activation energies for TGA and TLA treated PbS are highly encouraging. This implies interfacial recombination at the TiO_2–PbS interface and the open circuit voltage loss in TGA and TLA treated films are significantly lower. This result is crucial from the stand point that open circuit voltage loss has been reduced by a smaller size passivating ligand.

X-ray photoelectron spectroscopy (XPS) of PbS QD films passivated with the studied ligands has been carried out to better understand the surface properties. Since the ligands are anchored through the –SH group to the terminal Pb sites of the QD surface, we focused on the S 2p XPS peaks to determine the surface properties. The high-resolution XPS S 2p spectra for PbS QD films treated with MPA, TGA and TLA are presented in Fig. 6(a)–(c) respectively. Deconvolution of S 2p spectra is carried out based on previously published reports.[5,8,48] The S 2p doublet peaks for Pb–S are fitted with a splitting energy difference of 1.18 eV and a peak area ratio of 2 : 1. Further details of the XPS analysis are given in Table S1.† The S–C and S–S peaks in the spectra arise from the bound thiol contribution of the surface ligands.[8] Thus, atomic percent determination of S–C and S–S would provide valuable information regarding the surface coverage of different ligands on the PbS QD surface. The relative atomic percentages of MPA, TGA, and TLA treated PbS films for S–C are 14.3%, 20.4%, and 20.3%, respectively, and those for S–S are 12.4%, 16.1%, and 17.5%, respectively. The higher presence of the S–C and S–S bonds in PbS films for TGA and TLA ligands clearly suggests a higher surface coverage for the ligands than MPA. The higher surface coverage could possibly originate from lower steric repulsion in the case of shorter ligands. XPS S 2p spectra also indicate the presence of $PbSO_3$ and $PbSO_4$ (or R–S═O) on PbS films. The relative atomic percentages of the oxidative species for MPA, TGA, and TLA are 10%, 8.6% and 7.8%, respectively, indicating higher oxidation in MPA treated PbS samples. This is consistent with relative surface coverage (S–C and S–S) for the respective ligands as higher coverage leads to better preservation and lower oxidation of the PbS QD surface. This further explains higher stability in TGA and TLA treated photovoltaic devices as higher ligand coverage inhibits degradation processes that originate from the ambient operation.

It is observed and verified from complementary experimental techniques that shorter passivating ligands TGA and TLA yield higher open circuit voltages than MPA. Since the difference between the conduction band minimum of the n-type TiO_2 layer and the valence band maximum of the p-type PbS layer fundamentally controls the open circuit voltage generation, we posit to determine them from complementary absorption and ultraviolet photoelectron spectroscopic (UPS) techniques for the studied ligands (Fig. S9a–c†). Fig. S9d† shows the conduction band and valence band positions of the PbS QD films treated with various ligands. It can be seen that the valence band position of PbS QDs for different ligand types does not follow entirely the trend of V_{oc} generation in solar cell devices, for example, TGA despite having a shallower valence band energy produces higher V_{oc} than MPA. We attribute the V_{oc} generation to the interface (TiO_2/PbS) properties and electron trap formation in PbS QD films. Capacitance–voltage measurements and temperature dependent V_{oc} results show that MPA treated PbS possesses the highest free carrier density and more pronounced trap mediated recombination at the TiO_2/PbS interface. XPS study shows that MPA treated PbS

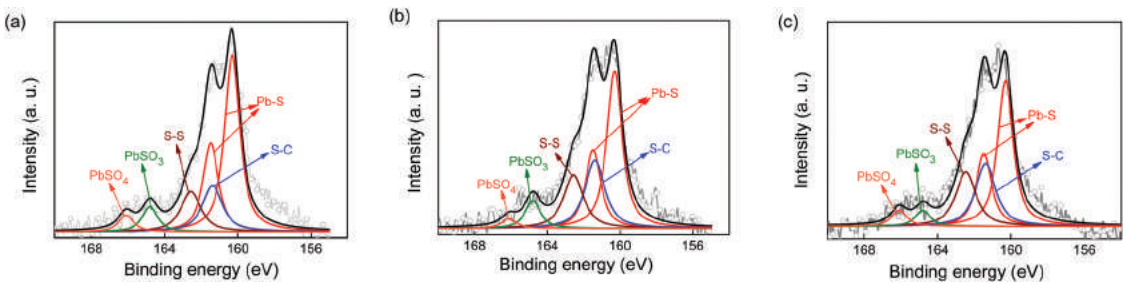

Fig. 6 Comparison of XPS S 2p spectra for (a) MPA, (b) TGA and (c) TLA passivated PbS QD films. Gray (scatter + line) represents the experimental data and the black line represents the fitted experimental results. Peak positions corresponding to binding energies 160.30 eV and 161.48 eV are attributed (red) to the doublet splitting of S for PbS. Peaks at 161.38 eV (blue), 162.56 eV (wine line), 164.8 eV (olive), and 166.1 eV (orange) correspond to the S–C bond, S–S bond, $PbSO_3$ and $PbSO_4$ respectively.

 This journal is © The Royal Society of Chemistry 2018

Published on 04 December 2017. Downloaded by National Chemical Laboratory, Pune on 4/9/2021 8:24:04 AM.

films possess the highest amount of oxidative compounds in the form of $PbSO_3$ and $PbSO_4$ at its surface which is known to form electron trap states near the conduction band of PbS QDs.[5] Therefore, we infer from the above observations that MPA treated films create the maximum number of electron trap states which limit the quasi-Fermi level splitting between the electrons and holes across the interface under illumination and results in the reduction in open circuit voltage. The origin of photocurrent generation and fill factor for different ligand types has been explained by mobility, dielectric constant, depletion width, and diode ideality factor. The reason for the lower hole mobility and the lower dielectric constant of PbS QD films for short chain ligands (TGA and TLA), as compared to MPA, however, is difficult to ascertain. Low hole mobility in TGA and TLA could possibly originate from higher hole trap density and trap energy distributions for holes (close to the valence band) in their respective PbS QD films.[16,36] Shallow hole traps near the valence band edge may result in lowering the hole mobility due to continuous trapping and de-trapping and subsequent increase in the carrier lifetime (Fig. 4a). The observed dielectric constant values may be rooted in the different dielectric constant of the ligands and packing of QD solids. Therefore in designing new short chain organic ligands, relative dielectric constant of the ligand should be taken into consideration along with other prevailing factors.

3. Conclusions

In summary, we have investigated photovoltaic figure of merits of PbS QD solar cells for various surface ligands with varied sizes and functionalities. We have shown the non-trivial behavior of the decrease in hole mobility and dielectric constant with the reduced ligand size for PbS QD solids. This underpins the importance of surface ligands in controlling the carrier transport properties of QD solids *via* trap state formation. We have shown that shorter ligands can produce a higher open circuit voltage in QD solar cells by diminishing surface oxidation and thereby eliminating electron trap states near the conduction band through a higher degree of surface passivation. High surface coverage for TGA and TLA leads to improvement in the stability of QD solar cells under ambient working conditions. Our study highlights the role of ligand chemistry in tuning various electronic properties of QD solids like mobility, dielectric constant and doping density through surface passivation which would be valuable in designing new surface ligands for QD based electronic and optoelectronic applications.

Conflicts of interest

There are no conflicts to declare.

Acknowledgements

This work is supported by DST Nanomission, India (no. SR/NM/NT-1011/2105 (G)) and SERB extramural funding, India (no. EMR/2015/002415).

References

1 J. M. Luther, J. B. Gao, M. T. Lloyd, O. E. Semonin, M. C. Beard and A. J. Nozik, *Adv. Mater.*, 2010, **22**, 3704–3407.
2 A. H. Ip, S. M. Thon, S. Hoogland, O. Voznyy, D. Zhitomirsky, R. Debnath, L. Levina, L. R. Rollny, G. H. Carey, A. Fischer, K. W. Kemp, I. J. Kramer, Z. J. Ning, A. J. Labelle, K. W. Chou, A. Amassian and E. H. Sargent, *Nat. Nanotechnol.*, 2012, **7**, 577–582.
3 C. H. M. Chuang, P. R. Brown, V. Bulovic and M. G. Bawendi, *Nat. Mater.*, 2014, **13**, 796–801.
4 M. X. Liu, O. Voznyy, R. Sabatini, F. P. G. de Arquer, R. Munir, A. H. Balawi, X. Z. Lan, F. J. Fan, G. Walters, A. R. Kirmani, S. Hoogland, F. Laquai, A. Amassian and E. H. Sargent, *Nat. Mater.*, 2017, **16**, 258–263.
5 J. Tang, L. Brzozowski, D. A. R. Barkhouse, X. H. Wang, R. Debnath, R. Wolowiec, E. Palmiano, L. Levina, A. G. Pattantyus-Abraham, D. Jamakosmanovic and E. H. Sargent, *ACS Nano*, 2010, **4**, 869–878.
6 A. Stavrinadis, S. Pradhan, P. Papagiorgis, G. Itskos and G. Konstantatos, *ACS Energy Lett.*, 2017, **2**, 739–744.
7 A. G. Pattantyus-Abraham, I. J. Kramer, A. R. Barkhouse, X. H. Wang, G. Konstantatos, R. Debnath, L. Levina, I. Raabe, M. K. Nazeeruddin, M. Gratzel and E. H. Sargent, *ACS Nano*, 2010, **4**, 3374–3380.
8 Y. M. Cao, A. Stavrinadis, T. Lasanta, D. So and G. Konstantatos, *Nat. Energy*, 2016, **1**, 16035.
9 M. A. Boles, D. Ling, T. Hyeon and D. V. Talapin, *Nat. Mater.*, 2016, **15**, 141–153.
10 C. R. Kagan, E. Lifshitz, E. H. Sargent and D. V. Talapin, *Science*, 2016, **353**, 5523.
11 R. L. Wang, Y. Q. Shang, P. Kanjanaboos, W. J. Zhou, Z. J. Ning and E. H. Sargent, *Energy Environ. Sci.*, 2016, **9**, 1130–1143.
12 M. J. Yuan, D. Zhitomirsky, V. Adinolfi, O. Voznyy, K. W. Kemp, Z. J. Ning, X. Z. Lan, J. X. Xu, J. Y. Kim, H. P. Dong and E. H. Sargent, *Adv. Mater.*, 2013, **25**, 5586–5592.
13 M. J. Yuan, M. X. Liu and E. H. Sargent, *Nat. Energy*, 2016, **1**, 16016.
14 O. Voznyy, D. Zhitomirsky, P. Stadler, Z. J. Ning, S. Hoogland and E. H. Sargent, *ACS Nano*, 2012, **6**, 8448–8455.
15 D. Zherebetskyy, M. Scheele, Y. J. Zhang, N. Bronstein, C. Thompson, D. Britt, M. Salmeron, P. Alivisatos and L. W. Wang, *Science*, 2014, **344**, 1380–1384.
16 K. S. Jeong, J. Tang, H. Liu, J. Kim, A. W. Schaefer, K. Kemp, L. Levina, X. H. Wang, S. Hoogland, R. Debnath,

Published on 04 December 2017. Downloaded by National Chemical Laboratory, Pune on 4/9/2021 8:24:04 AM.

L. Brzozowski, E. H. Sargent and J. B. Asbury, *ACS Nano*, 2012, **6**, 89–99.
17 P. R. Brown, D. Kim, R. R. Lunt, N. Zhao, M. G. Bawendi, J. C. Grossman and V. Bulovic, *ACS Nano*, 2014, **8**, 5863–5872.
18 Z. J. Ning, O. Voznyy, J. Pan, S. Hoogland, V. Adinolfi, J. X. Xu, M. Li, A. R. Kirmani, J. P. Sun, J. Minor, K. W. Kemp, H. P. Dong, L. Rollny, A. Labelle, G. Carey, B. Sutherland, I. G. Hill, A. Amassian, H. Liu, J. Tang, O. M. Bakr and E. H. Sargent, *Nat. Mater.*, 2014, **13**, 822–828.
19 M. Sytnykt, S. Yakunin, W. Schofberger, R. T. Lechner, M. Burian, L. Ludescher, N. A. Killilea, A. YousefiAmin, D. Kriegner, J. Stangl, H. Groiss and W. Heiss, *ACS Nano*, 2017, **11**, 1246–1256.
20 J. A. Tang and E. H. Sargent, *Adv. Mater.*, 2011, **23**, 12–29.
21 Z. J. Ning, Y. Ren, S. Hoogland, O. Voznyy, L. Levina, P. Stadler, X. Z. Lan, D. Zhitomirsky and E. H. Sargent, *Adv. Mater.*, 2012, **24**, 6295–6299.
22 S. Pradhan, A. Stavrinadis, S. Gupta, Y. Bi, F. Di Stasio and G. Konstantatos, *Small*, 2017, **13**, 1700598.
23 H. I. Wang, H. Lu, Y. Nagata, M. Bonn and E. Cánovas, *ACS Nano*, 2017, **11**, 4760–4767.
24 M. Shim and P. Guyot-Sionnest, *Nature*, 2000, **407**, 981–983.
25 S. J. Oh, D. K. Kim and C. R. Kagan, *ACS Nano*, 2012, **6**, 4328–4334.
26 A. R. Kirmani, A. Kiani, M. M. Said, O. Voznyy, N. Wehbe, G. Walters, S. Barlow, E. H. Sargent, S. R. Marder and A. Amassian, *ACS Energy Lett.*, 2016, **1**, 922–930.
27 J. J. Choi, C. R. Bealing, K. F. Bian, K. J. Hughes, W. Y. Zhang, D. M. Smilgies, R. G. Hennig, J. R. Engstrom and T. Hanrath, *J. Am. Chem. Soc.*, 2011, **133**, 3131–3138.
28 C. Giansante, I. Infante, E. Fabiano, R. Grisorio, G. P. Suranna and G. Gigli, *J. Am. Chem. Soc.*, 2015, **137**, 1875–1886.
29 D. Debellis, G. Gigli, S. Brinck, I. Infante and C. Giansante, *Nano Lett.*, 2017, **17**, 1248–1254.
30 Y. Liu, M. Gibbs, J. Puthussery, S. Gaik, R. Ihly, H. W. Hillhouse and M. Law, *Nano Lett.*, 2010, **10**, 1960–1969.
31 E. J. D. Klem, H. Shukla, S. Hinds, D. D. MacNeil, L. Levina and E. H. Sargent, *Appl. Phys. Lett.*, 2008, **92**, 212105.
32 W. K. Koh, S. R. Saudari, A. T. Fafarman, C. R. Kagan and C. B. Murray, *Nano Lett.*, 2011, **11**, 4764–4767.
33 M. Scheele, D. Hanifi, D. Zherebetskyy, S. T. Chourou, S. Axnanda, B. J. Rancatore, K. Thorkelsson, T. Xu, Z. Liu, L.-W. Wang, Y. Liu and A. P. Alivisatos, *ACS Nano*, 2014, **8**, 2532–2540.
34 D. Zhitomirsky, O. Voznyy, L. Levina, S. Hoogland, K. W. Kemp, A. H. Ip, S. M. Thon and E. H. Sargent, *Nat. Commun.*, 2014, **5**, 3803.
35 J. Zhang, J. Tolentino, E. R. Smith, J. Zhang, M. C. Beard, A. J. Nozik, M. Law and J. C. Johnson, *J. Phys. Chem. C*, 2014, **118**, 16228–16235.
36 J. Chang, Y. H. Ogomi, C. Ding, Y. H. Zhang, T. Toyoda, S. Hayase, K. Katayama and Q. Shen, *Phys. Chem. Chem. Phys.*, 2017, **19**, 6358–6367.
37 J. Tang, K. W. Kemp, S. Hoogland, K. S. Jeong, H. Liu, L. Levina, M. Furukawa, X. H. Wang, R. Debnath, D. K. Cha, K. W. Chou, A. Fischer, A. Amassian, J. B. Asbury and E. H. Sargent, *Nat. Mater.*, 2011, **10**, 765–771.
38 A. K. Rath, F. P. G. de Arquer, A. Stavrinadis, T. Lasanta, M. Bernechea, S. L. Diedenhofen and G. Konstantatos, *Adv. Mater.*, 2014, **26**, 4741–4747.
39 D. Mandal, P. N. Goswami and A. K. Rath, *Appl. Phys. Lett.*, 2017, **110**, 123902.
40 A. H. Ip, A. Kiani, I. J. Kramer, O. Voznyy, H. F. Movahed, L. Levina, M. M. Adachi, S. Hoogland and E. H. Sargent, *ACS Nano*, 2015, **9**, 8833–8842.
41 C.-H. M. Chuang, A. Maurano, R. E. Brandt, G. W. Hwang, J. Jean, T. Buonassisi, V. Bulović and M. G. Bawendi, *Nano Lett.*, 2015, **15**, 3286–3294.
42 M. Law, M. C. Beard, S. Choi, J. M. Luther, M. C. Hanna and A. J. Nozik, *Nano Lett.*, 2008, **8**, 3904–3910.
43 A. J. Mozer, N. S. Sariciftci, L. Lutsen, D. Vanderzande, R. Osterbacka, M. Westerling and G. Juska, *Appl. Phys. Lett.*, 2005, **86**, 112104.
44 K. W. Johnston, A. G. Pattantyus-Abraham, J. P. Clifford, S. H. Myrskog, S. Hoogland, H. Shukla, J. D. Klem, L. Levina and E. H. Sargent, *Appl. Phys. Lett.*, 2008, **92**, 122111.
45 X. Z. Lan, S. Masala and E. H. Sargent, *Nat. Mater.*, 2014, **13**, 233–240.
46 N. Zhao, T. P. Osedach, L. Y. Chang, S. M. Geyer, D. Wanger, M. T. Binda, A. C. Arango, M. G. Bawendi and V. Bulovic, *ACS Nano*, 2010, **4**, 3743–3752.
47 M. J. Speirs, D. N. Dirin, M. Abdu-Aguye, D. M. Balazs, M. V. Kovalenko and M. A. Loi, *Energy Environ. Sci.*, 2016, **9**, 2916–2924.
48 D. G. Castner, K. Hinds and D. W. Grainger, *Langmuir*, 1996, **12**, 5083–5086.

 This journal is © The Royal Society of Chemistry 2018

ACS APPLIED MATERIALS & INTERFACES

Research Article

Cite This: ACS Appl. Mater. Interfaces 2018, 10, 39074−39082

www.acsami.org

Quantum Dots Coupled to an Oriented Two-Dimensional Crystalline Matrix for Solar Cell Application

Debranjan Mandal and Arup K. Rath*

CSIR-National Chemical Laboratory, Dr. Homi Bhabha Road, Pune 411008, India

Supporting Information

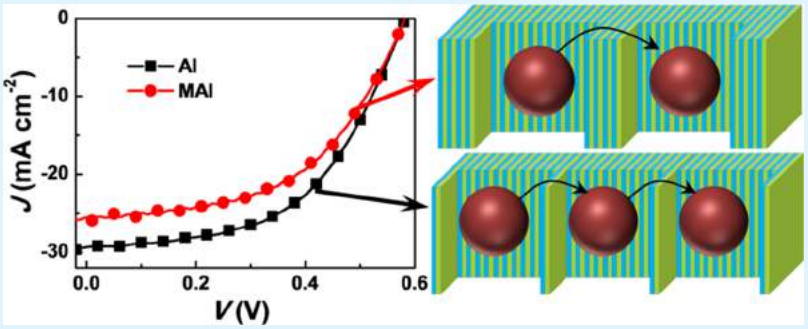

ABSTRACT: Colloidal quantum dots (QDs) have emerged as promising materials to harness panchromatic solar light, owing to their size-tunable optoelectronic properties. Advancements in surface passivation strategy and processing technique have contributed immensely to their developments in photovoltaic applications. Recently, surface passivation using halometallate ligands was shown to form a protective shell layer, which reduced the structural and energetic disorder in the QD solid. Here, we report lead sulfide (PbS) QDs coupled to an oriented two-dimensionally (2D) confined crystalline matrix by using a halometallate ligand. The QDs undergo surface reconstruction during the ligand treatment process, which leads to change in their shape, size, and axis length. We show that the 2D matrix is a combination of two distinct crystalline layers consisting of a crystalline Pb−amine complex and a 2D perovskite layer. The thickness of the matrix layer is modulated further by adjusting counter cations, which results in the enhancement in charge carrier mobility, carrier recombination lifetime, and diffusion length in the QD solid. 2D passivated QDs are implemented to fabricate photovoltaic devices with high power conversion efficiency of 9.1%.

KEYWORDS: *solar cells, quantum dot, 2D confinement, surface passivation, halometallate ligand*

INTRODUCTION

Size-tunable energy bandgap and monodispersity of colloidal quantum dots (QDs) make them promising building blocks for the development of solar cells.[1−4] The power conversion efficiency (PCE) of QD solar cells has grown steadily over time due to advancements in device engineering[2,3,5] and surface chemistry.[6−9] In view of the high surface to volume ratio in nanodimensional materials, the surface plays a pivotal role in determining the electronic properties of the QDs.[10] The unsaturated terminal atoms are vulnerable to QD fusion, which would compromise the monodispersity to increase the energy disorder in solid films.[4,10] The undercoordinated surface atoms often lead to intermediate trap states inside the QD band gap via oxidation or dangling bond formation.[11,12] Surface passivation using long-chain ligands or core/shell formation helps to attain monodispersity and clean energy band gap at the cost of charge carrier transport in QD films.[13] Postprocessing of QD films using short-chain ligand exchange process enhances the conductivity by orders of magnitude[14] which has been implemented to develop photovoltaic devices using a layer-by-layer (LBL) film growth process.[15−17] Besides the fact that LBL is a time-consuming and wasteful process for QDs and solvents, it further promotes inhomogeneity in QD films through random packing and heterogeneous aggregation. The inhomogeneous QD diffusion leads to site energy disorder, which inhibits the carrier transport process and limits the open-circuit voltage generation in QD solar cells.[18−20] The solution-based ligand exchange using halometallate [methylammonium lead iodide ($MAPbI_3$), $KPbI_3$ $CsPbI_3$, and PbI_3^-] ligands[21−24] has attracted significant attention in the recent past as it provides homogeneous surface passivation,[25] improved packing,[7] and deposition of a thick conducting QD film from a one-step spin-coating process.[7,21] Striking progress of $MAPbI_3$ perovskite material in solar cells[26,27] acts as a catalyst for their implementation as the first halometallate ligand[21] to passivate the QD surface. It is shown that both $MAPbI_3$ and PbS QDs possess similar crystal structure (tetragonal and cubic, respectively), comparable axis

Received: September 6, 2018
Accepted: October 23, 2018
Published: October 23, 2018

Downloaded via NATL CHEMICAL LABORATORY on April 9, 2021 at 07:25:11 (UTC).
See https://pubs.acs.org/sharingguidelines for options on how to legitimately share published articles.

 © 2018 American Chemical Society

DOI: 10.1021/acsami.8b15469
ACS Appl. Mater. Interfaces 2018, 10, 39074−39082

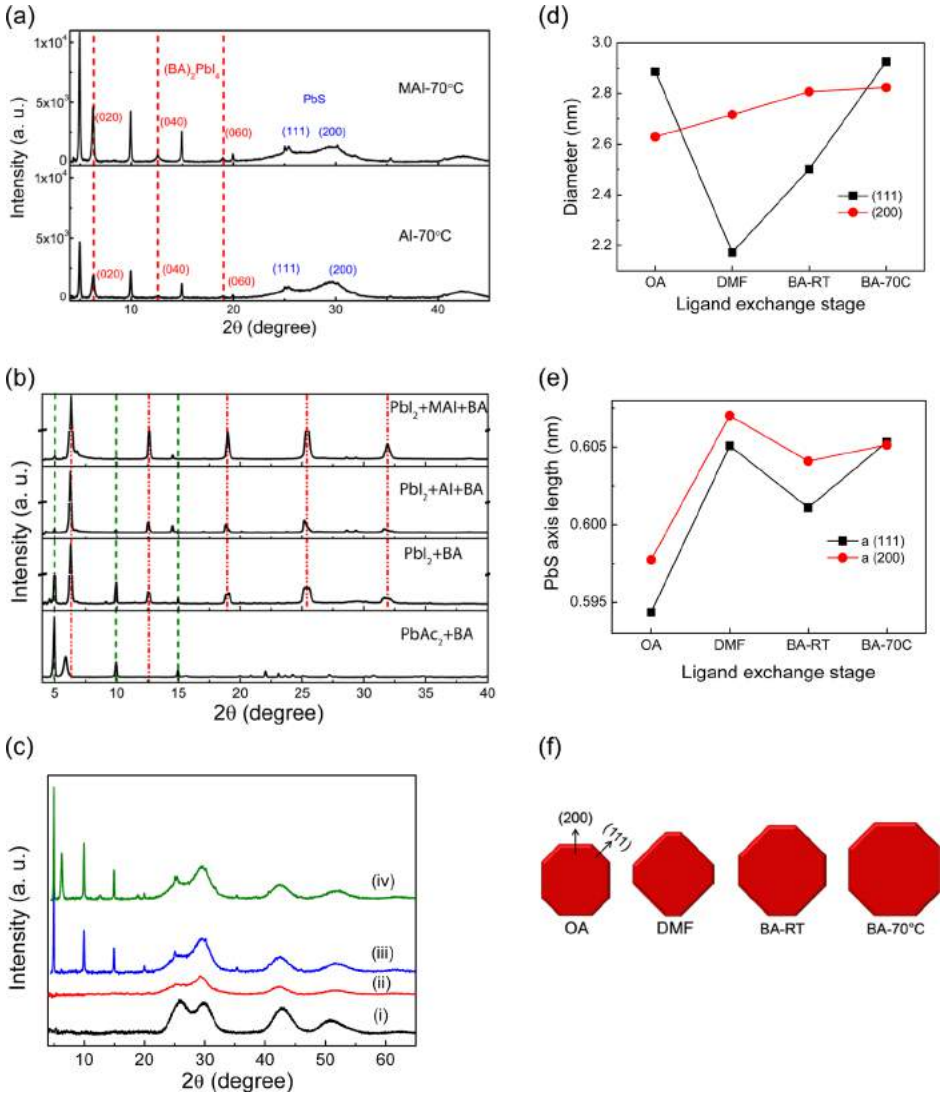

Figure 1. Structural characterization of the 2D crystalline matrix in the QD film: (a) XRD pattern of the annealed (70 °C) PbS QD film treated with AI and MAI. The peak positions corresponding to PbS and $(BA)_2PbI_4$ are marked in blue and red, respectively. (b) XRD spectra for different ligands. Olive and red lines indicate the equidistant peaks corresponding to the 2D Pb−amine complex and $(BA)_2PbI_4$ perovskite, respectively. (c) Evolution of the XRD pattern at various stages of the AI ligand exchange process. Thin films of PbS QDs are measured (i) pristine OA caped, (ii) intermediate stage of ligand exchange in DMF, (iii) deposited from BA but not annealed, and (iv) deposited from BA and annealed at 70 °C. Changes in (d) QD size and (e) PbS axis length at different stages of the ligand exchange process for both (111) and (200) planes (determined from the magnified view of Figure 1c) shown in Figure S3. (f) Schematic illustration of the change in QD size and shape at different stages of the ligand exchange process as deconstructed from the XRD results.

length ($MAPbI_3$: a = 6.26 Å; PbS: a = 5.94 Å), and low interfacial energy (10 meV $Å^{-2}$), which allow the room temperature epitaxial growth of 3D $MAPbI_3$ on the PbS QD surface.[25,28] Counter cations ($CH_3NH_3^+$ and Cs^+) compatible to form 3D perovskite with lead iodide (PbI_2) have been tested to develop hybrid ($MAPbI_3$) and inorganic ($CsPbI_3$) perovskite protecting shell layer for PbS QD.[21,24] It is, however, shown that high band gap perovskite shell forms type-I band alignment with the QD.[24] Therefore, a thick shell layer is likely to deter the carrier transport in the QD film. This could be a reason for low short-circuit current in $MAPbI_3$-shelled[21] (21.8 mA cm^{-2}) and $CsPbI_3$-shelled[24] (24.5 mA cm^{-2}) PbS QD solar cells. Significant improvement in the solar cell performance is achieved when the PbS QD surface is passivated by $[PbX_3]^-/[PbX]^+$ (X-halide) with the aid of small amount of ammonium acetate.[7] Not many efforts have been dedicated for controlling the perovskite shell growth until recently when a 2D layer matrix was formed by using longer chain hybrid−amine mixture to achieve a record PCE of 12% and short-circuit current of 30 mA cm^{-2} in PbS QDs-based solar cells.[8] The 2D confinement prevents the thick shell growth to improve the QD packing and carrier transport properties to record the highest reported efficiency in the QD solar cell to date. Therefore, we believe that further investigation on the halometallate passivation and shell growth strategy would be beneficial for the development of the QD solar cell.

We reason that favorable Goldschmidt tolerance factor for the methylammonium ion (MA^+) (t = 0.88) facilitates thick 3D $MAPbI_3$ perovskite shell growth over PbS QDs.[25,27] Replacing the MA^+ (ionic radius = 2.17 Å) with smaller ammonium ion (NH_4^+, ionic radius = 1.43 Å) will reduce the tolerance factor to 0.72, which may prevent the 3D growth of the perovskite layer. Furthermore, the ammonium iodide (AI) would be more favorable than the methylammonium iodide

DOI: 10.1021/acsami.8b15469
ACS Appl. Mater. Interfaces 2018, 10, 39074−39082

(MAI) in removal of the longer chain oleic acid from the QD surface because of its more reactive ammonium proton.[29] The ligand exchange process for the QDs is carried out with subtle modifications to the earlier reported process of 3D perovskite shelling[21] (please see the Method section for details). Typically, ligand exchange is a two-step process. In the first step, lead halide (3:1 combination of PbI_2 and $PbBr_2$) and AI (or MAI) are dissolved in equimolar ratios (0.1 mol/L) in dimethylformamide (DMF). The octane solution of oleic acid (OA)-capped PbS QDs (15 mg/mL) are mixed with the ligand solution and shaken for few minutes until the QDs are transferred to the DMF phase. This is followed by the precipitation of the QDs from the DMF phase by toluene using solvent-antisolvent approach. In the second step, the isolated QDs are redispersed in volatile butylamine (BA) solvent to form concentrated QD ink for one-step film deposition. Finally, the deposited films are annealed at 70 °C for 15 min for their optimum solar cell performance.

Herein, we report the photovoltaic application of the PbS QDs coupled to the 2D crystalline matrix. The halometallate ligand use for the solution phase ligand exchange leads to surface reconstruction of the PbS QDs; size, shape, and axis length alter notably as a result. The amine solvent (BA in this case) used for the final dispersion of the halometallate treated QDs plays an active role in the 2D confinement of the matrix layer during the film solidification process. The matrix layer is shown to consist of two 2D crystalline components which are identified to be a Pb−amine complex and a $(BA)_2PbI_4$ perovskite layer. Both the components show long-range crystal ordering in the QD film. Multilayer growth of the 2D matrix along *z*-direction is strongly influenced by the choice of the counter cation. Replacing MAI with AI in the ligand exchange process deters the thick shell growth to improve the QD packing in thin films. Subsequently, carrier transport in the QDs coupled to the thinner 2D matrix increases to yield higher performances in solar cells. Because the lead halide is common for both the ligand treatments, lead halide + AI- and lead halide + MAI-treated PbS QDs are represented as AI- and MAI-treated PbS QDs for the rest of the report.

■ RESULTS AND DISCUSSION

X-ray diffraction (XRD) pattern of the AI- and the MAI-treated PbS QD films annealed at 70 °C (represented as AI-70 °C and MAI-70 °C, respectively) are shown in Figure 1a. The XRD peaks at the 2θ value of 25.45° and 29.48° are originated from the (111) and the (200) planes, respectively, confirming the presence of PbS QDs in the film.[30,31] In addition to the PbS diffraction peaks, multiple sharp peaks are visible in their XRD pattern. A closer look reveals that there are two sets of equidistant peaks with the repetition of 4.99° and 6.35° 2θ values, running through their XRD spectrums. The equidistant sharp peaks are the signature of the 2D confined crystalline matrix. In Figure 1a, the peak intensity for the PbS(200) planes is normalized for AI-70 °C and MAI-70 °C films for their ready comparison. The peak intensities corresponding to the 2D layer structures are more than two times higher in MAI-70 °C, implying that for a fixed PbS QD film thickness, the 2D matrix thickness in MAI-70 °C film is higher than that in AI-70 °C film. The equidistant peaks with the repetition of 6.35° identically match with the 2D $(BA)_2PbI_4$ perovskite orthorhombic crystal structure and are assigned in the plot.[32,33] The origin of the pattern with the repetition of 4.99° is however elusive and could not be ascertained from the literature reports. The XRD spectrum of pure PbI_2 (Figure S1) does not match with the pattern. We posit that the pattern with repetition of 4.99° may originate from the layer structure of PbI_2−amine or Pb−amine complex formation. The XRD spectrum of the lead acetate ($PbAc_2$) and BA mixture film (Figure 1b) shows similar equidistant sharp peaks at identical positions with the repetition rate of 4.99°. This suggests that the pattern could be due to the 2D Pb−amine complex and eliminates the contribution from PbI_2−amine complex. The XRD patterns of the ligand films show similar equidistant peaks as observed in the ligand-passivated QD films (Figure 1b). When AI or MAI is added to the PbI_2 + BA ligand, the Pb−amine complex peak intensities reduce, and the $(BA)_2PbI_4$ peak intensities increase significantly. For all the PbI_2-based ligands, the $(BA)_2PbI_4$ perovskite peak intensities are much stronger than those for the Pb−amine complex, suggesting favored condition for the 2D perovskite growth. In the presence of the QDs, however, the Pb−amine complex peaks are significantly stronger than the $(BA)_2PbI_4$ perovskite peaks (Figure 1a,c). This indicates the critical role of the QD surface for the preferential growth of 2D Pb−amine complex over $(BA)_2PbI_4$. It is further found that the 2D confinement of the matrix layer is true for longer chain hexylamine (HA) as well. In the case of BA + HA (4:1) mix solvent, equidistant sharp peaks are also observed (Figure S2). The analysis of the XRD peaks shows the oriented growth of the 2D Pb−HA complex, and no peak corresponding to $(HA)_2PbI_4$ is observed.[34] We note that for both the ligands, AI and MAI, the ligand exchange process causes notable surface reconstruction of PbS QDs. The case study for AI ligand at different processing stages is shown in Figure 1c. For the pristine OA-capped PbS QDs, peak intensity for the PbS(111) planes is stronger than the (200) planes; however, in the case of AI-treated QDs, peak intensity of the (111) planes is lower than the (200) planes in all processing stages. The PbS QDs (dia.∼3 nm) are terminated by (111) and (200) facets at their surface,[10,35] making the planes prudent to determine the size from XRD measurement. The magnified view of the XRD spectrum pertaining to the (111) and (200) planes of PbS QD is shown in Figure S3a. Particle size estimation from the Debye−Scherrer equation[36] shows that (Figure 1d) there is a reduction in PbS diameter along the (111) plane at the intermediate DMF stage, which recovers partially in the BA room temperature (BA-RT) stage, and finally increases in the annealed sample (BA-70 °C). Particle size determined from the full width at half-maximum (fwhm) of the (200) plane shows that size increases systematically in each processing stage of the AI ligand treatment. We also note that along with the varied fwhm, the XRD peak positions for the (111) and (200) planes are also varied at different processing stages (Figure S3b), indicating different crystal strains at different stages of the ligand exchange process.[37] The axis length of the rock-salt PbS crystals determined from the diffraction peak position of the (111) and (200) planes at different stages of the ligand exchange process are shown in Figure 1e. The (111) facets of the PbS QDs are terminated by unsaturated lead atoms making the surface polar, whereas the (200) surfaces are charge neutral and terminated by alternating lead and sulfur atoms.[10,35] Due to dissimilar surface chemistry, interaction of ligand to these surfaces is different, which could be the origin for the facet-dependent surface strain. It is interesting to note that the QD size and the axis length determined from the (111) and (200) planes are similar for the annealed PbS QD films. This suggests that in the annealed films, PbS QDs are

DOI: 10.1021/acsami.8b15469
ACS Appl. Mater. Interfaces 2018, 10, 39074−39082

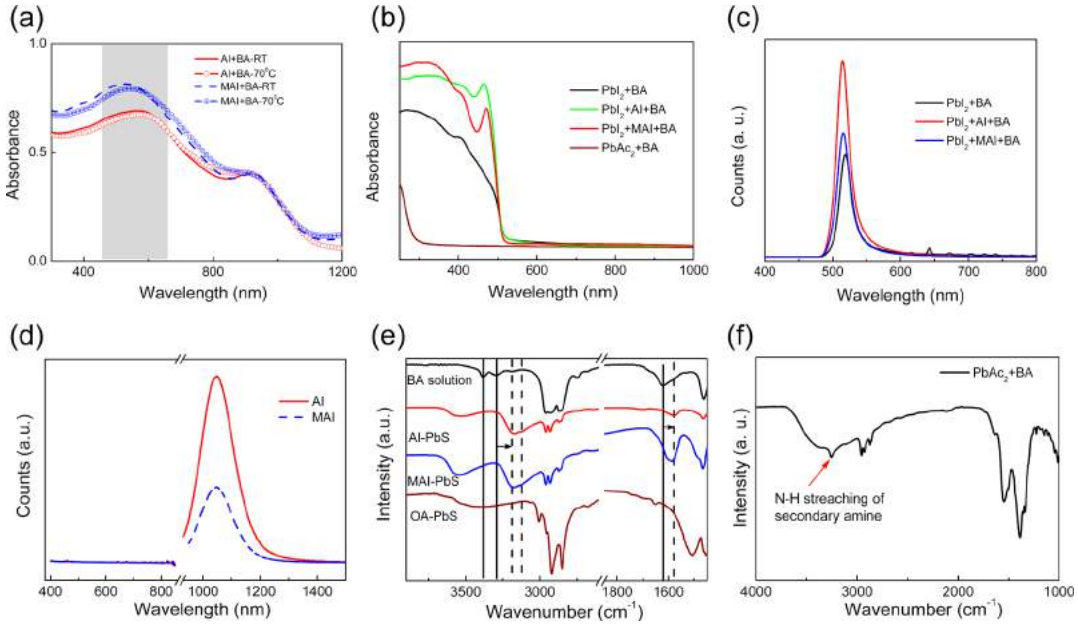

Figure 2. Spectroscopic characterization of the 2D crystalline matrix. (a) Absorption spectra of AI- and MAI-treated nonannealed and annealed PbS QD films. (b) Absorption and (c) PL spectra of thin films of the ligands deposited on the quartz substrate. (d) PL spectra of QD films on the quartz substrate. Excitation wavelength is 380 nm. (e) ATR−FTIR spectroscopy of the QD film treated with different ligands (as marked in the plot) and FTIR spectrum of pure BA in CCl_4 solution. The shift in the N−H stretching frequency and the N−H scissor mode frequency are shown in the plot. (f) ATR−FTIR spectra of the $PbAc_2$ + BA complex film. The appearance of single N−H stretching peak indicates the formation of a secondary amine.

more spherical and have similar surface strain in both (111) and (200) facets. Comparison of the XRD spectra of the annealed and room temperature-processed AI-treated PbS QD films (Figures 1c and S4) shows significant increases in 2D $(BA)_2PbI_4$ perovskite peak intensities in the annealed samples, implying that annealing helps the long-range ordering of the 2D $(BA)_2PbI_4$ perovskite crystals.

The schematic view of the PbS QD size and shape progression at different stages of the ligand exchange process is deconstructed from the XRD results and shown in Figure 1f. The crystal facets with the higher surface energy undergo selective etching under harsh ligand attack ($[PbI_3]^-$) in the DMF solvent, which reduces the size along the (111) direction and increases the exposed surface area of the (111) facets.[38] Nonannealed and annealed PbS QD films from BA show a progressive increase in the QD size along both the directions, while the increase along the (111) direction is much higher. We surmise that at the DMF phase, aggressive $[PbI_3]^-$ ions may etch some Pb atoms from the (111) facets and eventually passivate the (111) facets at the equilibrium.[38,39] In the presence of BA, the interaction of the $[PbI_3]^-$ ligand with the QD surface is relatively relaxed due to the formation of bulkier $[BAPbI_4]^-$ anion, which leads to the regrowth of the QDs along the highly reactive (111) facets. The neutral Pb−amine complex may act as "L" type ligand which would coordinate with the neutral (200) facets of PbS QDs.[10] This is supported by the fact that the growth of 2D Pb−amine complex is favorable in the presence of QDs, while only ligand films favored 2D $(BA)_2PbI_4$ perovskite formation.

The absorption profiles for the AI- and MAI-treated films are normalized to PbS excitonic peak position to illustrate the absorption contribution of the matrix layer (Figure 2a). The humps in the absorption spectra at around 530 nm (as shown by the shaded region) could be originated from the 2D $(BA)_2PbI_4$ perovskite absorption. The absorption spectrum of the ligand films is taken as the control experiment and shown in Figure 2b. It is found that both the PbI_2 + AI + BA and PbI_2 + MAI + BA ligand films show a strong excitonic feature of 2D $(BA)_2PbI_4$ perovskite peak at around (480 nm), whereas for the PbI_2 + BA film, the excitonic feature is less significant.[8,33] The absorption spectrum of the $PbAc_2$ + BA film shows no absorbance within the wavelength range. Furthermore, narrow fwhm (∼20 nm) of the photoluminescence (PL) spectrum (Figure 2c) of the ligand films supports the formation of the 2D $(BA)_2PbI_4$ perovskite.[8,33] The PL spectrum of the QD films (Figure 2d) shows no peak for the ligand emission and shows only band edge emission from the PbS QDs.[40] The absorbance peak of only $(BA)_2PbI_4$ red shifts by ∼50 nm in the QD films. The complete quenching of the PL emission and red shift in absorbance of $(BA)_2PbI_4$ perovskite in the QD films strongly suggest that the perovskite matrix does not form in isolation but is strongly coupled to the QD surface.[40] The excitonic peak position for the OA−PbS QD film (Figure S5) is red shifted by ∼50 nm for the AI- and MAI-treated films. The size for the PbS QDs estimated from the absorption spectrum matched closely with the increase in size as determined from XRD (Table S1), pointing toward the incremental increase in the size of PbS QDs being responsible for the red shift of the QD excitonic peak. Fourier transform infrared (FTIR) spectroscopy results show that the N−H stretching band (asymmetric and symmetric) of pure BA appears at 3384 and 3295 cm^{-1} and shifts to 3180 and 3122 cm^{-1} in the AI- and MAI-treated PbS QD film. The N−H scissor mode vibration peak also shifts from 1620 to 1580 cm^{-1} (Figure 2e). This further supports the chemical coordination of the amine in the 2D matrix layer.[8]

It is interesting to note that for the equivalent QD excitonic absorption, the 2D $(BA)_2PbI_4$ ligand absorbance is higher in

DOI: 10.1021/acsami.8b15469
ACS Appl. Mater. Interfaces 2018, 10, 39074−39082

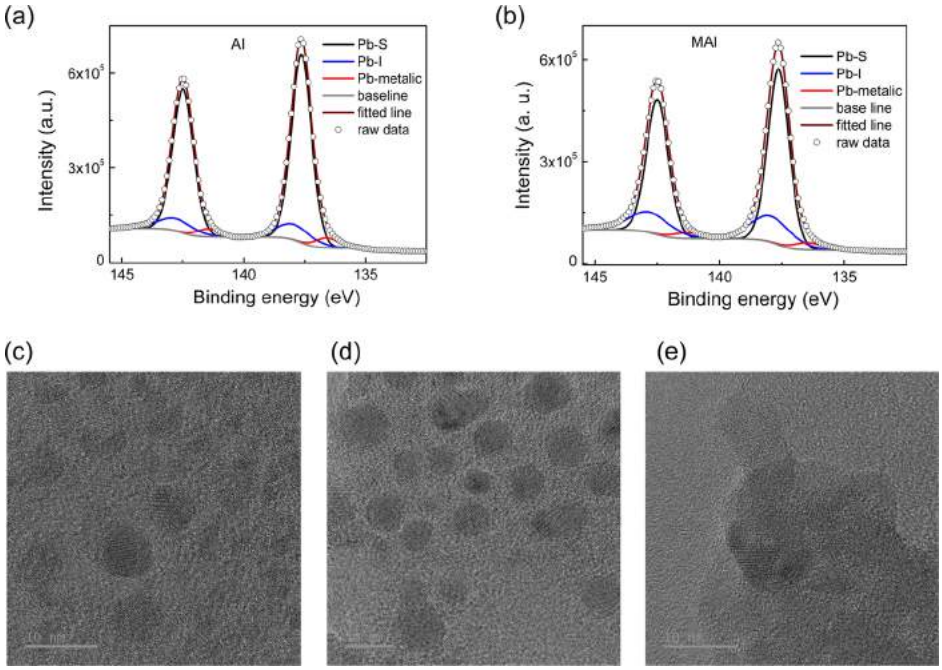

Figure 3. Compositional and structural analysis by XPS and TEM. (a,b) show the Pb 4f XPS signal of the AI- and MAI-treated QDs, respectively. The Pb 4f signal is deconvoluted to Pb−ligand, Pb−S, and Pb-metallic signals to fit the spectrum. The high-resolution TEM images of (c) oleic acid-capped PbS QDs, (d) AI- treated PbS QDs, and (e) MAI-treated PbS QDs deposited from BA and annealed at 70 °C.

the case of MAI-treated films, implying a higher proportion of the 2D perovskite. There is barely any change in the absorption intensity of $(BA)_2PbI_4$ in the annealed and the nonannealed samples. However, the XRD data show that the diffraction peak intensity of the 2D $(BA)_2PbI_4$ perovskite increases significantly (Figures 1c and S4) on annealing. This implies that annealing improves the crystallinity and long-range ordering of the 2D $(BA)_2PbI_4$ perovskite, but the relative amount remains unchanged in the film. Furthermore, there is no evidence of 3D $MAPbI_3$ perovskite formation from XRD, absorption, and PL data for both the AI- and MAI-treated PbS QD films. We surmise that the deposition of QD films from the linear chain amine (BA or HA) confined the perovskite growth to the 2D. On the basis of the observations from XRD and the spectroscopic results, we propose the following reaction mechanism for the Pb−amine complex and $(BA)_2PbI_4$ formation in the ligand exchange reaction.

Case-I: $(BA + PbI_2 + NH_4I/MAI)$

$$2BA + 2NH_4PbI_3(/2MAPbI_3) \rightarrow (BA)_2PbI_4 + PbI_2 + 2NH_3/CH_3NH_2\uparrow \quad \text{(i)}$$

$$nBA + nPbI_2 \rightarrow (CH_3CH_2CH_2CH_2NH\cdots PbI)_n + nHI \quad \text{(ii)}$$

Case-II: $(BA + PbI_2)$

$$nBA + nPbI_2 \rightarrow (CH_3CH_2CH_2CH_2NH\cdots PbI)_n + nHI \quad \text{(iii)}$$

$$nBA + nHI \rightarrow nBA^+I^- \quad \text{(iv)}$$

$$2BA^+I^- + PbI_2 \rightarrow (BA)_2PbI_4 \quad \text{(v)}$$

Case-III: $(BA + PbAc_2)$

$$nBA + nPbAc_2 \rightarrow (CH_3CH_2CH_2CH_2NH\cdots PbAc)_n + nAcOH \quad \text{(vi)}$$

In case-I, the mixture of PbI_2 and AI (or MAI) are taken in BA solution; AI (or MAI) protonates the BA to form BA^+ (butylammonium), which favors the formation of $(BA)_2PbI_4$, as shown in eq i.[41] The excess PbI_2 can further react with BA to form the Pb−amine complex, as shown in eq ii. In case-II, in the absence of AI (or MAI) in the reaction mixture, the intermediate "HI" can protonate BA to form $(BA)_2PbI_4$, as shown in eqs iii−v successively. When $PbAc_2$ is taken instead of PbI_2 (case-III) in BA solvent only, the Pb−amine complex is formed (vi). It is interesting to note here that for all the Pb−amine complexes, the amine is a secondary amine. In the case of PbI_2, however, the formation of $(BA)_2PbI_4$ perovskite makes it difficult to distinguish the secondary amine from the primary amine from their FTIR spectrum. We have probed the Pb−amine complex synthesized from $PbAc_2$ to check the proposed reaction mechanism. Attenuated total reflection (ATR)−FTIR spectrum shows the single N−H stretching peak of the secondary amine at 3255 cm^{-1} (Figure 2f), which supports the proposed mechanism.

X-ray photoelectron spectroscopy (XPS) of Pb 4f shows that the atomic percent for Pb−ligand contribution (Pb−I, Pb−amine, etc.) are 12.14 and 21.4%, respectively, for the AI- and MAI-treated PbS films (Figure 3a,b and Table S2). Higher Pb−ligand atomic percentage suggests a thicker ligand matrix for the MAI-treated PbS QD films. Comparison of S2p XPS spectrum shows that the S $2p_{3/2}$ and S $2p_{1/2}$ peaks are narrower in the case of AI-treated QDs (Figure S6 and Table S3). Considering the fact that undercoordinated surface "S" atoms have different XPS signature than fully coordinated "S" atoms in the bulk of the PbS QDs, the narrowing in the S 2p spectrum may be due to higher order replacement of the undercoordinated surface sulfur atoms by iodine.[16] The I/Pb

DOI: 10.1021/acsami.8b15469
ACS Appl. Mater. Interfaces 2018, 10, 39074−39082

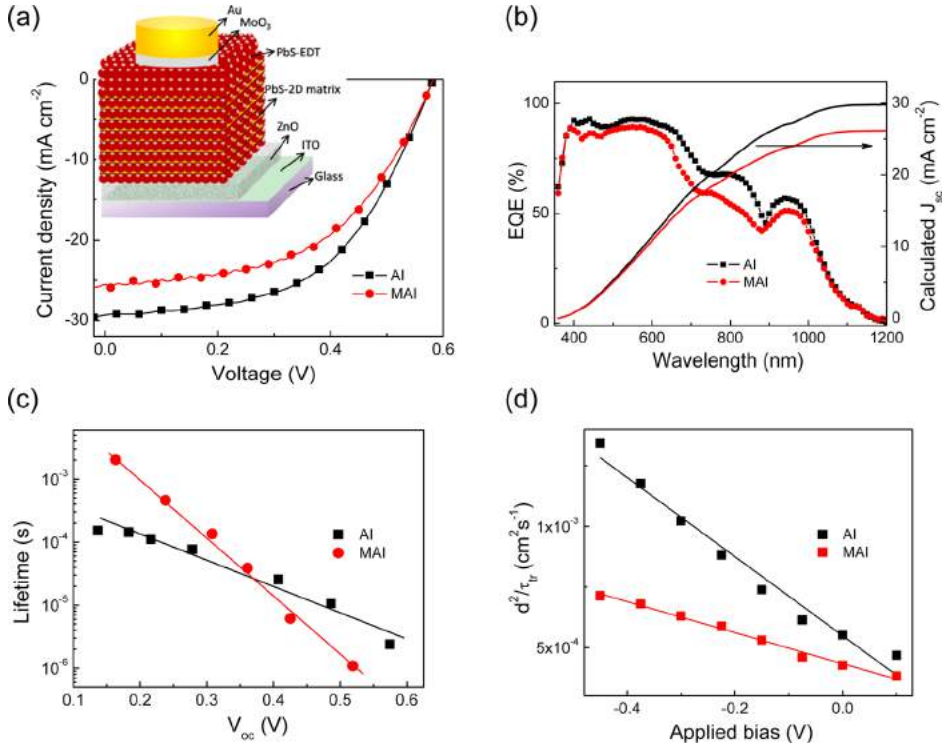

Figure 4. Enhanced solar cell performance in AI-treated devices. (a) $J-V$ characteristics (under reverse scan) of the solar cells under AM1.5 simulated solar illumination. (b) Full-spectrum EQE of AI- and MAI-treated solar cells. The axis on the right shows the calculated J_{sc} from the EQE under simulated solar illumination. (c) Carrier lifetime measured from TPV at different V_{oc}. The V_{oc} has been varied by changing the illumination intensity of the solar simulator. (d) Charge carrier mobility is estimated from the slope of d^2/τ_{tr} vs applied bias plot (where d is film thickness, and τ_{tr} is the carrier transit time).

and I/S ratios for the AI-treated film (0.55 and 0.90, respectively) are higher than the MAI-treated QD film (I/Pb = 0.49, I/S = 0.85) (Figure S7a). The higher proportion of iodine in the AI-treated QDs is likely to provide better surface passivation. The XPS spectrum of N 1s shows the peak at ~402 eV (Figure S7b), indicating transformation of amine to ammonium.[25] The high-resolution transmission electron microscope images show the individual particles in the case of OA and AI ligands, whereas the PbS QDs are connected together by the matrix layer when the MAI ligand is used (Figure 3c−e). Careful analysis of the lattice fringes reveals that the lattice spacing of 0.34 nm is overwhelmingly observed in all three cases, which corresponds to {111} plane spacing of cubic PbS. The crystal fringes of the matrix layer could not be separated from the QDs, probably because of lattice matching and coherent growth of the ligand on the QD surface.[21] In comparison to the AI-treated QDs, the higher amount of matrix is clearly visible in the MAI-treated sample. This further validates the observation of higher matrix presence in the MAI-treated PbS QDs.[21,34]

The light harvesting property of the 2D matrix-passivated PbS QDs are tested in solar cells. The device architecture is shown in the inset of Figure 4a and the cross-sectional image is shown in Figure S8. The optimized solar cell performance based on the AI- and MAI-treated PbS QDs under AM 1.5 (100 mW cm^{-2}) simulated solar illumination is shown in Figure 4a. Short-circuit current (J_{sc}) increases significantly from 25.37 mA cm^{-2} (in MAI−PbS) to 29.29 mA cm^{-2} in the AI-treated solar cells. Open-circuit voltage (V_{oc}) remains unchanged (0.58 V) while the fill factor (FF) rises a little to increase the PCE from 7.80 to 9.10% in the AI-treated solar cells. Both the solar cells show hysteresis in their $J-V$ characteristics (Figure S9). The photovoltaic parameters are summarized in Table 1.

Table 1. Photovoltaic Parameters of the AI- and MAI-Treated PbS QD Solar Cells

name of the ligand	scan direction	J_{sc} (mA cm^{-2})	V_{oc} (V)	FF (%)	PCE (%)
AI	reverse	29.29	0.58	53.6	9.10
	forward	28.57	0.58	47.2	7.82
MAI	reverse	25.37	0.58	53	7.80
	forward	25	0.58	43.1	6.24

The external quantum efficiency (EQE) for the solar cells is determined for the wavelength range of 360−1200 nm. The calculated J_{sc} from the EQE spectrum matched well with the measured J_{sc} for the solar cells, as shown in Figure 4b. The solar cells based on the AI-treated QDs show consistent high performance and little batch-to-batch variation as observed for ten batches of devices (Figure S10). The photo carrier lifetime is measured from transient photovoltage (TPV) decay technique at different open-circuit voltages.[42] Both the solar cells follow the general trend of decrease in carrier lifetime with the increase in light intensity (or V_{oc}),[42,43] however, the slopes are different, as shown in Figure 4c. In higher light bias conditions (close to 1 sun), the carrier lifetime for the AI-treated solar cell is higher, allowing greater leverage for the carrier transportation. Intermediate band trap density is estimated from the TPV decay and transient photocurrent (TPC) decay measurements.[43,44] We found very little difference in intermediate trap distribution of PbS QDs

DOI: 10.1021/acsami.8b15469
ACS Appl. Mater. Interfaces 2018, 10, 39074−39082

(Figure S11), suggesting analogous trap distribution for both the ligand treatments. Carrier transport property in the solar cells is measured using the bias-dependent TPC method as reported earlier.[45,46] The carrier transit time (τ_{tr}) is determined from the photocurrent decay, which corresponds to the time required to decay $1/e$ of the maximum current value. The photocurrent decay at varied applied biases for the AI- and MAI-treated solar cells are shown in Figure S12a,b, respectively. Carrier mobility (μ) is determined using the formula $\mu = \frac{d^2}{\tau_{tr} \times V}$, where d is the film thickness and V is the applied bias. From the slope of d^2/τ_{tr} versus V plot (Figure 4d), μ is determined to be 1.63×10^{-3} cm^2 V^{-1} s^{-1} and 6.4×10^{-4} cm^2 V^{-1} s^{-1} for the AI- and MAI-treated solar cells, respectively. The higher carrier mobility in the AI-treated PbS QD films may be rooted in their lower 2D matrix thickness in comparison to that in the MAI-treated PbS QD films. Diffusion width L_D is estimated using the formula $L_D = \sqrt{\mu(KT)\tau/q}$,[46] where K is the Boltzmann constant, T is the temperature (300 K), τ is the carrier lifetime, and q is the electronic charge. L_D is calculated to be 100 and 42 nm for the AI- and MAI-treated solar cells, respectively, under 1 sun operating condition. Higher diffusion length in the AI-treated solar cells would allow more efficient carrier collection from the thicker QD films. The thickness-dependent study shows that optimal thickness for the AI-treated solar cell is around 320 nm (J_{sc} = 29.29 mA cm^{-2}, FF% = 53.6, and PCE% = 9.1), whereas for the MAI-treated solar cell, optimal thickness is around 250 nm (J_{sc} = 25.37 mA cm^{-2}, FF% = 53, and PCE% = 7.80) (Figure S13). The increase in carrier extraction thickness closely matches the increase in diffusion length in the AI-treated solar cells.

■ CONCLUSIONS

In summary, we have shown PbS QDs in the oriented 2D matrix by subjecting the halometallate-treated QDs to linear chain amines such as BA and HA. The halometallate−ligand treatment is found to modify the size, shape, and axis length of PbS QDs through surface reconstruction. The 2D layer matrix is shown to consist of two 2D components in the form of a Pb−amine complex and a $(BA)_2PbI_4$ perovskite layer. The choice of the counter cation influences the growth of the 2D matrix layer in the PbS QD films. The enhancement in photovoltaic performances in the AI-treated QD films are correlated to the increase in carrier mobility, carrier lifetime, and diffusion length of the solar cells. Our study shows a general approach to develop the 2D matrix-passivated QD film which could be beneficial for the wide range of optoelectronic applications, such as the printable solar cell, tandem cell, photodetector, and light emitting diodes.

■ METHODS

Ligand Exchange of PbS QDs. Oleic acid-capped PbS QDs are synthesized and purified following the previously reported method.[47] The QD solution (15 mg/mL) is prepared in anhydrous octane for halometallate ligand treatment. The solution phase ligand exchange process developed for $MAPbI_3$ is modified for the QD treatment in this study.[21] Typically, 0.1 M NH_4I (or 0.1 CH_3NH_3I), 0.075 M PbI_2, and 0.025 M $PbBr_2$ are added to 5 mL of DMF to get a clear transparent yellow ligand solution. The PbS QDs solution (5 mL) is mixed with the DMF solution and vortexed for 2 min to transfer the PbS QDs from octane to DMF phase. Within 2 min, the PbS QDs are transferred from octane to DMF phase. The top octane supernatant layer is discarded, and the QD solution is cleaned another three times using octane. The ligand-exchanged QDs are precipitated from the DMF phase by adding 2.5 mL toluene and collected by centrifugation at 3500 rpm. The precipitated QDs are dried under vacuum for 20 min and finally dispersed in BA (200 mg/mL) for film fabrication.

Device Fabrication. Presynthesized ZnO nanocrystals[48] (100 mg/mL) are spin-coated from 10% BA: 90% toluene mixture solution on top of cleaned indium tin oxide substrates at 3500 rpm, and the substrates are heated at 250 °C for 40 min. The BA solution of QD ink is spin-coated on the ZnO substrate for the deposition of a thick QD layer. The rotation speed and the acceleration are varied to change the film thickness from 180 to 360 nm. The films are then annealed at 70 °C for 15 min inside an argon glove box. For the hole transport layer formation, two layers of 1,2 ethanedithiol (EDT)-treated PbS QD films are deposited using the LBL approach.[3] Typically, OA-capped PbS QD solution (45 mg/mL) from octane is spin-coated (2500 rpm) followed by soaking in EDT solution (0.02 vol % in acetonitrile) for 20 s and washing two times using acetonitrile under rotation. MoO_3 (8 nm), Au (30 nm), and Ag (100 nm) are deposited sequentially using a thermal evaporator (HHV BC-300) at the base pressure of 1×10^{-6} Torr.

Solar Cell Characterizations. $J-V$ characteristics are measured using a Keithley 2634B source meter and a solar simulator (PEC-L01). The illumination intensity is maintained at 100 mW cm^{-2} using a calibrated thermal detector (S302C-Thorlab). EQE measurements are carried out with the help of a monochromatic light source (SLS-M266). Light intensity at different wavelengths is measured using photodiode detectors from Thorlab (S120VC, S122C). Transient measurements (TPV and TPC) are performed using a laser diode (Newport LQA658-30C) modulated through a function generator (Tektronix, AFG 3021C) to produce short light pulses. For TPV measurement, white light bias intensity is varied with the help of neutral density filters, and the device under test is connected to an oscilloscope (Tektronix, MDO 3104) through a 1 MΩ resistance. Laser pulse intensities are modulated to keep the perturbation voltage below 10 mV. TPC measurements are done using laser pulse only, and the output is measured across a 50 Ω resistance. Charge carrier mobility is determined by bias-dependent photocurrent transient technique, as reported earlier.[45] A pulse laser diode (Newport LQA658-30C) controlled through a function generator (Tektronix, AFG 3021C) is used to create the light pulse of 500 ns. The device under test is excited by short pulses at the light bias of 1 sun (solar simulator PEC-L01). Different electrical bias are applied to the device through the inbuilt function generator of the oscilloscope (Tektronix, MDO 3104). The transient signal from the device is measured across a 50 Ω resistance using the same oscilloscope.

Materials Characterization. Optical absorption measurements are carried out using a Shimadzu UV−vis-IR-3600 Plus spectrophotometer. Total absorption of the thin films is measured with the help of an integrating sphere (ISR-603) attached to the instrument. Steady-state PL measurements are performed utilizing a spectrofluorometer (FS5, Edinburgh Instruments). IR absorption spectra of the solution are recorded on an FTIR spectrometer (Vertex-70, Bruker) with 2 cm^{-1} resolution at room temperature. ATR−FTIR spectra of thin films are obtained on a PerkinElmer Spectrum Two-spectrophotometer in the 4000−400 cm^{-1} wavelength range with a resolution of 4 cm^{-1}. XRD profiles are recorded on an X'Pert Pro model PANalytical diffractometer (Philips PANalytical) operated at a voltage of 40 kV and a current of 30 mA with Cu Kα (1.5418 Å) radiation. The QDs and ligand samples are scanned for the 2θ range of 4°−60° with a scan rate of 0.4° per minute. XPS is carried out using the thermo scientific K-Alpha + spectrometer under ultrahigh vacuum condition (10^{-9} mbar). XPS measurements are performed with a monochromatic Al Kα X-ray source (1486.6 eV) with the pass energy of 50 eV for individual core levels. The XPS spectra are calibrated to the C 1s peak at a binding energy of 284.8 eV. The fitting of the XPS spectra is performed using CasaXPS software. All measurements are carried out using an electron flood gun source for surface charge neutralization.

DOI: 10.1021/acsami.8b15469
ACS Appl. Mater. Interfaces 2018, 10, 39074−39082

■ ASSOCIATED CONTENT

Supporting Information

The Supporting Information is available free of charge on the ACS Publications website at DOI: 10.1021/acsami.8b15469.

XRD spectra of PbI_2 and $PbAc_2$ powder, comparison of XRD spectra, XPS spectrum of S2p orbital of PbS QD film, XPS signals of AI- and MAI-treated PbS QDs, absorption spectrum of the oleic acid-capped PbS QD film, SEM image of a representative solar cell device structure, $J-V$ characteristics, batch-to-batch device performance, transient photo current decay, trap density estimation, change in PCE with thickness for AI- and MAI-treated solar cells, PbS QD size determined from XRD and absorbance spectroscopy, atomic percent of different components determined from Pb 4f XPS spectrum of AI- and MAI-treated PbS QDs, fitting parameters and quantitative analysis of S 2p spectra of AI- and MAI-treated PbS QD films (PDF)

■ AUTHOR INFORMATION

Corresponding Author

*E-mail: ak.rath@ncl.res.in.

ORCID

Debranjan Mandal: 0000-0001-9782-4169

Arup K. Rath: 0000-0003-2261-7215

Notes

The authors declare no competing financial interest.

■ ACKNOWLEDGMENTS

The authors acknowledge the financial assistance from the SERB extramural funding, India (project code: EMR/2015/002415) and DST Nanomission, India (project code: SR/NM/NT-1011/2105 (G)). D.M. acknowledges the CSIR award 31/11(1036)/2018 EMR I for part of his fellowship.

■ REFERENCES

(1) McDonald, S. A.; Konstantatos, G.; Zhang, S.; Cyr, P. W.; Klem, E. J. D.; Levina, L.; Sargent, E. H. Solution-processed PbS Quantum Dot Infrared Photodetectors and Photovoltaics. *Nat. Mater.* **2005**, *4*, 138−142.

(2) Luther, J. M.; Gao, J. B.; Lloyd, M. T.; Semonin, O. E.; Beard, M. C.; Nozik, A. J. Stability Assessment on a 3% Bilayer PbS/ZnO Quantum Dot Heterojunction Solar Cell. *Adv. Mater.* **2010**, *22*, 3704−3707.

(3) Chuang, C.-H. M.; Brown, P. R.; Bulović, V.; Bawendi, M. G. Improved Performance and Stability in Quantum Dot Solar Cells Through Band Alignment Engineering. *Nat. Mater.* **2014**, *13*, 796−801.

(4) Kagan, C. R.; Lifshitz, E.; Sargent, E. H.; Talapin, D. V. Building Devices From Colloidal Quantum Dots. *Science* **2016**, *353*, aac5523.

(5) Pradhan, S.; Stavrinadis, A.; Gupta, S.; Konstantatos, G. Reducing Interface Recombination through Mixed Nanocrystal Interlayers in PbS Quantum Dot Solar Cells. *ACS Appl. Mater. Interfaces* **2017**, *9*, 27390−27395.

(6) Lan, X.; Voznyy, O.; de Arquer, F. P. G.; Liu, M.; Xu, J.; Proppe, A. H.; Walters, G.; Fan, F.; Tan, H.; Liu, M.; Yang, Z.; Hoogland, S.; Sargent, E. H. 10.6% Certified Colloidal Quantum Dot Solar Cells via Solvent Polarity-Engineered Halide Passivation. *Nano Lett.* **2016**, *16*, 4630−4634.

(7) Liu, M.; Voznyy, O.; Sabatini, R.; de Arquer, F. P. G.; Munir, R.; Balawi, A. H.; Lan, X.; Fan, F.; Walters, G.; Kirmani, A. R.; Hoogland, S.; Laquai, F.; Amassian, A.; Sargent, E. H. Hybrid Organic-inorganic Inks Flatten the Energy Landscape in Colloidal Quantum Dot Solids. *Nat. Mater.* **2017**, *16*, 258−263.

(8) Xu, J.; Voznyy, O.; Liu, M.; Kirmani, A. R.; Walters, G.; Munir, R.; Abdelsamie, M.; Proppe, A. H.; Sarkar, A.; de Arquer, F. P. G.; Wei, M.; Sun, B.; Liu, M.; Ouellette, O.; Quintero-Bermudez, R.; Li, J.; Fan, J.; Quan, L.; Todorovic, P.; Tan, H.; Hoogland, S.; Kelley, S. O.; Stefik, M.; Amassian, A.; Sargent, E. H. 2D Matrix Engineering for Homogeneous Quantum Dot Coupling in Photovoltaic Solids. *Nat. Nanotechnol.* **2018**, *13*, 456−462.

(9) Jumabekov, A. N.; Cordes, N.; Siegler, T. D.; Docampo, P.; Ivanova, A.; Fominykh, K.; Medina, D. D.; Peter, L. M.; Bein, T. Passivation of PbS Quantum Dot Surface with L-Glutathione in Solid-State Quantum-Dot-Sensitized Solar Cells. *ACS Appl. Mater. Interfaces* **2016**, *8*, 4600−4607.

(10) Boles, M. A.; Ling, D.; Hyeon, T.; Talapin, D. V. The Surface Science of Nanocrystals. *Nat. Mater.* **2016**, *15*, 141−153.

(11) Tang, J.; Brzozowski, L.; Barkhouse, D. A. R.; Wang, X.; Debnath, R.; Wolowiec, R.; Palmiano, E.; Levina, L.; Pattantyus-Abraham, A. G.; Jamakosmanovic, D.; Sargent, E. H. Quantum Dot Photovoltaics in the Extreme Quantum Confinement Regime: The Surface-Chemical Origins of Exceptional Air- and Light-Stability. *ACS Nano* **2010**, *4*, 869−878.

(12) Bakulin, A. A.; Neutzner, S.; Bakker, H. J.; Ottaviani, L.; Barakel, D.; Chen, Z. Charge Trapping Dynamics in PbS Colloidal Quantum Dot Photovoltaic Devices. *ACS Nano* **2013**, *7*, 8771−8779.

(13) Guyot-Sionnest, P. Electrical Transport in Colloidal Quantum Dot Films. *J. Phys. Chem. Lett.* **2012**, *3*, 1169−1175.

(14) Talapin, D. V.; Murray, C. B. PbSe Nanocrystal Solids for n- and p-Channel Thin Film Field-Effect Transistors. *Science* **2005**, *310*, 86−89.

(15) Luther, J. M.; Law, M.; Beard, M. C.; Song, Q.; Reese, M. O.; Ellingson, R. J.; Nozik, A. J. Schottky Solar Cells Based on Colloidal Nanocrystal Films. *Nano Lett.* **2008**, *8*, 3488−3492.

(16) Lan, X.; Voznyy, O.; Kiani, A.; de Arquer, F. P. G.; Abbas, A. S.; Kim, G.-H.; Liu, M.; Yang, Z.; Walters, G.; Xu, J.; Yuan, M.; Ning, Z.; Fan, F.; Kanjanaboos, P.; Kramer, I.; Zhitomirsky, D.; Lee, P.; Perelgut, A.; Hoogland, S.; Sargent, E. H. Passivation Using Molecular Halides Increases Quantum Dot Solar Cell Performance. *Adv. Mater.* **2016**, *28*, 299−304.

(17) Zhang, X.; Santra, P. K.; Tian, L.; Johansson, M. B.; Rensmo, H.; Johansson, E. M. J. Highly Efficient Flexible Quantum Dot Solar Cells with Improved Electron Extraction Using MgZnO Nanocrystals. *ACS Nano* **2017**, *11*, 8478−8487.

(18) Zhitomirsky, D.; Kramer, I. J.; Labelle, A. J.; Fischer, A.; Debnath, R.; Pan, J.; Bakr, O. M.; Sargent, E. H. Colloidal Quantum Dot Photovoltaics: The Effect of Polydispersity. *Nano Lett.* **2012**, *12*, 1007−1012.

(19) Erslev, P. T.; Chen, H.-Y.; Gao, J.; Beard, M. C.; Frank, A. J.; van de Lagemaat, J.; Johnson, J. C.; Luther, J. M. Sharp Exponential Band Tails in Highly Disordered Lead Sulfide Quantum Dot Arrays. *Phys. Rev. B: Condens. Matter Mater. Phys.* **2012**, *86*, 155313 1−5 .

(20) Chuang, C.-H. M.; Maurano, A.; Brandt, R. E.; Hwang, G. W.; Jean, J.; Buonassisi, T.; Bulović, V.; Bawendi, M. G. Open-Circuit Voltage Deficit, Radiative Sub-Bandgap States, and Prospects in Quantum Dot Solar Cells. *Nano Lett.* **2015**, *15*, 3286−3294.

(21) Yang, Z.; Janmohamed, A.; Lan, X.; de Arquer, F. P. G.; Voznyy, O.; Yassitepe, E.; Kim, G.-H.; Ning, Z.; Gong, X.; Comin, R.; Sargent, E. H. Colloidal Quantum Dot Photovoltaics Enhanced by Perovskite Shelling. *Nano Lett.* **2015**, *15*, 7539−7543.

(22) Dirin, D. N.; Dreyfuss, S.; Bodnarchuk, M. I.; Nedelcu, G.; Papagiorgis, P.; Itskos, G.; Kovalenko, M. V. Lead Halide Perovskites and Other Metal Halide Complexes As Inorganic Capping Ligands for Colloidal Nanocrystals. *J. Am. Chem. Soc.* **2014**, *136*, 6550−6553.

(23) Zhang, H.; Jang, J.; Liu, W.; Talapin, D. V. Colloidal Nanocrystals with Inorganic Halide, Pseudohalide, and Halometallate Ligands. *ACS Nano* **2014**, *8*, 7359−7369.

(24) Zhang, X.; Zhang, J.; Phuyal, D.; Du, J.; Tian, L.; Öberg, V. A.; Johansson, M. B.; Cappel, U. B.; Karis, O.; Liu, J.; Rensmo, H.; Boschloo, G.; Johansson, E. M. J. Inorganic CsPbI3 Perovskite Coating on PbS Quantum Dot for Highly Efficient and Stable

Infrared Light Converting Solar Cells. *Adv. Energy Mater.* **2018**, *8*, 1702049.
(25) Ning, Z.; Gong, X.; Comin, R.; Walters, G.; Fan, F.; Voznyy, O.; Yassitepe, E.; Buin, A.; Hoogland, S.; Sargent, E. H. Quantum-Dot-in-Perovskite Solids. *Nature* **2015**, *523*, 324−328.
(26) Burschka, J.; Pellet, N.; Moon, S.-J.; Humphry-Baker, R.; Gao, P.; Nazeeruddin, M. K.; Grätzel, M. Sequential Deposition As a Route to High-Performance Perovskite-Sensitized Solar Cells. *Nature* **2013**, *499*, 316−319.
(27) Leijtens, T.; Eperon, G. E.; Noel, N. K.; Habisreutinger, S. N.; Petrozza, A.; Snaith, H. J. Stability of Metal Halide Perovskite Solar Cells. *Adv. Energy Mater.* **2015**, *5*, 1500963.
(28) Sytnyk, M.; Yakunin, S.; Schöfberger, W.; Lechner, R. T.; Burian, M.; Ludescher, L.; Killilea, N. A.; YousefiAmin, A.; Kriegner, D.; Stangl, J.; Groiss, H.; Heiss, W. Quasi-epitaxial Metal-Halide Perovskite Ligand Shells on PbS Nanocrystals. *ACS Nano* **2017**, *11*, 1246−1256.
(29) Balazs, D. M.; Dirin, D. N.; Fang, H.-H.; Protesescu, L.; ten Brink, G. H.; Kooi, B. J.; Kovalenko, M. V.; Loi, M. A. Counterion-Mediated Ligand Exchange for PbS Colloidal Quantum Dot Superlattices. *ACS Nano* **2015**, *9*, 11951−11959.
(30) Bakueva, L.; Gorelikov, I.; Musikhin, S.; Zhao, X. S.; Sargent, E. H.; Kumacheva, E. PbS Quantum Dots With Stable Efficient Luminescence in the Near-IR Spectral Range. *Adv. Mater.* **2004**, *16*, 926−929.
(31) Bertolotti, F.; Dirin, D. N.; Ibáñez, M.; Krumeich, F.; Cervellino, A.; Frison, R.; Voznyy, O.; Sargent, E. H.; Kovalenko, M. V.; Guagliardi, A.; Masciocchi, N. Crystal Symmetry Breaking and Vacancies in Colloidal Lead Chalcogenide Quantum Dots. *Nat. Mater.* **2016**, *15*, 987−994.
(32) Mitzi, D. B. Synthesis, Crystal Structure, and Optical and Thermal Properties of (C4H9NH3)2MI4(M = Ge, Sn, Pb). *Chem. Mater.* **1996**, *8*, 791−800.
(33) Cao, D. H.; Stoumpos, C. C.; Farha, O. K.; Hupp, J. T.; Kanatzidis, M. G. 2D Homologous Perovskites as Light-Absorbing Materials for Solar Cell Applications. *J. Am. Chem. Soc.* **2015**, *137*, 7843−7850.
(34) Yang, Z.; Voznyy, O.; Walters, G.; Fan, J. Z.; Liu, M.; Kinge, S.; Hoogland, S.; Sargent, E. H. Quantum Dots in Two-Dimensional Perovskite Matrices for Efficient Near-Infrared Light Emission. *ACS Photonics* **2017**, *4*, 830−836.
(35) Zherebetskyy, D.; Scheele, M.; Zhang, Y.; Bronstein, N.; Thompson, C.; Britt, D.; Salmeron, M.; Alivisatos, P.; Wang, L.-W. Hydroxylation of the Surface of PbS Nanocrystals Passivated with Oleic Acid. *Science* **2014**, *344*, 1380−1384.
(36) Patterson, A. L. The Scherrer Formula for X-Ray Particle Size Determination. *Phys. Rev.* **1939**, *56*, 978−982.
(37) Norton, C. S. M. G. *X-Ray Diffraction: Apractical Approach*; Plenum Press: New York, USA, 1998.
(38) Wang, Z.; Yang, G.; Zhang, Z.; Jin, M.; Yin, Y. Selectivity on Etching: Creation of High-Energy Facets on Copper Nanocrystals for CO2 Electrochemical Reduction. *ACS Nano* **2016**, *10*, 4559−4564.
(39) Xia, Y.; Xiong, Y.; Lim, B.; Skrabalak, S. E. Shape-Controlled Synthesis of Metal Nanocrystals: Simple Chemistry Meets Complex Physics? *Angew. Chem., Int. Ed.* **2009**, *48*, 60−103.
(40) Hyun, B.-R.; Zhong, Y.-W.; Bartnik, A. C.; Sun, L.; Abruña, H. D.; Wise, F. W.; Goodreau, J. D.; Matthews, J. R.; Leslie, T. M.; Borrelli, N. F. Electron Injection from Colloidal PbS Quantum Dots into Titanium Dioxide Nanoparticles. *ACS Nano* **2008**, *2*, 2206−2212.
(41) Lin, Y.; Bai, Y.; Fang, Y.; Chen, Z.; Yang, S.; Zheng, X.; Tang, S.; Liu, Y.; Zhao, J.; Huang, J. Enhanced Thermal Stability in Perovskite Solar Cells by Assembling 2D/3D Stacking Structures. *J. Phys. Chem. Lett.* **2018**, *9*, 654−658.
(42) Zhao, N.; Osedach, T. P.; Chang, L.-Y.; Geyer, S. M.; Wanger, D.; Binda, M. T.; Arango, A. C.; Bawendi, M. G.; Bulovic, V. Colloidal PbS Quantum Dot Solar Cells with High Fill Factor. *ACS Nano* **2010**, *4*, 3743−3752.
(43) Pradhan, S.; Stavrinadis, A.; Gupta, S.; Bi, Y.; Di Stasio, F.; Konstantatos, G. Trap-State Suppression and Improved Charge Transport in PbS Quantum Dot Solar Cells with Synergistic Mixed-Ligand Treatments. *Small* **2017**, *13*, 1700598.
(44) Ip, A. H.; Thon, S. M.; Hoogland, S.; Voznyy, O.; Zhitomirsky, D.; Debnath, R.; Levina, L.; Rollny, L. R.; Carey, G. H.; Fischer, A.; Kemp, K. W.; Kramer, I. J.; Ning, Z.; Labelle, A. J.; Chou, K. W.; Amassian, A.; Sargent, E. H. Hybrid Passivated Colloidal Quantum Dot Solids. *Nat. Nanotechnol.* **2012**, *7*, 577−582.
(45) Li, Z.; Gao, F.; Greenham, N. C.; McNeill, C. R. Comparison of the Operation of Polymer/Fullerene, Polymer/Polymer, and Polymer/Nanocrystal Solar Cells: A Transient Photocurrent and Photovoltage Study. *Adv. Funct. Mater.* **2011**, *21*, 1419−1431.
(46) Bi, Y.; Pradhan, S.; Gupta, S.; Akgul, M. Z.; Stavrinadis, A.; Konstantatos, G. Infrared Solution-Processed Quantum Dot Solar Cells Reaching External Quantum Efficiency of 80% at 1.35 μm and J(sc) in Excess of 34 mA cm(-2). *Adv. Mater.* **2018**, *30*, 1704928.
(47) Rath, A. K.; Bernechea, M.; Martinez, L.; Konstantatos, G. Solution-Processed Heterojunction Solar Cells Based on p-type PbS Quantum Dots and n-type Bi2S3 Nanocrystals. *Adv. Mater.* **2011**, *23*, 3712−3717.
(48) Rath, A. K.; de Arquer, F. P. G.; Stavrinadis, A.; Lasanta, T.; Bernechea, M.; Diedenhofen, S. L.; Konstantatos, G. Remote Trap Passivation in Colloidal Quantum Dot Bulk Nano-heterojunctions and Its Effect in Solution-Processed Solar Cells. *Adv. Mater.* **2014**, *26*, 4741−4747.

DOI: 10.1021/acsami.8b15469
ACS Appl. Mater. Interfaces 2018, 10, 39074−39082

ACS APPLIED MATERIALS & INTERFACES

Research Article

Cite This: ACS Appl. Mater. Interfaces 2019, 11, 26100−26108

www.acsami.org

Thiol and Halometallate, Mutually Passivated Quantum Dot Ink for Photovoltaic Application

Debranjan Mandal,[†,‡] Prasenjit N. Goswami,[†] and Arup K. Rath*[,†,‡]

[†]CSIR-National Chemical Laboratory, Dr. Homi Bhabha Road, Pune 411008, India

[‡]Academy of Scientific and Innovative Research (AcSIR), Ghaziabad 201002, India

Supporting Information

ABSTRACT: Tunable-band-gap colloidal QDs are a potential building block to harvest the wide-energy solar spectrum. The solution-phase surface passivation with lead halide-based halometallate ligands has remarkably simplified the processing of quantum dots (QDs) and enabled the proficient use of materials for the development of solar cells. It is, however, shown that the hallometalate ligand passivated QD ink allows the formation of thick crystalline shell layer, which limits the carrier transport of the QD solids. Organic thiols have long been used to develop QD solar cells using the solid-state ligand exchange approach. However, their use is limited in solution-phase passivation due to poor dispersity of thiol-treated QDs in common solvents. In this report, a joint passivation strategy using thiol and halometallate ligand is developed to prepare the QD ink. The mutually passivated QDs show a 50% reduction in shell thickness, reduced trap density, and improved monodispersity in their solid films. These improvements lead to a 4 times increase in carrier mobility and doubling of the diffusion length, which enable the carrier extraction from a much thicker absorbing layer. The photovoltaic devices show a high efficiency of 10.3% and reduced hysteresis effect. The improvement in surface passivation leads to reduced oxygen doping and improved ambient stability of the solar cells.

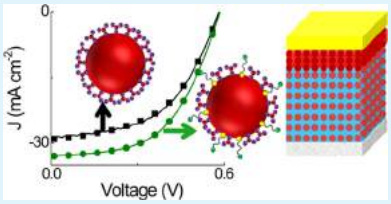

KEYWORDS: *solar cell, quantum dot, surface passivation, ligand, mobility*

INTRODUCTION

The quantum confinement effect of inorganic semiconductors has opened up the renewed possibility for the low-band-gap semiconductors, which were earlier deemed unfit for single-junction solar cell applications.[1,2] Wide material scope, solution-phase processability, and unique optical properties have established quantum dots (QDs) as one of the promising candidates for the low cost, high-efficiency third-generation photovoltaic technology. Lead sulfide (PbS)-based QDs are at the forefront of the QD-based solar cell research due to their wide-band-gap tunability, low-temperature processability, and ambient stability.[3] Since their inception, the performance of PbS solar cells has shown steady improvements, and recently, they have shown an appreciable efficiency of 12.4% in single-junction solar cells.[4−9] Tunable and deep NIR coverage of low-band-gap PbS QDs finds useful application to boost the performance of silicon and perovskite-based solar cell in the tandem configuration.[10−12] The long-perused solid-state layer-by-layer ligand exchange strategy[13−15] has lately been substituted by solution-phase ligand exchange[13,16,17] to develop production compatible QD ink for large-area manufacturing. The ease of processing in solution-phase ligand exchange also facilitates regular arrangement and reduced energy disorder of QDs in solid films to attain record photovoltaic performance.[18]

Due to the aforementioned processing advantages and superior electronic properties, the solution-phase ligand exchange process has gained significant research attention lately.[9,10,16,19,20] In solution-phase ligand exchange, the surfactants are required to passivate the surface states of the QDs; alongside, they should enable the dispersion of QDs in a volatile organic solvent for thin-film deposition. Lead halides in conjugation with different organic and inorganic halide salts (CH_3NH_3I, NH_4I, CsI, and $CH_3CH_2COONH_4$) have been used as surfactants to perform solution-based ligand exchange in dimethylformamide (DMF). In DMF solution, the surfactants dissociate to form $[PbI_3]^-$ and $[X]^+$ (X = CH_3NH_3, NH_4, Cs), where the halometallate anions bind to the unsaturated Pb atoms of the PbS QD and the $[X]^+$ cations form a diffusive layer to provide colloidal stability and charge balance to the QD surface.[18] However, deposition of thick QD film, using spin coating from DMF solution is challenging due to its high boiling point and viscosity. Volatile butylamine (BA) or mix-amine (BA and a small proportion of hexylamine) are used as solvents to deposit thick QD films using spin coating.[9,18] It has been shown recently that BA (or HA) reacts with $[PbI_3]^-$ $[X]^+$ ligands to form thick shell layer on the QD surface.[9,20] In solid films, the QDs are shown to be embedded in the two-dimensional (2D) matrix of BA_2PbI_4 perovskite[9] and Pb−amine complex.[20,21] The matrix layer is shown to form lattice matching solder between the PbS QDs.[19,22] The carrier transport in such QD solids is, however, sensitive to the thickness of the shell layer, from the perspectives of both electronic tunneling and resonance energy transfer. Control

Received: May 1, 2019
Accepted: July 1, 2019
Published: July 1, 2019

Downloaded via NATL CHEMICAL LABORATORY on April 9, 2021 at 07:25:46 (UTC).
See https://pubs.acs.org/sharingguidelines for options on how to legitimately share published articles.

 © 2019 American Chemical Society

DOI: 10.1021/acsami.9b07605
ACS Appl. Mater. Interfaces 2019, 11, 26100−26108

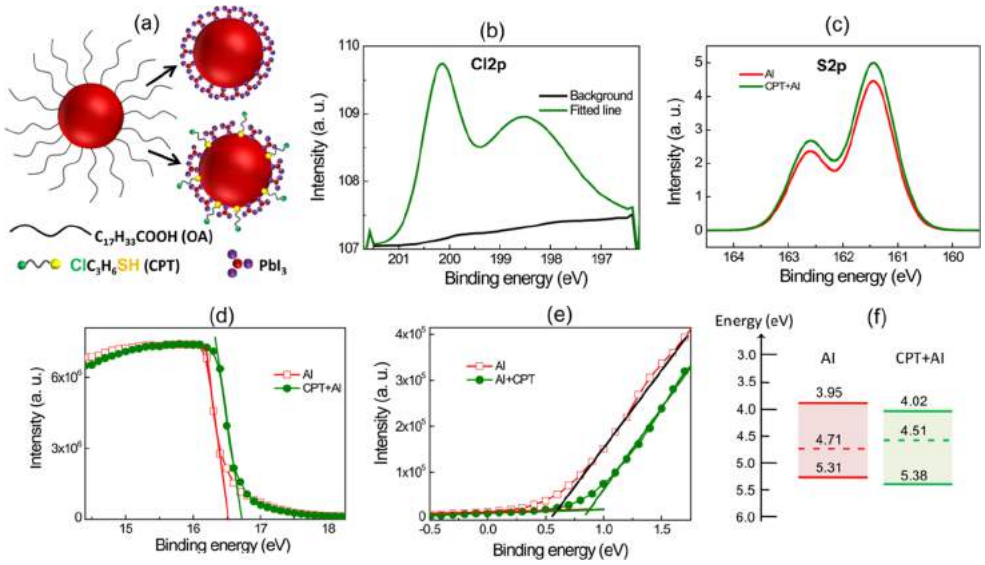

Figure 1. Hybrid passivation and band energy modification of PbS QDs. (a) Schematic representation of oleic acid (OA)-capped, AI- and CPT + AI-treated PbS QD surface. (b) High-resolution XPS image of Cl 2p orbital of CPT + AI-treated PbS QD film. (c) XPS image of S 2p orbital, indicating increase in intensity and broadening of S $2p_{3/2}$ and S $2p_{1/2}$ peaks for CPT + AI-treated QD films. The background signal has been subtracted for the presentation. (d, e) Magnified views of the UPS image to illustrate the secondary cutoff and valance band onset regions, respectively. (f) Energy band positions of PbS QDs for different surface passivation deduced from their UPS and absorption measurements (Figure 2a).

over the matrix growth would be beneficial for the efficient transport of the photocarriers in photovoltaic devices. Recently, use of NH_4I instead of CH_3NH_3I has reduced the shell thickness of PbS QDs, which lead to higher carrier mobility and greater photovoltaic performance.[20] Small-chain organic molecules with thiol as anchoring group have been studied widely to passivate the QD surface and used extensively in layer-by-layer solar cell building.[23,24] A monolayer of thiol molecules can proficiently passivate the QD surface. However, the thin films deposited using the layer-by-layer process suffer from inhomogeneous ligand exchange, QD aggregation, and leftover organic residue, which limit their charge transport.[24] Poor dispersity of small thiol molecule passivated QDs in organic solvents so far renders their use in solution-phase ligand exchange.[25] Mutual passivation of QD surface using thiol and halide ligands have been achieved in the past, using the layer-by-layer approach,[26,27] where dispersity of the QDs was not a concern. Such hybrid passivation enables higher ligand loading on the QD surface, reduces trap states, and improves carrier mobility to boost the solar cell performance.[26−28] Earlier studies on solution-phase ligand exchange use the combination of lead halide and organic salts (CH_3NH_3I, NH_4I, and $CH_3CH_2COONH_4$), but the organic part does not participate directly to passivate the terminal QD surface sites.[9,16,20] Iodine atoms are shown to passivate the unsaturated metal atoms of the QD surface, while the role of the organic part is limited to provide colloidal stability and charge balance to the QD.[29] We envisage that solution-phase hybrid passivation of QDs using halometallate and thiol molecule would be rewarding in providing greater surface coverage to attain cleaner energy band gap QD solids.

Here, we report a hybrid passivation strategy compatible with solution-phase ligand exchange, where the PbS QD surface is passivated mutually by 3-chloro-1-propanethiol (CPT) and lead halide-NH_4I-based halometallate ligand (AI). To the best of our knowledge, this is the first report on the all solution-phase hybrid passivation of QDs using inorganic halometallate and organic thiol molecule. The hybrid passivation gives rise to high solar cell performance of 10.3% under simulated solar illumination. The optical and electronic properties of PbS QDs improved considerably due to increase in monodispersity and reduced electronic trap states in the case of hybrid passivation. The most significant impact of hybrid passivation is realized in matrix shell layer growth, which is reduced by 50%, enabling a four times increase in carrier transport. Improved carrier mobility and reduced trap states allow the efficient collection of photocarriers from a much thicker QD absorber layer, leading to the enhancement in J_{sc} and PCE of the photovoltaic devices. The hybrid passivation also reduces the oxygen doping to the light-absorbing QD layer to improve the stability of the unencapsulated solar cells under ambient operation.

■ RESULTS AND DISCUSSION

The hybrid passivation with CPT and halometallate ligand has been carried out in two steps. In the first step, the as-synthesized oleic acid (OA) passivated PbS QDs are partially ligand-exchanged with CPT (see the Methods section for details). In partial ligand exchange step, some of the OA ligands are replaced by CPT molecules; however, a critical number of OA ligands remain on the QD surface to disperse them in organic nonpolar solvents. The first excitonic peak of OA-capped PbS QD is red-shifted by 10 nm due to CPT partial ligand exchange (Figure S1), indicating a small increase in PbS QD size due to thiol binding. The QDs are then cleaned and taken in octane for halometallate (lead halide and ammonium iodide) ligand treatment, following the earlier report to prepare the QD ink.[20] The particular halometallate ligand treatment is known to form $[PbI_3]^-$ Stern layer on the QD surface, while the cationic component $[NH_4]^+$ forms the diffuse layer to provide the charge balance and colloidal dispersity to the QDs in DMF solvent.[18] The schematic illustration of the QD surfaces, decorated with inorganic

DOI: 10.1021/acsami.9b07605
ACS Appl. Mater. Interfaces 2019, 11, 26100−26108

Table 1. Atomic Ratio of Different Elements for AI- and CPT + AI-Treated PbS QDs from XPS

	atomic ratio (%)						
name of ligand	Cl	O	I	Pb	N	S	C
AI	0	0.899	23.570	35.694	1.416	22.423	15.997
CPT + AI	1.387	0.618	19.588	36.271	0.711	24.005	17.419

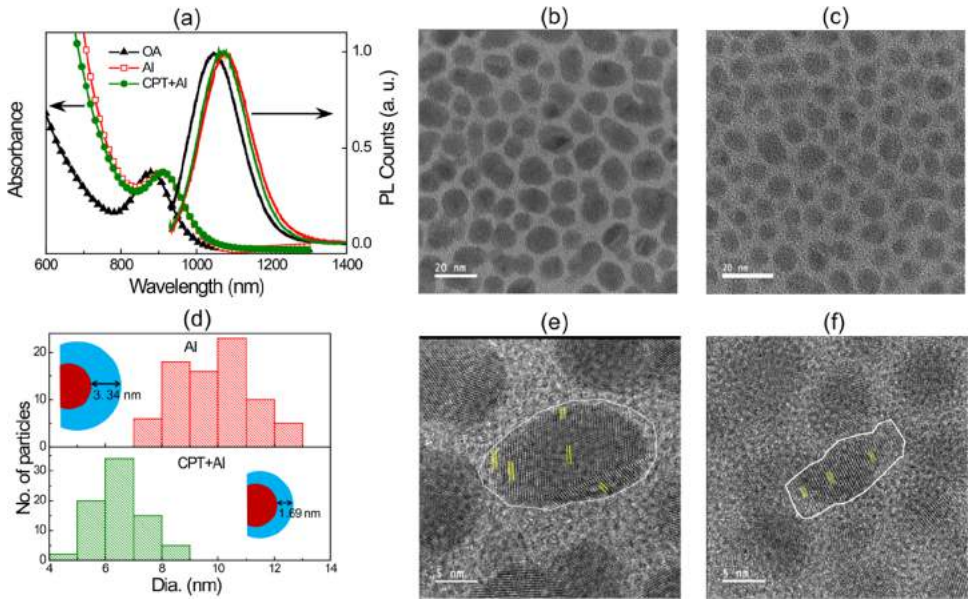

Figure 2. Optical and structural properties of hybrid passivated QDs. (a) Normalized absorption and photoluminescence of PbS QD films treated with different surface ligands. The emission spectra are recorded for the excitation wavelength of 550 nm. Transmission electron microscopy (TEM) images of (b) AI and (c) CPT + AI passivated PbS QDs. (d) Distribution of particle size (PbS core and ligand shell) for different ligand treatments. The average shell thicknesses for the respective ligands are shown in the inset. (e, f) HR-TEM images of AI- and CPT + AI-treated QDs. The ligand shell layer is found to grow quasi-epitaxially on the QD surface.

$[PbI_3]^-$ and hybrid CPT + $[PbI_3]^-$ ligands, is shown in Figure 1a. It is imperative to check whether the CPT passivation survives the halometallate ligand treatment. We carried out X-ray photoelectron spectroscopy (XPS) for the CPT + AI- and only AI-treated PbS QDs. For XPS study, thin films of PbS QDs are deposited from their BA dispersion on Au-coated silicon substrates. The Cl 2p orbital peaks (Cl $2p_{3/2}$ and Cl $2p_{1/2}$) are found in the CPT + AI-treated QD film (Figure 1b), implying the presence of CPT molecule on the QD surface. No Cl 2p peaks are observed in only AI-treated films. Further analysis of the XPS image shows that the atomic contribution (%) of S increases in CPT + AI film, compared to AI-only film (Table 1 and Figure 2c). Deconvolution of S 2p, Pb 4f, and I 3d binding energy spectra for AI- and CPT + AI-treated QDs are shown in Figure S2 of the Supporting Information. With respect to AI-treated PbS film, the full width at half-maximum (FWHM) increases for S $2p_{3/2}$ (0.87−0.89 eV) and S $2p_{1/2}$ (0.85−0.87 eV) binding energies in the case of CPT + AI film. This could be due to the fact that the surface-bound thiol molecules have different binding energies compared to the Pb−S bond of PbS QDs. The attachment of thiol molecule to the undercoordinate surface Pb atoms, therefore, leads to the broadening of the S 2p binding energies. The XPS data clearly suggest that the Pb−thiol bond is robust enough to endure the assault of halometallate ligand treatment. The effect of hybrid passivation is evident in the electronic landscape of the QDs, as observed through the ultraviolet photoelectron spectroscopy (UPS) measurement. The full-range UPS images are shown in Figure S3, and the magnified portions of high- and low-binding-energy regions are shown in Figure 1d,e respectively. The Fermi energy is determined from the high-binding-energy cutoff using the equation[30] (E_F = 21.22 eV − $E_{cut\ off}$), and the difference between the valance band edge and Fermi energy is determined from the low-energy threshold as shown in Figure 1e.[31] The energy band gap for the PbS QDs determined from the first excitonic peak position (Figure 2a) is 1.36 eV.[32] The energy band edges, as determined from UPS and absorbance data for AI- and CPT + AI-treated PbS QDs, are shown for comparison in Figure 1f. It is interesting to note here that the conduction band edge and valence band edge values are deeper by 0.07 eV while the Fermi energy is 0.2 eV shallower in CPT + AI-treated PbS QDs. This may appear to be in contrast to the established knowledge that thiol passivation leads to shallower energy band values and p-type doping, whereas iodine passivation leads to deeper band edge positions and n-type doping to the PbS QDs.[30] A closer look at the XPS data (Table 1) shows that the oxygen content of the AI-treated films is much higher compared to that of CPT + AI-treated QDs, when processed in ambient condition. As oxygen is known as p-type dopant[33−35] to the PbS QDs, the higher oxygen content in AI-treated film may lead to the p-type doping (deep Fermi energy) and shallow band edge values. Further, the UPS measurements for ZnO-electron transport layer and 1,2-ethanedithiol-treated PbS QDs hole transport layer (HTL) are performed to determine their band alignment with the active PbS QD layer (Figure S4). The energy band positions of the constituent layers used in the photovoltaic device fabrication are shown in Figure S5.

DOI: 10.1021/acsami.9b07605
ACS Appl. Mater. Interfaces 2019, 11, 26100−26108

The value added to the QD properties due to mutual passivation is probed by several optical and structural characterization tools. Absorbance and photoluminescence (PL) measurements for AI and CPT + AI passivation are carried out on the thin films of PbS QDs, spin-coated from BA solution, for their resemblance with the solar cells. The as-synthesized OA-capped PbS QD film (formed from octane) is used as the reference. The first excitonic and PL peak intensities for OA, AI, and CPT + AI passivated PbS QD films are normalized for their comparison (Figure 2a and Table 2).

Table 2. Absorbance and Emission Properties of PbS QD Films for Different Surface Passivation

ligand name	1st excitonic peak position (nm)	FWHM [absorbance] (nm)	PL peak position (nm)	FWHM [PL] (nm)	Stokes shift (nm)
OA	874	141	1057	155	183
AI	898	158	1080	155	182
CPT + AI	902	149	1072	150	170

The absorbance and PL peaks are fitted with Gaussian-type fitting to determine their full width at half-maxima (FWHM). With respect to AI passivation, hybrid passivation reduces the FWHM of absorbance (9 nm) and PL (5 nm) peaks. Further, the Stokes shift is minimum in the case of CPT + AI-treated QDs. Narrow absorbance and emission peak, and less Stokes shift suggest higher monodispersity of PbS QDs in the case of CPT + AI ligand passivation.[32] In DMF solution, the relative emission intensity of the CPT + AI-treated QD is 3 times higher than that of AI-treated QDs (Figure S6), for the fixed QD concentration. Increase in monodispersity and PL intensity implies superior QD surface properties in the case of hybrid passivation.

It is shown that the halometallate-treated PbS QDs spin-coated from volatile BA form a crystalline matrix in their solid films where the matrix layer consists of 2D BA_2PbI_4 perovskite[9] and 2D Pb−amine complex.[20] To probe the matrix layer, the ligand solution (one molar solution of PbI_2 and NH_4I in BA solvent) is spin-coated on glass substrates for the formation of the matrix layer. The XRD spectrum of the ligand film shows two sets of equidistant peaks with 2θ repetition of 4.99 and 6.26°, pertaining to 2D Pb−amine complex and 2D BA_2PbI_4 perovskite, respectively, as reported earlier (Figure S7).[20] The absorption characteristic of the ligand film shows the first excitonic peak at 465 nm and a narrow band edge emission peak centered at 515 nm, which further supports the formation of the BA_2PbI_4 perovskite phase (Figure S8).[9,20] The full wavelength range absorption characteristic of PbS QD films for different ligand passivation (the magnified view is shown in Figure 2a) is shown in Figure S9. In addition to the PbS excitonic peak (∼910 nm), a broad hump centered around 500 nm is observed due to the perovskite shell formation, in AI- and CPT + AI-treated QD films. The broadening and the red shift in perovskite hump are attributed to the strong coupling and interfacial strain of perovskite shell with the PbS QD core.[20] The high-band-gap shell layer (∼2.1 eV) forms type-I band alignment with the core PbS QD (∼1.36 eV). Hence, a thicker shell layer is likely to deter the carrier transport in solid films.[20] The transmission electron microscopy (TEM) images of the PbS QDs treated with AI and CPT + AI are shown in Figure 2b,c respectively. The average diameter of PbS QD plus the crystalline ligand shell in the case of AI ligand is 9.8 nm, and for CPT + AI, it is 6.5 nm. The distribution of the size for the core−shell particles (PbS QD core and ligand shell) is shown in Figure 2d. The average diameter of the as-synthesized OA-capped PbS QDs, observed from the TEM data, is 3 nm (Figure S10a). The absorption data (Figure 2a)

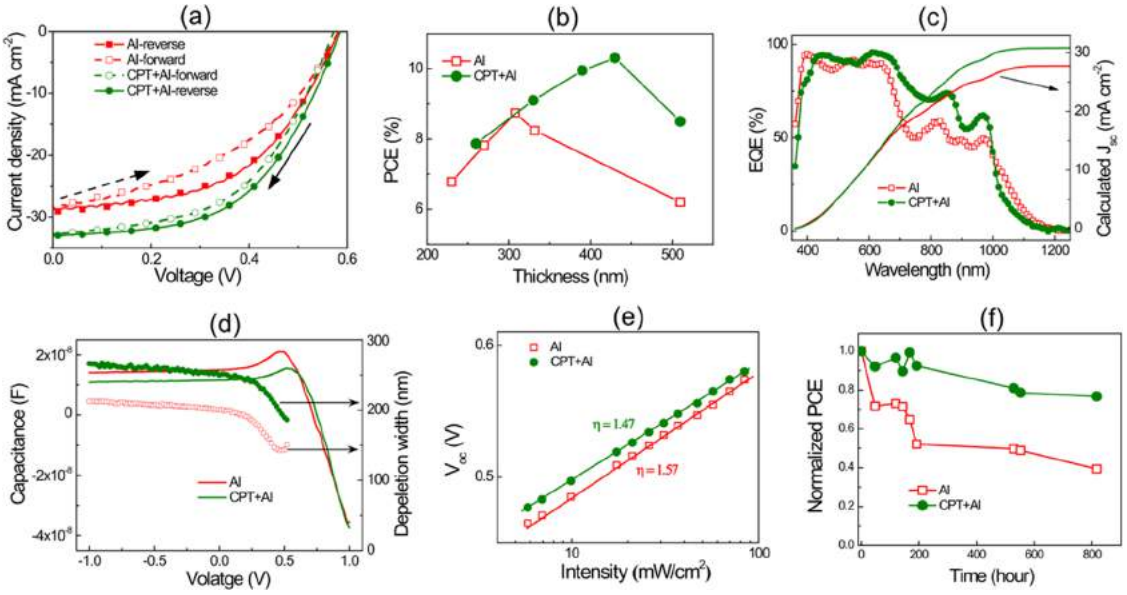

Figure 3. Solar cell characteristics. (a) Reverse and forward scan J−V characteristics (scan rate, 0.1 V s^{-1}) for AI- and CPT + AI-treated solar cells under AM1.5 simulated solar illumination. (b) Evolution of PCE of the solar cells with absorber layer thickness for different ligands. (c) EQE (%) of the solar cells. The right-hand-side axis indicates the predicted J_{sc} under simulated solar illumination, from the EQE spectra. (d) Capacitance−voltage characteristics of the solar cells measured at 1 kHz at a scan rate of 0.1 V s^{-1}. The depletion widths for the respective solar cells (right-hand-side axis) at different voltages are shown. (e) Change of V_{oc} at various light intensities (ϕ). From the slope of the V_{oc} vs ln(ϕ) plot, the diode ideality factor (η) is determined for the solar cells. (f) Stability data for the unencapsulated solar cells stored in Argon glovebox and measured at different time intervals in ambient air.

DOI: 10.1021/acsami.9b07605
ACS Appl. Mater. Interfaces 2019, 11, 26100−26108

suggest that the excitonic peak of OA-capped PbS QDs red-shifts by ~25 nm when treated with AI or CPT + AI ligands. The red shift could be due to diffusion of Pb and S atoms during the ligand exchange process. The absorbance red shift would account to approximately 0.12 nm increases in QD diameter due to the quantum confinement effect. Therefore, the excess increase in diameter in the case of AI- and CPT + AI-treated QDs as observed in the TEM images is attributed to the thickness of the ligand shell. The situation is depicted schematically in the inset of Figure 2d, where the respective shell thicknesses for AI (3.34 nm) and CPT + AI (1.69 nm) are marked. The scanning electron microscopy (SEM) images show that the thick shell layer in the case of Al-treated QD film leads to the formation of nanostructures at their surface, whereas the hybrid passivated films are smoother and free from such nanostructure formation (Figure S11). Bigger grains are also observed in the AFM image of AI-treated QD film (Figure S12). As a result, the average roughness in AI-treated film (15 nm) is much higher than that in CPT + AI-treated (5 nm) QD film. The HRTEM images show the crystal fringes for AI- and CPT + AI-treated PbS QDs (Figure 2e,f respectively). The interplanar spacing in both cases is found to be 3.15 ± 0.03 Å. The *d*-spacing of the only ligand matrix as observed from the HRTEM image (Figure S13) matches identically with the *d*-spacing spacing of AI- and CPT + AI-treated PbS QDs. Further, the *d*-spacing of PbS (111) plane is 3.40 Å (Figure S10b), which comes close to the interplanar spacing of the matrix layer, which may enable the quasi-epitaxial growth of the shell layer on the PbS QD surface. TEM study clearly suggests that in the case of mutual passivation, the shell thickness is reduced by 50%. This could be due to the fact that addition of CPT ligand reduces the nucleation centers ($[PbI_3]^-$) and increases inhomogeneity at the QD surface, which deters the growth of thick perovskite shell layer. It is envisaged that the thinner shell layer would decrease the interdot distances and benefit the carrier transport, in mutually passivated films.

The solar cells are fabricated with the following device structure: ITO/ZnO (ETL-100 nm)/PbS-CPT + AI (/AI)/PbS-EDT (HTL-60 nm)/MoO_3 (8 nm)/Au (30 nm)/Ag (100 nm). The cross-sectional image of a typical solar cell, indicating all of the layers, is shown in Figure S14. The effect of shell thickness is readily evident in the performance of the solar cells. The solar cell made of CPT + AI-treated QDs shows lower hysteresis and higher J_{sc} in their $J-V$ characteristics (Figure 3a). The statistical variation of photovoltaic parameters, for different batches of solar cells, shows a clear improvement in PCE in the case of hybrid passivation (Figure S15). Photovoltaic parameters for the representative optimized solar cells for AI and CPT + AI passivation are shown in Table 3 for their comparison. The thickness-dependent $J-V$ curves for AI- and CPT + AI-treated solar cells are given in Figure S16. The optimum thicknesses of the PbS QD layer for CPT + AI and AI passivations are found to be 430 and 310 nm, respectively (Figure 3b). Higher absorber layer thickness in the case of CPT + AI-treated solar cells leads to the increase in J_{sc} without significant reduction in the FF. The external quantum efficiency (EQE (%)) data clearly indicate the enhancement in the NIR photoconversion efficiency (Figure 3c). The calculated J_{sc} from the EQE spectrum (shown in the right axis of Figure 3c) for the respective solar cells matches closely with their experimentally measured J_{sc} under simulated solar illumination. Carrier depletion width is determined from the capacitance−voltage characteristics, measured in the dark (Figure 3d). The CPT + AI-treated solar cell shows depletion widths of 250 and 230 nm, respectively, at zero bias and maximum power point in comparison to 200 and 180 nm for AI-treated solar cells. Higher depletion width facilitates the efficient carrier collection from thicker QD layer in the case of CPT + AI-treated solar cells. Diode ideality factors for the solar cells are determined using the intensity-dependent generation of V_{oc}, using the equation[36] $V_{oc} = \frac{\eta KT}{q} \ln(\phi)$, where η is the diode ideality factor, K is the Boltzmann constant, T is the temperature, q is the electronic charge, and ϕ is the photon flux. Lower η value implies lesser trap recombination in CPT + AI-treated solar cells (Figure 3e).[37] The stability of the AI- and CPT + AI-treated solar cells is further studied, in unencapsulated devices, at different time intervals. The solar cells are exposed to ambient condition for the performance testing, otherwise stored in an Ar glovebox. After 800 h, the CPT + AI-treated solar cells retain 80%, when AI passivation loses 50% of their initial performance (Figure 3f).

It is envisaged that the reduced shell thickness would impact favorably on the carrier transport properties of the QD solid. Charge carrier mobility is determined using the photoinduced carrier extraction by linearly increasing voltage (photo-CELIV) technique, for solar cell devices.[23,38] Initially, a short light pulse is applied to the solar cell to create free photocarriers. After a time delay of a few microseconds, a linearly increasing voltage pulse with a suitable voltage ramp is applied in reverse bias to extract the free carriers from the solar cell (details of photo-CELIV measurement are given in the Experimental Section in the Supporting Information). The evolution of current under the influence of linearly increasing voltage pulse for AI- and CPT + AI-treated PbS QD solar cells is shown in Figure 4a and 4b, respectively. Charge carrier mobility is estimated using the equation[38] $\mu_h = \frac{2d^2}{3At_{max}^2\left(1 + 0.36\frac{\Delta J}{J_d}\right)}$, where A is the voltage ramp rate, t_{max} is the time for the transient current signal to reach its maximum value, ΔJ is the maximum drift current, J_d is the displacement current, and d is the PbS QD layer thickness. The QD layer thicknesses of 420 and 593 nm are used for AI and CPT + AI, respectively, for the photo-CELIV study. The carrier mobilities for AI- and CPT + AI-treated solar cells are found to be 1.10×10^{-3} and 4.38×10^{-3} cm^{-2} V^{-1} s^{-1}, respectively, indicating 4 times increase in carrier mobility in hybrid passivated QD solid. Higher shell thickness as observed in TEM images is further corroborated by the XPS results. The atomic ratio of N (and I), which constitutes the shell layer, is found to be higher in the case of AI-treated QDs (Table 2 and Figure 4c). The average shell thickness of CPT + AI-treated QDs (1.69 nm) is 50% lower than that of AI-treated QDs (3.34 nm), which leads to 4 times increase in carrier mobility in the hybrid passivated QDs. The carrier extraction depth in solar cells is controlled by the product of carrier mobility and

Table 3. Photovoltaic Parameters for Optimized Solar Cells

name of the ligand	scan direction	J_{sc} (mA cm^{-2})	V_{oc} (V)	FF (%)	PCE (%)
AI	reverse	28.43	0.58	53.06	8.74
	forward	28.4	0.58	43.01	7.08
CPT + AI	reverse	32.94	0.59	53.07	10.31
	forward	32.68	0.57	52.06	9.71

DOI: 10.1021/acsami.9b07605
ACS Appl. Mater. Interfaces 2019, 11, 26100−26108

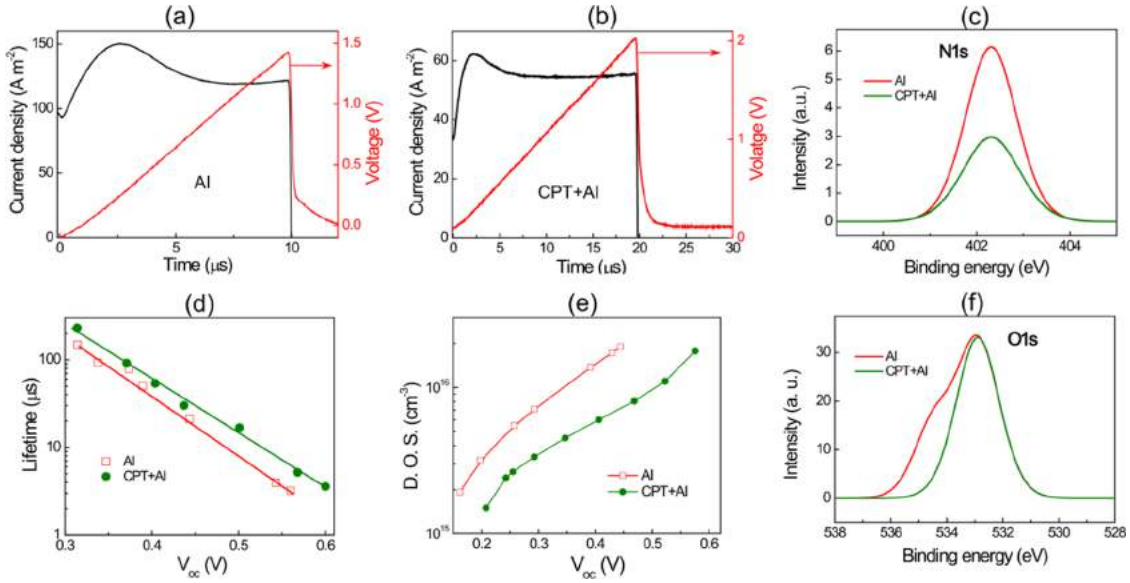

Figure 4. Photocarrier dynamics of the solar cells. Photo-CELIV measurement of (a) AI- and (b) CPT + AI-treated solar cells. The evolution of solar cell current under the influence of linearly increasing voltage pulse is shown. (c) High-resolution XPS image of N1s orbital for AI- and CPT + AI-treated PbS QD films. (d) Photocarrier lifetime and (e) density of trap states at different V_{oc} values. (f) High-resolution XPS image of O 1s orbital for different ligand-treated PbS QD films.

lifetime. We cared to measure the photocarrier lifetime using transient photovoltage measurement at different light biases.[23,34] The carrier lifetime in the case of CPT + AI is found to be marginally higher than AI-treated solar cells at all open-circuit voltages (Figure 4d). At full solar illumination, the carrier diffusion lengths for AI and CPT + AI solar cells are estimated to be 95 and 200 nm, respectively, from the carrier mobility and lifetime values.[23] The density of trap state is further determined using the transient photovoltage and transient photocurrent measurements, as reported earlier (details in Figure S17 of the Supporting Information).[20,26,39] The density of trap states at any given V_{oc} is found to be lower in CPT + AI-treated devices. Lower trap density and thinner shell layer would jointly result in higher carrier mobility and lifetime values for the mutually passivated QDs. Oxygen is known to form intermediate trap states inside the band gap of PbS QDs.[40,41] The comparison of high-resolution O 1s XPS image shows one peak for CPT + AI and two peaks for AI-treated PbS QDs. The peak at 532.5 eV is attributed to the hydroxyl peak (Pb−OH), which is commonly present at the PbS(111) surface;[42] however, the peak at higher energy (534.1 eV) is attributed to the oxygen adsorption (in the form of COO− and CO_2) at the QD surface.[31] This excess oxygen doping in AI-treated QDs would likely be the reason for their higher trap density (Figure 4e) and deeper Fermi energy (Figure 1f). From the above results, it can be inferred that some of the surface sites of PbS QDs are left unpassivated by the halometallate ligands, which are vulnerable to the oxygen attack. The implementation of mutual passivation covers the surface sites more efficiently to protect the QDs from oxidation and improve their size selectivity in solid films. Further, the mutual passivation leads to the formation of trap deprived QD solids with high carrier mobility, which helps to reduce recombination and enhance carrier collection to increase the solar cell performance.

■ CONCLUSIONS

In summary, a hybrid passivation scheme has been commenced to decorate the PbS QD surface with thiol and halometallate ligands. The passivation strategy is compatible with solution-phase ligand exchange process and allows developing quantum dot ink for the one-step deposition of thick and conducting QD film. Advancement in surface engineering enables higher monodispersity and lower trap density in QD solids. Mutually passivated QDs show lower shell growth and reduced oxygen doping, which help to attain 4 times increase in carrier mobility, doubles the diffusion length, and produces cleaner energy band gap in solid films. As a result, the photovoltaic devices show higher PCE% and lower hysteresis in their $J-V$ characteristics. Thiol passivation is particularly useful to passivate the surface sites, which are otherwise inaccessible to hallometalate ligands to improve resilience toward oxygen attack and prolong the lifetime of the solar cells. We envisage that the developed mutual passivation strategy can be extended to other organic and inorganic ligand combinations as well and would be beneficial for the development of QD-based optoelectronic devices like light-emitting diodes and tandem solar cells.

■ METHODS

Chemicals. PbO (99%), oleic acid (90%), octadecene (90%), bis(trimethylsilyl)sulfide $(TMS)_2S$, lead iodide (99%), lead bromide (99%), ammonium iodide (99%), 1,2-ethanedithiol (EDT) (98%, GC), 3-chloro-1-propanethiol (CPT) (98%), zinc acetate dihydrate, butylamine (99.5%), and potassium hydroxide are procured from Sigma-Aldrich. Dry toluene, methanol, octane, acetone, and dimethylformamide are purchased from Sigma-Aldrich.

Partial Ligand Exchange with CPT. Oleic acid-capped PbS QDs are synthesized by a previously reported method.[20] The as-synthesized QDs solution is transferred to a glovebox without any cleaning step being performed. CPT (1 mmol) in 2.5 mL of ODE is injected into the PbS QDs solution and stirred for half an hour at 70 °C. Then, the mixture is allowed to settle to room temperature and cleaned two times by acetone precipitation and toluene dispersion.

DOI: 10.1021/acsami.9b07605
ACS Appl. Mater. Interfaces 2019, 11, 26100−26108

Finally, CPT-treated PbS QDs are dispersed in octane for halometallate ligand exchange.

Halometallate Ligand Exchange of PbS QDs.[20] In 5 mL of DMF, 0.1 M NH_4I, 0.075 M PbI_2, and 0.025 M $PbBr_2$ are mixed to get a clear transparent yellow solution. PbS QDS (5 mL, 15 mg/mL) are added with DMF ligand precursor and mixed vigorously for 2 min. Within 2 min, PbS QDs are transferred from octane to DMF phase. Top octane layer is discarded and the DMF phase is cleaned further two times by addition of octane. The ligand exchange QDs are precipitated by toluene addition and collected by centrifugation. The QDs are then dried under vacuum for 20 min and finally dispersed in BA (250 mg/mL) for film deposition. The aforementioned procedure is followed to treat the CPT-treated QDs for mutual passivation and OA-capped QDs for only halometallate passivation.

Device Fabrication. Presynthesized ZnO NCs[20] are deposited on top of cleaned ITO by spin coating at 3000 rpm and the substrates are heated around 250 °C for 40 min. On top of ZnO substrate, the QDs ink is spin-coated. The films were then transferred to a glovebox to anneal at 70 °C for 15 min. By changing acceleration and rotation speed, device thickness is varied from 160 to 500 nm. The hole transport layer (60 nm) is deposited using 1,2-ethanedithiol (EDT)-treated PbS QDs following the reported layer-by-layer method. To complete the device fabrication, electrode deposition is carried out by a thermal evaporator (HHV BC-300) at the base pressure of 1×10^{-6} Torr, and 8 nm of MoO_3, 30 nm of Au, and 100 nm of Ag are deposited sequentially.

Device Characterization. All of the electrical characterizations are carried out in ambient condition at laboratory condition.

***J*−*V* Characterization.** Current−voltage measurements are carried out with a Keithley 2634B sourcemeter under a solar simulator (PEC-L01). The solar intensity is set to AM1.5G using a Thorlab thermal detector (S302C). Intensity-dependent *I*−*V* measurements are carried out by changing the solar intensity using different neutral density filters.

EQE Measurement. External quantum efficiency is measured by directing the cell under monochromatic illumination. Monochramator (SLS-M266) contains power Arc high-intensity 75 W Xe light source and suitable cutoff filters. Monochramator light intensity is measured by Thorlabs photodiode detectors S120VC (in the wavelength range of 300−1100 nm) and S122C (700−1800 nm). The response of the solar cells is recorded by a Keithley 2634B sourcemeter.

Capacitance−*V* Measurement. Cap−*V* measurements are performed by a PSM1735 (N4L) LCR meter. The measurement is performed at a frequency of 1 kHz and an ac perturbation voltage of 50 mV.

Transient Photovoltage (TPV) and Transient Photocurrent (TPC) Measurement. A diode laser of 658 nm (Newport LQA658-30C) modulated through a function generator (Tektronics, AFG 3021C) is used to generate short light pulses. A solar simulator (Peccell, PEC-L01) is used to provide light bias to the solar cells. Different V_{oc} values are attained by varying the intensity of the light bias. For TPV measurement, the device is connected to the oscilloscope (Tektronics, MDO 3104) through 1 MΩ resistance. Laser pulse intensities are modulated to keep the perturbation voltage below 10 mV. For TPC measurements, the laser pulse is kept the same as used for TPV measurement, while the output resistance is changed to 50 Ω.

Photo-CELIV Measurement. A function generator (Tektronics, AFG 3021C) is used to generate voltage pulses of suitable ramp and also to generate light pulses by triggering the 658 nm diode laser (Newport LQA658-30C). The short light pulses of 500 ns are applied to the solar cells to generate photocarriers. A suitable time delay (2−5 μs) is maintained between laser pulse and voltage ramp. The voltage ramp is applied in the reverse bias condition. A digital oscilloscope (Tektronics, MDO 3104) is used to record the applied voltage ramp and the corresponding current evolution data. To measure the current evolution, output resistance is set to 50 Ω.

Materials Characterization. Optical absorption measurements are carried out by a Shimadzu UV−vis−IR (UV-3600 Plus) spectrophotometer. Thin-film absorption is measured using a integrating sphere (ISR-603), attached to a Shimadzu UV-3600 plus spectrophotometer. Steady-state photoluminescence measurements are performed utilizing Spectroflurometer FS5 (Edinburgh Instruments). XPS is carried out using the Thermo Scientific K-Alpha$^+$ spectrometer in ultrahigh vacuum condition (10^{-9} mbar). XPS measurements are performed with a monochromatic Al Kα X-ray source (1486.6 eV) with pass energy 50 eV for individual core levels. The XPS images are calibrated to the C 1s peak at a binding energy of 284.8 eV. The fitting of the XPS images is performed by Casa XPS software. All of the measurements were carried out using electron flood gun source for surface charge neutralization. UPS measurement is also carried out by the same instrument. He-Iα radiation of energy 21.22 eV is used for the UPS measurement. Cross-sectional and surface images of device are taken by a field emission scanning electron microscope (NNS 450). High-resolution images of QDs are captured by a high-resolution transmitted electron microscope (JEOL JEM 2200FES).

■ ASSOCIATED CONTENT

Supporting Information

The Supporting Information is available free of charge on the ACS Publications website at DOI: 10.1021/acsami.9b07605.

Experimental section; additional absorption; PL, UPS, TEM, SEM, and *I*−*V* data (PDF)

■ AUTHOR INFORMATION

Corresponding Author

*E-mail: ak.rath@ncl.res.in.

ORCID

Arup K. Rath: 0000-0003-2261-7215

Notes

The authors declare no competing financial interest.

■ ACKNOWLEDGMENTS

The authors acknowledge the financial assistance from the SERB extramural funding, India (Project code: EMR/2015/002415), and DST Nanomission, India (Project code: SR/NM/NT-1011/2105 (G)). D.M. acknowledges the CSIR fellowship 31/11(1036)/2018 EMR I for the support.

■ REFERENCES

(1) Carey, G. H.; Abdelhady, A. L.; Ning, Z. J.; Thon, S. M.; Bakr, O. M.; Sargent, E. H. Colloidal Quantum Dot Solar Cells. *Chem. Rev.* **2015**, *115*, 12732−12763.

(2) Yuan, M. J.; Liu, M. X.; Sargent, E. H. Colloidal Quantum Dot Solids for Solution-Processed Solar Cells. *Nat. Energy* **2016**, *1*, No. 16016.

(3) Kramer, I. J.; Sargent, E. H. The Architecture of Colloidal Quantum Dot Solar Cells: Materials to Devices. *Chem. Rev.* **2014**, *114*, 863−882.

(4) McDonald, S. A.; Konstantatos, G.; Zhang, S. G.; Cyr, P. W.; Klem, E. J. D.; Levina, L.; Sargent, E. H. Solution-Processed PbS Quantum Dot Infrared Photodetectors and Photovoltaics. *Nat. Mater.* **2005**, *4*, 138−142.

(5) Luther, J. M.; Gao, J. B.; Lloyd, M. T.; Semonin, O. E.; Beard, M. C.; Nozik, A. J. Stability Assessment on a 3% Bilayer PbS/ZnO Quantum Dot Heterojunction Solar Cell. *Adv. Mater.* **2010**, *22*, 3704−3707.

(6) Rath, A. K.; Bernechea, M.; Martinez, L.; de Arquer, F. P. G.; Osmond, J.; Konstantatos, G. Solution-Processed Inorganic Bulk Nano-Heterojunctions and Their Application to Solar Cells. *Nat. Photonics* **2012**, *6*, 529−534.

(7) Chuang, C. H.; Brown, P. R.; Bulovic, V.; Bawendi, M. G. Improved Performance and Stability in Quantum Dot Solar Cells

DOI: 10.1021/acsami.9b07605
ACS Appl. Mater. Interfaces 2019, 11, 26100−26108

Through Band Alignment Engineering. *Nat. Mater.* **2014**, *13*, 796−801.
(8) Lan, X. Z.; Voznyy, O.; de Arquer, F. P. G.; Liu, M. X.; Xu, J. X.; Proppe, A. H.; Walters, G.; Fan, F. J.; Tan, H. R.; Liu, M.; Yang, Z. Y.; Hoogland, S.; Sargent, E. H. 10.6% Certified Colloidal Quantum Dot Solar Cells via Solvent Polarity-Engineered Halide Passivation. *Nano Lett.* **2016**, *16*, 4630−4634.
(9) Xu, J. X.; Voznyy, O.; Liu, M. X.; Kirmani, A. R.; Walters, G.; Munir, R.; Abdelsamie, M.; Proppe, A. H.; Sarkar, A.; de Arquer, F. P. G.; Wei, M. Y.; Sun, B.; Liu, M.; Ouellette, O.; Quintero-Bermudez, R.; Li, J.; Fan, J.; Quan, L. N.; Todorovic, P.; Tan, H. R.; Hoogland, S.; Kelley, S. O.; Stefik, M.; Amassian, A.; Sargent, E. H. 2D Matrix Engineering for Homogeneous Quantum Dot Coupling in Photovoltaic Solids. *Nat. Nanotechnol.* **2018**, *13*, 456−462.
(10) Kim, T.; Firdaus, Y.; Kirmani, A. R.; Liang, R. Z.; Hu, H. L.; Liu, M. X.; El Labban, A.; Hoogland, S.; Beaujuge, P. M.; Sargent, E. H.; Amassian, A. Hybrid Tandem Quantum Dot/Organic Solar Cells with Enhanced Photocurrent and Efficiency via Ink and Interlayer Engineering. *ACS Energy Lett.* **2018**, *3*, 1307−1314.
(11) Karani, A.; Yang, L.; Bai, S.; Futscher, M. H.; Snaith, H. J.; Ehrler, B.; Greenham, N. C.; Di, D. W. Perovskite/Colloidal Quantum Dot Tandem Solar Cells: Theoretical Modeling and Monolithic Structure. *ACS Energy Lett.* **2018**, *3*, 869−874.
(12) Bi, Y.; Pradhan, S.; Gupta, S.; Akgul, M. Z.; Stavrinadis, A.; Konstantatos, G. Infrared Solution-Processed Quantum Dot Solar Cells Reaching External Quantum Efficiency of 80% at 1.35 mu m and J(sc) in Excess of 34 mA cm(-2). *Adv. Mater.* **2018**, *30*, No. 1704928.
(13) Kagan, C. R.; Lifshitz, E.; Sargent, E. H.; Talapin, D. V. Building Devices From Colloidal Quantum Dots. *Science* **2016**, *353*, No. aac5523.
(14) Lu, K. Y.; Wang, Y. J.; Liu, Z. K.; Han, L.; Shi, G. Z.; Fang, H. H.; Chen, J.; Ye, X. C.; Chen, S.; Yang, F.; Shulga, A. G.; Wu, T.; Gu, M. F.; Zhou, S. J.; Fan, J.; Loi, M. A.; Ma, W. L. High-Efficiency PbS Quantum-Dot Solar Cells with Greatly Simplified Fabrication Processing via "Solvent-Curing". *Adv. Mater.* **2018**, *30*, No. 1707572.
(15) Zhang, X. L.; Johansson, E. M. J. Reduction of Charge Recombination in PbS Colloidal Quantum Dot Solar Cells at the Quantum Dot/ZnO Interface by Inserting a MgZnO Buffer Layer. *J. Mater. Chem. A* **2017**, *5*, 303−310.
(16) Yang, Z.; Janmohamed, A.; Lan, X. Z.; de Arquer, F. P. G.; Voznyy, O.; Yassitepe, E.; Kim, G. H.; Ning, Z. J.; Gong, X. W.; Comin, R.; Sargent, E. H. Colloidal Quantum Dot Photovoltaics Enhanced by Perovskite Shelling. *Nano Lett.* **2015**, *15*, 7539−7543.
(17) Zhang, X. L.; Oberg, V. A.; Du, J.; Liua, J. H.; Johansson, E. M. J. Extremely Lightweight and Ultra-Flexible Infrared Light-Converting Quantum Dot Solar Cells With High Power-Per-Weight Output Using a Solution-Processed Bending Durable Silver Nanowire-Based Electrode. *Energy Environ. Sci.* **2018**, *11*, 354−364.
(18) Liu, M.; Voznyy, O.; Sabatini, R.; de Arquer, F. P. G.; Munir, R.; Balawi, A. H.; Lan, X. Z.; Fan, F. J.; Walters, G.; Kirmani, A. R.; Hoogland, S.; Laquai, F.; Amassian, A.; Sargent, E. H. Hybrid Organic-Inorganic Inks Flatten the Energy Landscape in Colloidal Quantum Dot Solids. *Nat. Mater.* **2017**, *16*, 258−263.
(19) Zhang, X. L.; Zhang, J. D.; Phuyal, D.; Du, J.; Tian, L.; Oberg, V. A.; Johansson, M. B.; Cappel, U. B.; Karis, O.; Liu, J. H.; Rensmo, H.; Boschloo, G.; Johansson, E. M. J. Inorganic CsPbI3 Perovskite Coating on PbS Quantum Dot for Highly Efficient and Stable Infrared Light Converting Solar Cells. *Adv. Energy Mater.* **2018**, *8*, No. 1702049.
(20) Mandal, D.; Rath, A. K. Quantum Dots Coupled to an Oriented Two-Dimensional Crystalline Matrix for Solar Cell Application. *ACS Appl. Mater. Interfaces* **2018**, *10*, 39074−39082.
(21) Yang, Z. Y.; Voznyy, O.; Walters, G.; Fan, J. Z.; Liu, M.; Kinge, S.; Hoogland, S.; Sargent, E. H. Quantum Dots in Two-Dimensional Perovskite Matrices for Efficient Near-Infrared Light Emission. *ACS Photonics* **2017**, *4*, 830−836.
(22) Ning, Z. J.; Gong, X. W.; Comin, R.; Walters, G.; Fan, F. J.; Voznyy, O.; Yassitepe, E.; Buin, A.; Hoogland, S.; Sargent, E. H. Quantum-dot-in-perovskite solids. *Nature* **2015**, *523*, 324−328.
(23) Goswami, P. N.; Mandal, D.; Rath, A. K. The Role of Surface Ligands in Determining the Electronic Properties of Quantum Dot Solids and Their Impact on Photovoltaic Figure of Merits. *Nanoscale* **2018**, *10*, 1072−1080.
(24) Tang, J. A.; Sargent, E. H. Infrared Colloidal Quantum Dots for Photovoltaics: Fundamentals and Recent Progress. *Adv. Mater.* **2011**, *23*, 12−29.
(25) Fischer, A.; Rollny, L.; Pan, J.; Carey, G. H.; Thon, S. M.; Hoogland, S.; Voznyy, O.; Zhitomirsky, D.; Kim, J. Y.; Bakr, O. M.; Sargent, E. H. Directly Deposited Quantum Dot Solids Using a Colloidally Stable Nanoparticle Ink. *Adv. Mater.* **2013**, *25*, 5742−5749.
(26) Ip, A. H.; Thon, S. M.; Hoogland, S.; Voznyy, O.; Zhitomirsky, D.; Debnath, R.; Levina, L.; Rollny, L. R.; Carey, G. H.; Fischer, A.; Kemp, K. W.; Kramer, I. J.; Ning, Z. J.; Labelle, A. J.; Chou, K. W.; Amassian, A.; Sargent, E. H. Hybrid Passivated Colloidal Quantum Dot Solids. *Nat. Nanotechnol.* **2012**, *7*, 577−582.
(27) Pradhan, S.; Stavrinadis, A.; Gupta, S.; Bi, Y.; Di Stasio, F.; Konstantatos, G. Trap-State Suppression and Improved Charge Transport in PbS Quantum Dot Solar Cells with Synergistic Mixed-Ligand Treatments. *Small* **2017**, *13*, No. 1700598.
(28) Hong, J.; Hou, B.; Lim, J.; Pak, S.; Kim, B. S.; Cho, Y.; Lee, J.; Lee, Y. W.; Giraud, P.; Lee, S.; Park, J. B.; Morris, S. M.; Snaith, H. J.; Sohn, J. I.; Cha, S.; Kim, J. M. Enhanced Charge Carrier Transport Properties in Colloidal Quantum Dot Solar Cells via Organic and Inorganic Hybrid Surface Passivation. *J. Mater. Chem. A* **2016**, *4*, 18769−18775.
(29) Dirin, D. N.; Dreyfuss, S.; Bodnarchuk, M. I.; Nedelcu, G.; Papagiorgis, P.; Itskos, G.; Kovalenko, M. V. Lead Halide Perovskites and Other Metal Halide Complexes As Inorganic Capping Ligands for Colloidal Nanocrystals. *J. Am. Chem. Soc.* **2014**, *136*, 6550−6553.
(30) Brown, P. R.; Kim, D.; Lunt, R. R.; Zhao, N.; Bawendi, M. G.; Grossman, J. C.; Bulovic, V. Energy Level Modification in Lead Sulfide Quantum Dot Thin Films through Ligand Exchange. *ACS Nano* **2014**, *8*, 5863−5872.
(31) Cao, Y. M.; Stavrinadis, A.; Lasanta, T.; So, D.; Konstantatos, G. The Role of Surface Passivation for Efficient and Photostable PbS Quantum Dot Solar Cells. *Nat. Energy* **2016**, *1*, No. 16035.
(32) Moreels, I.; Lambert, K.; Smeets, D.; De Muynck, D.; Nollet, T.; Martins, J. C.; Vanhaecke, F.; Vantomme, A.; Delerue, C.; Allan, G.; Hens, Z. Size-Dependent Optical Properties of Colloidal PbS Quantum Dots. *ACS Nano* **2009**, *3*, 3023−3030.
(33) Yuan, M. J.; Zhitomirsky, D.; Adinolfi, V.; Voznyy, O.; Kemp, K. W.; Ning, Z. J.; Lan, X. Z.; Xu, J. X.; Kim, J. Y.; Dong, H. P.; Sargent, E. H. Doping Control Via Molecularly Engineered Surface Ligand Coordination. *Adv. Mater.* **2013**, *25*, 5586−5592.
(34) Zhao, N.; Osedach, T. P.; Chang, L. Y.; Geyer, S. M.; Wanger, D.; Binda, M. T.; Arango, A. C.; Bawendi, M. G.; Bulovic, V. Colloidal PbS Quantum Dot Solar Cells with High Fill Factor. *ACS Nano* **2010**, *4*, 3743−3752.
(35) Kirmani, A. R.; Sheikh, A. D.; Niazi, M. R.; Haque, M. A.; Liu, M. X.; de Arquer, F. P. G.; Xu, J. X.; Sun, B.; Voznyy, O.; Gasparini, N.; Baran, D.; Wu, T.; Sargent, E. H.; Amassian, A. Overcoming the Ambient Manufacturability-Scalability-Performance Bottleneck in Colloidal Quantum Dot Photovoltaics. *Adv. Mater.* **2018**, *30*, No. 1801661.
(36) Chuang, C. H.; Maurano, A.; Brandt, R. E.; Hwang, G. W.; Jean, J.; Buonassisi, T.; Bulovic, V.; Bawendi, M. G. Open-Circuit Voltage Deficit, Radiative Sub-Bandgap States, and Prospects in Quantum Dot Solar Cells. *Nano Lett.* **2015**, *15*, 3286−3294.
(37) Speirs, M. J.; Dirin, D. N.; Abdu-Aguye, M.; Balazs, D. M.; Kovalenko, M. V.; Loi, M. A. Temperature Dependent Behaviour of Lead Sulfide Quantum Dot Solar Cells and Films. *Energy Environ. Sci.* **2016**, *9*, 2916−2924.
(38) Mozer, A. J.; Sariciftci, N. S.; Lutsen, L.; Vanderzande, D.; Osterbacka, R.; Westerling, M.; Juska, G. Charge Transport and Recombination in Bulk Heterojunction Solar Cells Studied by the Photoinduced Charge Extraction in Linearly Increasing Voltage Technique. *Appl. Phys. Lett.* **2005**, *86*, No. 112104.

DOI: 10.1021/acsami.9b07605
ACS Appl. Mater. Interfaces 2019, 11, 26100−26108

(39) Shuttle, C. G.; O'Regan, B.; Ballantyne, A. M.; Nelson, J.; Bradley, D. D. C.; de Mello, J.; Durrant, J. R. Experimental Determination of the Rate Law for Charge Carrier Decay in a Polythiophene: Fullerene Solar Cell. *Appl. Phys. Lett.* **2008**, *92*, No. 093311.

(40) Tang, J.; Brzozowski, L.; Barkhouse, D. A. R.; Wang, X. H.; Debnath, R.; Wolowiec, R.; Palmiano, E.; Levina, L.; Pattantyus-Abraham, A. G.; Jamakosmanovic, D.; Sargent, E. H. Quantum Dot Photovoltaics in the Extreme Quantum Confinement Regime: The Surface-Chemical Origins of Exceptional Air- and Light-Stability. *ACS Nano* **2010**, *4*, 869−878.

(41) Boles, M. A.; Ling, D.; Hyeon, T.; Talapin, D. V. The Surface Science of Nanocrystals. *Nat. Mater.* **2016**, *15*, 141−153.

(42) Zherebetskyy, D.; Scheele, M.; Zhang, Y. J.; Bronstein, N.; Thompson, C.; Britt, D.; Salmeron, M.; Alivisatos, P.; Wang, L. W. Hydroxylation of the Surface of PbS Nanocrystals Passivated With Oleic Acid. *Science* **2014**, *344*, 1380−1384.

DOI: 10.1021/acsami.9b07605
ACS Appl. Mater. Interfaces 2019, 11, 26100−26108